5-2005

Characterizing Deformation, Damage Parameters, and Clay Composition in Fault Zones: Insights from the Chelungpu Thrust, Taiwan, and Mozumi Right Lateral Fault, Japan

Angela J. Isaacs
Utah State University

CHARACTERIZING DEFORMATION, DAMAGE PARAMETERS, AND CLAY COMPOSITION IN FAULT ZONES: INSIGHTS FROM THE CHELUNGPU THRUST, TAIWAN, AND MOZUMI RIGHT LATERAL FAULT, JAPAN

by

Angela J. Isaacs

A thesis submitted in partial fulfillment
of the requirements for the degree

of

MASTER OF SCIENCE

in

Geology

Approved:

James P. Evans Major Professor	Susanne U. Janecke Committee Member
Peter T. Kolesar Committee Member	Laurens H. Smith, Jr. Interim Dean of Graduate Studies

UTAH STATE UNIVERSITY
Logan, Utah

2005

ABSTRACT

Characterizing Deformation, Damage Parameters, and Clay Composition in Fault Zones: Insights from the Chelungpu Thrust, Taiwan, and Mozumi Right Lateral Fault, Japan

by

Angela J. Isaacs, Master of Science

Utah State University, 2005

Major Professor: Dr. James P. Evans
Department: Geology

The Chelungpu thrust fault, Taiwan, and the Mozumi right-lateral fault, Japan, provide an opportunity to characterize active faults in clastic sedimentary rocks and provide constraints to seismologic models. The northern Chelungpu fault has a 10-30 m wide primary damage zone characterized by dense fractures and chemical alteration. The southern Chelungpu fault has a 25-70 m wide primary damage zone characterized by dense fractures, alteration, intensely sheared rock, and secondary faults. The complexity of the damage zone, geochemistry, and clay mineralogy of the southern fault zone reflects its greater maturity (~1 Ma) relative to the northern fault zone (~46-100 Ka). A transition exists from smectite in exhumed fault core to illite-rich fault core at depth (200 - 1000 m) due to co-seismic fluid flow and radiated seismic energy. Clay composition plays a role in fault weakening.

Microstructures in deformed Mozumi siltstone indicate syn-tectonic fluid pressurization and flow, and shear concentrated in sericite-rich matrix. Kaolinite and illite clays dominate the host rock and fault breccia; illite, smectite, and kaolinite dominate clay-rich fault breccia. Whole-rock geochemistry shows a depletion of most oxides in fault rocks relative to unaltered host rock (up to ~90%). Resistivity values are depressed by 0-50 ohm-m, and ν_p and ν_s are decreased by ~0.30 km/s and ~0.40 km/s across the main fault relative to wall rock, and an average of ~0.70 km/s and ~1.0 km/s relative to host rock, respectively. Calculated values of Young's modulus and Poisson's ratio of fault rocks range from 16.2 to 44.9 GPa and 0.263 to 0.393, respectively. The protolith has a calculated Young's modulus of 55.4 GPa and a Poisson's ratio of 0.242. Lowest values of Young's modulus and highest values of Poisson's ratio correspond to fault breccia with high fluid content, and are offset from the most altered and damaged fault rocks. Fluid-rich pockets, and thus alteration, apparently migrate through the fault zone and may facilitate creep on the Mozumi fault because these fluid rich rocks are unable to sustain the shear stresses needed for brittle failure. The Chelungpu and Mozumi faults illustrate the temporally dynamic and heterogeneous nature of active fault zones.

(216 pages)

ACKNOWLEDGMENTS

Financial support for this work was provided by Drilling, Observation and Sampling of the Earth's Continental Crust, Inc. (DOSECC), American Association of Petroleum Geologists (AAPG) Grants in Aid Program, the Eastern Asia Pacific Summer Institute Program (EAPSI) and the National Science Foundation (NSF), Taiwan, and the United States Geological Survey (USGS) National Earthquake Hazard Reduction Program (NEHRP). Dr. Seng-Rong Song of National Taiwan University was my host while in Taiwan on the EAPSI Program, and helped me coordinate field and laboratory work. Li-Wei Kuo and Shao-Yi Huang were of enormous help to me while in Taiwan, as well as good friends. And thank you to Hiroyukin Nakayama for translating figure captions and tables in Japanese.

I would like to thank my advisor, Jim Evans, for his endless guidance and support during my work as both an undergraduate and a master's student. Jim has a way of making those who work with him feel like they have the greatest ideas in the world, and that every discovery is something grand and new (even though he has known about your "discovery" for years). His excitement and love for geology is infectious – what an awesome experience a thesis is when working with Jim! I would also like to thank my committee members. To Pete Kolesar, I am grateful for the introduction to geology, as well as battling the demon that is the XRD machine with me. Pete spent a great deal of time teaching me XRD techniques and interpretations, and has been critical to the clay mineralogy presented in this thesis. Pete has also been a good friend for my entire career

as a geologist at USU. To Susanne Janecke, I would like to extend my appreciation for great edits and input towards the final product of my thesis.

I would also like to thank John Solum for his expertise and guidance into the small and frightening world of modeling clay mineralogy. Also, a big thank you to all of the faculty here at USU. I have enjoyed working with each faculty member and owe my success to everyone in this department. And Lori Hirschi . . . what would the department be without her? Thanks to Lori for good talks, good advice, lots of help, and good laughs. I also owe Alex Steely, Sarah Draper, Scott Freidman, Ben Kessel, and Joe Jacobs my appreciation for their friendship, a little sanity, and good times (even though I am not what one would call a party animal). And finally, thanks to my awesome family for their support (even to those who STILL think that I am an archeologist) and especially my husband, Kyle. Thanks Kyle for believing that I'm the smartest woman in the world.

Angela Isaacs

CONTENTS

Page

LIST OF TABLES

LIST OF FIGURES

CHAPTER 1

INTRODUCTION

1-1. INTRODUCTION

The composition and structure of the near-surface portion of brittle fault zones can be divided into three components: the fault core, damage zone, and protolith (Chester and Logan, 1986; Chester et al., 1993, 2004; Evans and Chester, 1995; Caine et al., 1996; Wilson et al., 2003). The fault core is the portion of the fault zone that accommodates most of the slip on a fault and reflects high shear strain. It is typically characterized by geochemically altered and comminuted rocks such as fault gouge and can be millimeters to meters thick (Chester et al., 1993; Caine et al., 1996). Clay fault gouge is a clay-dominated, low-temperature fault rock (Vrolijk and van der Pluijm, 1999) that develops due to brittle deformation such as cataclasis associated with near-surface faulting (Scholz, 1990; Sibson, 1997) and alteration of the protolith (Goddard and Evans, 1995; Caine and Forester, 1999; Vrolijk and van der Pluijm, 1999; Solum et al., 2005). Clay gouge is present in the fault core and damage zone of many faults, including the Lewis Thrust, Canada, the Moab fault, Utah, the San Gabriel fault, California, and the Chelungpu Fault, Taiwan (Chester et al., 1993; van der Pluijm et al., 2001; Solum et al., 2005; Heermance et al., 2003). Within the fault core and fault gouge materials, a central ultracataclasite or several bands of ultracataclasite often define extremely localized slip surfaces (Chester and Logan, 1986, 1987; Anderson et al., 1983; Wallace and Morris, 1986; Chester et al., 1993) on the order of mm's thick (Heermance et al., 2003, Wilson et al., 2003).

The fault core is surrounded by a damage zone that is typically much thicker than the core and is characterized by an increased density of subsidiary faults, fractures, veins, foliation, and folding relative to the host rock (Chester and Logan, 1986; Caine et al., 1996). The damage zone records deformation inherited from past fault motion, presumably by repeated earthquakes (Chester and Logan, 1986; Caine et al., 1996; Schulz and Evans, 1998). The damage zone can further be divided into the primary damage zone (PDZ) and the secondary damage zone (SDZ; Jacobs, 2005). The primary damage zone surrounds the fault core, and, although it is not an area that accommodates significant slip, it is intensely fractured, and contains an increased abundance of secondary faults. The primary damage zone can exhibit significant chemical alteration as compared to the host rock, whereas the composition of the secondary damage zone more closely approximates the host rock. In many cases, the rock in the primary damage zone is shattered or highly fractured, and original rock structure is obscured. The secondary damage zone surrounds the fault core and primary damage zone and contains deformation associated with faulting, but with less intensity than the primary damage zone. Often bedding or foliation is recognizable in the secondary damage zone, but the rocks are fractured, folded and/or faulted in places. The protolith hosts the fault core and damage zone and is basically undamaged by faulting, but may contain regional structures. The host rock, or protolith, is an important control for background deformation structures and composition.

Faults, fractures, and clay mineralogy all influence fluid flow properties, fault strength, and the distribution of seismic energy in the fault zone. The orientation of microfractures and phyllosilicates may influence a fluid's ability to flow across the fault

core (Caine and Forster, 1999). Comminution and geochemical reactions in the fault core result in mineral precipitation, phyllosilicate growth, and reduced permeability causing the fault core to act as a barrier to fluid flow. Meanwhile, the highly fractured damage zone may promote fault-parallel fluid migration (Caine et al., 1996; Evans et al., 1997; Caine and Forester, 1999). Observations of exhumed large-displacement faults of the San Andreas system by Chester et al. (1993) suggest that coseismic dilatancy and microfractures create permeability in the fault core and fluid is pumped into the fault core. During interseismic periods, healing of fractures and compaction serve to trap pore fluids in the core and create high pore pressures. Chester et al. (1993) propose this mechanism as an explanation for the weak nature of the San Andreas Fault.

Another hypothesis suggests that rocks with original low permeability may show enhanced fluid flow in the fault core due to clay alteration such as the reaction:

$$\text{smectite} + Al^{3+} + K^{+} \longrightarrow \text{illite} + Si^{4+} \text{ (Ho et al., 1999)} \qquad [1]$$

where less permeable smectite is converted to illite via co-seismic heat flow (Vrolijk and van der Pluijm, 1999; Solum et al., 2005). Concentration of clay and trapped water in the fault core may serve to weaken the fault both mechanically and by creating a pore-fluid pressure gradient across the fault zone (Solum et al., 2005).

The reaction of smectite (S) to illite (I) in sedimentary basins is well documented and is a considered a classic reaction of clastic diagenesis. The formation of illite from smectite requires the addition of Al and the removal of Si (Abercrombie et al., 1994). Therefore, Si is a byproduct of the S-I reaction (Figure 1-1). Smectite (montmorillonite) becomes increasingly unstable with rising temperature due to burial, igneous activity, or

hydrothermal fluids, and dewaters to form illite interlayered with smectite (Wang, 1984). This process continues with burial and the percentage of illite in I-S increases until smectite converts entirely to illite by ~ 400^{o}C (Wang, 1984; Abercrombie et al., 1994). I-S interlayers begin to form at ~ 100^{o}C – 150^{o}C as sheet structure smectite breaks down to illite and/or chlorite (Freed and Peacor, 1989; Moore and Vrolijk, 1992). The transition from the upper aseismic to lower seismic zone in subduction thrust systems is coincident with the temperature range where the smectite to illite conversion initiates (Hyndman, 2004).

The process by which illitization occurs – whether dissolution of smectite and subsequent mineralization of illite in the presence of K^{+}, solid solution, or a mixture of processes – is unclear (Abercrombie et al., 1994; Moore and Reynolds, 1997). The reaction does, however, seem to rely on three variables: 1) time, 2) heat, and 3) the availability of K^{+} (Moore and Reynolds, 1997) and is heavily affected by a fourth variable: presence and composition of fluids that can provide heat and transport ions (Whitney, 1990). Laboratory experiments by Whitney (1990) show that the illitization reaction is enhanced with increasing water to rock ratios. This effect is most pronounced at lower temperatures (250^{o}C vs. 400^{o}C in these experiments). In addition, the crystalline byproducts of the illitization reaction are dependent upon the ratio of fluids to rock. Fluid-deficient samples produce opal-CT (amorphous hydrous quartz), while fluid-rich samples produce chlorite and cristobalite or quartz.

Vrolijk and van der Pluijm (1999) observed illite in fault cores surrounded by smectite-dominated host rocks without indication of burial depths or fluid interactions (veins) sufficient to drive the S-I reaction. In the absence of heat or fluid flow as driving

forces, they propose that seismic energy (shear stress and coseismic heat flow) overcomes the kinetic barrier and drives smectite to illite reactions. This has important implications for fault zone and seismological studies, as the frictional properties of illite and smectite differ. Smectite (montmorillonite) has a coefficient of friction of ~ 0.2 when wet, while illite has coefficient of friction of ~ 0.45 (Lockner and Beeler, 2002). Montmorillonite behavior is described by stable sliding (aseismic) and illite behavior is described by stick-slip (seismic), which has been proposed as an analog for the earthquake cycle (Brace and Byerlee, 1966). Phyllosilicates in the fault core have been identified by many workers as an important mechanism for fault weakening (Wu, 1978; Chester et al., 1993; Evans and Chester, 1995; Wintsch et al., 1995). Smectite has been documented as a major constituent of fault gouge (Wu, 1978; Chester and Logan, 1986; Solum et al., 2003; Jacobs, 2005) as has illite (Vrolijk and van der Pluijm, 1999; Solum et al., 2005) and other clays including chlorite, kaolinite, and palygorskite (Solum and van der Pluijm, 2004; Hashimoto et al., *in press*; Jacobs, 2005; this study).

Evaluation of fault zone structures and composition provides insight into issues of fluid flow, fault strength, and fault maturity or accumulated damage on a fault. The relation of outcrop and micro-scale fault properties to fault geometry helps to determine the causes of specific fault rupture styles. Additionally, shale- and clay-rich fault zones are not typically well preserved because they weather easily, and are therefore not well studied at the microstructural and outcrop scale. The two faults evaluated in this study, the Chelungpu Fault (CLF), Taiwan, and the Mozumi Fault (MF), Japan, provide a valuable opportunity to characterize shale- and clay-rich fault zones. Seismic models and earthquake physics studies require data of the type provided by this study (Beroza, 1991;

Spudich et al., 2001). Data and interpretation made in this study will provide an important building block in our knowledge of fluid flow properties of shale- and clay-rich faults and energy distribution of faults.

Motivation

Characterization of fine-grained, clay-rich fault zones is important for several reasons:

1) Faults act as conduits or barriers to fluid flow (Caine et al., 1996; Evans et al., 1997). Fault zone studies clarify the fault's role as seal or leak in petroleum systems and other natural and man-made systems (such as CO_2 sequestration). X-ray diffraction (XRD) analyses have identified illite, kaolinite, smectite, and chlorite in the Chelungpu fault and Mozumi fault zones. These data can be used for detailed studies of clay gouge and associated fluid flow properties as proposed by Solum et al. (2003), Vrolijk and van der Pluijm (1999), and Chester and Logan (1986).

2) The Chelungpu fault offers an opportunity to study changing fault styles and composition along strike in the same fault. In addition, regional tectonics, climatic factors, and other variables are held nearly constant for this single fault, and evaluation of rupture styles can be made without the complications of comparing different faults. Damage zones and associated deformation clearly increase in size and intensity and change in character from the northern to southern fault segments of the Chelungpu fault at both microstructural and outcrop scales (Heermance et al., 2003). The maturity of the fault zone segments or amount of accumulated damage may be an important key to characteristic differences along the fault trace. Seismological studies (Bouchon, 1997; Spudich et al., 2001) suggest that faults have variable stresses on them due in part to fault

composition. Variations in rupture style could be due to compositional differences and fault maturity along strike of the Chelungpu fault. The Mozumi fault offers an important opportunity to study the in-situ properties of an active fault. Geophysical logs are available for the Mozumi fault, which, when used in combination with core samples from the fault zone, provide a physical and mechanical description of an active, strike-slip fault.

3) Fault zone studies are essential to providing geologic data to the seismological community. Seismological data provide powerful insights into fault zone structure, but require verification from real fault zones. Models of fault zones currently debated in the seismological community include the interpretation of fault-zone-guided waves and the nature of slip on faults (Li and Vidale, 1996; Bouchon, 1997). Fault-zone-guided waves are earthquake-generated waves trapped in the damage zone of a fault, and can greatly amplify ground motion, resulting in increased damage. The study of fault zone guided waves can result in the ability to map areas of increased seismic hazard (Spudich and Olsen, 2001). This has a direct effect on society, as many lives can be saved with our increased ability to design earthquake models appropriate to an area based on its specific geology. Our work can address issues of along-strike variations in fault strength and slip properties, which may greatly affect the rupture velocity, acceleration, and displacement at a given point (Beroza, 1991; Bouchon, 1997). The data from the Mozumi fault enable us to make observations of the fault zone, compare structure, and relate these to petrophysical and geophysical data of the fault zone.

1-2. METHODOLOGY

Field Methods

A transect sampling method was employed for all Chelungpu fault outcrop sites in this study. Samples were collected for laboratory tests at a maximum spacing of 5 m throughout the fault zone (fault core, primary damage zone, secondary damage zone). Areas of special interest, such as the primary damage zone and fault core, were sampled using 1 m sample spacing and picking samples of interest. Structural samples of fault gouge were oriented and collected for petrographic analysis. All distances were recorded east and west from the location of the 1999 rupture trace when possible. A detailed transect map through the hanging wall of each field site was created. Transect maps were used to record widths of fault zone components, orientations and qualitative abundance of fractures, secondary faults, strands of gouge, folding, bedding orientations, and other structural and lithological elements.

The width of the fault core is defined by the distance from the fault plane to the edge of the fault gouge. Fault gouge is recognized in the field as a tacky, clay-rich material with nearly-ductile behavior when wet, often foliated and sheared, and typically distinguishable from the surrounding wall rock by its appearance, feel, and often color. The width of the primary damage zone is defined by the transect length from the outside edge of the fault core to a significant decrease in density of macroscopic damage elements. The change from primary damage zone to secondary damage zone is marked by any combination of: the first appearance of bedding, a decrease in fracture density, color changes, decrease in alteration, a decrease in the amount of subsidiary faults, fault gouge and shear zones, and on changes in the dominant type of deformation. Both the

width of fault core and the width of the primary damage zone are measured only for the hanging wall rocks. Footwall rocks of the Chelungpu fault are usually gravel and show little recognizable damage. The lack of damage is likely due to the character of the footwall surficial deposits. They are commonly unconsolidated boulder conglomerates with well-rounded clasts that are stronger than the hanging wall siltstones. The void space created by the size of the boulders, their strength, and the unconsolidated nature of the gravels allows the boulders to move and resist deformation that can be later recognized as fault-related. Abbreviated field notes and transect details are located in Appendix A.

No surface exposures are available across the Mozumi fault. Thus, I examined 10 core samples from the Mozumi fault zone, and interpreted tunnel mapping supplied by mine geologists. Map-scale and mesoscopic structural data were provided by Japan Nuclear Fuel Cycle staff from an internal report. Core is critical for examining microstructural properties, obtaining a geochemical signature, and evaluating the mechanical and hydrologic properties of the Mozumi fault. In addition, data available for this study from the Mozumi fault include core logs and borehole geophysical data, allowing a direct comparison of the nature of rock deformation, alteration and mechanical and physical properties.

Laboratory Methods

Sample chips for thin section study of the Chelungpu fault and Mozumi fault were prepared at Utah State University, and were used by Burnham Petrographics to create thin sections. Fragile samples were vacuum impregnated with *Petropoxy 154*^{tm}.

Optical microscopy was completed for samples from core and outcrop of the Chelungpu fault and core across the Mozumi fault zone.

Bulk and clay x-ray diffraction (XRD) was used to determine sample mineralogy and clay composition and relative amounts for the Chelungpu fault zone. The XRD was performed using Department of Geology facilities at Utah State University and National Taiwan University. Un-oriented powdered bulk samples were analyzed over a range of 5^o to 75^o 2θ using copper K-alpha radiation and a Cu target with voltage = 45 kV and current = 40 mA. Bulk powder samples were used for preliminary evaluation of relative amounts of clay in samples. This method is valid because powder was end-packed into identical sample holders, assuring that sample size and amount were the same for all bulk XRD samples.

Clay XRD analyses was performed using clay samples with preferential orientation of the 001 set of planes, and therefore enhanced intensity of the 001 clay peaks on XRD patterns. Clay samples were analyzed over a range of 3^o to 33^o 2θ. Ethylene glycol was used to expand the clay samples and test for swelling clays (smectite, C-S and I-S). Heating samples to 550^oC helped distinguish kaolinite from chlorite, as the structure of kaolinite collapses with heat. Some methods for the preparation of samples for clay XRD are listed in Appendix B.

Newmod™ (Reynolds and Reynolds, 1996) was used in some cases for a quantitative estimation of the amount of illite, smectite, and I-S clays. Newmod™ software calculates synthetic XRD patterns for comparison to real patterns and models the amount of clays using peak positions and relative intensities. The parameters of the XRD machine are entered into Newmod™ and other parameters can be varied including

clay type, Fe and K content, and ordering (Reichweite). The "file mixer" function of Newmod™ can be used to combine synthetic clay patterns, and was used to create a synthetic XRD pattern for discrete illite, discrete smectite, and mixed-layer I-S in a single pattern. Details for the use of Newmod™ can be found in the Newmod™ user manual and Moore and Reynolds (1997, references therein). A script written for Matlab and provided by J.G. Solum was also used to match Newmod™-generated I-S patterns to real XRD patterns.

Geochemical analyses using x-ray fluorescence (XRF) and Inductively Coupled Plasma (ICP) Mass Spectrometry (MS) $LiBO_2$ fusion analysis were used to detect the percent amounts of major, minor, and trace elements with a detection limit of 0.01% for major and minor oxides and 10 ppm for trace elements. Loss on ignition (LOI) of volatiles, primarily H_2O and CO_2, was determined from baking the samples and recording the weight loss. These analyses aid in the investigation of compositional changes in the fault due to deformation or fluid flow (translocation of elements). The XRF work was completed at National Taiwan University and ICP MS by XRAL Laboratories (SGS) in Ontario, Canada. Appendix C lists raw ICP MS data.

Weathering can cause complications when working with the geochemistry and mineralogy of exhumed fault rocks. Surficial weathering processes can overprint the fault zone signature. This issue is dealt with in two ways. First, we compare host rock and fault zone samples from drill holes to exhumed fault rocks to determine the mineralogical and geochemical differences and get a sense of alteration. Second, we develop a crystallinity index after Moore and Reynolds (1997) and Solum et al. (2003). Large crystallites are interpreted as representing neoformed clay minerals and small

crystallites as representing clay minerals formed by weathering processes (Moore and Reynolds, 1997). The crystallinity index uses the width of clay peaks from XRD patterns because peak width is dependent on crystallite size.

MultiVariate Statistical Package 3.1 by Kovach Computing Services was used to perform principal component analysis (PCA) on the oxides, trace elements, and LOI ICP results in order to determine the most significant variables. Principal component analysis extracts axes from a cluster of data that describe the variance of the data set. The first axis is aligned with the greatest variance, the second axis with the second greatest variance, and so forth. Each variable, in this case the values for oxides and trace elements, are assigned a component loading. Component loading is the relative importance of each variable in each of the extracted PCA axes. Thus, the variables with the greatest component loading, either positive or negative, account for the greatest amount of variance in the data set, and are termed "significant variables." Principal component analysis can account for the variance in data sets of this study using two axes. Principal component analysis assumes an open data set, however the geochemical data are given in percentages (closed data set). A log 10 transformation was used to convert to an open data set prior to Principal Component Analysis.

1-5. SUMMARY OF WORK

This thesis presents the results of field work on the Chelungpu fault, Taiwan and laboratory work on Chelungpu fault and Mozumi fault zone, Japan samples. Chapter 2 characterizes the Chelungpu fault and discusses variations of fault zone properties both

along strike and with depth. I discuss the implications of deformation and clay mineralogy for fault evolution and earthquake rupture.

Chapter 3 characterizes the microstructures, mineralogy, and geochemistry of the Mozumi fault zone rocks. These properties are compared to well logs, and the implications of the velocity structure and physical properties of the Mozumi fault are discussed.

Chapter 4 concludes and summarizes the work described in chapters 2 and 3, draws some relationships between the study of the Chelungpu fault and Mozumi fault zones, and examines the implications of the fault zone studies for earthquake processes and seismic models.

References

Abercrombie, H.J., I.E. Hutcheon, J.D. Bloch, and P. de-Caritat (1994). Silica activity and the smectite-illite reaction, *Geology* **22**, 539-542.

Anderson, J.L., R.H. Osborne, and D.F. Palmer (1983). Cataclastic rocks of the San Gabriel fault – an expression of deformation at deeper crustal levels in the San Andreas fault zone, *Tectonophysics* **98**, 209-251.

Brace, W.F., and J.D. Byerlee (1966). Stick-slip as a mechanism for earthquakes, *Science* **153**, 990-992.

Beroza, G.C. (1991). Near-source modeling of the Loma Prieta earthquake: evidence for heterogeneous slip and implications for earthquake hazard, *Bull. Seism. Soc. Am.* **81**, 1603-1621.

Bouchon, M. (1997). The state of stress on some faults of the San Andreas system as inferred from near-field strong motion data, *J. Geophys. Res.* **B102**, 11731-11744.

Caine, J.S., and C.B. Forster (1999). Fault zone architecture and fluid flow; insights from field data and numerical modeling, *Geophys. Monograph* **113**, 101-127.

Caine, J.S., J.P. Evans, and C.B. Forster (1996). Fault zone architecture and permeability structure, *Geology* **24**, 1025-1028.

Chester, F.M., and J.M. Logan (1986). Implications for mechanical properties of brittle faults from observation of the Punchbowl fault zone, California, *Pageoph.* **124**, 79-106.

Chester, F.M., and J.M. Logan (1987). Composite planar fabric of gouge from the Punchbowl Fault, California, *J. Struc. Geol*. **9**, 621-634.

Chester, F.M., J.P. Evans, and R.L. Biegel (1993). Internal structure and weakening mechanisms of the San Andreas Fault, *J. Geophys. Res*. **98**, 771-786.

Chester, F.M., J.M. Chester, D.L. Kirschner, S.E. Schulz, and J.P. Evans (2004). Structure of large-displacement, strike-slip fault zones in the brittle continental crust, in *Rheology and Deformation of the Lithosphere at Continental Margins,* G. D. Karner, J.D. Morris, N.W. Driscoll, and E.A. Silver (Editors), Columbia University Press, New York, New York, 223-260.

Evans, J. P., and F. M. Chester (1995). Fluid-rock interaction in faults of the San Andreas system: Inferences from San Gabriel fault rock geochemistry and microstructures, *J. Geophys. Res*. **100**, 13007-13020.

Evans, J.P., C.B. Forster, and J.V. Goddard (1997). Permeability of fault-related rocks, and implications for hydraulic structure of fault zones, *J. Struc. Geol*. **19**, 1393-1404.

Freed, R.L., and D.R. Peacor (1989). Variability in temperature of the smectite/ illite reaction in Gulf Coast sediments, *Clay Min*. **24**, 171-180.

Goddard, J.V., and J.P. Evans (1995). Chemical changes and fluid-rock interaction in faults of crystalline thrust sheets, northwestern Wyoming, U.S.A., *J. Struc. Geol*. **17**, 533-547.

Grim, R.E. (1962). Clay mineralogy, *Science*, **135**, 890-898.

Hashimoto, Y., K. Ujiie, A. Sakaguchi, and H. Tanaka (*in press*). Characteristics and implication of clay minerals in the northern and southern Chelung-pu fault, Taiwan, to *Tectonophysics*.

Heermance, R.V., Z.K. Shipton, and J.P. Evans (2003). Fault structure control on fault slip and ground motion during the 1999 rupture of the Chelungpu fault, Taiwan, *Bull. Seism. Soc. Am*. **93**, 1034-1050.

Ho, N.C., D.R. Peacor, and B.A. van der Pluijm (1999). Preferred orientation of phyllosilicates in Gulf Coast mudstones and relation to the smectite-illite transition, *Clay Clay Min*. **47**, 495-504.

Hyndman, R.D. (2004). Controls on subduction thrust earthquakes: downdip changes in composition and state, in *Rheology and Deformation of the Lithosphere at Continental Margins,* G.D. Karner, B. Taylor, N.W. Driscoll, and D.L. Kohlstedt (Edsitors), Columbia University Press, New York, New York, 166-178.

Jacobs, J.R. (2005). Examination of exhumed faults in the western San Bernardino mountains, California: Implications for fault growth and earthquake, *Master's Thesis*, Utah State University, Logan, Utah.

Li, Y.G., and J.E Vidale (1996). Low-velocity fault-zone guided waves: Numerical investigations of trapping efficiency, *Bull. Seism. Soc. Am*. **86**, 371-378.

Lockner, D.A., and N.M. Beeler (2002). Rock failure and earthquakes, in *International Handbook of Earthquake & Engineering Seismology*, W. H. K. Lee, H. Kanamori, P.C. Jennings, and C. Kisslinger (Editors), Academic Press, San Diego, California, 505-533.

Moore, D.M., and R.C. Reynolds Jr. (1997). *Individual Clay Minerals, X-ray Diffraction and the Identification and Analysis of Clay Minerals*, Oxford University Press, New York, New York.

Moore, J.C., and P. Vrolijk (1992). Fluids in accretionary prisms, *Rev. Geophys.* **30**, 113-135.

Reynolds Jr., R.C., and R.C. Reynolds III (1996). *NEWMOD*™, *a computer program for the calculation of one-dimensional diffraction patterns of mixed-layered clays,* http://www.angelfire.com/md/newmod/.

Scholz, C.H. (1990). The mechanics of earthquakes and faulting, *Science* **250**, 1758-1759.

Schulz, S. E., and J. P. Evans (1998). Spatial variability in microscopic deformation and composition of the Punchbowl Fault, Southern California; implications for mechanisms, fluid-rock interaction, and fault morphology, *Tectonophysics* **295**, 223-224.

Sibson, R. H. (1997). Fault rocks and fault mechanisms, *J. Geol. Soc. London* **133**, 190-213.

Solum, J. G., and B. A. van der Pluijm (2004). Phyllosilicate mineral assemblages of the SAFOD Pilot Hole and comparison with an exhumed segment of the San Andreas Fault System, *Geophys Res. Lett*. **31**, doi: 10.1029/2004GL019909.

Solum, J. G., B. A. van-der Pluijm, C. M. Hall, and D. R. Peacor (2005). Neocrystallization, fabrics and age of clay minerals from an exposure of the Moab Fault, Utah, *J. Struc. Geol*. **27**, 1563-1576.

Solum, J. G., B. A. van der Pluijm, D. R Peacor, and L. N. Warr (2003). Influence of phyllosilicate mineral assemblages, fabrics, and fluids on the behavior of the Punchbowl Fault, Southern California, *J. Geophys. Res*. **B108**, doi: 10.1029/2003GL02098.

Spudich, P., and K.B. Olsen (2001). Fault zone amplified waves as a possible seismic hazard along the Calaveras fault in central California, *Geophys. Res. Lett*. **28**, 2533-2536.

van der Pluijm, B. A., C. M. Hall, and P. J. Vrolijk (2001). The dating of shallow faults in the Earth's crust, *Nature* **412**, 172-175.

Vrolijk, P. J., and B. A. van der Pluijm (1999). Clay Gouge, *J. Struc. Geol*. **21**, 1039-1048.

Wallace, R. E., and H. T. Morris (1986). Characteristics of faults and shear zones in deep mines, *Pure Appl. Geophys* **124**, 107-125.

Wang, C. Y. (1984). On the constitution of the San Andreas Fault zone in Central California, *J. Geophys Res*. **89**, 5858-5866.

Whitney, G. (1990). Role of water in the smectite-to-illite reaction. *Clays Clay Min*. **38**, 343-350.

Wilson, J. E., J. S. Chester, and F. M. Chester (2003). Microfracture analysis of fault growth and wear processes, Punchbowl fault, San Andreas system, California, *J. Struc. Geol*. **25**, 1855-1873.

Wintsch, R. P., R. Christofferson, and A. K. Kronenberg (1995). Fluid-rock reaction weakening of fault zones, *J. Geophys Res*., **100**, 13021-13032.

Wu, T. F. (1978). Mineralogy and physical nature of clay gouge, *Pageoph.* **116**, 655-679.

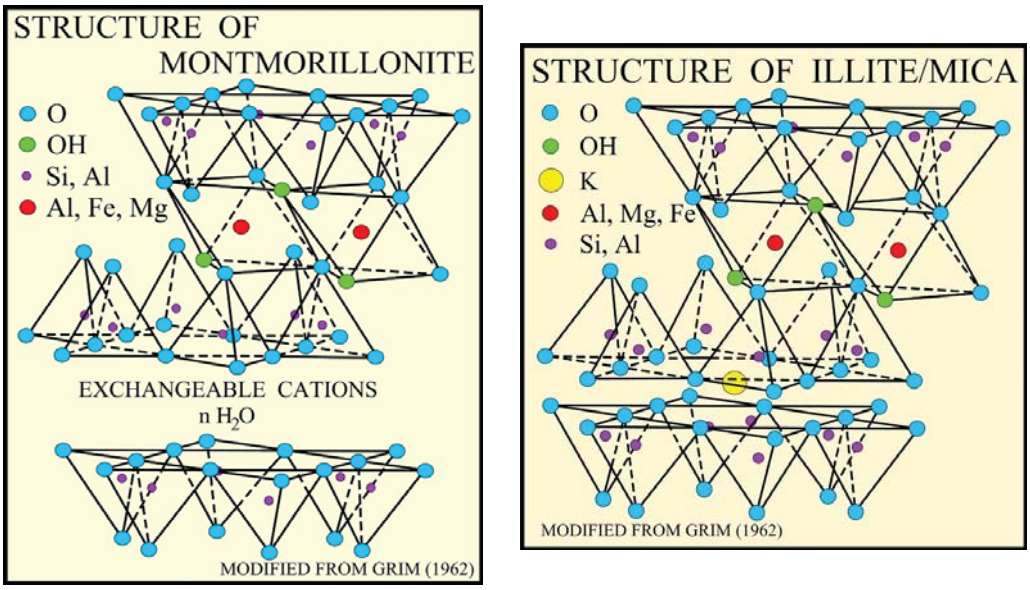

Smectite-Illite Reaction Sequence

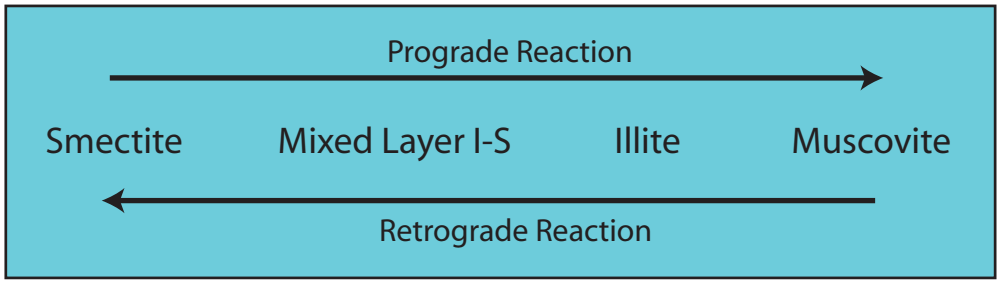

Figure 1-1. The structures of montmorillonite (smectite) and illite are shown above (Grim, 1962). Montmorillonite and illite have the same structure, but montmorillonite lacks the K present in illite, and has more Si and H_2O than illite. The reactions in the box below illustrate the sequence of clay products in the smectite-illite reaction.

CHAPTER 2

STRUCTURAL, MINERALOGICAL, AND GEOCHEMICAL CHARACTERIZATION OF THE CHELUNGPU THRUST FAULT, TAIWAN[1]

ABSTRACT

The Chelungpu fault, Taiwan, produced a northward propagating rupture on September 21, 1999 resulting in an M_w 7.6 earthquake and an ~90 km long N-S trending fault scarp. The mineralogic and physical character of the fault-related rocks within the Chelungpu fault zone, as measured at 9 sites along 70 km of the 1999 rupture trace, changes significantly along strike and with depth. The northern section of the Chelungpu fault has a 10-30 m-wide primary damage zone that is characterized by increased fracture density and alteration, but little microstructural damage as close as 1 m from the main fault. The southern section of the Chelungpu fault has a 20-70 m wide primary damage zone that is characterized by increased fracture density and alteration, intensely sheared rock, and numerous secondary faults and gouge zones as far as 240 m from the main fault. The complexity of the damage zone, geochemistry, and clay mineralogy of the southern fault zone reflects its relative maturity (~1 Ma) compared to the northern fault zone (~46-100 Ka). The major down-dip variation is a transition from 10-30% smectite in the illite + smectite clay fraction of exhumed fault cores to <10% or no smectite in the illite + smectite clay fraction of illite-rich clay gouge in the fault core at sampled depths of 200 to 1000 m. This transition may be influenced by weathering processes at the surface, however co-seismic fluid flow probably plays a role in illite-smectite reactions.

[1]Co-authored manuscript by A.J. Isaacs, J.P. Evans, S.R. Song, and P.T. Kolesar

The composition of clays has important seismologic implications as clays play a role in fault weakening and probably the transition from the seismic to up-dip aseismic zone.

2-1. INTRODUCTION

Study Area

The Chelungpu thrust fault (CLF) is part of the fold-and-thrust belt of the western Taiwan orogen (Figure 2-1; Chen and Kao, 2000) that cuts shallow marine upper Miocene and Pliocene siltstone, shale, and sandstone of the Kueichulin, Chinshui, and Cholan Formations (Covey, 1984), and defines the boundary between the western foothills and foreland basin to the west (Figure 2-2; Chiu, 1971; Suppe, 1987; Heermance et al., 2003). Near the surface, the fault dips to the east 52^{o} to 60^{o} along the northern segment and places siltstones of the Chinshui and Kueichulin Formations on Quaternary gravels and siltstones of the Chinshui or Kueichulin Formation (Figure 2-3a; Lee et al., 2001; Heermance et al., 2003). The Chelungpu fault flattens overall to approximately 25^{o}-35^{o} E in the southern segment (Koa and Chen, 2000; Heermance et al., 2003) and places siltstones of the Chinshui and Kueichulin Formations on Quaternary gravels and Pleistocene Toukoshan gravels (Figure 2-3b; Heermance, 2002; Tanaka et al., 2002). An exception is the southern terminus of the Chelungpu fault where the fault is steeply dipping. The northern segment has an overall hanging wall flat on footwall flat geometry, whereas the southern segment has an overall hanging wall flat on footwall ramp geometry (Heermance et al., 2003). The Chelungpu fault cuts up-section within the Chinshui shale (E.C. Yeh, *submitted*) and locally, the fault cuts across bedding; thus, the fault does not strictly have a hanging wall flat geometry.

The September 21, 1999 M_w 7.6 earthquake produced a northward propagating rupture resulting in an ~90 km long north-south trending surface rupture on the Chelungpu fault (Figure 2-3c; Ma et al., 2000; Chen et al., 2001b). Co-seismic slip increased northward along the fault trace with an average throw of 2 m on the southern section of the fault as compared to a throw of 5-7 m (as much as 12-15 m at the Tachia River) and 7-9 m of horizontal displacement on the northern segment of the fault (Ma et al., 2000; Chen et al., 2001b; Lin et al., 2001). Strong ground motion, including high frequency acceleration and rupture velocity, decreased from south to north (Lin et al., 2001). The displacement was nearly pure thrust slip near the epicenter in the southern portion of the fault, and changed to oblique thrust with a strong left-lateral component in the north (Dalguer et al., 2001; Chen et al., 2001b; Lin et al., 2001). To the north, the rupture occurred in the hanging wall of an older fault strand called the Sanyi fault, whereas the rupture remained on the older established Chelungpu fault to the south (Figure 2-1, Figure 2-3c; Ho and Chen, 2000; Heermance et al., 2003). The new northern strand of the fault has so little displacement that rocks in the footwall and hanging wall are still in their original stratigraphic order across the fault at depth.

Lithology

The geologic formations involved in the Chelungpu fault zone include the Miocene Kueichulin Formation, Pliocene Chinshui shale, Plio-Pleistocene Cholan Formation, and the upper Pleistocene Toukoshan Conglomerate (Figure 2-2).

Kueichulin Formation

The Kueichulin Formation consists of light-gray, fine-grained massive sandstone interbedded with dark gray shale and sandy shale, with some white to brown-gray, fine-grained, loosely consolidated sandstone (Chiu, 1971). Ho (1975) divides the Kueichulin into lower, middle, and upper members. The lower Kuantaoshan Sandstone member is a fine to medium-grained light blue to gray sandstone interbedded with occasional dark shale and a few bands of pebbles. The sandstone is massive or thickly bedded with some muddy lenses, coal stringers, and abundant shale fragments. The thickness of the Kuantaoshan Sandstone is 250-300 m (Ho, 1975).

The middle member is named the Shihliufeng Shale and consists of dark gray shale with abundant fossils including foraminifera, mollusks, and crabs. This member is approximately 100-200 m thick (Ho, 1975).

The upper member, the Yetengping Sandstone, is a gray fine-grained, thick to medium-bedded sandstone with a muddy matrix, and interbedded with shale. It ranges from 250 to 550 m in thickness (Ho, 1975). The Kueichulin Formation lies conformably on top of the Nanchuang Formation (Ho, 1975).

Chinshui Shale

Ho (1975) describes the Chinshui Shale as dark gray shale interbedded with thin siltstone, mudstone, lenticular dark gray sandstone, and local marly nodules. It is characterized in outcrop by a spheroidal exfoliation, and contains shallow marine to deep neritic fauna including crabs, gastropods, foraminifera, and coral. The thickness varies considerably, from 80 to 400 m or greater (Ho, 1975). The Chinshui Shale contains a

higher percentage of the clay mineral montmorillonite than neighboring formations (Kuan, 1964).

Cholan Formation

The late Plio-early Pleistocene Cholan Formation consists of alternating sandstone, siltstone, shale, and mudstone layers (Ho, 1975). The sandstones are light blue-gray graywacke to subgraywacke, are fine-grained, and slightly micaceous. Sandstone beds are on the order of centimeters to 2 meters thick, and overall are poorly lithified (Ho, 1975). The mudstone and shale components are blue-gray to dark gray in 20 to 50 cm-thick beds, with some thicker shale beds (Ho, 1975). Sedimentary structures include cross stratification, ripples, slumps, load casts, ball and pillow structures in sandstone, reverse grading, normal grading, and conglomerate lenses and massive muddy sandstone in the upper part of the formation (Lee, 1963; Ho, 1975). In addition, fossilized drift wood, coal, echinoids, crabs, mollusks, and foraminifera can be found in the Cholan Formation (Ho, 1975). Ho (1975) reports that the Cholan Formation is 40-60% sandstone near the trace of the Chelungpu fault. South of the field area, the Cholan Formation changes to dominant siltstone and mudstone. The sandstone also exhibits better sorting and decreased mud content from the foothills to the west (Lee, 1963).

Toukoshan Conglomerate

The upper Pleistocene Toukoshan Conglomerate lies conformably on the Cholan Formation (Chou, 1977). The lower Hsiangshan Sandstone member is a light gray to brown-gray, fine to course-grained lithic graywacke and subgraywacke (including abundant slate, quartz, and feldspar grains) interbedded with blue-gray or gray shale and

some pebbly conglomerate beds (Ho, 1975; Chou, 1977). Clay is also reported in the sandstones (Lee, 1963). The grain size of sandstone decreases and becomes less muddy and better sorted from the foothills towards the west, but is overall coarser than Pliocene sands (Lee, 1963; Chou, 1977). Sedimentary structures include cross stratification, ripples, bioturbation, reverse grading, normally graded bedding, and slump features (Lee, 1963; Chou, 1977). The Hsiangshan Sandstone member is thickest at the western foothills (~2000 m) and thins to the west (~300 m; Chou, 1977).

The upper Huoyenshan Conglomerate member is chiefly (50%) quartzite pebbles, cobbles, and boulders and sedimentary clasts interbedded with a few thin, light to dark gray fine to coarse-grained lithic graywacke and subgraywacke sandstone beds and shale (Lee, 1963; Ho, 1975; Chou, 1977). Sedimentary structures include ripples, cross stratification, imbrication, some graded bedding, and slumps (Lee, 1963; Ho, 1975; Chou, 1977). The formation also contains occasional reef limestone (Chou, 1977). The Huoyenshan Conglomerate is ~1000 to 1500 m thick near the foothills and thins to 100s of meters to the west (Ho, 1975; Chou, 1977).

2-2. STUDY SITES OF THE FAULT ZONE

Fault exposures and drilled core through the Chelungpu fault zone show that the character and composition of the fault zone change significantly along strike and with depth at many scales. We examine portions of the core from 3 drilling projects and detailed transects and samples from 6 field sites (from 15 to 300 m long) to determine fault structure and composition, and the parameters that control deformation and alteration due to faulting, fluid flow, and exhumation of a fault zone (Figure 2-1).

Ten field sites were examined along the Chelungpu fault where the 1999 rupture is or was exposed in river cuts and excavation sites. Of the 10 field sites initially examined, 6 were selected to be fully analyzed and are presented in this study. The other 4 field sites were not included because they are intensely weathered and/or there are poor constraints on the location of the Chelungpu fault at these sites.

This study also incorporates mineralogical and geochemical data from previous and current studies of 3 drill holes; the Fengyuan, Nantou, and Taiwan Chelungpu-fault Drilling Project (TCDP), and samples from the Taiwan Chelungpu-fault Drilling Project. The structures of the Fengyuan and Nantou drill holes were described by Heermance (2002), Heermance et al. (2003), and Tanaka et al. (2002). The mineralogy and chemical composition of the Fengyuan and Nantou drilled cores was described by Liao (2003), Lu (2004), and Hashimoto et al. (*in press*). The Fengyuan drill site is located 2.1 km east-northeast of Fengyuan city. The drill hole is oriented 50^{o} to the west and reached a depth of 455.30 m along the borehole (348.78 m true vertical depth). The Nantou drill site is located 2.5 km southeast of Nantou city. The drill hole is vertical and reached a depth of 211.20 m. The TCDP site is located near TaKeng city, and is a vertical drill hole that reached a depth of 2003 m. Host rock samples were collected from the TCDP core primarily to provide a geochemical and mineralogical standard for comparison with samples from the exhumed fault zone at field sites. The Chelungpu fault zone was also observed in the TCDP drilled core. The locations of field sites and drill sites are shown on the geologic map of the Chelungpu fault area (Figure 2-1).

Field sites are described and numbered from north to south. Samples collected along a transect line at field sites are designated in two parts: 1) the component of the

fault zone to which each sample belongs, including the main fault or fault core (FC), fault gouge in subsidiary faults (FG), primary damage zone (PDZ), and secondary damage zone (SDZ), and 2) the numerical distance that each sample was collected from the main rupture trace, with the main fault being set at a value of zero. For example, FC 0+0 is a sample collected from fault core of the main fault, FG 0+3 is fault gouge collected from a secondary fault located 3 m into the hanging wall of the main fault trace, and PDZ 0+5 is a sample taken from the primary damage zone 5 m into the hanging wall along the line of transect. Additional details of transects and abbreviated field notes, as well as photographs, are located in Appendix A.

Drill sites are listed by name, and sample numbers typically incorporate an abbreviation of the drill site and the depth from which the sample was collected. Abbreviations of drill site names are adopted from previous publications and include BH 1A for the Fengyuan drill site (Tanaka et al., 2002; Heermance et al., 2003), CLF for the Nantou drill site (Tanaka et al., 2002; Heermance et al., 2003), and TCDP for the Taiwan Chelungpu-fault Drilling Project site (e.g. Sone et al., *submitted*). The number of samples used for laboratory analyses for each study site is listed in Table 2-1.

Characteristics of fault components at each field site or drill site will be compared to each other first. For example, the geochemistry of fault core, primary damage zone, and secondary damage zone rocks for a single field site is compared. Unaltered host rock, or protolith is not exposed in outcrop at the field sites. Thus, the secondary damage zone is assumed to be the least altered, and, where available, is contrasted with primary damage zone and fault core rocks to determine the progression of alteration from secondary damage zone through the fault core. Host rock is present in drilled cores, and

is used for comparison to fault rocks at each drill site. After each study site is characterized, data across the entire Chelungpu fault system will be compared. Percent changes of oxides in exhumed fault rocks was calculated using host rock samples from the TCDP, Fengyuan, and Nantou drill sites, and the nature of alteration indicated by these calculations will be discussed. Finally, the along-strike and down-dip variation in the Chelungpu fault will be summarized.

Field Site 1: Tachia River (大甲溪)
224823 E, 2686232 N

The northernmost field site along the trace of the Chelungpu fault is located on the Tachia River where the 1999 rupture created a waterfall and broke the Pifung Bridge (Figure 2-4; Chen and Lin, 1999). The fault places Chinshui Shale in the hanging wall against the Kueichulin Formation in the footwall (Heermance et al., 2003), had a throw of 11.5 m (Chen et al., 2001a), and an orientation of 050^{o}, 40^{o} SE at the surface. Bedding throughout this outcrop is uniform and strikes 045^{o} with dips ranging between 34^{o} and 56^{o} SE (Heermance et al., 2003; this study). The primary damage zone is characterized by an increased number and orientations of fractures until ~17 m into the hanging wall (Figure 2-4). Within the primary damage zone, there is a narrow brecciated zone (Figure 2-5; Heermance et al., 2003). No fault gouge is preserved in the outcrop, and the primary slip surface is below the water level, so it is unknown whether gouge was associated with this fault or not. A conjugate fracture set dominates the secondary damage zone with bearings of ~022^{o} and ~070^{o}. Minor slip has occurred on some of the 022^{o} joints, and these are more continuous than the 070^{o} fracture set. There are a few secondary faults

that are sub-parallel to the main fault and bedding with very little offset (Figure 2-4; Lee et al., 2002; this study).

Thin sections of samples collected from site 1 show intact rock with relatively little damage except a few micro-fractures and no evidence for shear within 1 m of the fault. There are a few quartz grains with intragranular fractures, but no foliation is developed in very fine-grained clayey layers (PDZ 0+1; Figure 2-6a). Pteropod fossils that are originally circular in cross section (Scholle, 1978) show no sign of elongation within 1 m of the fault trace (PDZ 0+1; Figure 2-6b). Quartz is the dominant mineral in thin section, with minor amounts of twinned feldspar, pyrite and/or hematite, and lithic fragments. Calcite cement and fine-grained brown matrix are also present. Fine-grained rocks in a secondary fault ~25 m into the hanging wall are not foliated (SDZ 0+25; Figure 2-6c). Occasionally, clay is concentrated in very thin, opaque, dark bands, but there is no evidence that these clays are related to or modified by faulting.

X-ray diffraction analysis (XRD) identifies quartz, feldspar, calcite, and clay minerals including kaolinite, illite, and chlorite (clinochlore) $\pm$ smectite (montmorillonite) in all samples collected at site 1. The abundance of the clay mineral smectite increases towards the fault trace, and kaolinite + chlorite decrease toward the fault (Figure 2-7). Clay XRD affirms the presence of smectite in the primary damage zone rocks mixed with chlorite, illite, and kaolinite (PDZ 0+0, PDZ 0+1, PDZ 0+10; Figure 2-8). Mixed layer illite-smectite (I-S) is likely present in a sample collected 1 m from the main fault (PDZ 0+1) identified by decreased peak intensity at ~6^{o} 2θ, 8^{o} 2θ and 17.7^{o} 2θ upon glycolation, and a peak shift from ~8^{o} 2θ to slightly higher values of 2θ (Moore and Reynolds, 1997). There is also the possibility of a peak at ~3.4^{o} 2θ in

sample PDZ 0+1, which indicates R1 (ordered) I-S. Newmod^{TM} (Reynolds and Reynolds, 1996) and Matlab (J.G. Solum) modeling indicate 35-50% I-S (65% illite interlayers in I-S), 50-60% discrete illite, and <5% discrete smectite in samples PDZ 0+0 and PDZ 0+1 (Figure 2-9).

Whole-rock geochemical analysis shows that the oxides MgO, Al_2O_3, K_2O, CaO, TiO_2, and FeO_3, trace elements Sr, Y, Nb, Ba, Sc, and loss on ignition (LOI) of the primary damage zone are depleted relative to the secondary damage zone, whereas SiO_2, Na_2O, and Zr are enriched in the primary damage zone (Figure 2-10). The geochemical signature of the primary damage zone is primarily depleted from that of the secondary damage zone. Principal component analysis shows that CaO, SiO_2, and Na_2O are the most significant variables, or account for the greatest variance in the data set (Figure 2-11). These and other oxides follow aforementioned trends consistently.

Field Site 2: Tali River (大里溪)
222105 E, 2674552 N

Heermance (2002) describes a temporary outcrop exposed by excavation north of Taichung city and 6 km south of the Fengyuan drillsite. This field site is part of the northern section of the Chelungpu fault. Net surface displacement in 1999 at this site was ~7.3 m (Chen and Lin, 1999). The fault is oriented 320^o, 48^o E, and bedding strikes due north with dips ranging from 40^o-66^o E (Heermance et al., 2003). At this site, the Chelungpu fault places siltstone of the Chinshui Shale or Kueichulin Formation on Quaternary gravel (Figure 2-12; Heermance et al., 2003, Fig. 6). The fault core consists of a 20-cm thick clay gouge in sharp contact with the surrounding damage zone rocks. Within the fault gouge, there is also a sharp contact between 15 cm of gray gouge on the

hanging wall side with a siltstone protolith, and 5 cm of red-brown gouge on the footwall side with a gravel protolith. The primary damage zone is ~30 m wide and is characterized by dense fractures and no relict bedding. Two secondary faults were identified in the hanging wall with <1 m of throw.

Microstructures include thin parted surfaces which are proposed to be the slip surfaces within the foliated fault gouge (CDR-8 – FC 0+0). There is little microstructural deformation within 1 m of the main fault (CDR-1 – PDZ 0+0.7, CDR-7 – PDZ 0+1). At ~0.7 m there is the possibility of a very weak alignment of phyllosilicates and sheared calcite, but no strong foliation or grain alignment is observed. At ~1 m, fine-grained matrix material shows no evidence for shear. Sample CDR-5 collected ~20 cm above the main fault has a fine-grained matrix with very weak foliation, but foraminifera appear undeformed (Heermance, 2002).

Clay XRD identifies abundant smectite in the secondary damage zone (~50 m from the fault, sample CDR-11; Heermance et al., 2003, Fig. 15; this study) and to a lesser extent in the fault gouge and near-fault primary damage zone rocks (CDR-1 – PDZ 0+0.7, CDR-2 – FC 0+0, CDR-4 – PDZ 0+0.4, CDR-6 – FC 0+0, CDR-8 – FC 0+0; Figure 2-7). The clay XRD pattern of the fault core illustrates a shift in the smectite peak, and also a small split upon glycolation (CDR-8 – FC 0+0; Figure 2-8). This indicates that the peak at ~6^{o} 2θ is a result of smectite, mixed with a lesser amount of chlorite or possibly vermiculite. Sample CDR-9 collected ~2 m into the hanging wall contains the least amount of smectite. Illite, kaolinite, and chlorite or vermiculite are also present in all components of the fault zone (Heermance et al., 2003; this study). Geochemical analysis is not available for this site.

Field Site 3: Pu Tze River (廍子溪)
223036 E, 2672882 N

At the Pu Tze River, the Chelungpu fault places Pliocene Chinshui Shale or Kueichulin Formation on unconsolidated Quaternary river gravel (Figure 2-13a) and is oriented 040, ~35^{o} E. Field site 3 is at the southern-most end of the northern section of the Chelungpu fault and had ~6 m of net surface displacement in the 1999 rupture. Here, the fault core is 40-60 cm thick with several bands of mm to cm thick black ultracataclasite. The primary damage zone is ~10 m wide and is characterized by increased fractures relative to the secondary damage zone, leached yellow color, and no relict bedding for 1-2 m into the hanging wall (Figure 2-13b). The secondary damage zone, which extends for the remaining 100 m of the outcrop, is characterized by folded bedding (Figure 2-13c), fractures, a few secondary faults, and a weakly developed fault gouge at ~40 m into the hanging wall. Secondary faults in this outcrop truncate folds and therefore have accommodated more movement than secondary faults at field site 1, but have little or no increase in damage surrounding them and have no associated fault gouge, and therefore are presumably small and relatively small offset structures.

Thin sections of samples collected from the main fault and wall rock show a coarse fault gouge with thin, dark, ultracataclasite ribbons surrounded by intact wall rock (FC 0+0; Figure 2-14). A thin zone (<0.5 mm) of broken grains forms a transition between the gouge and primary damage zone rocks. The primary damage zone is fractured with zones of broken quartz grains, but also contains areas of predominantly pristine quartz grains. Thin sections of the primary damage zone located ~30 cm into the hanging wall of the fault display open fractures and comminuted grains, bordered again

by relatively intact rock. The mineralogy of the fault core and primary damage zone observed in thin section is similar to that of field site 1, with quartz being the dominant mineral, as well as some calcite and feldspar.

X-ray diffraction analysis identifies quartz as the most abundant mineral for all field site 3 samples, with minor feldspar and calcite. Clays consist of illite, kaolinite, smectite and/or chlorite or vermicullite. Smectite is most abundant in the fault gouge, whereas kaolinite + chlorite and illite increase through the primary damage zone and are most abundant in the secondary damage zone samples (Figure 2-7).

X-ray fluorescence and ICP analyses show that, with the exception of SiO_2, Zr, and Sc, oxides and trace elements are depleted in the fault core and primary damage zone with respect to the secondary damage zone rocks (Figure 2-10). The fault core is enriched in SiO_2, and notably depleted in MgO, MnO, CaO, and LOI relative to the primary damage zone. Principal component analysis reveals CaO and SiO_2 to be the most significant variables.

Field Site 4: Wu River (烏溪)
218125 E, 2656546 N

Field site 4 along a northern branch of the Wu River belongs to the southern section of the Chelungpu fault. At this site, the Chelungpu fault places siltstone of the Chinshui Shale on unconsolidated Quaternary gravels and is oriented ~040^o, 25^o E. Approximately 2 m of throw were recorded at this site (Chen and Lin, 1999). Alternating sandstone, shale, and siltstone of the Cholan Formation occur in the secondary damage zone. A probable location for the main fault was identified along a gully where siltstone overlies gravel (Figure 2-15). There is some uncertainty in this location because the

gully is filled with waste to the west of the outcrop. Also, a portion of the outcrop appears suspect, and may be an out-of-place block; however, other parts of the outcrop appear continuous down dip with in-place siltstone. In addition, there is a lithology change across the gully from siltstone to the east to gravel to the west. The gully corresponds to damaged structures, a scarp in the road above, and the presence of clay gouge and altered rocks. We believe that this contact is the 1999 rupture.

The fault gouge is 20-40 cm of saturated, tacky orange clay in contact with gravel in the footwall and light gray clay in contact with siltstone in the hanging wall. The primary damage zone is characterized by veins and leaching along a dense network of fractures and shear fabric (0-5 m; Figure 2-16b), no relict bedding, and is approximately 20-25 m wide. Figure 2-16a is a stylized sketch of the exposure at field site 4 showing the main features of the outcrop.

The secondary damage zone comprises the remaining outcrop and is characterized by folds that increase in wavelength away from the main fault. Black clay gouge is distributed throughout the secondary damage zone along secondary faults and in fold limbs between sandstone and siltstone beds (Figure 2-16c, Figure 2-16d). The transition from primary damage zone to secondary damage zone is within several meters of the appearance of thin cm-thick sandstone beds. A second 10-m wide fracture and shear zone is located at ~80 m into the hanging wall with numerous small offset faults at high angles to the main fault (Figure 2-16e). This fracture zone lacks relict bedding in several places.

Quartz is the dominant mineral in thin section. Thin sections display foliated fault gouge (FG 0+30) and massive clay (SDZ 0+140) that may be primary clay or may be

gouge overprinted by weathering and subsequent mineral precipitation. Transitions between gouge and host rock are abrupt. Evidence for multiple deformation events include displaced and rotated porphyroclasts of gouge and quartz-rich wall rock (FG 0+30), multiple generations of foliated gouge at differing orientations that are either truncated by micro faults, or younger bands of fault gouge (FG 0+30, FG 0+148; Figure 2-17). Fine-grained, thin shear bands contain comminuted quartz grains that are apparently sheared off of the wall of more intact rock (FG 0+46). Small-scale bedding and gouge strands are commonly truncated by microfaults. There is some evidence for plastically deformed quartz grains (SDZ 0+140). Again, quartz dominates the mineral phase observed in thin section, but some grains of chlorite, calcite, and feldspar are also present.

Bulk XRD patterns for samples collected at field site 4 show that the dominant mineral is quartz, with lesser amounts of feldspar, calcite, and clays including kaolinite, illite, chlorite and/or smectite. Within the near-fault primary damage zone, Chlorite/smectite increases towards the fault core, whereas illite roughly decreases towards the main fault. No trend for kaolinite was determined (Figure 2-7). Quartz also increases towards the fault core. Clay XRD reveals that smectite is present in the secondary damage zone rocks (SDZ 0+133, SDZ 0+155, SDZ 0+190), as well as in primary damage zone rocks (PDZ 0+0, PDZ 0+5). A significant amount of smectite is present in the primary fault gouge; however; fault gouge in secondary faults range from having significant smectite (FG 0+39.8) to being smectite-poor (FG 0+53; Figure 2-8). Sample FG 0+39.8 has as much as 10% smectite in the I-S, illite, and smectite fraction of

the clay (Figure 2-9). Secondary fault gouge with variable mineralogy makes the trends in Figure 2-7 much more complex.

X-ray fluorescence and ICP results for field site 4 are more complex than those from sites 1 and 3. The ICP values show that fault gouge (FC 0+0, FG 0+39.8, FG 0+41, FG 0+53.2) and primary damage zone samples (PDZ 0+0, PDZ 0+5, PDZ 0+10, PDZ 0+20) are depleted in MgO, CaO, MnO, and LOI relative to the secondary damage zone (SDZ 0+170, SDZ 0+185; Figure 2-10). The fault core is enriched Al_2O_3, and the fault core and primary damage zone are enriched in SiO_2 relative to the secondary damage zone rocks. In general, and with the exception of CaO, fault gouge is enriched in oxides and trace elements with respect to the primary damage zone, and depleted in oxides relative to the secondary damage zone (Figure 2-10). Principal component analysis determined MnO and CaO to be the most significant oxides.

Field Site 5: Dong Pu Ruey River (東埔蚋溪)
219604 E, 2631775 N

Field site 5, part of the southern section of the Chelungpu fault, is an excavation site along the Dong Pu Ruey River. A throw of 1.5 m was recorded at this site where the uplift dammed the river for a time (Chen and Lin, 1999). The outcrop is located completely within the hanging wall of the Chelungpu fault, so only fault gouge from secondary faults was sampled. We infer that the outcrop represents part of the primary damage zone due to the high concentration of slip surfaces, shear bands and clay gouge, and the projected trend of the scarp that dammed the river. Yellow leached bands of siltstone follow fractures and gouge strands throughout the outcrop. The siltstone is also

leached yellow at the base of the overlying terrace gravels due to groundwater flow along the contact of the two lithologies.

Quartz is the dominant mineral in thin section, with abundant clay and some feldspar and calcite. Thin sections from field site 5 show several generations of faulting marked by the texture and orientation of different phases of gouge. Brecciated and comminuted quartz grains are common. Gouge is folded and truncated by younger micro faults and strands of foliated fault gouge, and porphyroclasts show rotation and shear tails (Figure 2-18).

Bulk XRD analysis identifies quartz, kaolinite, illite, and smectite/chlorite in secondary fault gouge and primary damage zone rocks. Clay XRD patterns show that smectite is present in most samples, but there is no obvious trend. Illite and kaolinite are major constituents of the fault rocks. The ICP and XRF results yield no definitive trend from fault gouge to primary damage zone rocks. This is most likely due to the difficulty in finding samples within the extent of the outcrop that did not contain shear bands and fault gouge. Only 2 primary damage zone samples were collected, and one of these is sandstone that does not provide a good comparison to the sheared siltstones.

Field Site 6: Chin-sui River (清水溪)
214402 E, 2616438 N

Field site 6 is located near the southern terminus of the 1999 rupture trace, and is the final field site of the southern section of the Chelungpu fault. At field site 6, the Chelungpu fault places Chinshui Shale on Toukoshan Conglomerate and is oriented ~030^{o}, 80^{o} E at the surface (Lin et al., 2005; this study). Where the 1999 rupture broke the Tungtou Bridge, 2 m of right-lateral strike-slip displacement and 0.4 m of throw were

recorded (Chen and Lin, 1999). Lin et al. (2005) report that cataclasites and gouge of the main fault are distributed along a 3-5 m wide zone, but determine that coseismic slip was likely localized within a <50-cm zone. The trace of the 1999 rupture has subsequently been destroyed by construction of a new bridge.

The outcrop is characterized by a very wide primary damage zone (~65 m) and an extensive secondary damage zone (>200 m) that is the remainder of the outcrop (Figure 2-19a). The primary damage zone is dominated by sheared and foliated siltstone with thin sandstone beds. It has innumerable secondary faults and anastomosing gouge, all of which are very steeply dipping. The gouge is black, extremely tacky, and is often located at contacts between siltstone or mudstone and fine-grained graywacke. One particularly interesting fault gouge is located at ~64 m into the hanging wall (Figure 2-19b). The gouge is ~20 cm thick, and black with a gold-green luster not observed in other gouges. Curved slicken lines were present on at least one fault plane at ~41 m from the main fault. Slicken lines were observed on fault planes in very fragile clay films at ~41 m and 55 m from the main fault (Figure 2-19c), suggesting that many surfaces were activated in the recent rupture, as these slicken lines could not be long-lived in this tropical setting. Other features of the primary damage zone include siltstone and sandstone fault breccia zones located at 4-9 m and 31 m along the line of transect, intense fracturing, and disrupted and discontinuous bedding. Relict bedding can, in some places, be defined by strands of gouge separating siltstone from sandstone, but these contacts are very irregular, disrupted, and difficult to trace. In many areas of the primary damage zone, where shear fabric and fault gouge dominates, there is no relict bedding.

Within the secondary damage zone, bedding is apparent, however still disrupted, and commonly folded. Numerous secondary faults are present, however there is less fault gouge present in the secondary damage zone than in the primary damage zone. There are several significant faults in the secondary damage zone, including a fault ~250 m into the hanging wall (fault 50) that offsets Quaternary terrace gravels capping the outcrop. Large round boulders are present in the footwall of this fault that are not present in the hanging wall (Heermance et al., 2003; this study). There is also an ~3 m high scarp at the surface. Fault gouge associated with this fault is 20-30 cm thick, contains brecciated clasts, and is foliated, zoned, and well developed. This evidence indicates that there has probably been a significant amount of offset on this fault (Heermance et al., 2003; this study). We do not know if this fault was activated in the 1999 rupture.

Thin sections of fault gouge from field site 6 are very fine-grained with well developed foliation and a high intensity of deformation microstructures (FG 0+40, FG 0+64, FG 0+240; Figure 2-20). Multiple deformation events are clearly recorded by cross-cutting relationships of veins, multiple generations of foliated fault gouge, fractures, and microfaults (FG 0+64, FG 0+40; Figure 2-20a; Figure 2-20b). Many fractures are simply due to the drying of clays, but some fractures are filled with microbreccia or vein fill (FG 0+64). Small, broken, floating quartz grains or pockets of wall rock are incorporated into gouge (FG 0+45/112-7, FG 0+240), and primary damage zone rocks that border gouge have fairly intact quartz grains, but show evidence for increased porosity and deformed matrix (FG 0+30, FG 0+240; Figure 2-20c). Foliated fault gouge with shear fabric is common and well-defined (FG 0+40, FG 0+64, FG

0+41.5, FG 0+58, FG 0+45/112-7, FG 0+10; Figure 2-20d). Microfaults that offset foliated fault gouge are filled with calcite, and imply syn-tectonic fluid flow (FG 0+64).

X-ray diffraction analysis identifies quartz, feldspar, calcite, and clay minerals including kaolinite, illite, chlorite, and smectite in most samples collected at this site. Clay is more abundant in fault gouge samples than in surrounding siltstone samples of the primary damage zone (Figure 2-7). Samples from the odd lustrous gouge (FG 0+64) are almost entirely montmorillonite. Samples from the primary damage zone and other clay gouge zones are composed of a mixture of chlorite, smectite, illite, and kaolinite (FG 0+10, FG 0+40, FG 0+41.5, FG 0+58, FG 0+64, FG 0+250, PDZ 0+31, PDZ 0+55; Figure 2-8). Illite and kaolinite are major constituents of secondary fault gouge, and again we find that smectite is present in some secondary fault gouge samples, (FG 0+58, FG 0+64, FG 0+250) and is barely detectable or absent in other gouge samples (FG 0+10, FG 0+40, FG 0+41.5; Figure 2-8). Primary damage zone samples contain a significant amount of smectite, illite, and kaolinite, as well as some chlorite (PDZ 0+31, PDZ 0+55).

Although samples from this site are compositionally complex, XRF and ICP values indicate that the percent amounts of oxides and trace elements are less in fault gouge (FG 0+10, FG 0+33, FG 0+64, FG 0+250) than in the primary damage zone PDZ (0+21, PDZ 0+27, PDZ 0+40, PDZ 0+55), with the exception of SiO_2 and Zr, which are enriched with respect to the primary damage zone (Figure 2-9). The lustrous gouge sample (FG 0+64) has a unique geochemical signature that includes a very low K_2O, consistent with the XRD determination that this sample is rich in smectite. In addition, it has the highest value for LOI probably due to interlayer water trapped in the smectite. Sample FC 0+64 follows the trends of other secondary fault gouge samples for Al_2O_3,

CaO, TiO_2, Y, and Zr. Principal component analysis identifies Al_2O_3, Na_2O, TiO_2, and LOI as the most significant variables.

2-3. THE CHELUNGPU FAULT AT SHALLOW DEPTHS

The Fengyuan drill hole was drilled at an incline and penetrated the northern section of the Chelungpu fault at 327.6 m depth along the bore hole (Heermance et al., 2003). The Nantou drill was a vertical hole that penetrated the southern section of the Chelungpu fault at ~177 m vertical depth (Tanaka et al., 2002; Heermance et al., 2003). Detailed core logs of the Fengyuan and Nantou cores can be found in Heermance (2002, Appendices). The Taiwan Chelungpu-fault Drilling Project drill hole was a vertical hole that penetrated the northern section of the Chelungpu fault at ~1111 m depth.

Northern Drillsite: Fengyuan (豐原)

Approximately 4 m of throw and ~9 m of horizontal displacement in the direction of 340^o were recorded in this area for the 1999 rupture along a steeply dipping (52^o E) fault (Heermance, 2002; Heermance et al., 2003, references therein). The fault places the Chinshui Shale on the Kueichulin Formation (Heermance et al., 2003; Tanaka et al., 2002). The Chinshui Shale is present in the core below soil and Quaternary gravels from 3.8 m to ~220-225 m along the borehole (Heermance et al., 2003; Tanaka et al., 2002). The first major fracture zone (N-MFZ-1) encountered in the drill hole is located at what was determined as the base of the Chinshui Shale and is characterized by sharp boundaries between undeformed host rock and fault rocks including a 20 cm-wide zone of random fabric fault breccia (Tanaka et al., 2002; Heermance, 2002). The second major

fracture zone (N-MFZ-2) is located within the Kueichulin Formation from 285.40 to 327.6 m along the borehole (Heermance, 2002). The last 1.5 m of this zone has the highest fracture density of the entire borehole. At the base is a 7 mm-thick fault gouge, which is determined to be the primary slip surface of the 1999 rupture (Heermance, 2002; Heermance et al., 2003). The Fengyuan core shows a normal stratigraphic sequence across the Chelungpu fault; good evidence for a youthful Chelungpu fault in this area (Heermance, 2002; Heermance et al., 2003).

Thin sections of samples from the Fengyuan drill core show little foliation or other microstructures within 2 m of the main fault as well as little foliation developed in the fine-grained matrix of random fabric fault breccia surrounding the fault (Heermance et al., 2003). Brecciated siltstone with clay-rich matrix 20 cm into the hanging wall of the main fault shows only a very weak foliation and grain alignment (Heermance et al., 2003).

X-ray diffraction results from Liao (2003) identify quartz, feldspar, and combinations of illite, kaolinite, chlorite, and smectite clays in core samples collected from secondary fault gouge and surrounding wall rock at depths of ~222-330 m along the Fengyuan borehole. While smectite is detected in most samples collected from the Fengyuan core, it is either absent from fault gouge samples or reduced relative to the surrounding wall rock, having been replaced by illite and I-S (Liao, 2003; Hashimoto et. al., *in press*). The concentration of all measured oxides are decreased in fault gouge relative to host rocks, with CaO being the most depleted, and MgO and SiO_2 also significantly depleted (Figure 2-10e; Liao, 2003; this study).

Southern Drillsite: Nantou (南投)

The 1999 rupture in the area of the Nantou well had 1-2 m of surface displacement and thrust the Chinshui Shale over the Toukoshan Conglomerate (Tanaka et al., 2002). The Chelungpu fault in this area strikes north-south and dips ~35^{o} E (Lee et al., 2001). The Chinshui Shale is present in the core directly below the soil and Quaternary deposits at 8.65 m depth and continues down to 177.68 m depth (Tanaka et al., 2002). The widest fracture zone in the core (S-MFZ) was located from 153.8 to 176.8 m depth and is characterized by foliated fault breccia. The base of this fracture zone consists of 1.1 m of foliated fault gouge above a dark gray, fine-grained fragile material with angular grains and a random fabric (Heermance, 2002; Tanaka et al., 2002). In the 70 m of core above the foliated gouge, there is less than 15 m of undeformed shale (Heermance, 2002). Below this fracture zone, the Chinshui Shale is juxtaposed against the Toukoshan conglomerate below.

Lu (2004) used quantitative XRD of samples from the Nantou core to show that illite and kaolinite become increasingly enriched from host rock to damage zone to fault gouge, and that smectite and chlorite become increasingly depleted from host rock to fault gouge. X-ray diffraction of samples from the Nantou drilled core shows that smectite is absent in some secondary fault gouge samples (Hashimoto et al., *in press*; Lu, 2004). As determined by XRF, the concentrations of NaO, SiO_2, and CaO are most changed from the host rock. These three major element oxides are all significantly depleted (Figure 2-10f; Lu, 2004; this study).

Taiwan Chelungpu-Fault Drilling Project (TCDP): Taichung (台中)

Net displacement during the 1999 rupture of the Chelungpu fault in the area of the Taiwan Chelungpu-fault Drilling Project was ~6 m. The Taiwan Chelungpu-fault Drilling Project consists of two parts. Drilling of borehole A commenced in January, 2004 and reached a depth of 2003 m in December, 2004. Preparations for drilling a second hole (borehole B) through the fault zone from borehole A began in December, 2004. Samples collected and referenced in this study come from the upper half of borehole A. The onsite geologists of the Taiwan Chelungpu-fault Drilling Project propose that the Chelungpu fault zone is located within the lower part of the Chinshui Shale (Figure 2-21). The most likely candidates for the 1999 slip surface are located at ~1111 m and 1153 m depth. Wireline logs including ν_p, ν_s, and resistivity have anomalously low values across these depths (Hung, et al., *submitted*). Massive and foliated fault gouge and a curiously hard, black material are present.

Currently, the fault zone at ~1111 m depth is being interpreted as the 1999 slip surface by the Taiwanese and Japanese scientists actively working on this project (for example, Hung et al., *submitted*; Sone et al., *submitted*; Figure 2-22). The following descriptions of the fault zone in borehole A of the Taiwan-Chelungpu fault drilling project are summarized from work by Sone et al. (*submitted*). The fault zone at ~1111 m depth contains <1 m of light gray, wet, massive clay that grades into ~10-15 cm of foliated fault gouge. At the base of the foliated clay gouge is a 12 cm section of black fault gouge including several cm-thick layers of hard, brittle, black material. This material was split in the core when it came out of the casing, and slicken lines were

observed on the inside surface. The onsite geologists can not verify whether or not any material was lost where the core was split (E.C. Yeh, pers. comm.). Below the black material is ~10-15 cm of clay gouge and drilling mud followed by a brecciated zone that is ~20 cm thick.

Preliminary clay mineralogy has identified illite, kaolinite, chlorite, smectite, and possibly R1 I-S in the fault gouge, (L.W. Kuo, S.R. Song, and J.G. Solum, pers. comm.). Overall, illite is more abundant and smectite is less abundant in fault gouge relative to wall rocks (L.W. Kuo and S.R. Song, pers. comm.). There is an ~1 cm-wide strip at 1111.29 m within the black fault gouge that contains a large smectite component of the clay fraction (L.W. Kuo, S.R. Song, pers. comm.). Bulk XRD of a 1 cm strip indicates that quartz is the dominant mineral phase (L.W. Kuo, pers. comm.; this study). It has been proposed that the high concentration of smectite relative to illite-rich surrounding fault rock is due to devitrification of glass (L.W. Kuo and S.R. Song, pers comm.). Small fragments or grains of amorphous material are present in thin section of this sample, but the mineralogy and nature of the amorphous material has not been verified to date.

A fault zone at ~1153 m depth is also a candidate for the 1999 slip surface. The wireline anomalies encompass the both the 1111 m and the 1153 m depth fault zones, so they can not differentiate between the two fault zones. The fault zone at 1153 m depth contains less water that the fault zone at 1111 m depth (E.C. Yeh, *submitted*), and smectite and kaolinite are abruptly absent within the illite-dominated fault gouge (L.W. Kuo and S.R. Song, pers. comm.). Preliminary friction tests of the fault gouge material, including the hard black material, have yielded strong coefficients of friction (0.5-0.7) for all samples (D. Lockner, pers. comm.). This is due to the abundance of quartz grains

within the fault gouge. It is possible that the actual slip zone has not been identified or sampled. It may have been located within the split section of the fault core and was lost during drilling.

For this study, two host rock samples were collected from each of the formations in the TCDP drill hole. The Cholan Formation was sampled at 512 m and 796 m depth, the Chinshui Shale at 1016.5 m and 1030.9 m depth (Figure 2-23a), and Kueichulin Formation at 1300 m (Figure 2-23b) and 1304.7 m depth. These samples, especially those from the Chinshui Shale and Kueichulin Formation, are used to determine the geochemical alteration of exhumed Chelungpu fault zone rocks. They provide the initial composition of un-weathered Chinshui Shale and Kueichulin Formation rocks. Two samples from the fault zones at 1111 m and 1153 m depth, both within the Chinshui Shale at the upper contact of the Kueichulin Formation, were also sampled (Figure 2-21).

The host rock samples collected from 512 m, 796 m, 1030 m, and 1300 m depth are siltstone or sandy siltstone. Samples from 1016 m and 1304 m depth are fine-grained graywacke. Quartz is the dominant mineral in thin sections of host rocks, and feldspar, calcite, chlorite, pyrite, and other black opaque minerals are also present. Samples from 512 m and 1016 m depth both contain thin swelling-clay lenses, indicating the presence of smectite. The sample collected from 1304 m depth contains some plastically deformed quartz grains. Gastropods and foraminiferas can be identified at 796 m (Cholan Formation) and 1300 m depth (Kueichulin Formation), and are most abundant in the deeper fault zone sample. The fault zone located at 1111 m depth is associated with a 60-100 cm thick gouge zone. The sample from this fault zone appears to be relatively undeformed and closely resembles the fine-grained siltstone sample at 1030 m depth

(Figure 2-23c, Figure 2-23d). The fossils at ~1152 m depth are not elongated or otherwise deformed, and show no evidence for shear tails in the surrounding matrix, although they are recrystallized. Bioclasts have retained their original shape. Other features of this sample, which is associated with a 30-40 cm thick gouge zone, include increased intragranular microfractures and calcite veins, iron-oxide staining and lined fractures, broken grains, and large recrystallized echinoids (Figure 2-23e, Figure 2-23f).

Bulk XRD analysis identifies quartz, feldspar, calcite, and clays in all TCDP samples available for this study. Clay XRD shows that smectite is a major component of protolith samples and is more abundant than in damage zone samples (Figure 2-8). Ordered (R1) I-S is possibly present in the fault gouge samples (J.G. Solum, pers. comm.; this study). Illite, kaolinite, and chlorite are also present throughout TCDP samples collected for this study. The ICP results for host rock and fault zone samples show that the two graywacke samples most closely match, except for the amount of CaO. The fault zone sample at ~1152 m depth is also overall coarser than the other host rock samples, and its geochemical signature generally lies between the graywacke and siltstone samples (Figure 2-9). The two greywacke samples and the coarse fault zone sample are depleted in all oxides except for SiO_2 (and CaO in the case of TCDP 1016) with respect to other TCDP samples (Figure 2-9). Since most of the exhumed fault zone rocks sampled in this study are siltstone and the shape of their ICP patterns more closely resembles those of the siltstone host rocks, TCDP-1030 and TCDP-1300 are used as the reference samples for determining geochemical changes in the exhumed fault zone.

2-4. MINERALOGICAL AND GEOCHEMICAL ANALYSIS

Geochemical Changes in Fault Zone Rocks

The geochemical alteration of fault rocks at field sites 1, 3, 4 and 6 were determined using the values of oxides in Chinshui and Kueichulin host rock samples from the TCDP core (TCDP 1030 and TCDP 1300) and averaged values of Fengyuan and TCDP host rock as a reference (Figure 2-10). Geochemical studies indicate that Ti, Mn, P, and to a lesser extent Mg are immobile elements (Goddard and Evans, 1995; references therein). Using the method described by Goddard and Evans (1995), percent changes of exhumed fault rocks from host rock were calculated. The value of TiO_2 was used as the immobile oxide.

The values of Fe_2O_3, P_2O_5, Cr_2O_3, Al_2O_3 and K_2O lie fairly close to the immobile TiO_2 axis for all sites. One exception is the pattern of FG 0+64 at field site 6; the lustrous, smectite gouge. The absence of illite accounts for the depletion of K_2O. In addition, the high LOI value is consistent with interlayer water trapped in the smectite, and enrichment of Fe and Mg may also be due to an Fe-Mg montmorillonite composition. The Kueichulin Formation (TCDP 1300) is shown in Figure 2-10 as the host rock for site 3 based on work by Heermance et al. (2003), but using the Chinshui Shale as the reference results in the same pattern. The value of SiO_2 is enriched in the fault core and primary damage zone relative to the host rock at each site. With the exception of some damage zone rocks at field site 3 (PDZ 0+3, SDZ 0+15) and sample FC 0+64 from site 6, the values of MnO, CaO, LOI, and often MgO are notably depleted in all components of the fault relative to the host rock, and are increasingly depleted toward the main fault at

each site. The extreme depletion of CaO (~60-90%) in fault gouge and primary damage zone rocks) indicates the transport of this mobile oxide out of the fault core and surrounding damage zone. The SiO_2 enrichment trend indicates transport and precipitation of SiO_2 in the fault core and primary damage zone rocks. Fault gouge and damage zone rocks from the Fengyuan and Nantou drilled cores are significantly depleted in CaO, MnO, Na_2O, and SiO_2. The geochemical changes indicate significant fluid-rock interaction.

The extreme depletion of MnO is perplexing, because it is typically considered immobile (Goddard and Evans, 1995; references therein), and therefore we would expect it to have values closer to that of the host, or enriched relative to the host rock. Values of MnO comparable to the Chinshui host rock were present only in a sample collected from the TCDP borehole at ~1152 m depth, a shale sample from the secondary damage zone of field site 4 (SDZ 0+128), and a fault core sample from field site 4 (FC 0+0). Either this particular portion of the TCDP core has an anomalous abundance of MnO, or MnO has actually been removed from the fault rocks. We believe that the MnO trends are due to high values of MnO in the host rock that are not necessarily representative, but also not unique. Of the values of MnO for Fengyuan and Nantou host rocks reported by Lu (2004) and Liao (2003) as well as TCDP samples, 4 of 15 host rock samples had high values of MnO; an average of 0.4% higher than the other 11 host rock samples. This is a significant amount given that the typical values of MnO are $0.07 \pm 0.01\%$.

Patterns in Clay Mineralogy and Crystallinity Indices

Some patterns can be determined from the clay mineralogy of the Chelungpu fault rocks. Figure 2-7 shows that smectite is most abundant in the fault core and decreases away from the fault in the northern section of the Chelungpu fault. Conversely, kaolinite + chlorite, and possibly illite are least abundant in the fault core and increase away from the main fault. It is much harder to distinguish trends for the southern Chelungpu fault; however, smectite seems to be most abundant in the fault core and in some secondary fault gouge. We propose that the complex mineralogy of the southern Chelungpu fault zone is due to the greater maturity of this section of the fault relative to the northern section. The southern Chelungpu fault has accumulated more damage and alteration, and has numerous secondary faults with fault gouge. These secondary faults and associated alteration perturb any signature identifiable with this method.

We have shown that smectite is present in the fault core of the exhumed fault zone and absent or depleted in the fault core at shallow depths. Weathering has been proposed as the agent that forms smectite in exhumed fault gouge (Solum et al., 2003). If, however, weathering is responsible for the smectite, the primary damage zone should presumably be most affected. The primary damage zone is heavily fractured, and should provide a good conduit for fluid flow. The primary damage zone rocks can be as (if not more) chemically altered as fault core rocks (Figure 2-10). Also, the yellow color of some primary damage zone rocks at field sites 3, 4, and 5 indicates leaching. The geochemical data suggest that translocation of SiO_2 and CaO, and thus the presence of reaction-driving fluids, is significant in the primary damage zone rocks.

One test used to determine the conditions under which clays formed is the crystallinity index (Moore and Reynolds, 1997). The width of a peak recorded by XRD is dependent upon the size of the crystallites and the number of smectite interlayers (Figure 24a). The width of peaks can be influenced by the expandability of smectite layers, resulting in wider peaks for clays with many smectite interlayers. Large crystallites (narrow peaks) are formed under relatively high P/T conditions, and therefore are thought to represent recrystallized, neoformed clay minerals such as those formed during fault activity or in burial diagenesis (Moore and Reynolds, 1997). Small crystallites (broad peaks) are formed under relatively low P/T conditions, and are thought to represent formation by weathering processes (Moore and Reynolds, 1997; Solum et al., 2003).

A crystallinity index was created for the northern and southern sections of the Chelungpu fault by calculating peak widths from glycolated clay XRD patterns (Figure 2-24). The same samples that were used for ICP MS and clay XRD analyses were used to create the crystallinity index. The crystallinity index for the northern Chelungpu fault has no distinguishable pattern. The lack of pattern suggests that clays throughout the fault have a similar origin, and possibly have not been exposed to conditions that would preferentially alter fault gouge over host rocks. The lack of a pattern in the crystallites may be a reflection of the youth of this section of the fault.

The crystallinity index for the southern Chelungpu fault has a more interesting pattern. The most prominent feature is the division of smectite in the fault core. Smectite breaks into 3 distinct groups representing the multiple phases of fault gouge identified in the southern Chelungpu fault. Group 1 has high crystallinity indices of smectite due to a

far greater abundance of smectite than other samples. These indices correspond to sample FG 0+64 from field site 6, which is nearly 100% smectite. Group 2 samples are all from secondary fault gouge. Group 3 has smectite crystallinity indices equal to zero because these samples contain no smectite. Group 2 is of most interest. This group has a moderate component of smectite, more comparable to the amounts of smectite found in damage zone and TCDP host rocks. The plot illustrates that the smectite crystallites of the fault core and primary damage zone rocks of group 2 are larger (smaller peak widths) than the less deformed secondary damage zone and host rocks. This indicates that the mineralogical signature due to faulting has not been completely overprinted by surficial (low P/T) weathering processes; some fault signal remains.

2-5. DISCUSSION

The data presented above document the mineralogical, geochemical, textural, and micro- and macro-scale structural characteristics at 6 sites along-strike and 3 sites down-dip of the Chelungpu fault along ~70 km of the fault. The meso-scale structures, microstructures, and geochemical signature of the Chelungpu fault zone change along strike, and appear to correlate with variations in fault geometry, ground motion, and total fault displacement. This work allows us to discuss the along-strike and down-dip variations in these aspects of the fault, evaluate fault zone structure, and discuss these results in light of earthquake processes. The variation in the characteristics of the Chelungpu fault at each study site is summarized in Figure 2-25.

Along-Strike Variations

Our data from outcrops along the Chelungpu fault demonstrate that the primary damage zone (defined by the area of greatest damage surrounding the main rupture trace) of the northern section is 10-30 m wide, whereas in the southern section of the fault, the primary damage zone is 25-70 m wide. Given that the northern section of the Chelungpu fault is a relatively new structure in the hanging wall of the old Chelungpu fault/Sanyi fault (Ho and Chen, 2000; Heermance, 2002), we assume that the total displacement along the northern portion of the fault (500 m – 1.5 km; Heermance, 2002; references therein) is much less than along the southern portion (8-15 km; Heermance, 2002; references therein). It is also important to consider the intensity of damage within the primary damage zone. Exposures of the primary damage zone along the northern section of the fault are characterized by an increased fracture density relative to the secondary damage zone, whereas the primary damage zone of the southern Chelungpu fault is characterized by intense fracturing as well as the presence of sheared siltstone, abundant fault gouge, and multiple deformation events as recognized by cross-cutting relationships observed in outcrops and thin sections.

These differences are mirrored in the Fengyuan and Nantou drill cores, with a 7 mm thick fault gouge surrounded by a primary damage zone with increased fracture density at Fengyuan, and 1.1 m of foliated fault gouge with 70 m of sheared shale in the hanging wall at Nantou (Heermance, 2002; Tanaka et al., 2002). Fault cores, however, remain in a range of 10's of centimeters-thick for all study sites, and within these gouge zones, coseismic slip may have been localized within the gouge along a slip surface <0.3 cm thick (Lin et al., 2005). This is consistent with the idea that narrow slip surfaces

develop early in the life of a fault and continue to experience localized slip along narrow zones (Evans et al., 2000).

Lin et al. (2001) report coseismic flexural-slip folding structures sub-parallel to the 1999 rupture of the Chelungpu fault. Folds are observed in the hanging wall, and can be a few tens to a few hundreds of meters wide. Coseismic folding of rice paddies, roads, and terraces created folds with axes that are oriented northeast-southwest to north-south. Where there are jogs in the Chelungpu fault, however, Lin et al. (2001) report fold axes oriented east-west to northwest-southeast. Folds present in the hanging wall at field site 4 have experienced slip along bedding planes based on the presence of fault gouge in the fold limbs. Hanging wall folds are also common at field site 3, and are present at field site 6. The axes of folds at field site 3 and filed site 4 trend east-west to northeast-southwest. This folding is coseismic and is part of the internal deformation of the Chelungpu fault zone.

The orientation of the folds at field sites 3 and 4 may be due to the complexity of the fault system at this location. A popular model for the Chelungpu fault involves southward-propogating lateral ramps at the extreme northern end of the Chelungpu fault where the fault makes a 90^{o} turn to the east (Johnson et al., 2001; Johnson and Segall, 2004). As the lateral ramps (Sanyi, Holi, and Chelungpu) propagated south, the northern section of the Chelungpu fault also progressively steps to the east into the hanging wall. The Sanyi (old Chelungpu) and Holi faults are projected to converge with the southern section of the Chelungpu fault near Wufeng where the 1999 rupture trace has a right-stepping jog (Figure 2-1). Field site 3 is just north of where the faults converge, and field site 4 is just south of where the faults converge. The eastward-propagation of the

Chelungpu fault seem to hinge near Wufeng, and may influence the orientations of the complex suite of folds at field sites 3 and 4. It may be more appropriate to label site 3 as transitional, instead of belonging completely to the northern section of the Chelungpu fault. Indeed we see that field site 3 has more accumulated damage, manifested in folding and ultracataclasites within fault gouge, than sites 1 and 2.

Optical microscopy of samples across the northern Chelungpu fault shows relatively undamaged wall rock surrounding coarse fault gouge. Optical microscopy of fault zone samples from the southern Chelungpu fault reveals several generations of relatively fine-grained, foliated fault gouge that is folded and truncated by microfaults and veins. This fault gouge is found in secondary faults throughout the outcrop, and towards the end of our transect lines at 240+ m away from the main rupture trace. Calcite-filled microfaults offset foliated gouge, and some of these veins are themselves broken by fractures and microfaults. These observations are evidence for multiple deformation events and syn-tectonic fluid flow. Strong evidence for multiple deformation events is not found in thin sections of samples from the northern Chelungpu fault. These textures provide additional evidence for the maturity of the southern Chelungpu fault relative to the northern Chelungpu fault.

The geochemical data of the northern Chelungpu fault have systematic changes through fault zone components with increasing distance from the fault, whereas the geochemical and mineralogical variations throughout the southern fault zone are more enigmatic with respect to location along the transect line. Gouge-bearing secondary faults are present throughout the primary damage zone and secondary damage zone of the southern Chelungpu fault, and perturb the geochemical signature with distance from the

fault. As a result, geochemistry and mineralogy of the primary damage zone are more variable in the southern Chelungpu fault than the northern Chelungpu fault. Secondary fault gouge of the southern Chelungpu fault can be illite-rich, mixed clays, or smectite-rich. These differences in geochemistry and mineralogy may be due to the maturity of the southern fault system relative to the north.

Field site 6 contains a fault gouge whose physical properties, mineralogy, and geochemistry are unlike any other fault gouge found elsewhere in that outcrop, at other outcrops, or in the cores (with the possible exception of preliminary results from Taiwan-Chelungpu fault drilling project within the fault zone at 1111 m depth). This gouge could represent a phase of fluid flow or fault deformation not recorded elsewhere. This may be due to its position at the southern terminus of the Chelungpu fault as it steps to the southwest and joins with the Meishan fault and interacts with the Kukeng strike-slip fault (Figure 2-3; Chen et al., 2001b). The damage zones of these faults may communicate and transport fluids from different sources to field site 6.

The variations in Chelungpu fault from north to south may illustrate the evolution of a fault through time. The northern segment has been active since at least ~46 ka, but does not appear to have been active for more than ~100 ka (Heermance, 2002) and illustrates the microstructures and more ordered mineralogy and geochemical signature of a young fault. The southern section, which has 8-15 km of total displacement, and has been active since ~1 Ma (Hung and Wilschko, 1993), provides a comparison to the northern Chelungpu fault and gives insights into the evolution of the Chelungpu fault to its current, more mature state. Some of the variability of the fault zone along strike may be a function of fault maturity and accumulated damage.

Several other factors may influence the along-strike variations in the Chelungpu fault. In the southern section of the Chelungpu fault, siltstones are thrust over the Toukoshan Conglomerate in a hanging wall ramp, whereas in the north, the thrust is bed-parallel and lies within siltstones. The additional frictional resistance due to the conglomerate in the footwall as well as the added stress of the footwall wall ramp geometry may cause the southern section of the Chelungpu fault to accumulate more damage than the northern Chelungpu fault (Heermance, 2002). Other examples include a model by Zeng and Chen (2001) in which they propose that the 1999 slip distribution along the Chelungpu fault was due to geometric barriers that caused rupture deceleration, and then acceleration once the rupture propagated past the barrier. Oglesby and Day (2001) suggest that the peak ground motions and physical characteristics of the 1999 rupture are a factor of fault geometry and the interaction of the rupture with the earth's free surface. Fluid pressurization along the major decollements of the Taiwan fold and thrust belt has been proposed by Suppe and Wittke (1977). In addition, thermal fluid pressurization in the northern Chelungpu fault, but absent in the southern Chelungpu fault has also been proposed (D. Lockner, pers. comm.).

Along-strike variations in the number and character of slip surfaces, including fluid-rock interactions and mineralogy of fault cores, may influence the rupture style along faults (Evans and Chester, 1995), and may play a role in the variable rupture pattern along the Chelungpu fault. Further investigation into the variation of composition, amount, and texture of clay present in fault cores along the Chelungpu fault trace may provide additional insight into the variable rupture style of the 1999 event. Co-seismic slip increased northward along the fault trace, however, strong ground motion

including high-frequency ground acceleration and fast rupture velocity decreased from south to north (Lin et al., 2001; Heermance et al., 2003). The wide damage zone (up to 70 m) and multiple slip surfaces in the southern Chelungpu fault zone indicate that seismic energy is dispersed across a wider zone, and may account for the decrease in slip along this section of the fault (Heermance et al., 2003). Also the more complex and variable composition of fault gouge of secondary faults may play a role in fault rupture. Illite-rich clays in secondary fault gouge may impede fault propagation to the free surface slightly over fault core in the north with a smectite component.

Variations with Depth

Comparison of geochemistry and mineralogy of core samples from the Chelungpu fault zone and host rock at shallow depths indicates that smectite "consumption" takes place locally in fault gouge and to a lesser extent in damaged rock. Smectite is a dominant clay mineral in host rocks of the Chelungpu fault, especially the Chinshui Shale (Kuan, 1964), and is partially or completely replaced by illite in fault gouge samples (Liao, 2003; Lu, 2004; Hashimoto, *in press*).

The drilled core samples examined were not at sufficient depths to drive the smectite to illite reaction by burial temperature alone. The smectite to illite reaction requires temperatures of 100^{o} - 150^{o}C (Freed and Peacor, 1989; Hyndman, 2004). A simple calculation using a geothermal gradient of ~20^{o}C/km (Lin, 2000) and an average surface temperature of 22^{o}C yields a burial temperature of only ~50^{o}C for the deepest core samples used in this study (around 1200 m for damage zone rocks). Temperatures recorded at the base of the Fengyuan and Nantou bore holes were ~28^{o}C at 460 m along

the borehole (352.4 m TVD) and ~25^{o}C at 180 m depth, respectively (Tanaka et al., 2002). These temperatures could be slightly depressed due to drilling mud, but are still well below the temperature requirement for the smectite to illite reaction, despite the findings of Liao (2003) and Lu (2004) described earlier.

The hypocenter of the September 21 1999 earthquake was between 7 and 10 km deep (Ma et al., 2000; Ogelsby and Day, 2001), which corresponds to ambient temperatures of 140 – 200^{o}C; this depth has sufficient temperatures to initiate the smectite to illite reaction. Data from other earthquakes in western Taiwan with magnitudes $\geq$ M5 indicate that most seismicity occurs at depths $\geq$ 5 km, with a few exceptions of earthquakes as shallow as 1 km (Shin and Teng, 2001). As shown earlier, smectite is absent or reduced in the fault core at much shallower depths (~200-1000 m) than the seismogenic zone. There are at least two possible explanations for this observation. First, seismic energy may play a role in initiating the smectite-illite reaction at shallow depths in the fault core (Jacobs and Evans, *submitted*; Vrolijk and van der Pluijm, 1999), assisted by fluid-flow in and around the fault core. Second, illite and I-S mineralogy may be the result of reactions at depth subsequently thrust higher to the levels penetrated by drilling. All of the samples studied from the Fengyuan and Nantou drilled cores were collected from the hanging wall of the Chelungpu fault zone. Preliminary results from footwall rocks of the TCDP core show the same mineralogical trends in the footwall as in the hanging wall, suggesting that the illite to smectite reaction may in fact occur at shallow depths (L.W. Kuo, pers. comm.).

We estimate a total vertical uplift on the fault of 5-7 km. These estimates are based on calculations of a vertical uplift rate of 5-7 mm/yr by Heermance (2002) and Lee

et al. (2001). The vertical uplift on the Sanyi and Holi faults must be added to that of the northern Chelungpu fault because the northern Chelungpu fault rocks have been carried in the hanging walls of these two thrusts. These faults have been active in sequence with the southern Chelungpu fault (Johnson and Segall, 2004); therefore a vertical uplift of 5-7 km can be estimated for the complete Chelungpu fault system. Based on this calculation, the sampled fault rocks have been at seismogenic depths and at temperatures sufficient to drive the smectite-illite reaction. The relative simplicity of the mineralogic signature of the northern Chelungpu fault may be do to less accumulated fluid flow and radiated seismic energy along the newest branch of the fault relative to the southern Chelungpu. A portion of the mineralogical signature of all sampled fault rocks may be due to their travel from seismogenic depths through the aseismic portion of the Chelungpu fault zone to the near-surface and surface.

The exhumed fault zone has a mineralogical, and, to some extent (SiO_2), a geochemical trend that are seemingly reversed from the fault at shallow depths. Smectite is more abundant in the exhumed fault core than in the exhumed damage zone rocks (Figure 2-7; Figure 2-9), whereas smectite is often absent in the fault core at shallow depths. Host rocks from drilled core and exhumed secondary damage zone rocks also commonly have significant amounts of smectite. Primary damage zone samples and fault gouge from secondary faults are rich in illite, and often have the least smectite. These observations indicate that some of the exhumed portions of the fault zone have undergone a retrograde reaction from illite to smectite.

We call on fluid flow in and around the fault zone to drive the retrograde illite to smectite reaction. One explanation for the “reversed” mineralogical signature of the

exhumed fault zone is that it is due entirely to surficial weathering processes. Fault core rocks at shallow depths are rich in illite, however, the increased surface area of finer-grained fault gouge samples may allow the retrograde reaction of I-S to occur at an accelerated rate. Solum et al. (2003) found that fine-grained, pore-filling smectite-rich clay formed in exhumed portions of the Punchbowl fault, and was most abundant in the most intensely deformed ultracataclasites. They also observe that the mineralogy of the ultracataclasite and the host rock consists of smectite, detrital chlorite, and illite. Cataclasite contained neoformed illite and chlorite. They suggest that this is due to greater dissolution and recrystallization in the most fine-grained and deformed portions of fault zones resulting in retrograde reactions. The cataclasite has been less altered from its composition at depth, where it was altered by fault activity.

We propose an addition to this model that involves the seismic cycle and faulting, and, if active, works in conjunction with surficial weathering. If smectite is converted to illite in the fault core by seismic energy as proposed by Vrolijk and van der Pluijm (1999), then, as mentioned previously, one byproduct of the reaction is aqueous silica (Abercrombie et al., 1994). Silica may be translated along the fault during seismic dilatancy (Goddard and Evans, 1995) and fault-valve action with the relatively large volume of dehydration water from the smectite to illite reaction (Moore and Reynolds, 1997). Fluids charged with silica accompanied by seismic energy may help to drive a retrograde reaction of illite to smectite by freeing Al^{3+} and K^{+} and fluxing the system with aqueous Si^{4+} (Figure 2-26). Chlorite in fault gouge of drilled core samples (Hashimoto et al., *in press*) and microstructural observations of this study indicate the presence of fluids when the smectite to illite reaction occurred (Whitney, 1990).

Retrograde diagenesis of illite to I-S and smectite in sedimentary rocks induced by hydrothermal fluids has been documented (Zhao et al., 1999; referenced therein). Liao (2003) finds illite-rich gouge in a shallow fault zone at 223.45 m (171.17 m TVD) in the Fengyuan borehole, and Lu (2004) finds illite-rich gouge as shallow as 123.08 m depth along the Nantou borehole, so we can constrain the retrograde reaction to above 100-200 m depth. This retrograde reaction may serve to weaken the fault at very shallow depths, and allow the rupture to reach the free surface more easily.

Hyndman (2004) discusses the transition from the upper aseismic to lower seismic zone in subduction thrust systems. The transition corresponds to temperatures of ~100^{o}C-150^{o}C, coincident with the initiation temperature of the smectite to illite transition. (Hyndman, 2004). The upper smectite-bearing portion of the fault core does not radiate seismic energy, but is instead passively "pushed along". Samples used for this study were not from seismogenic depths, but they provide an illustration of the transition from seismic illite and illite-rich I-S to aseismic smectite-rich I-S and smectite. The hypocenter of the September 21 1999 earthquake was within Hyndman's temperature range for the seismogenic portion of a fault zone. Our compositional characterization of minerals down-dip along the Chelungpu fault provides useful constraints on the role of mineralogy in fault movement at the near surface. The mineralogy and proposed reactions documented in this study indicate that the smectite-illite reaction may take place up-dip of the seismic-aseismic transition, and indicate that Hyndman's model is oversimplified. Clay reaction may be driven by fluids and seismic energy all along the fault, and thus the effects of clay on fault weakening are much more complex than Hyndman suggests. It is also important to remember that Hyndman's hypothesis is not

based on his own mechanical experiments. Other frictional experiments support the idea that illite is seismic and smectite is aseismic (for example, Brace and Byerlee, 1966), but the amount of clay needed for this case to be true is unknown; however, 50% has been suggested (Hyndman, 2004; references therein). Quartz is a dominant mineral in fault cores of the shallow Chelungpu fault, and may control the frictional strength of the fault gouge material. If this is the case, clays may help to weaken the frictional strength of the fault, but other factors such as high pore-fluid pressures (initially proposed by Hubbert and Rubey, 1959) and dynamic rupture effects (examples in Lockner and Beeler, 2002) may be needed to completely explain the seismic to upper aseismic transition and weak nature of natural faults.

Marone and Saffer (*in press*; Saffer and Marone, 2003) show experimentally that smectite has a lower coefficient of friction than illite. However, both clay types display velocity strengthening, or stable sliding behavior over a range of normal stresses, shear strains, and sliding velocity. These results also suggest that, while clay type may play a role in weakening faults, it can not solely account for the seismic to upper aseismic transition. Another idea involves lithification of fault gouge (Marone and Saffer, *in press*; Saffer and Marone, 2003). Marone and Saffer (*in press*) propose that the transition from seismic to upper aseismic is a result of a change from localized shear within consolidated fault gouge at seismogenic depths to distributed shear within unconsolidated fault gouge, where consolidated and lithified gouge behaves as a frictional solid resulting in stick-slip, and unconsolidated gouge has the properties of a granular material resulting in stable sliding (Morrow et al., 1992; Beeler et al., 1996). Fault gouge lithification is attributed to increased effective stress, pressure solution, porosity reduction, and the

release of silica-rich fluids in the illite-smectite reaction that may precipitate silica in pore spaces (Marone and Saffer, *in press*; Saffer and Marone, 2003). The black material immediately surrounding what is determined to be the main Chelungpu fault in the TCDP drill hole is considerably more consolidated, hard, and brittle than the exhumed fault gouge. This observation simply suggests that we can not rule out the fault gouge lithification theory, and that more work needs to be done in regards to this theory. It is should also be noted that frictional experiments such as those by Marone and Saffer (*in press*) and Saffer and Marone (2003) are performed with dry clay powder; however, experiments with fluid-saturated samples and equilibrated fluid-pressures are more applicable to fault zones (Moore and Lockner, *in press*).

In addition to the unanswered questions briefly discussed above, the frictional properties of interlayer I-S are unknown. This study indicates that there are significant variations in clay mineralogy down-dip along the Chelungpu fault, and these changes probably culminate in significant smectite to illite reactions at seismogenic depths. Results of frictional tests conducted on montmorillonite and illite indicate that montmorillonite is much weaker than illite. Additionally, the frictional strength of physical mixtures of smectite and illite was tested by Morrow et al. (1992). They found that mixtures had frictional strengths intermediate to typical values for montmorillonite and illite. The frictional properties of natural *mixed layer* I-S have not been tested, however, and may prove to be different than a physical mixture of the two clays. The mixed layer I-S documented in this study, by Solum et al. (2005) and Vrolijk and van-der Pluijm (1999) suggest that further experimental work should be conducted to address the properties of this clay type.

2-6. CONCLUSIONS

We examine core data and field samples from 9 study sites along the Chelungpu fault, Taiwan. We show that the northern section of the Chelungpu fault that ruptured in the hanging wall of the old Chelungpu fault/Sanyi fault has less intense damage surrounding the fault core, a systematic geochemical and mineralogical trend across fault components, and most slip localized to a single slip surface. The southern Chelungpu fault is more intensely damaged with more complex geochemistry and mineralogy, and numerous faults that have developed a fault core and have probably accommodated slip over a dispersed area.

We show that, although smectite is absent or reduced in the fault core at shallow depths of 200 to 1200+ m, it is abundant in the fault core and present in some secondary fault gouge of the exhumed portion of the Chelungpu fault. The fault core has undergone a retrograde reaction of illite to smectite at the very near surface and surface portions of the fault. This reaction is facilitated by surficial weathering processes, but possibly also by fluid flux along the fault core while the fault is seismically active. The mineralogical variations are important to document because they have significant implications on how the fault reaches the earth's surface. Major conclusions of this study are:

1) The northern section of the Chelungpu fault may be a proxy for a young thrust fault (~45-100 Ka old), whereas the southern Chelungpu fault shows the progression into a more mature fault zone (~1 Ma old).

2) An increase in damage along the southern Chelungpu fault relative to the northern Chelungpu fault correlates with decreased co-seismic slip and increasing strong

ground motion in 1999. The wide damage zone (up to 70 m) and multiple slip surfaces in the southern Chelungpu fault zone indicate that seismic energy is dispersed across a wider zone, and may account for the decrease in slip along this section of the fault (Heermance et al., 2003). Also the more complex and variable composition of fault gouge of secondary faults may play a role in fault rupture. Illite-rich clays in secondary fault gouge may impede fault propagation to the free surface slightly over fault core in the north with a smectite component.

3) Smectite in fault gouge at the surface may not be due entirely to surficial weathering, but is also influenced by fault-related processes.

4) Illite and smectite clays may play an important role in the transition from the upper aseismic to lower seismic zone and fault weakening, although clay type alone probably does not account for the seismic to up-dip aseismic zone.

5) Mixed layer illite-smectite clay needs to be tested for frictional strength, as it may not have the same properties as a physical mixture of the two clays.

6) Regardless of whether the illite to smectite reaction is critical to fault strength and rupture style, or whether it is one of a suite of processes that influences fault strength and rupture style, the study of illite, smectite, and other clays is important for our understanding of fault weakening.

The Chelungpu fault provides a valuable opportunity to study shale and clay-rich fault zones. Data presented in this work provide an important characterization of the along-strike and down-dip variations of the near surface and exhumed portions of the Chelungpu fault. These types of data are essential for the understanding of fluid flow properties and energy distribution of shale and clay-rich faults zones.

References

Abercrombie, H.J., I.E. Hutcheon, J.D. Bloch, and P. de-Caritat (1994). Silica activity and the smectite-illite reaction, *Geology* **22**, 539-542.

Beeler, N.M, T.E. Tullis, M.L. Blanpied, and J.D. Weeks (1996). Frictional behavior of large displacement experimental faults, *J. Geophys. Res.* **B101**, 8697-8715.

Brace, W.F., and J.D. Byerlee (1966). Stick-slip as a mechanism for earthquakes, *Science* **153**, 990-992.

Chen, C.H., and C.C. Lin (1999). Surface ruptures along the Chelungpu fault during the Chi-Chi earthquake, Taiwan, Central Geologic Survey, Ministry of Economic Affairs, R.O.C., scale 1:25,000.

Chen, W., and H. Kao (2000). The Chi-Chi Earthquake Sequence of 1999: dual, out-of-sequence thrust faulting in Taiwan, in *International Workshop on Annual Commemoration of Chi-Chi Earthquake*, Taiwain, 18-20 September 2000, 71-81.

Chen, W.S., B.S., Huang, Y.G. Chen, Y.H. Lee, C.N. Yang, C.H. Lo, and K.J. Lee (2001a). 1999 Chi-Chi earthquake: a case study on the role of thrust-ramp structures for generating earthquakes, *Bull. Seism. Soc. Am*. **9**1, 986-994.

Chen, Y.G., W.S. Chen, J.C. Lee, Y.H. Lee, C.T. Lee, H.C. Chang, and H.C. Lo (2001b). Surface rupture of 1999 Chi-Chi earthquake yields insights on active tectonics of central Taiwan, *Bull. Seism. Soc. Am*. **91**, 977-985.

Chui, H.T. (1971). Folds in the northern half of western Taiwan, *Petrol. Geol. Taiwan* **8**, 7-19.

Chou, J.T. (1977). Sedimentology and paleogeography of the Pleistocene Toukoshan Formation in western Taiwan, *Petrol. Geol. Taiwan* **14**, 25-36.

Covey, M. (1984). Lithofacies analysis and basin reconstruction, Plio-Pleistocene Western Taiwan foredeep, *Petrol. Geol. Taiwan* **20**, 53-83.

Dalguer, L.A., J.D. Irikura, J.D. Riera, and H.C. Chiu (2001). The importance of the dynamic source effects on strong ground motion during the 1999 Chi-Chi, Taiwan, earthquake: brief interpretation of the damage distribution on buildings, *Bull. Seism. Soc. Am*. **91**, 1112-1127.

Evans, J.P., and F.M. Chester (1995). Fluid-rock interaction in faults of the San Andreas system: Inferences from San Gabriel fault rock geochemistry and microstructures, *J. Geophys. Res*. **100**, 13007-13020.

Evans, J.P., Z.K. Shipton, M.A. Pachell, S.J. Lim, and K. Robeson (2000). The structure and composition of exhumed faults, and their implications for seismic processes, in *Proceedings of the 3rd Conference on Tectonic Problems of the San Andreas Fault System,* G. Bokelmann and R.L. Kovach (Editors), Stanford University Press, Stanford, California, 67-76.

Freed, R.L., and D.R. Peacor (1989). Variability in temperature of the smectite/ illite reaction in Gulf Coast sediments, *Clay Min.* **24**, 171-180.

Goddard, J.V., and J.P. Evans (1995). Chemical changes and fluid-rock interaction in faults of crystalline thrust sheets, northwestern Wyoming, U.S.A., *J. Struc. Geol.* **17**, 533-547.

Hashimoto, Y., K. Ujiie, A. Sakaguchi, and H. Tanaka (*in press*). Characteristics and implication of clay minerals in the northern and southern Chelung-pu fault, Taiwan, *Tectonophysics*.

Heermance, R.V. (2002). Geometry and physical properties of the Chelungpu Fault, Taiwan, and their effect on fault rupture, *Master's Thesis*, Utah State University, Logan, Utah.

Heermance, R.V., Z.K. Shipton, and J.P. Evans (2003). Fault structure control on fault slip and ground motion during the 1999 rupture of the Chelungpu fault, Taiwan, *Bull. Seism. Soc. Am*. **93**, 1034-1050.

Ho, C.S. (1975). *An introduction to the geology of Taiwan-explanatory text of the geologic map of Taiwan*, Central Geol. Survey, Ministry of Economic Affairs, R.O.C., 153 pp.

Ho, H.C., and M.M. Chen (2000). *The geologic map and explanatory text of Taichung, Taiwan, sheet 24*, Central Geologic Survey, Ministry of Economic Affairs, R.O.C., scale 1:50,000.

Hubbert, M.K., and W.W. Rubey (1959). Role of fluid pressure in the mechanics of overthrust faulting, *Bull. Geol. Soc. Am.* **70**, 115-166.

Hung, J.H., and D.V. Wiltschko (1993). Structure and kinematics of arcuate thrust faults in the Mioli-Cholan area of western Taiwan, *Petrol. Geol. Taiwan* **28**, 59-96.

Hyndman, R.D. (2004). Controls on subduction thrust earthquakes: downdip changes in composition and state, in *Rheology and Deformation of the Lithosphere at Continental Margins,* G.D. Karner, B. Taylor, N.W. Driscoll, and D.L. Kohlstedt (Editors), Columbia University Press, New York, New York, 166-178.

Johnson, K.M., Y.J. Hsu, P. Segall, and S.B. Yu (2001). Fault geometry and slip distribution of the 1999 Chi-Chi, Taiwan earthquake imaged from inversion of GPS data, *Geophys. Res. Lett.* **28**, 2285-2288.

Johnson, K.M., and P. Segall (2004). Imaging the ramp-decollement geometry of the Chelungpu fault using coseismic GPS displacements from the 1999 Chi-Chi, Taiwan earthquake, *Tectonophysics* **378**, 123-139.

Kao, H., and Chen, W. (2000). The Chi-Chi earthquake sequence: active, out-of-sequence thrust faulting in Taiwan, *Science* **228**, 2346-2349.

Kuan, M.Y. (1964). Clay mineral stain test of the subsurface formations in the Chinshui gas field, Miaoli, Taiwan, *Petrol. Geol. Taiwan* **3**, 141-149.

Lee, P.J. (1963). Lithofacies of the Toukoshan-Cholan Formation of western Taiwan, *Proc. Geol. Soc. China* **6**, 41-50.

Lee, J.C., H.T., Chu, J. Angelier, Y.C. Chan, J C. Hu, C.Y. Lu, and R.J. Rau (2002). Geometry and structure of northern surface ruptures of the 1999 Mw=7.6 Chi-Chi, Taiwan, earthquake: influence from inherited fold belt structures*, J. Struc. Geol*. **24**, 173-192.

Lee, J.C., Y.G. Chen, K. Sieh, K. Mueller, W.S. Chen, H.T. Chu, Y.C. Chan, C. Rubin, and R. Yates (2001). A vertical exposure of the 1999 surface rupture of the Chelungpu fault at Wufeng, western Taiwan: structural and paleoseismic implications for an active thrust fault, *Bull. Seism. Soc. Am*. **91**, 914-929.

Liao, C.F. (2003). Analysis of fault rock deformation and clay minerals from fault cores of Chelungpu fault zone, *Master's Thesis*, National Taiwan University, Taipei, Taiwan (in Chinese with English summary).

Lin, C.H. (2000). Thermal modeling of continental subduction and exhumation constrained by heat flow and seismicity in Taiwan, *Tectonophysics* **324**, 189-201.

Lin, A., T. Ouchi, A. Chen, and T. Maruyama (2001). Co-seismic displacements, folding and shortening structures along the Chelungpu surface rupture zone occurred during the 1999 Chi-Chi (Taiwan) earthquake, *Tectonophysics* **330**, 225-244.

Lin, A., C.T. Lee, T. Maruyama, and A. Chen (2005). Meso- and microstructural analysis of coseismic shear zone of the 1999 Mw 7.6 Chi-Chi earthquake, Taiwan, *Bull. Seism. Soc. Am.* **95**, 486-501.

Lockner, D.A., and N.M. Beeler (2002). Rock failure and earthquakes, in *Internationa. Handbook of Earthquake Engineering Seismology,* W.H.K. Lee, H. Kanamori,

P.C. Jennings, and C. Kisslinger (Editors), Academic Press, San Diego, California, 505-533.

Lu, C.B. (2004). Fluid infiltration after seismic faulting: examining chemical and mineralogical composition of the fault rocks in the drilling cores from Nantou well of the Chelungpu fault, *Master's Thesis*, National Central University, Jhongli, Taiwan (in Chinese with English summary).

Ma, K.F., T.R.A. Song, S.J. Lee, and H.I. Wu (2000). Spatial slip distribution of the September 20, 1999, Chi-Chi, Taiwan, earthquake (M_w 7.6) – Inverted from teleseismic data, *Geophys. Res. Lett.* **27**, 3417-3420.

Marone C., and D.M. Saffer (*in press*). Fault friction and the upper transition from seismic to aseismic faulting, in *The Seismogenic Zone of Subduction Thrust Faults,* T.H. Dixon, J.C. Moore, and R.D. Hyndman (Editors), Columbia University Press, New York, New York.

Moore, D.M., and D.A. Lockner (*in press*). Friction of the smectite clay montmorillonite: a review and interpretation of data, in *The Seismogenic Zone of Subduction Thrust Faults,* T.H. Dixon, J.C. Moore, and R.D. Hyndman (Editors), Columbia University Press, New York, New York.

Moore, D.M., and R.C. Reynolds Jr. (1997). *Individual Clay Minerals, X-ray Diffraction and the Identification and Analysis of Clay Minerals*, Oxford University Press, New York, New York.

Morrow, C. Radney, B., and Byerlee, J. (1992). Frictional strength and the effective pressure law of montmorillonite and illite clays, in *Fault Mechanics and Transport Properties of Rocks, A Festschrift in Honor of W. F. Brace,* B. Evans, and T.F. Wong (Editors), Academic Press, San Diego, California, 69-88.

Ouchi, T., A. Lin, A. Chen, and T. Maruyama (2001). The 1999 Chi-Chi (Taiwan) earthquake: earthquake fault and strong ground motions, *Bull. Seism. Soc. Am.* **91**, 966-976.

Ogelsby, D.D., and S.M. Day (2001). The effect of fault geometry on the 1999 Chi-Chi (Taiwan) earthquake, *Geophys. Res. Lett*. **28**, 1831-1834.

Reynolds Jr., R.C., and R.C. Reynolds III (1996). *NEWMOD*™, *a computer program for the calculation of one-dimensional diffraction patterns of mixed-layered clays,* http://www.angelfire.com/md/newmod/.

Saffer, D.M., and C. Marone (2003). Comparison of smectite- and illite-rich gouge frictional properties; application to the updip limit of the seismogenic zone along subduction megathrusts, *Earth Plan. Sci. Lett.* **215**, 219-235.

Shin, T.C., and T. Teng (2001). An Overview of the 1999 Chi-Chi, Taiwan, earthquake, *Bull. Seis. Soc. Am.,* **91**, 895-913.

Scholle, P.A. (1978). *A color illustrated guide to carbonate rock constituents, textures, cements, and porosities*, **Memoir 27**, Am. Assoc. Petrol. Geol., Tulsa, Oklahoma.

Solum, J.G., B.A. van-der Pluijm, C.M. Hall, and D.R. Peacor (2005). Neocrystallization, fabrics and age of clay minerals from an exposure of the Moab Fault, Utah, *J. Struc. Geol*. **27**, 1563-1576.

Solum, J.G., B.A. van der Pluijm, D.R. Peacor, and L. Warr (2003). Influence of phyllosilicate mineral assemblages, fabrics, and fluids on the behavior of the Punchbowl Fault, Southern California, *J. Geophys. Res.* **B108**, doi: 10.1029/2002JB001781.

Suppe, J. (1987). The Active Taiwan Mountain Belt, in *The Anatomy of Mountain Ranges*, J.P. Schaer and J. Rodgers (Editors), Princeton University Press, Princeton, New Jersey.

Suppe, J., and J.H. Wittke (1977). Abnormal pore-fluid pressure in relation to stratigraphy and structure in the active fold-and-thrust belt of northwestern Taiwan, *Petr. Geol. Taiwan* **14**, 11-24.

Tanaka, H., C.Y. Wang, W.M. Chen, A. Sakaguchi, K. Ujiie, H. Ito, and M. Ando (2002). Initial science report of shallow drilling penetrating into the Chelungpu fault zone, Taiwan, *TAO* **13**, 227-251.

Vrolijk, P.J., and B.A. van der Pluijm (1999). Clay Gouge, *J. Struc. Geol*. **21**, 1039-1048.

Whitney, G. (1990). Role of water in the smectite-to-illite reaction, *Clays Clay Min*. **38**, 343-350.

Zeng, Y., and C.H. Chen (2001). Fault rupture process of the 20 September 1999 Chi-Chi, Taiwan, earthquake, *Bull. Seism. Soc. Am.* **91**, 1088-1098.

Zhao, G., D.R. Peacor, and S.D. McDowell (1999) “Retrograde Diagenesis” of clay minerals in the Precambrian Freda sandstone, Wisconsin, *Clays Clay Min.* **47**, 199-130.

Table 2-1
Number of field and core samples used for optical microscopy and analyzed by XRD, XRF, and/or ICP MS in this study (*these samples were analyzed in previous studies by Liao, 2003 and Lu, 2004. Results are used for this study).

Study Site	Thin Sections	Bulk XRD	Clay XRD	XRF/ICP
FIELD SITES				
Field Site 1	3	9	5	4
Field Site 2	0	0	8	0
Field Site 3	7	18	9	9
Field Site 4	9	33	9	17
Field Site 5	2	22	4	6
Field Site 6	11	24	11	14
DRILL SITES				
Fengyuan	0	0	25*	12*
Nantou	0	0	74*	12*
TCDP	8	8	4	8

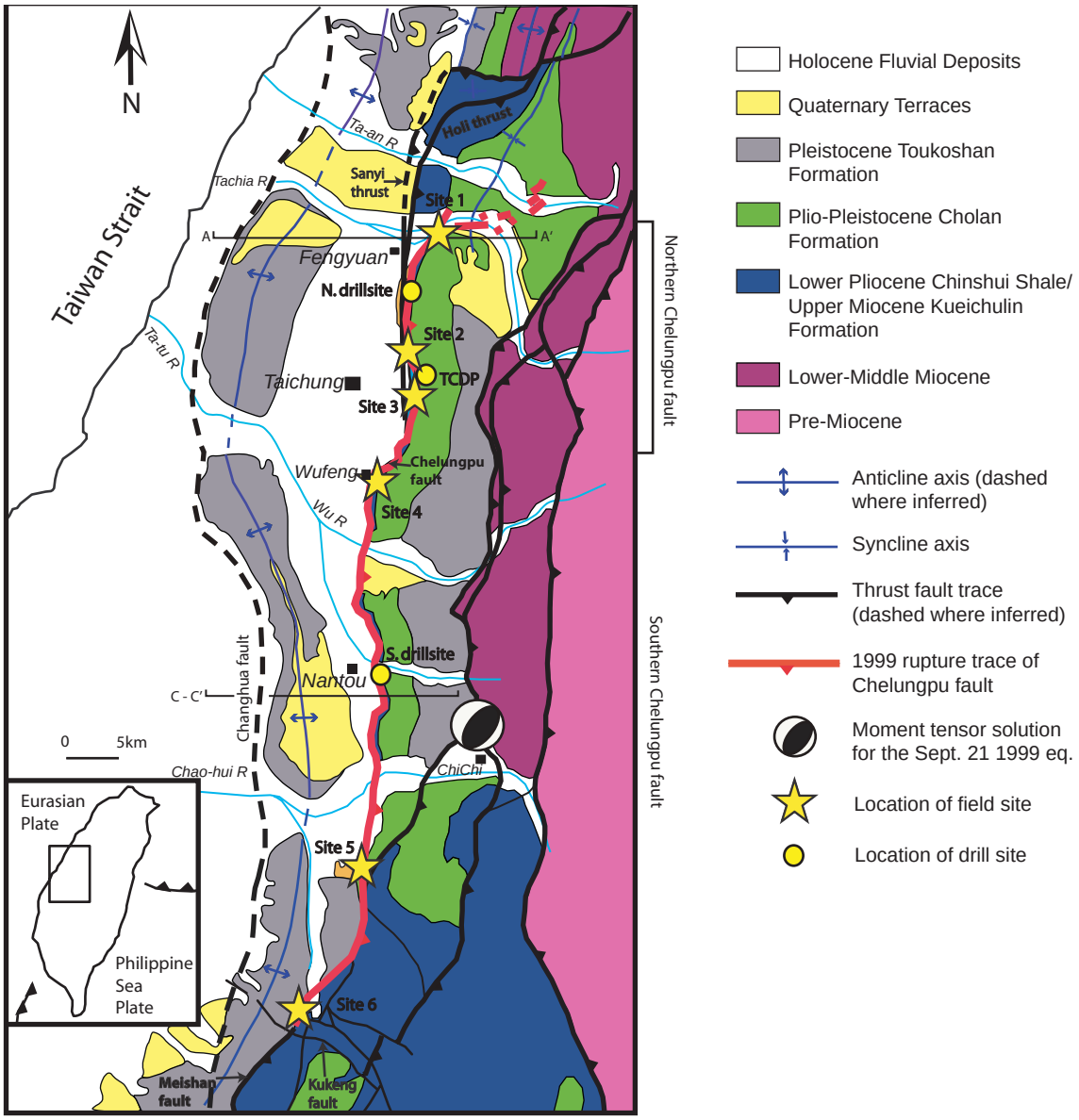

Figure 2-1. Geologic map of the Chelungpu fault area and the extent of the Sept. 21, 1999 rupture. Additional west vergent faults are shown. Map modified from Chui (1971), Ouchi et al. (2001), and Heermance et al. (2003).

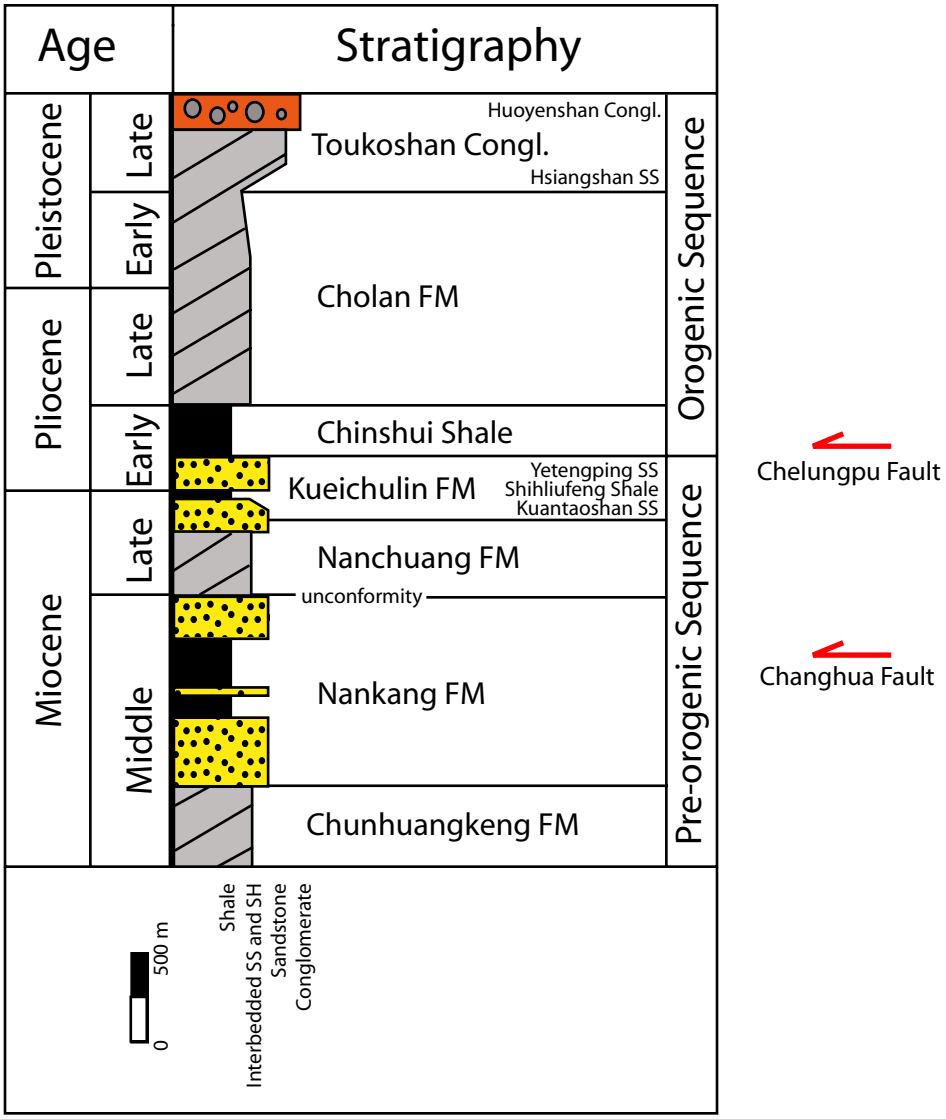

Figure 2-2. Stratigraphic column of sedimentary units of the western foothills fold and thrust belt, Taiwan. The position of the Chelungpu fault in the sequence is labeled. The formations involved with the Chelungpu fault include the Kueichulin, Chinshui Shale, Cholan, and Toukoshan Conglomerate formations (modified from Hung and Wiltschko, 1993).

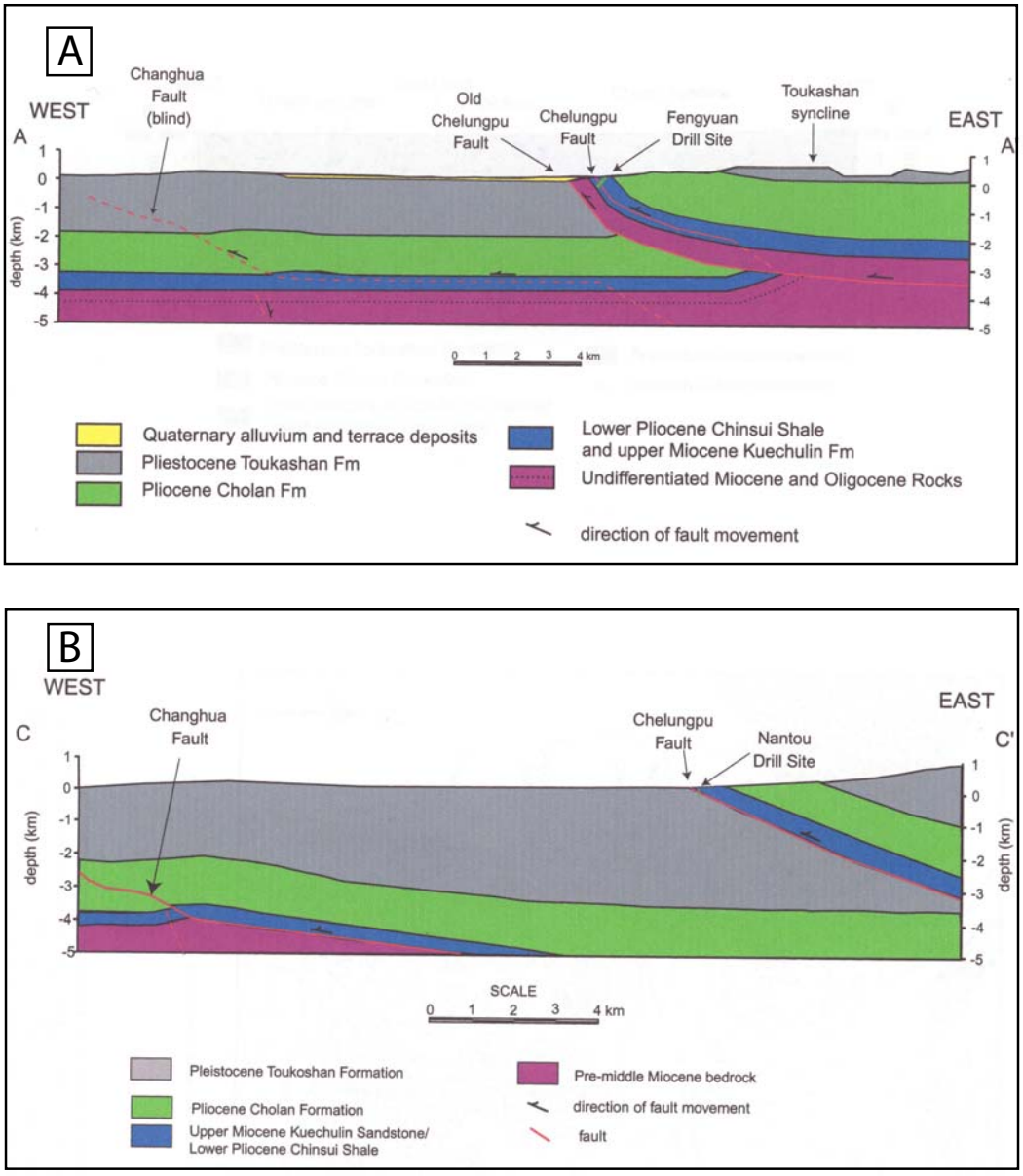

Figure 2-3. Cross sections across the Chelungpu fault. a) Cross section near Fengyuan (northern drillsite) showing a new strand of the Chelungpu fault in the hanging wall of the old Chelugnpu fault. The new Chelungpu fault cuts the Chinshui Shale and places it on Chinshui Shale or Kuechulin Formation and Quaternary gravels. b) Cross section near Nantou (southern drillsite) showing the Chelungpu fault thrusting Chinshui Shale on Toukoshan Conglomerate (Heermance, 2002). c) Schematic cross section across Taiwan showing the approximate location of the main shock in red,with selected aftershocks in black (Heermance, 2002; references therein).

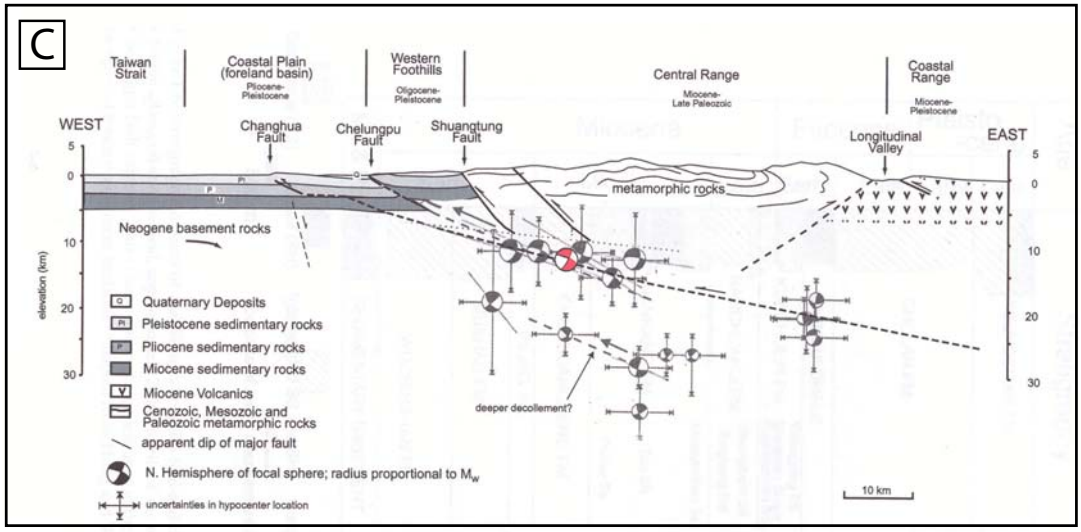

Figure 2-3 continued.

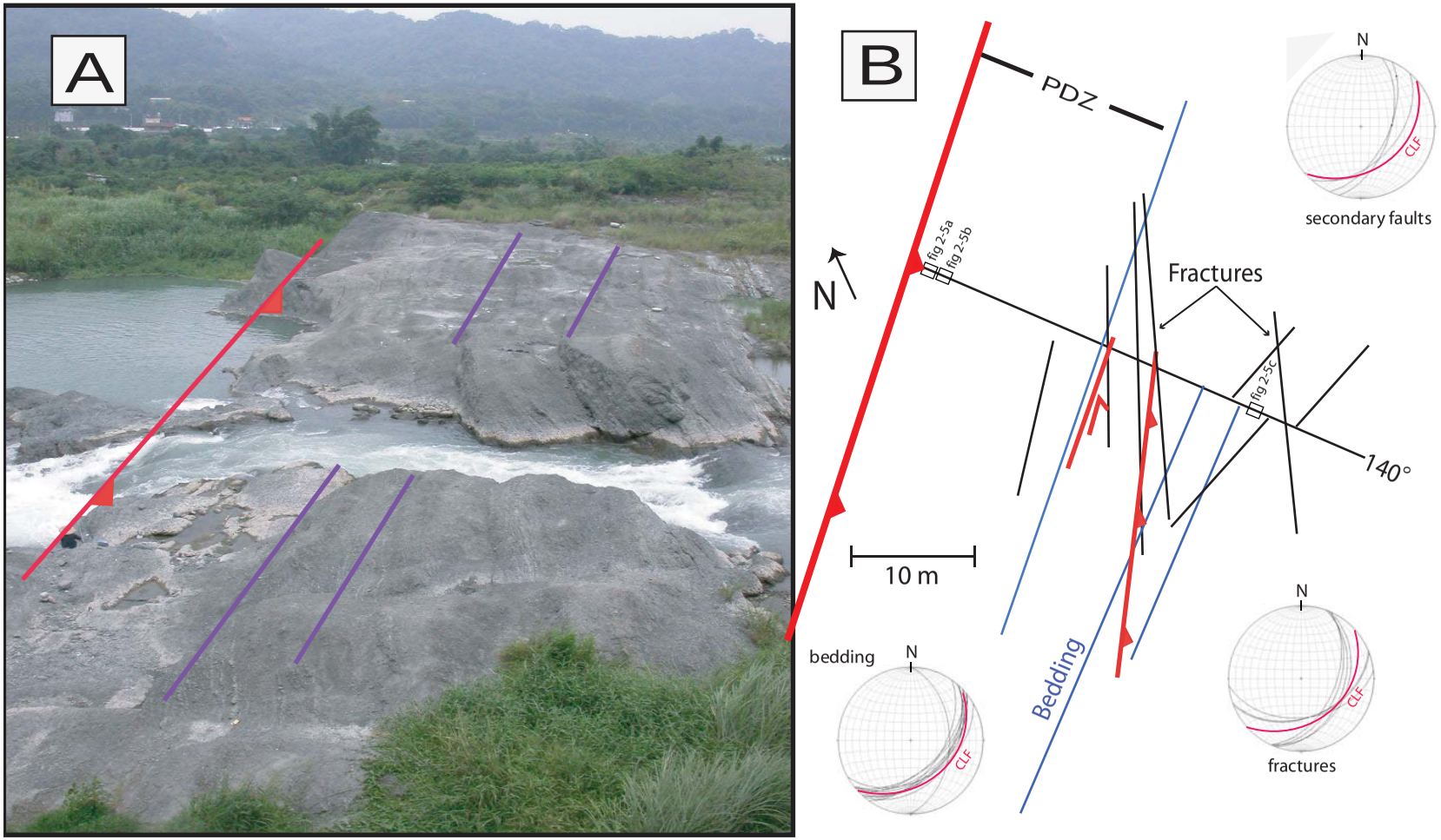

Figure 2-4. Field site 1. a) View to the north of the Tachia waterfall created in the 1999 rupture of the Chelungpu fault (photo taken in 2004). The red line indicates the trace of the surface rupture, and blue lines indicate bedding. b) Transect of site 1 (plan view) illustrating the orientation of the 1999 rupture, fractures, bedding, and secondary faults. River flow is to the left (west).

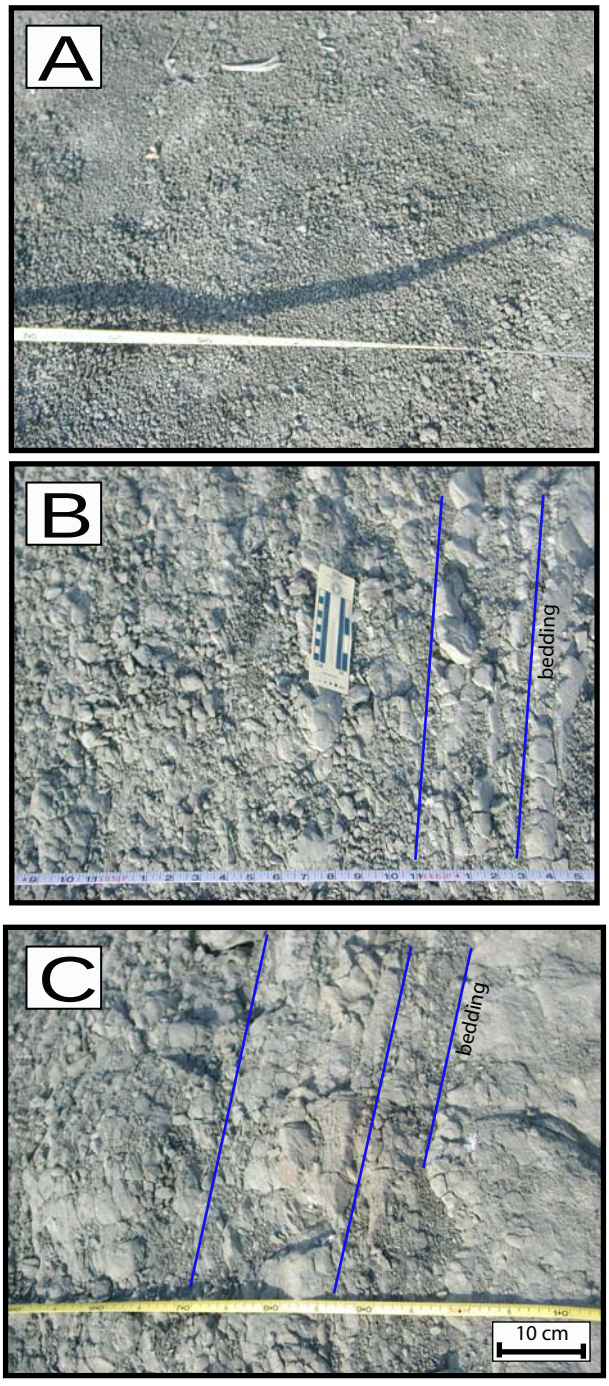

Figure 2-5. Examples of the damage zone at field site 1. a) Brecciation zone ~ 70 cm from 1999 rupture trace. b) Intact bedding within 3 m of the 1999 rupture trace. c) Bedding and typical rounded weathering and fracture pattern of the Chinshui Shale at ~ 32 m from the 1999 rupture trace.

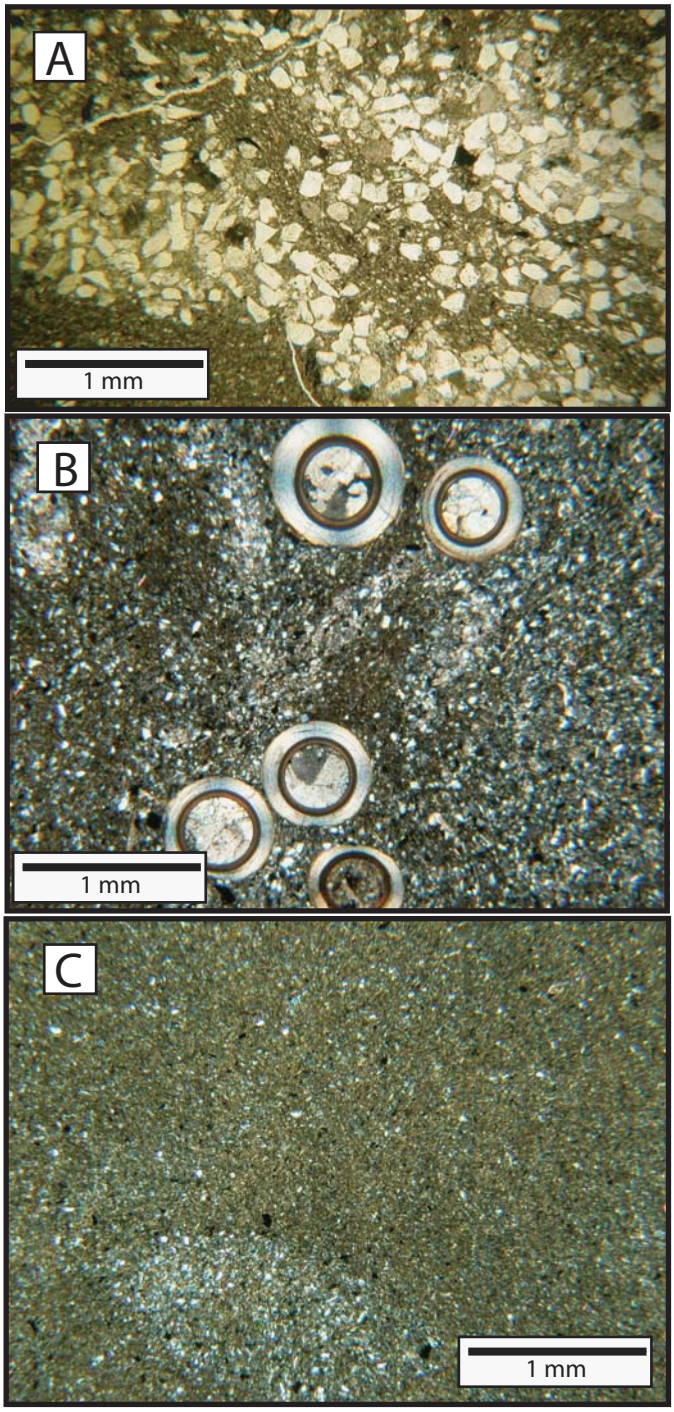

Figure 2-6. Photomicrographs of field site 1 samples. a) Photomicrograph showing intact host rock ~1 m from the 1999 rupture at field site 1, Tachia River. Some inter-granular microfractures are present, but grains are undamaged, and fine-grained layers show no shear fabric (polarized light). b) Cross-sections of pteropods show no evidence of shear ~1 m from the main fault (polarized light). c) Very fine-grained layers of shale along a secondary fault show no development of shear fabric ~25 m into the hanging wall (polarized light).

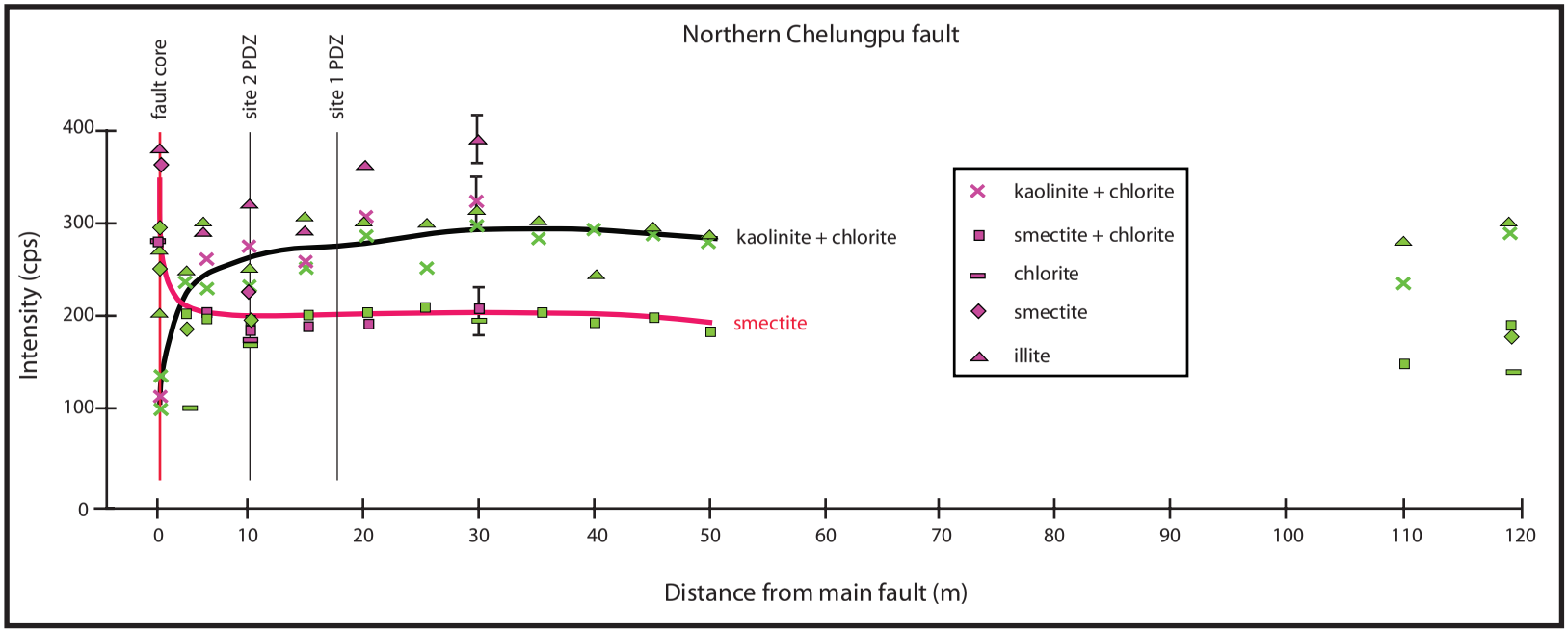

Figure 2-7. Plot of peak intensities from XRD patterns for major clay constituents of the northern Chelunpgu fault rocks. Peak intensity is a function of the amount of the mineral present in a sample, and can therefore be used as a proxy for relative abundance. Each clay type can only be compared to itself, not other types of clay using this method. Northern Chelungpu fault: purple symbols = field site 1 samples, green symbols = field site 2. Smecite is most abundant in the fault core and primary damage zone rocks, and kaolinite + chlorite and possibly illite (field site 3) are least abundant in the fault core. Southern Chelungpu fault: blue symbols = field site 4 fault gouge, green symbols = field site 4 damage zone, red symbols = field site 6 fault gouge, orange symbols = field site 6 damage zone. There is not an easily distinguishable pattern of clay mineral abundances, however smectite may be most abundant in the fault core and other fault gouge. Error bars = +/- 2 standard deviations.

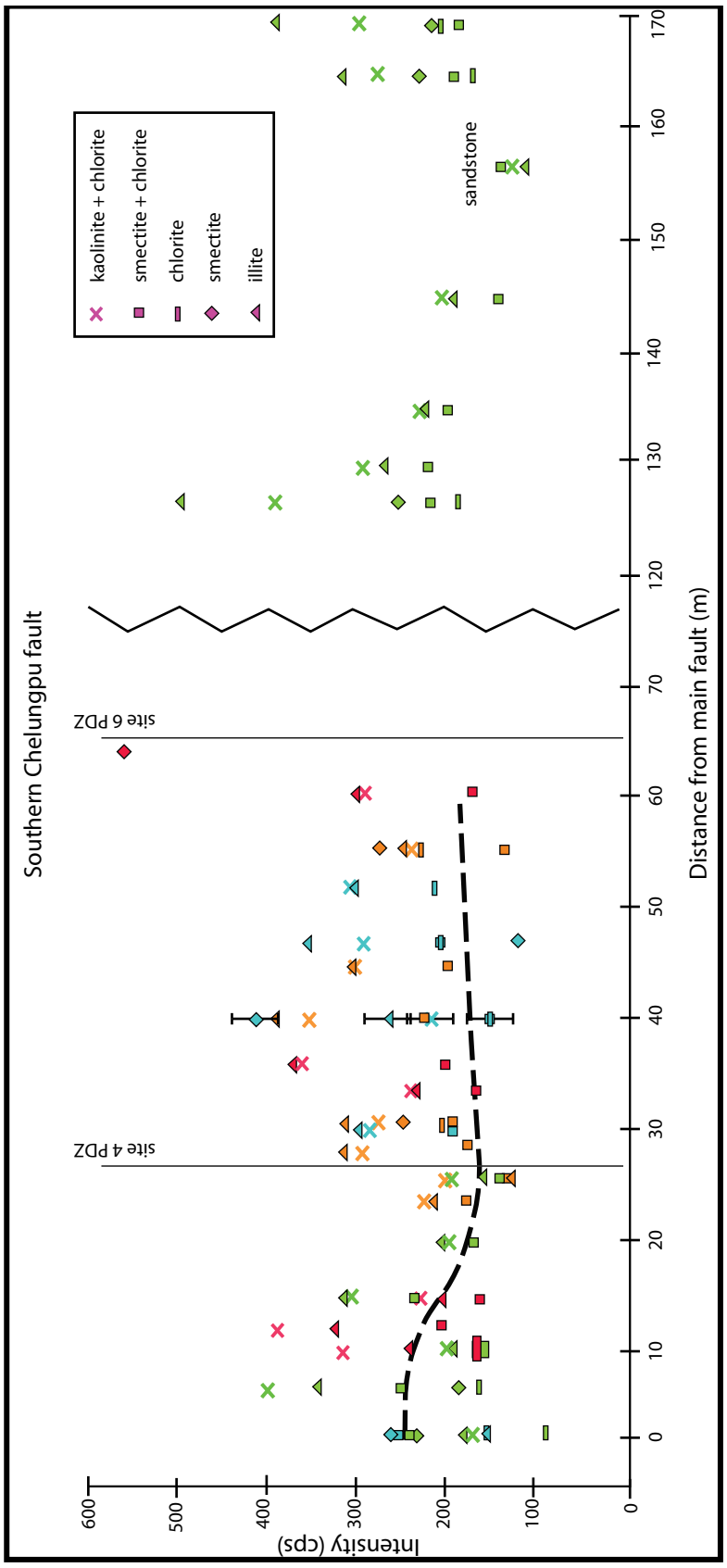

Figure 2-7 continued.

Figure 2-8. Oriented clay XRD results for fault core clay samples from each study site, where available. No fault gouge was found at field site 1, so the clay pattern show here is of the primary damage zone (PDZ). All other patterns are for fault gouge from the main fault core (FC), or from fault gouge in secondary faults (FG). The distance from the 1999 rupture is indicated in the legend for individual patterns.

X-ray Diffraction Patterns for the Northern Chelungpu Fault Field Sites

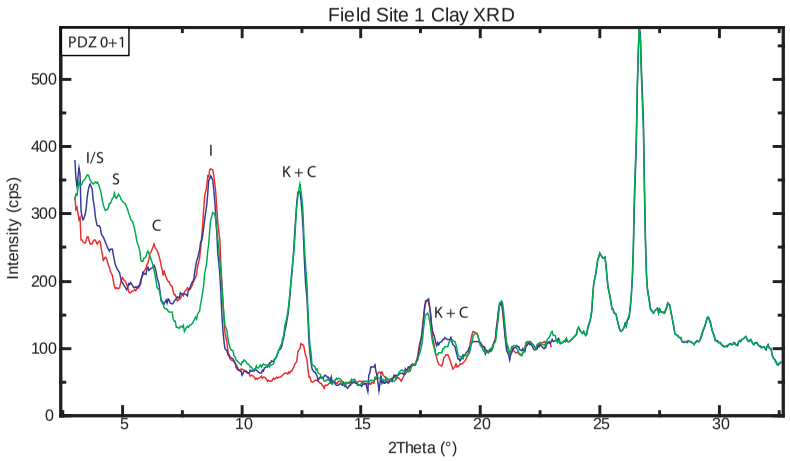

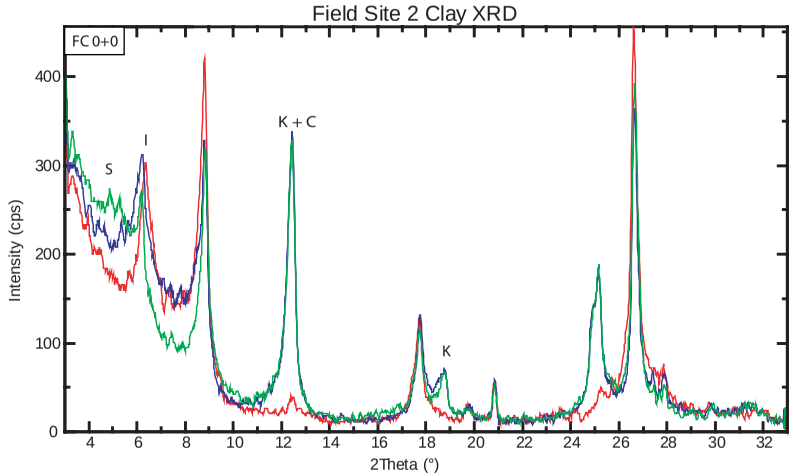

heat
air-dried
ethylene glycol

FC = fault core/gouge

PDZ = primary damage zone

SDZ = secondary damage zone

TCDP = Taiwan Chelunpu fault Drilling Project

S = smectite

C = chlorite

K = kaolinite

I = illite

I/S = mixed layer illite-smectite

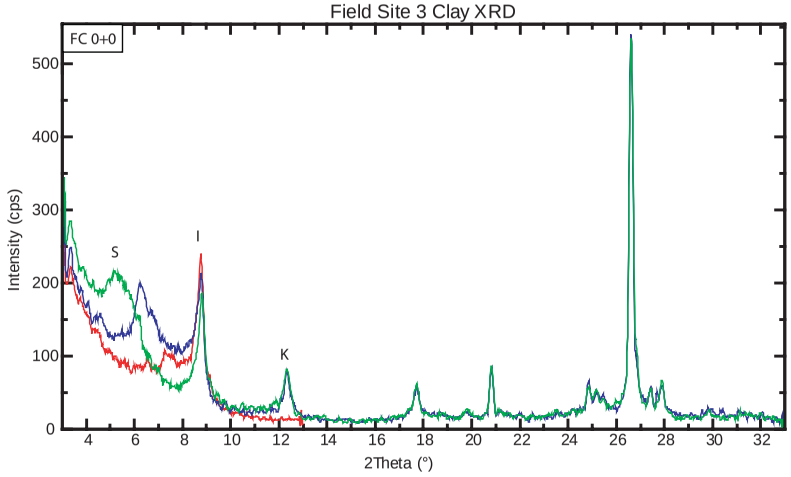

Figure 2-8 continued.

X-ray Diffraction Patterns for the Southern Chelungpu Fault Field Sites

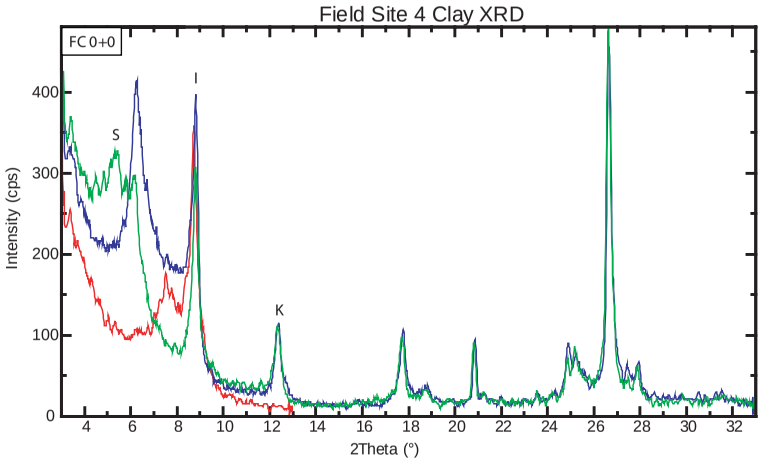

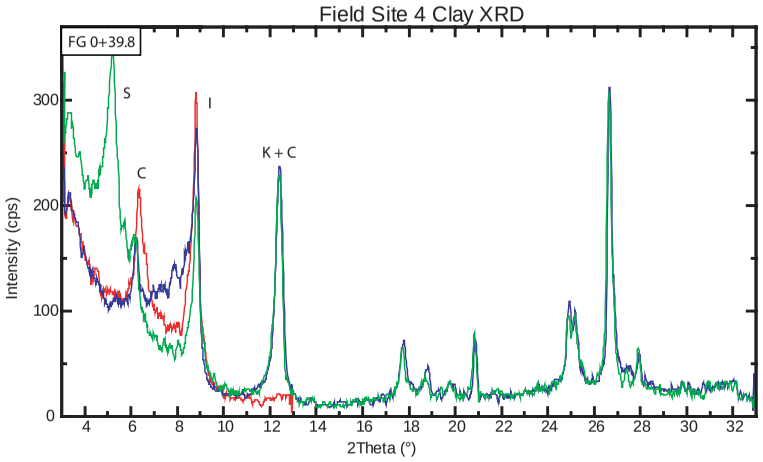

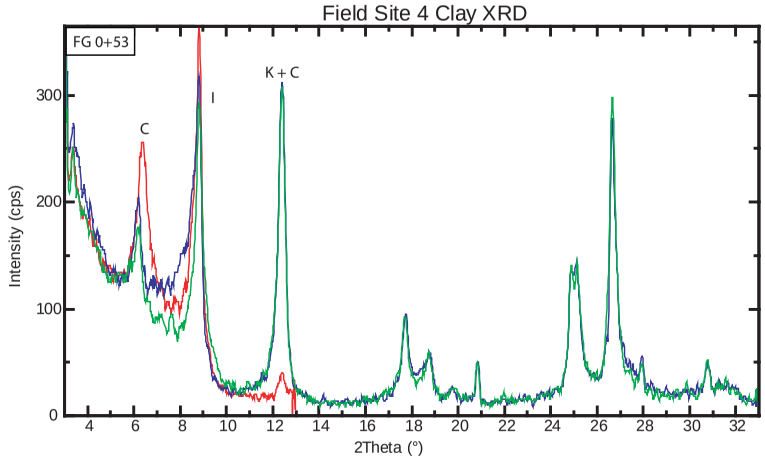

heat
air-dried
ethylene glycol

FC = fault core/gouge

PDZ = primary damage zone

SDZ = secondary damage zone

TCDP = Taiwan Chelunpu fault Drilling Project

S = smectite

C = chlorite

K = kaolinite

I = illite

I/S = mixed layer illite-smectite

Figure 2-8 continued.

X-ray Diffraction Patterns for the Southern Chelungpu Fault Field Sites

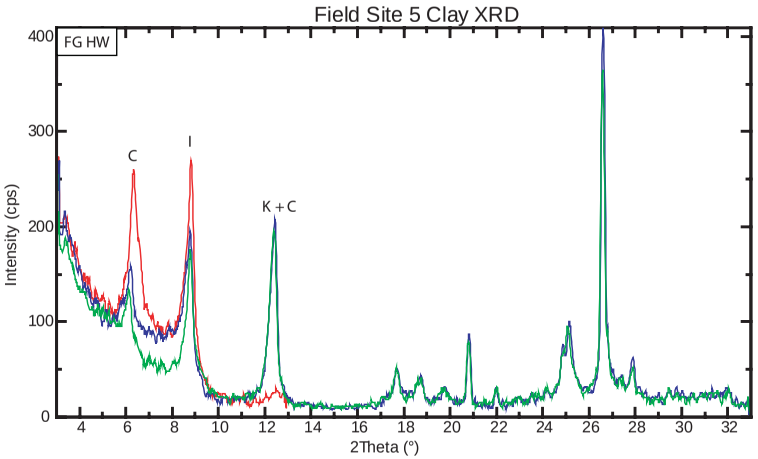

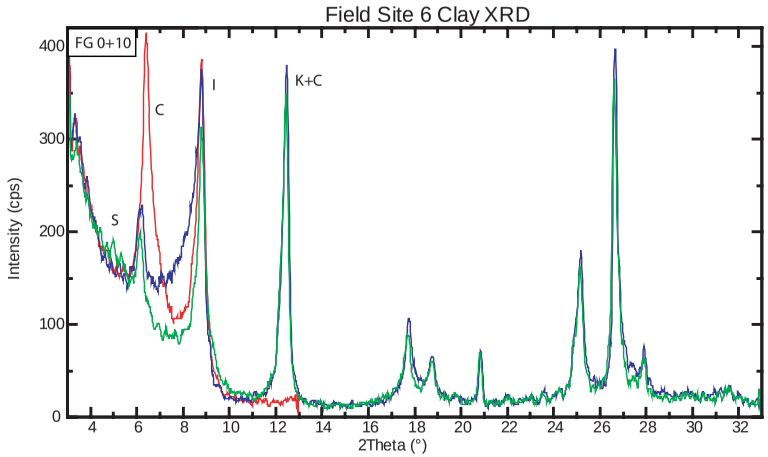

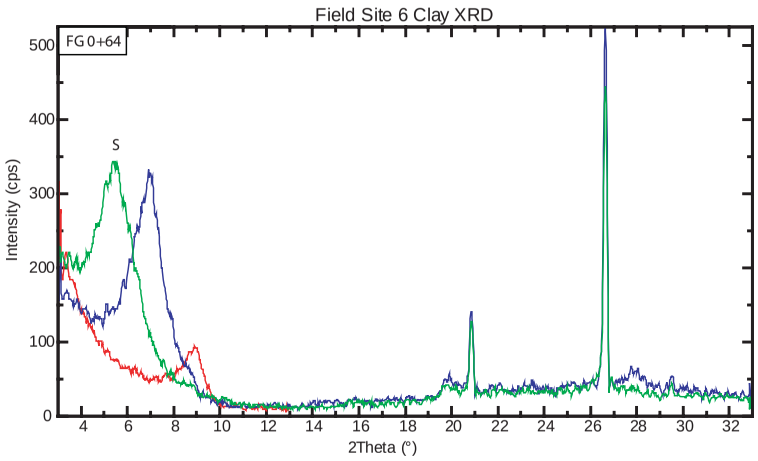

heat
air-dried
ethylene glycol

FC = fault core/gouge

PDZ = primary damage zone

SDZ = secondary damage zone

TCDP = Taiwan Chelunpu fault Drilling Project

S = smectite

C = chlorite

K = kaolinite

I = illite

I/S = mixed layer illite-smectite

Figure 2-8 continued.

X-ray Diffraction Patterns for the
Southern Chelungpu Fault Field Site 6

X-ray Diffraction Patterns for the
Northern Chelungpu Fault Drill Site

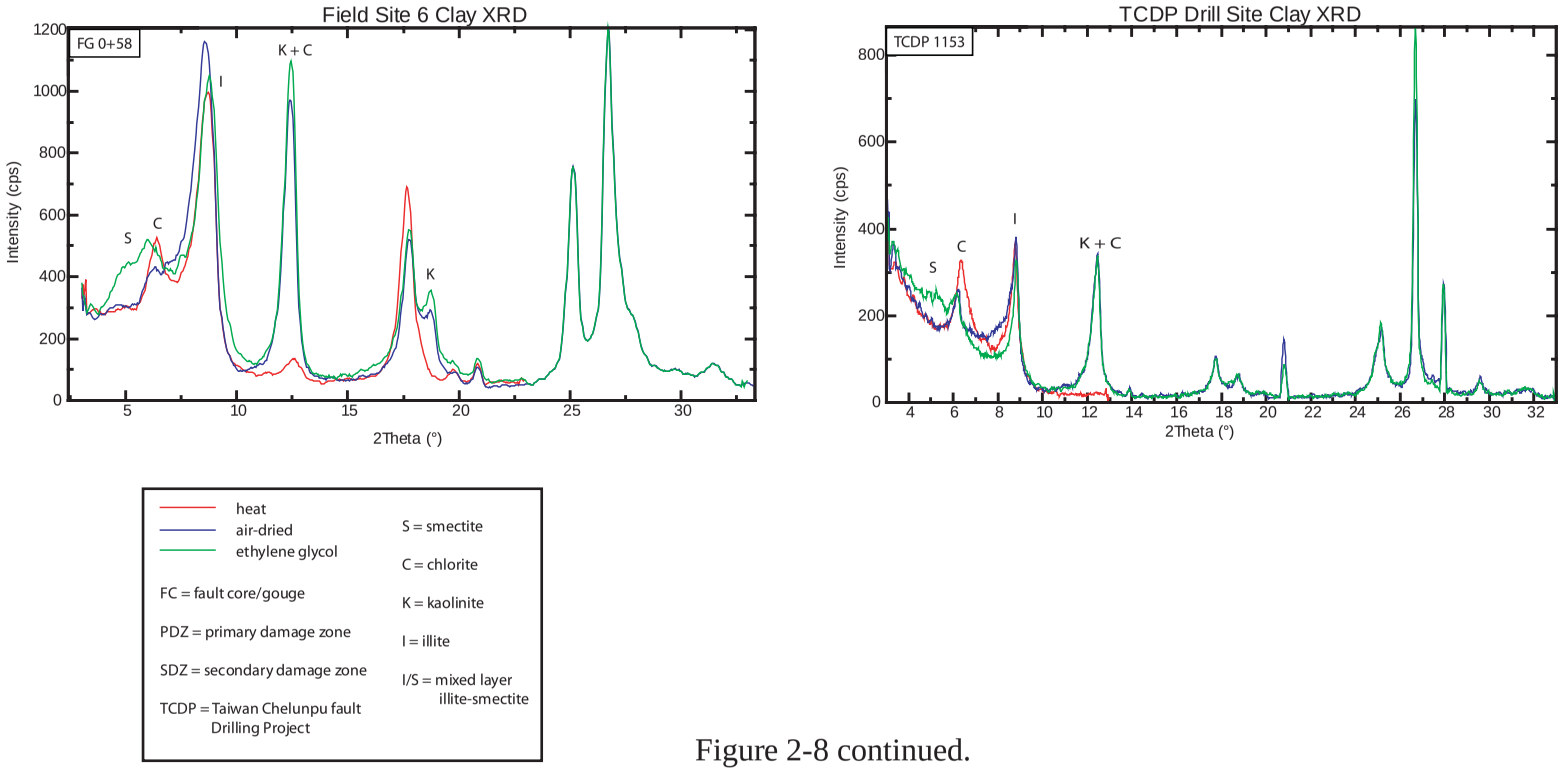

Figure 2-8 continued.

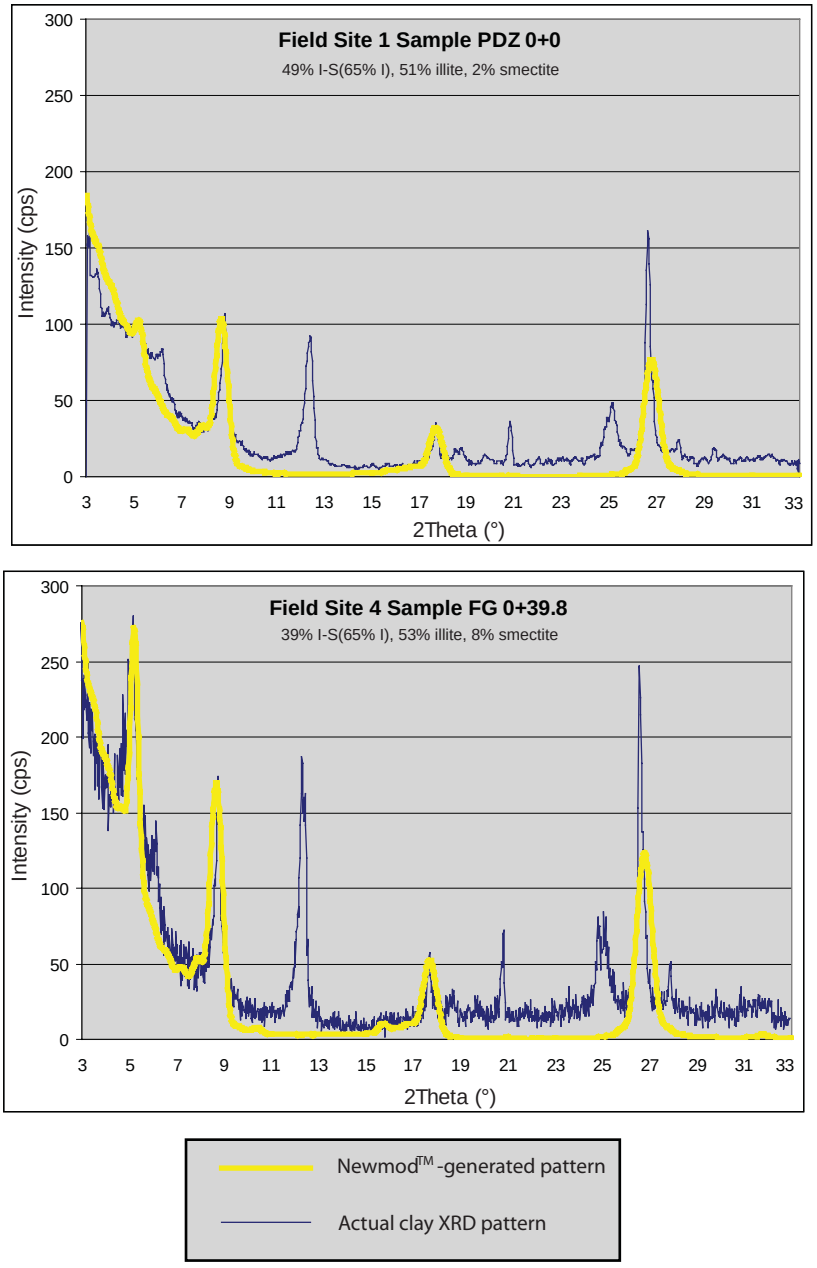

Figure 2-9. Examples of NEWMOD™-generated patterns for I-S, illite, and smectite clays. The poor match of the peaks at ~27° 2 theta is due to fine-grained quartz present in the Chelungpu fault zone samples, as illite and quartz have a common peak at this position.

Figure 2-10. Geochemical results for the fault core (FC), primary damage zone (PDZ), and secondary damage zone (SDZ) where available for field sites 1, 3, 4, and 6 and the Fengyuan (northern) and Nantou (southern) drill sites. Raw data for each field site are shown, as well as calculated percent changes between TCDP host rock and averaged values of host rocks in multiple drill sites, and exhumed fault rocks after the method of Goddard and Evans (1995). The Goddard and Evans method shows that SiO_2 is typically enriched, and CaO, MnO, MgO, and LOI are significantly depleted in fault rocks relative to host rocks. Patterns for drill sites were generated using data from Master's thesis work by Liao (2003) and Lu (2004). Sample names for drill site samples are the same as used in previous work. Oxides have an associated error of 0.01%; trace elements have an associated error of 10 ppm, which is shown on the first trace elements plot between TCDP host rocks and exhumed fault samples from field sites 1, 2, 4, and 8. Percent changes generally increase towards the fault, with SiO_2 typically enriched, and CaO, MnO, MgO, and LOI significantly depleted relative to host rocks.

Geochemical Data for Field Site 1

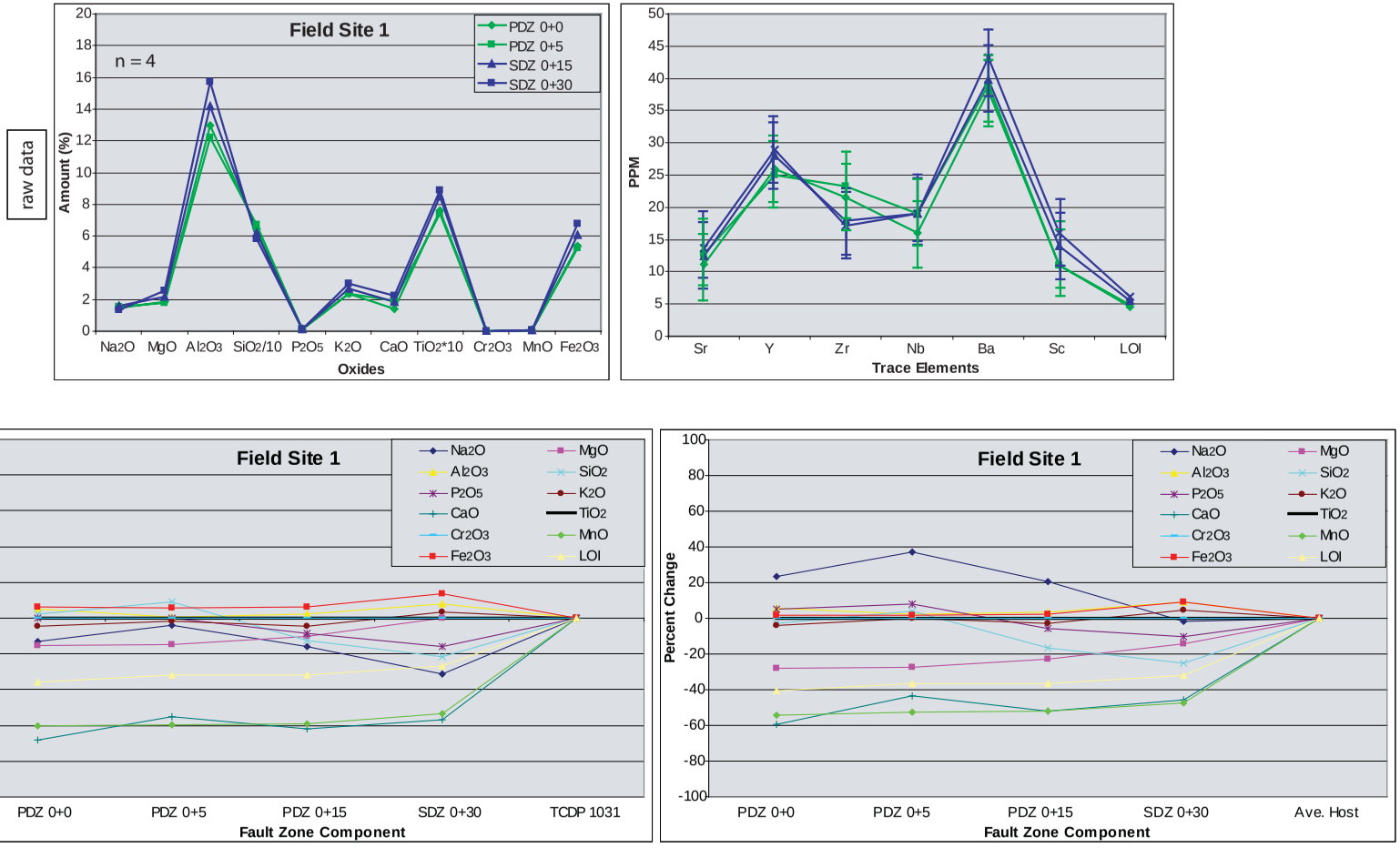

Figure 2-10 continued.

Geochemical Data for Field Site 3

raw data

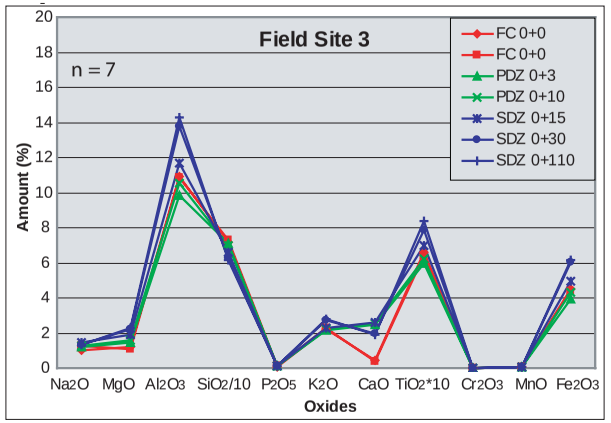

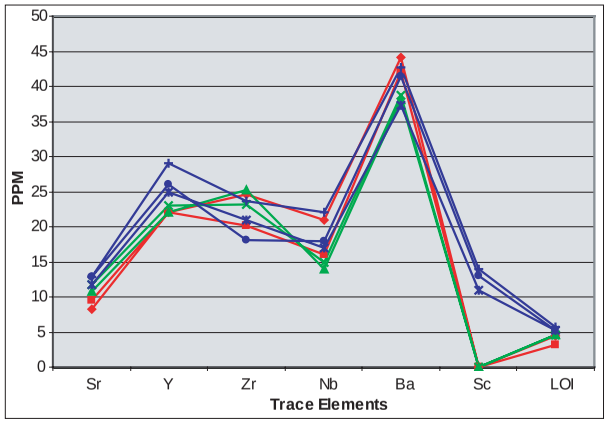

Goddard and Evans method

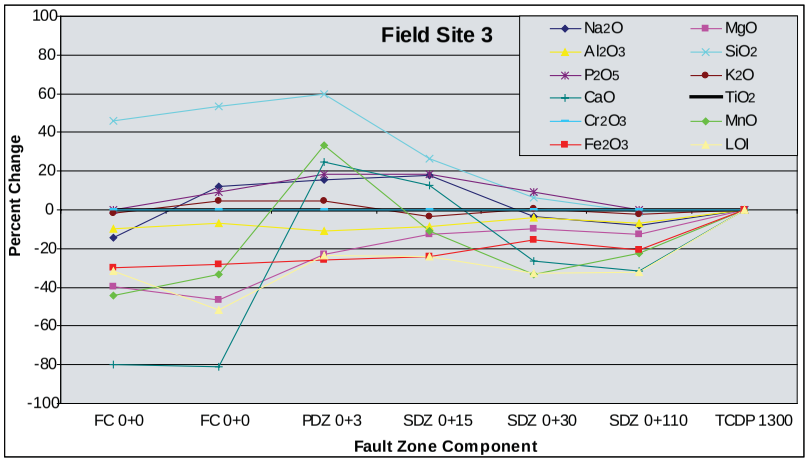

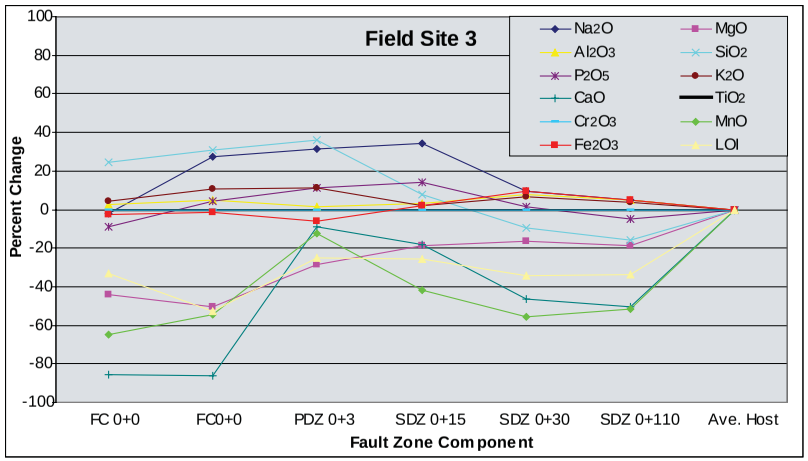

Figure 2-10 continued.

Geochemical Data for Field Site 4

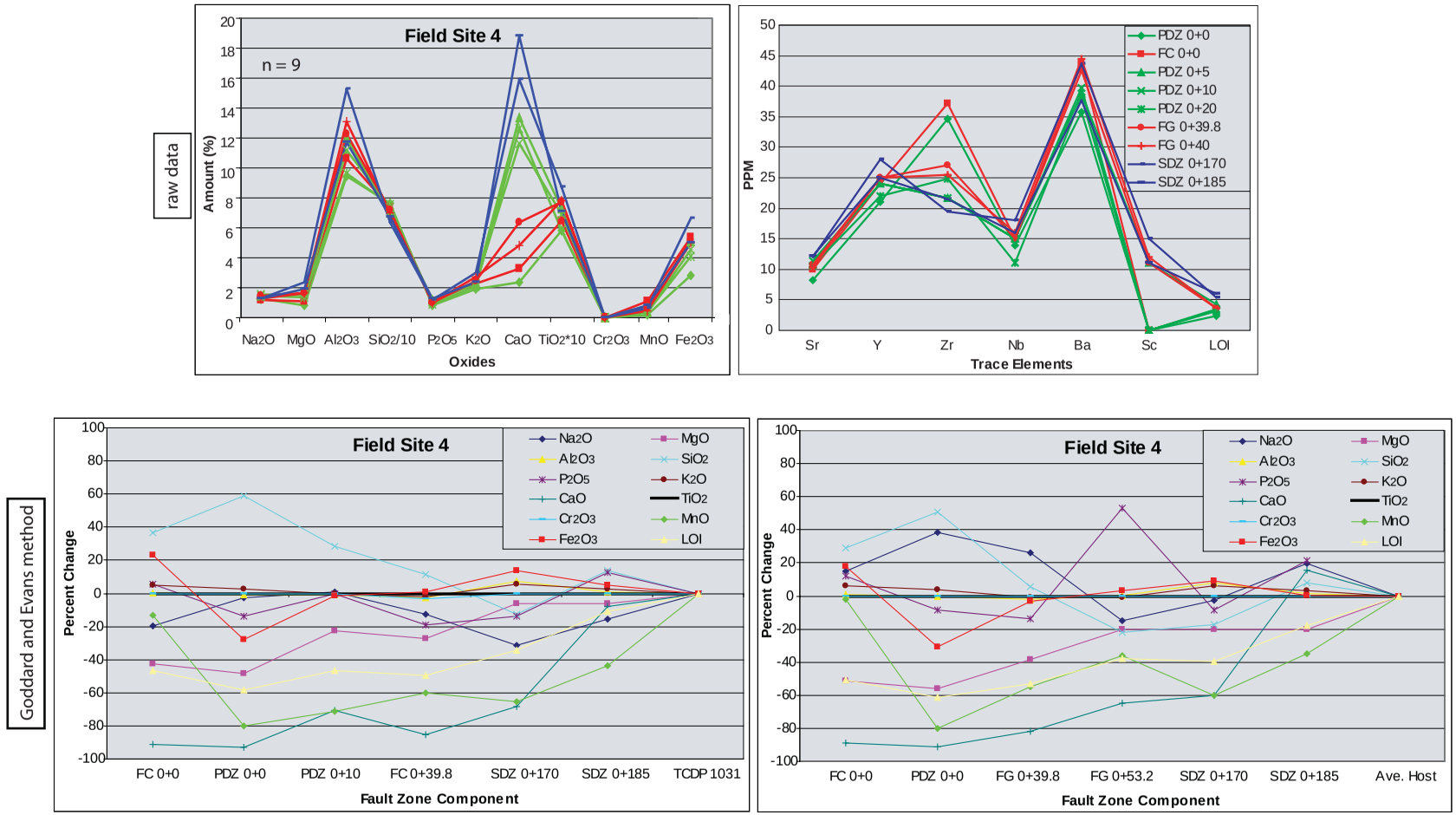

Figure 2-10 continued.

Geochemical Data for Field Site 6

raw data

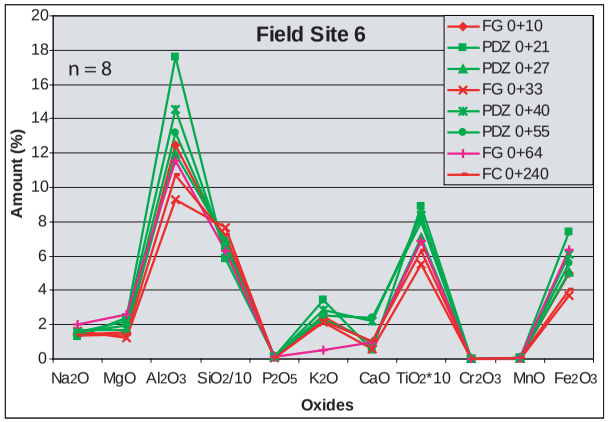

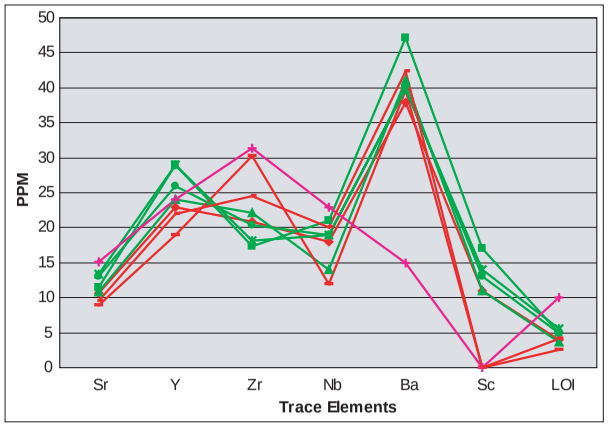

Goddard and Evans method

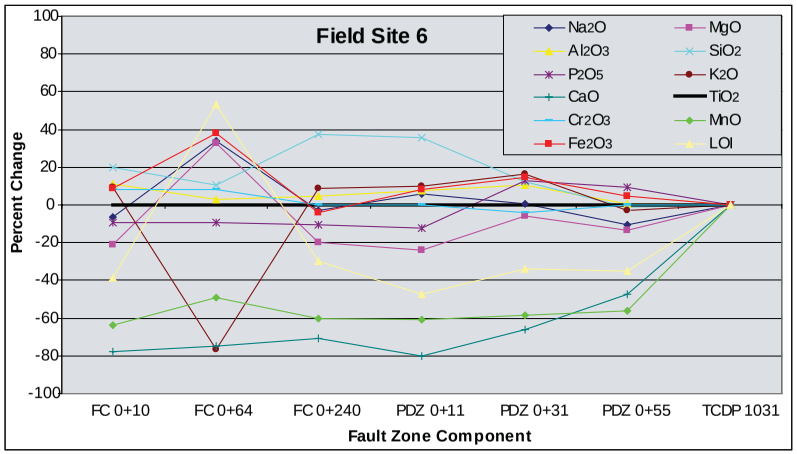

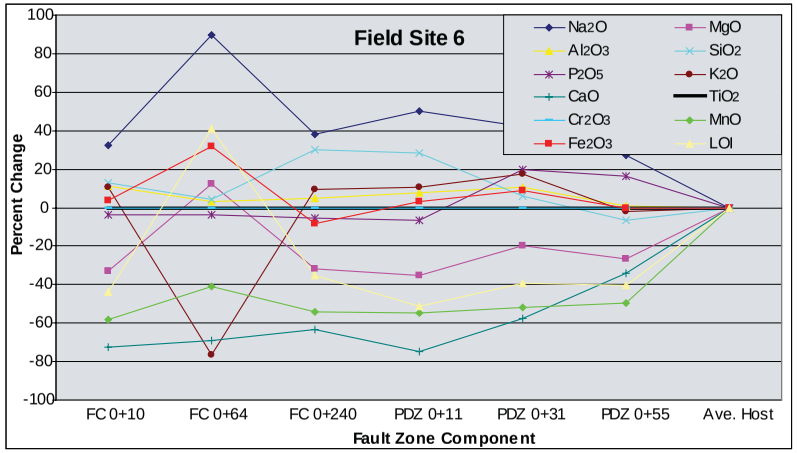

Figure 2-10 continued.

Geochemical Data for Drill Sites

raw data

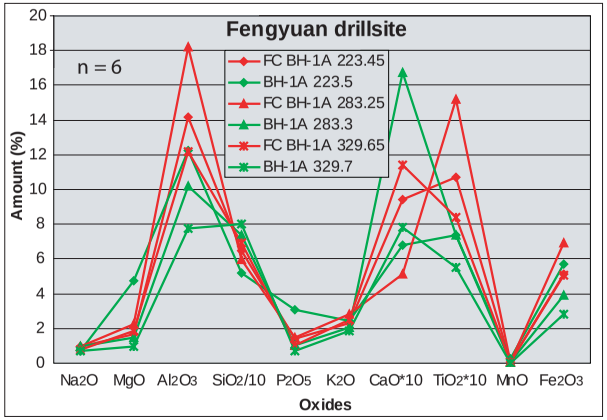

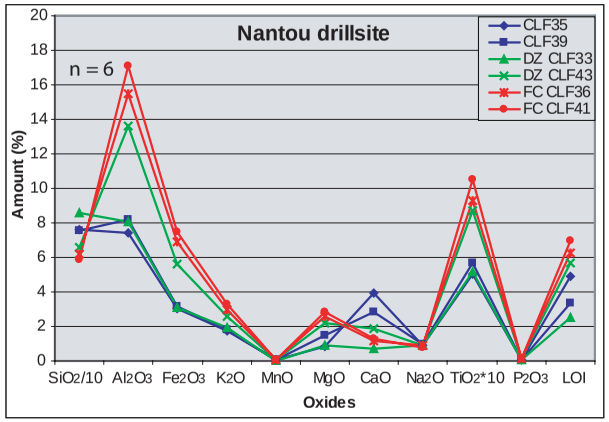

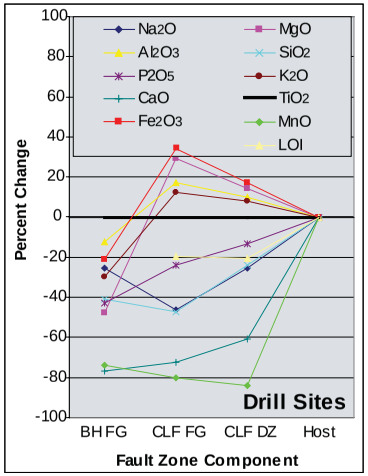

Goddard and Evans method

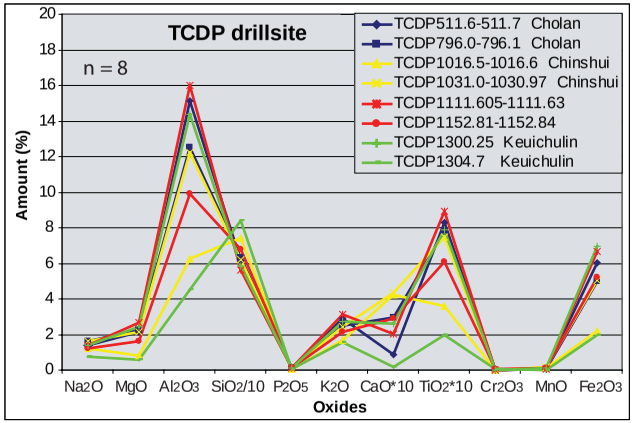

Figure 2-10 continued.

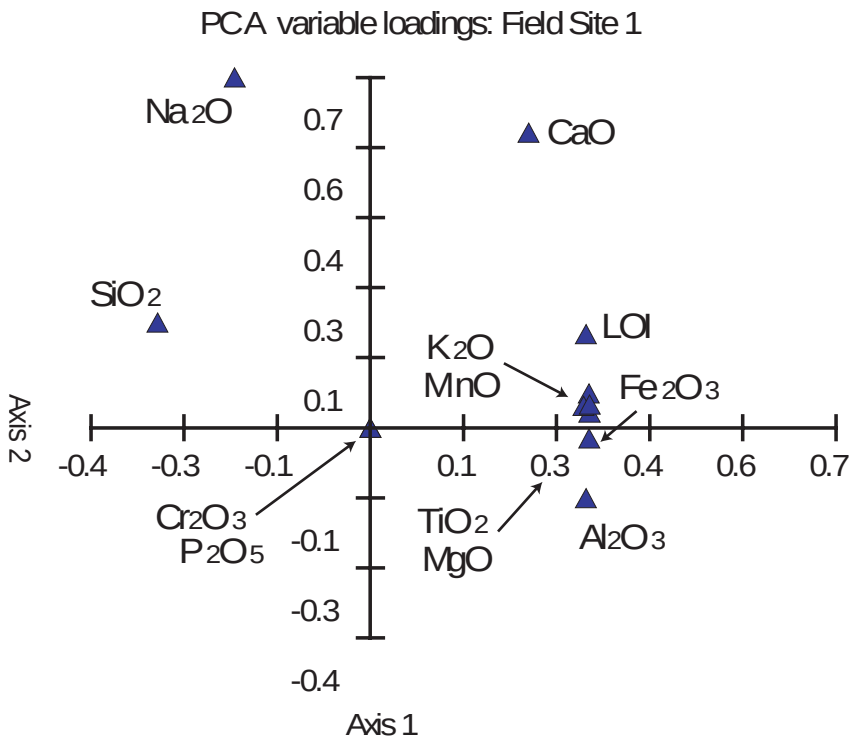

Figure 2-11. Principal component analysis (PCA) for field site 1. ICP results using standardized Log_{10} transformed data in MultiVariate Statistical Package (Kovach Computing Services). Oxides plotting furthest from the origin are the most significant. Principal component analyses for all study sites are done in the same manner.

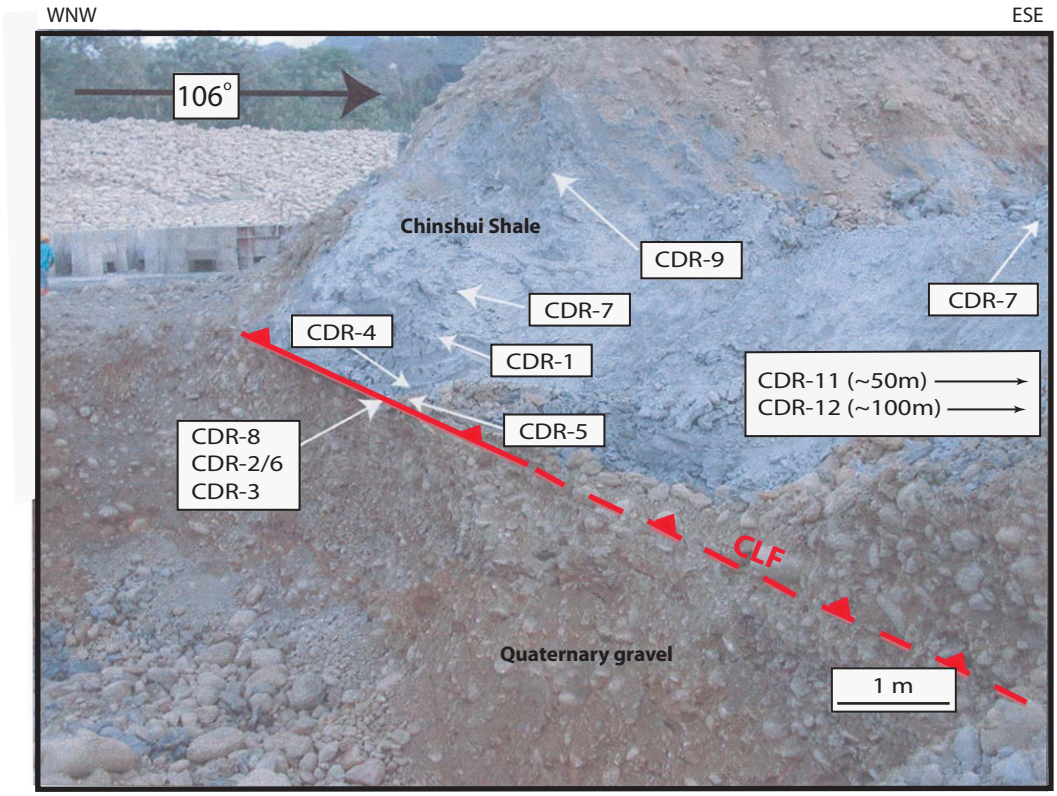

Figure 2-12. Photograph of outcrop at field site 2 near the Tali River showing the locations of samples collected and used for thin sections and XRD (Heermance, 2002; Heermance et al., 2003; this study). Figure modified from Heermance et al. (2003; fig. 6).

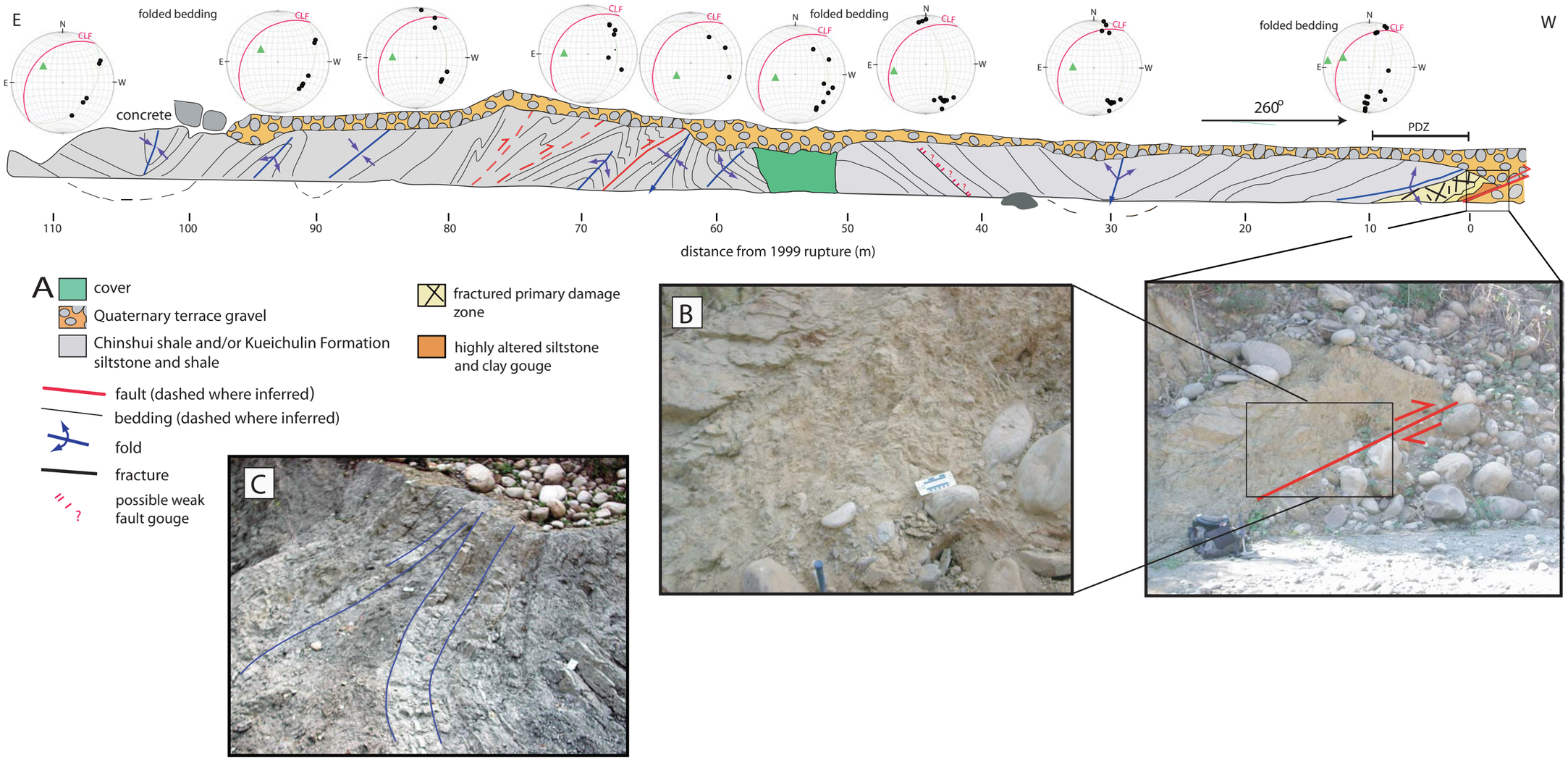

FIGURE 2-13. Outcrop map of field site 3. a) Sketch of outrcrop at field site 3 showing the distribution of fault zone components and damage elements. Pliocene siltstone has been thrust onto Quaternary alluvium. Stereonets of poles to folded bedding are shown. Green triangles mark the orientation of the fold axis, and the Chelungpu fault is indicated. Stereonets were reflected so that the directions match the map; origonal stereonets are included in Appendix A. Transect line is measured at the base of the outcrop. b) Primary damage zone (PDZ) and fault core at field site 3. The fault core contains ultracataclasite and cataclasite, and the primary damage zone has increased fracture density relative to the secondary damage zone, alteration in color of siltstone, and no relict bedding. c) Example of a west-vergent fold in the secondary damage zone.

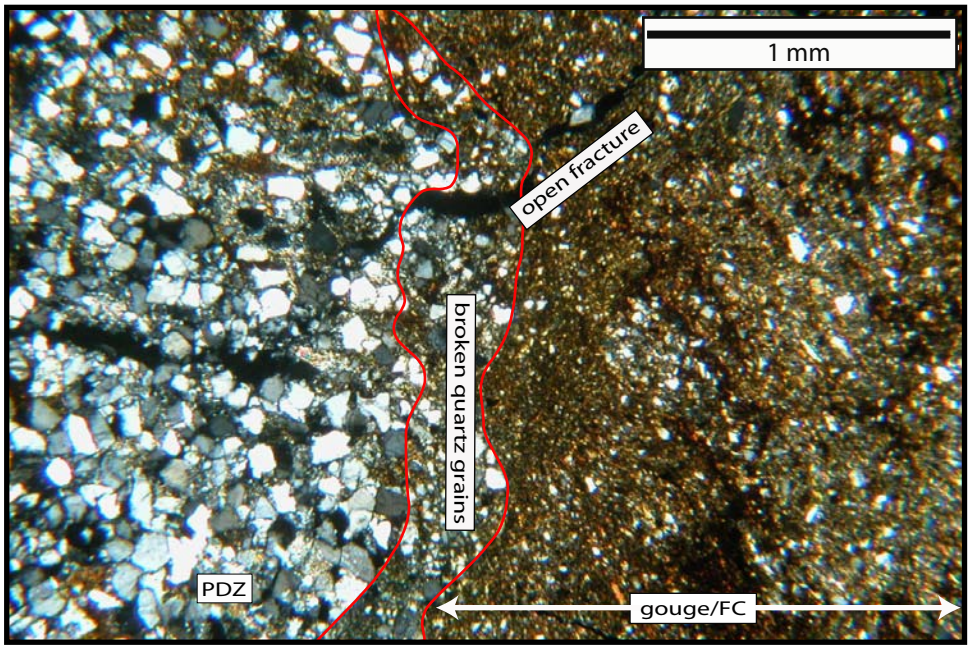

Figure 2-14. Photomicrograph of the Chelungpu fault and associated fault gouge collected at field site 3 at ~10 cm from the contact with Quaternary gravel. Brown fault gouge is on the right, bordered by relatively undeformed primary damage zone (PDZ) rock on the left. The area surrounded by the red line is a transitional area of decreased grain size (polarized light).

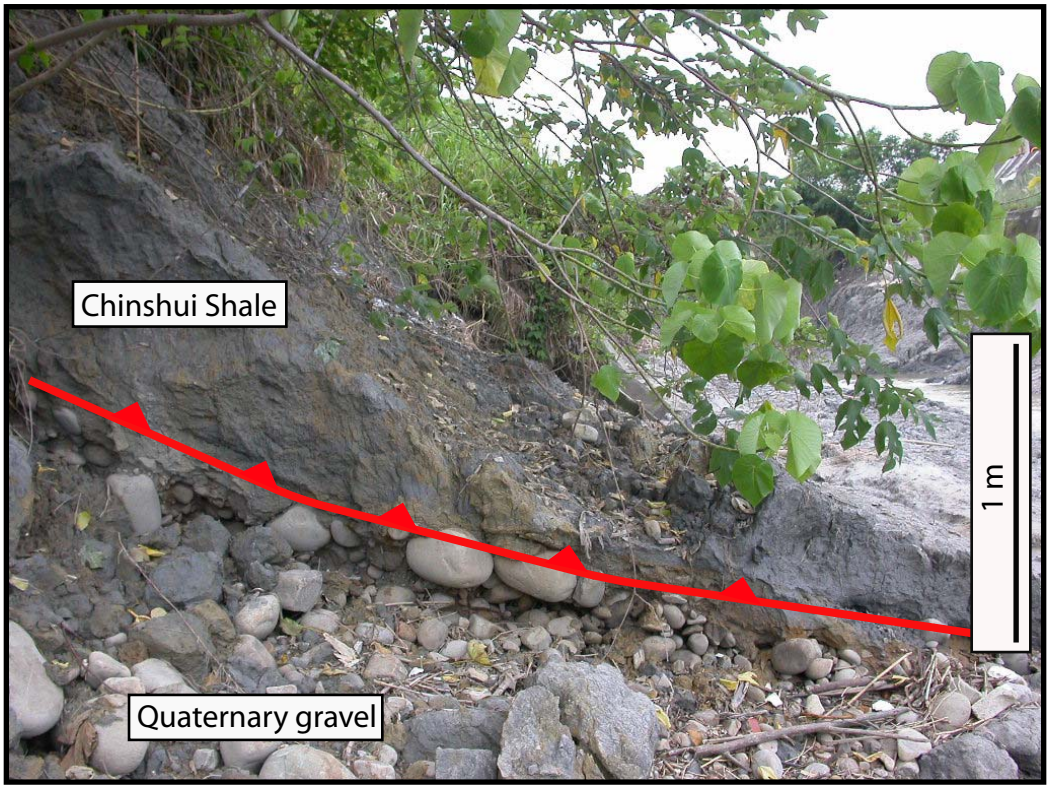

Figure 2-15. Field site 4. View to the northwest of the 1999 rupture of the Chelungpu fault. Siltstones of the Chinshui Shale have been thrust onto Quaternary gravel. Although this contact appears suspect in places, it seems to be continous with in-place siltstone down dip, and correlates to damaged buldings and a fault scarp on the road above.

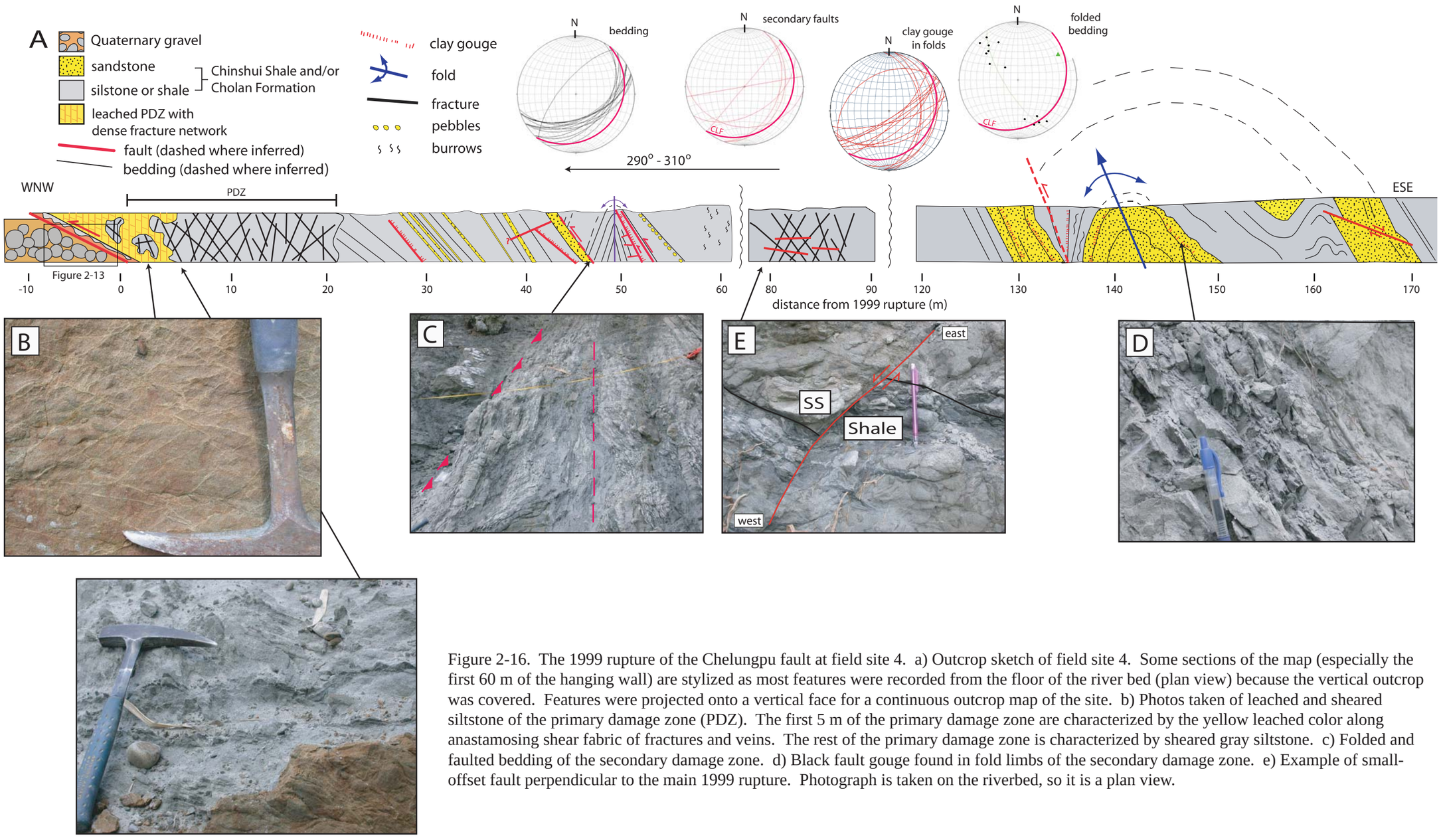

Figure 2-16. The 1999 rupture of the Chelungpu fault at field site 4. a) Outcrop sketch of field site 4. Some sections of the map (especially the first 60 m of the hanging wall) are stylized as most features were recorded from the floor of the river bed (plan view) because the vertical outcrop was covered. Features were projected onto a vertical face for a continuous outcrop map of the site. b) Photos taken of leached and sheared siltstone of the primary damage zone (PDZ). The first 5 m of the primary damage zone are characterized by the yellow leached color along anastamosing shear fabric of fractures and veins. The rest of the primary damage zone is characterized by sheared gray siltstone. c) Folded and faulted bedding of the secondary damage zone. d) Black fault gouge found in fold limbs of the secondary damage zone. e) Example of small-offset fault perpendicular to the main 1999 rupture. Photograph is taken on the riverbed, so it is a plan view.

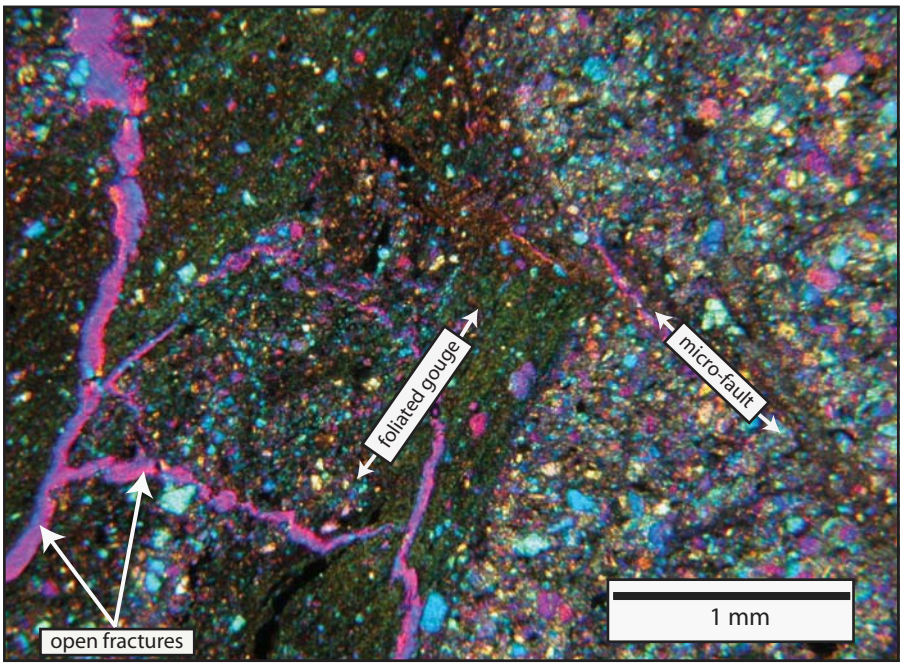

Figure 2-17. Photomicrograph of fault gouge sample from field site 4 (FG 0+30). Microstructures show evidence for multiple deformation events including multiple generations of foliated gouge at differing orientations that are either truncated by micro-faults or younger bands of fault gouge (polarized light with 530 nm plate).

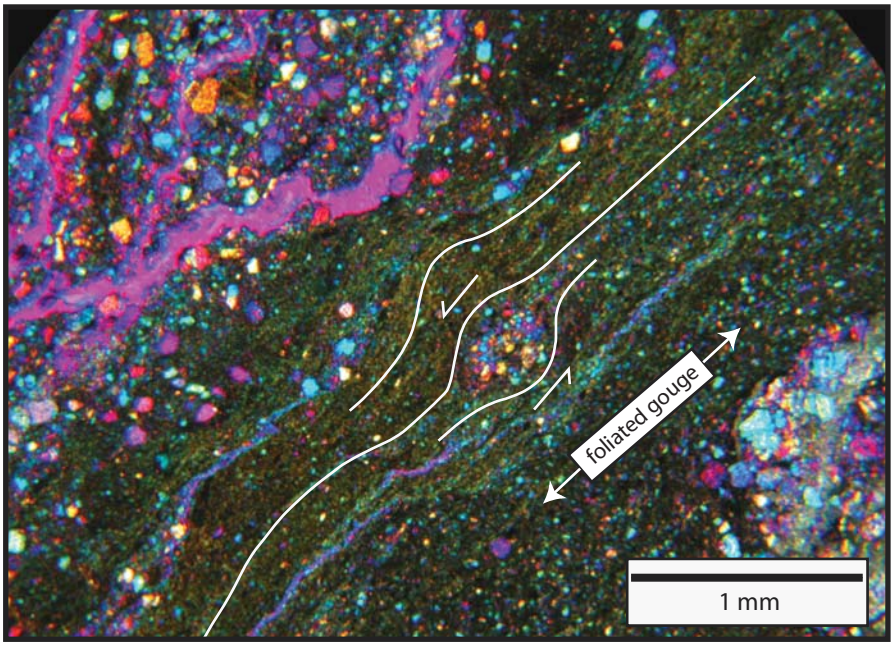

Figure 2-18. Photomicrograph of fault gouge from field site 5 (T5-2). Foliated fault gouge, comminuted quartz grains, and microfaults are common microstructures. A rotated porphyroclast of wall rock with associated shear tails is present at the center of the photo (polarized light with 530 nm plate).

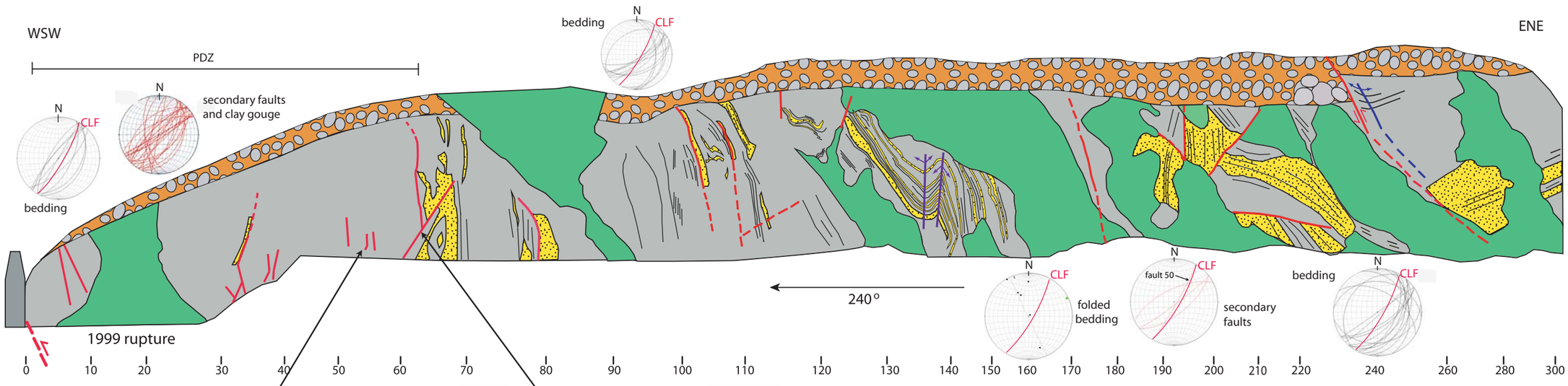

Figure 2-19. The 1999 rupture of the Chelungpu fault at field site 6. a) Outcrop sketch map of field site 6 illustrating the main features of the fault zone including a very wide primary damage zone (PDZ) and secondary damage zone and numerous secondary faults. The primary damage zone is characterized by sheared siltstone, disturbed bedding or no relict bedding, intense fracturing, and innumerable secondary faults with clay fault gouge and/or slicken lines. Transect distances are measured along the base of the outcrop. b) Photo of primary damage zone showing typical near-vertical faults and gouge bands. c) Example of primary damage zone rocks showing fragile clay films and gouge on a secondary slip surface

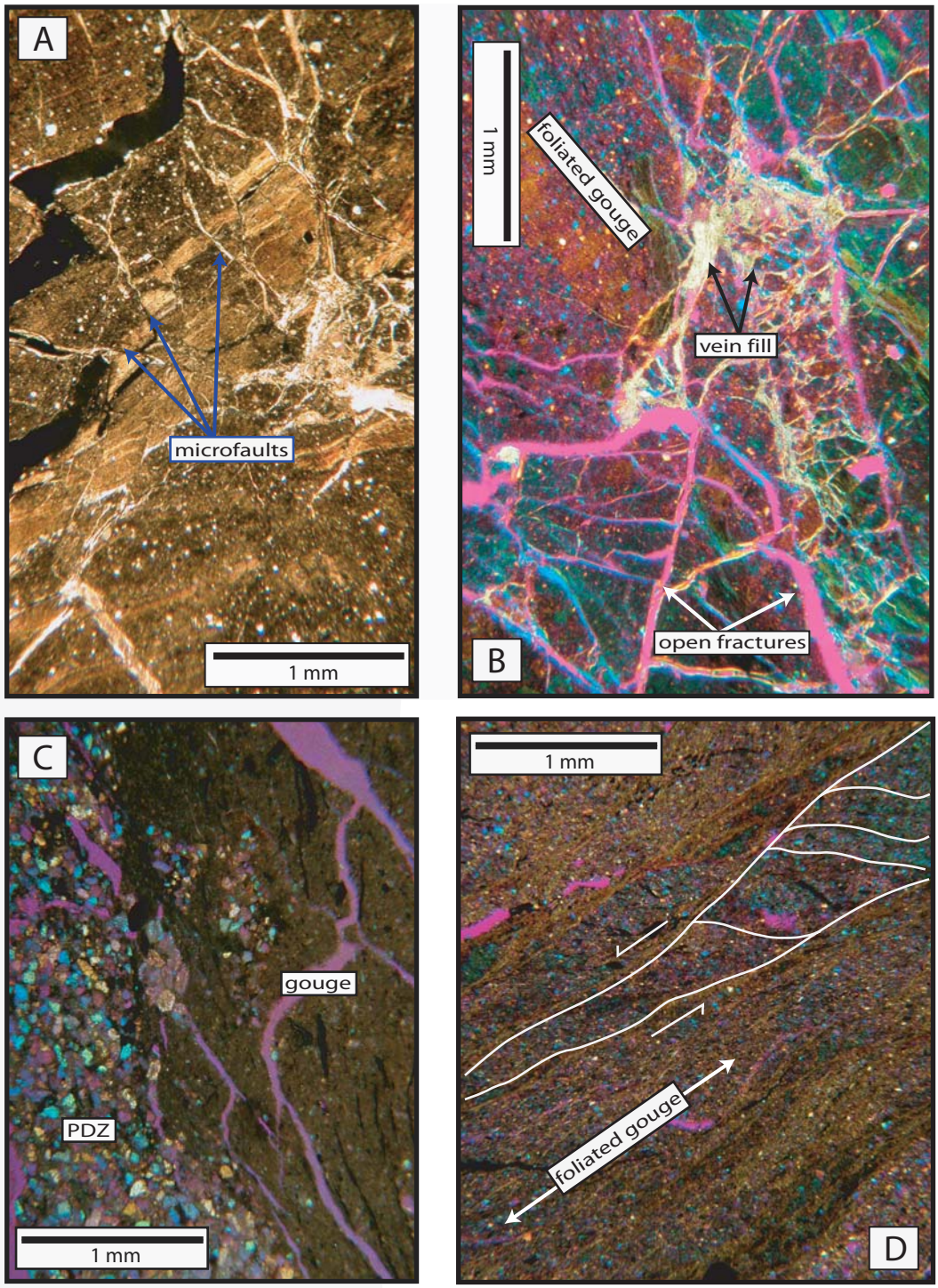

Figure 2-20. Photomicrographs of field site 6 samples clearly demonstrate multiple deformation events based on cross-cutting relationships. a) Foliated fault gouge (FG 0+64). b) Microfaults filled with calcite offset foliated clay gouge - evidence for multiple deformation events and syn-tectonic fluid flow (FG 0+64). c) More massive fault gouge in contact with primary damage zone (FG 0+10). d) Fault gouge with well-defined foliation (FG 0+40). a= plain light; b,c, d= polarized light with 530 nm plate.

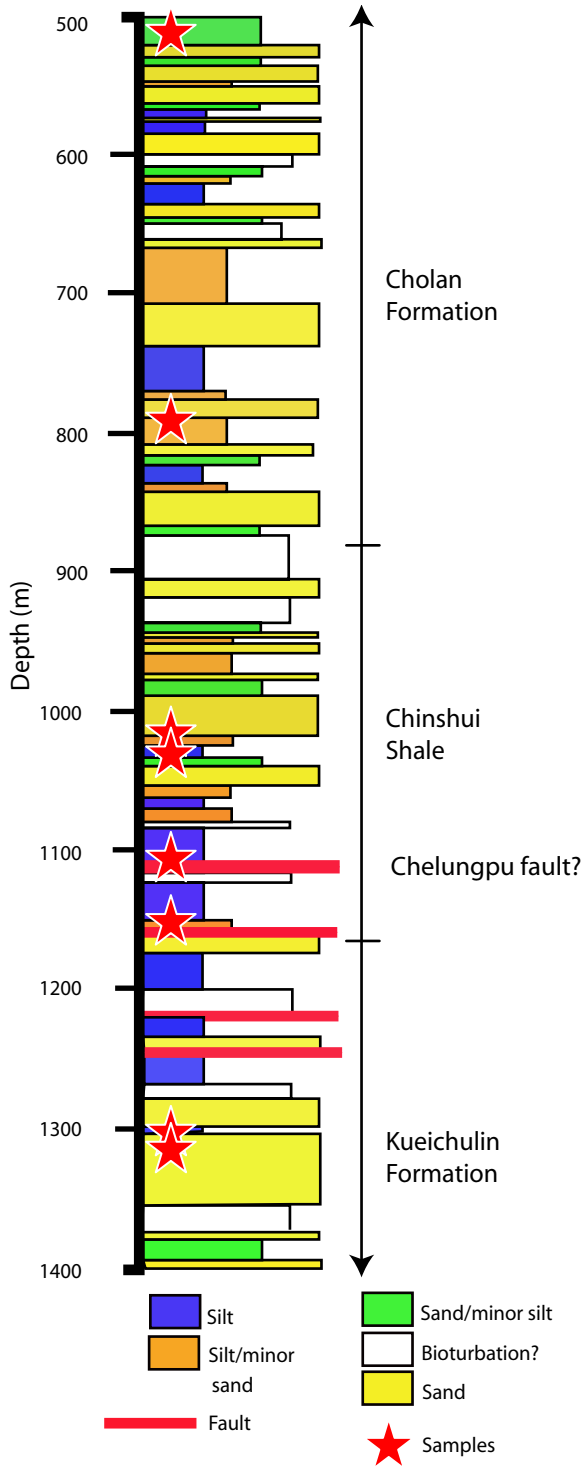

Figure 2-21. Generalized lithology of the Taiwan Chelungpu-fault Drilling Project and locations of faults. Formation boundaries are based on nannofossil assemblages (Wu et al., *submitted*). Locations of samples used in this study are indicated by red stars.

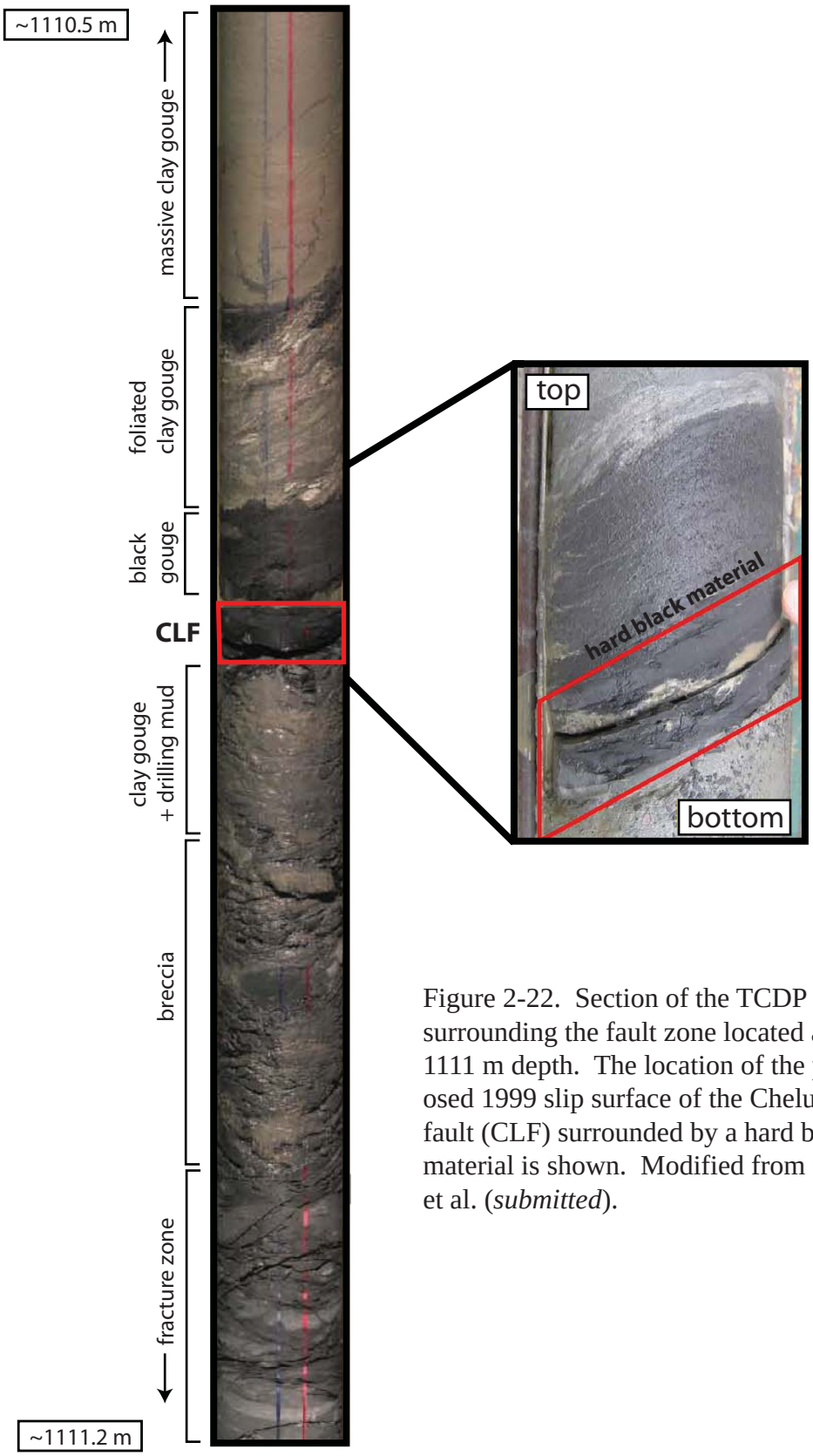

Figure 2-22. Section of the TCDP core surrounding the fault zone located at ~ 1111 m depth. The location of the proposed 1999 slip surface of the Chelungpu fault (CLF) surrounded by a hard black material is shown. Modified from Sone et al. (*submitted*).

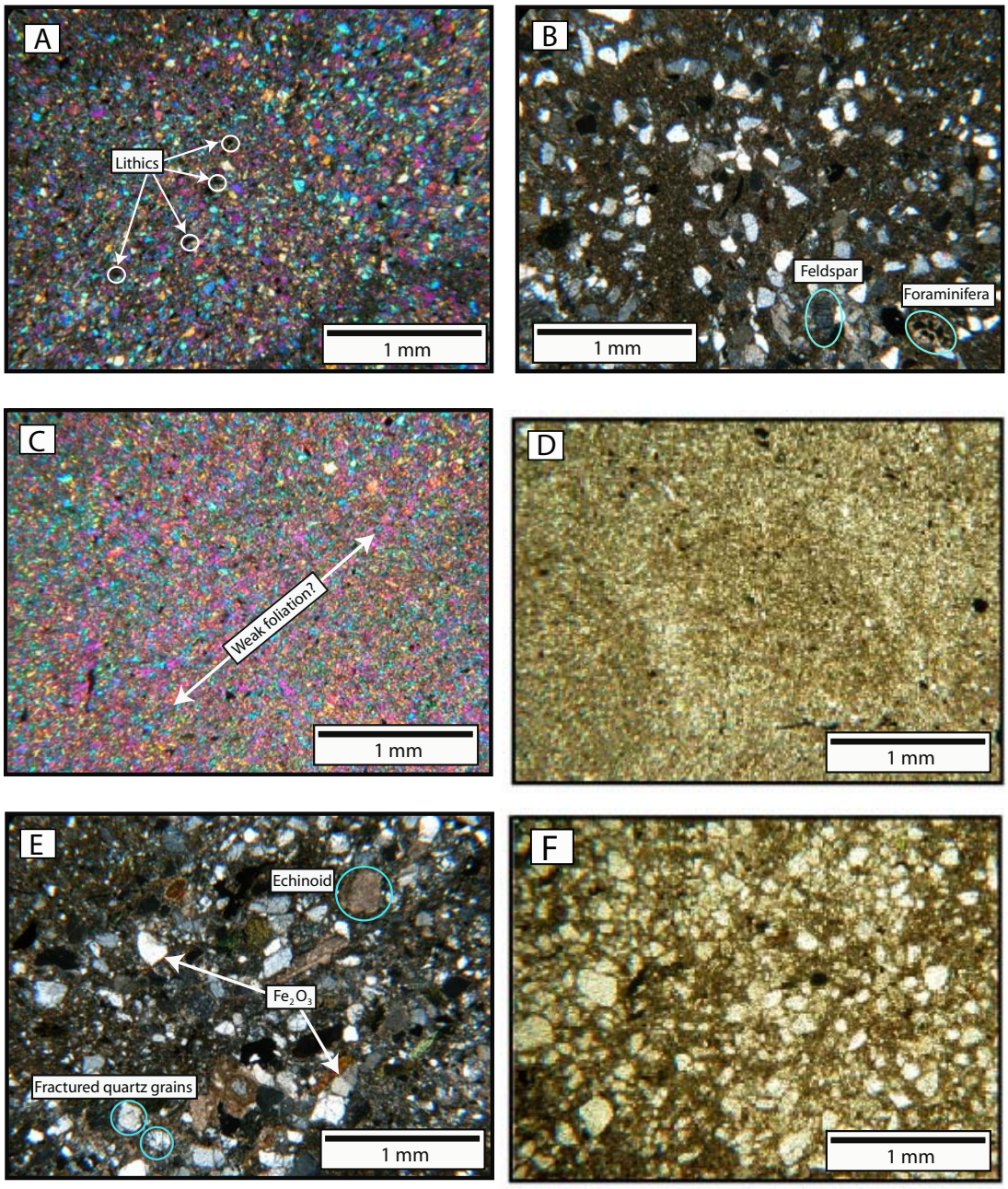

Figure 2-23. Photomicrographs of TCDP core samples. a) Siltstone sample of the Chinshui Shale (TCDP 1031, polarized light with 530 nm plate). b) Siltstone sample of the Kueichulin Formation (TCDP 1300, polarized light). c) Sample from the fault zone located at ~1111 m. Chinshui Shale is very fine-grained undeformed (polarized light with 530 nm insert). d) Sample from the fault zone at ~1111 m (plain light). e) Sample from the fault zone located at ~115 m depth within the Chinshui Shale (polarized light). f) Sample from the fault zone located at ~1152 m depth within the Chinshui Shale (plain light).

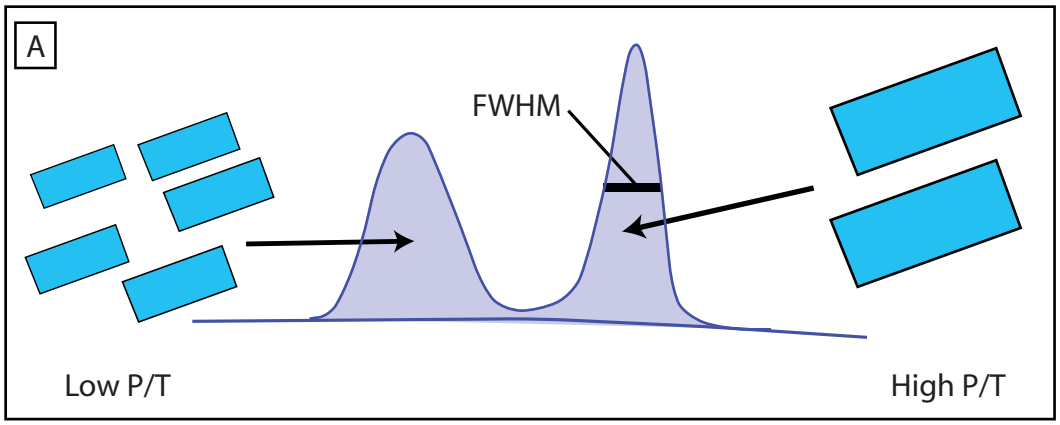

Figure 2-24. Crystallinity indices. a) Crystallinity describes the size of the crystallites that make up a clay. Small crystallites are manifest on an XRD pattern by broad peaks and indicate formation at low P/T (weathering) conditions. Large crystallites are indicated by narrow peaks on an XRD pattern, and are formed under higher P/T (recrystallization) conditions (Solum, 2005; Moore and Reynolds, 1997). The width of a clay peak is measured at half the hight of the peak (FWHM). b) The northern crystallinity index shows no major trends. c) The southern crystallinity index illustrates that some mineralogical signature due to faulting remains in the fault core and primary damage zone rocks. This is based on the larger crystallites (smaller peak widths) of fault core and primary damage zone smectite (and possibly chlorite) in relation to secondary damage zone and host smectite.

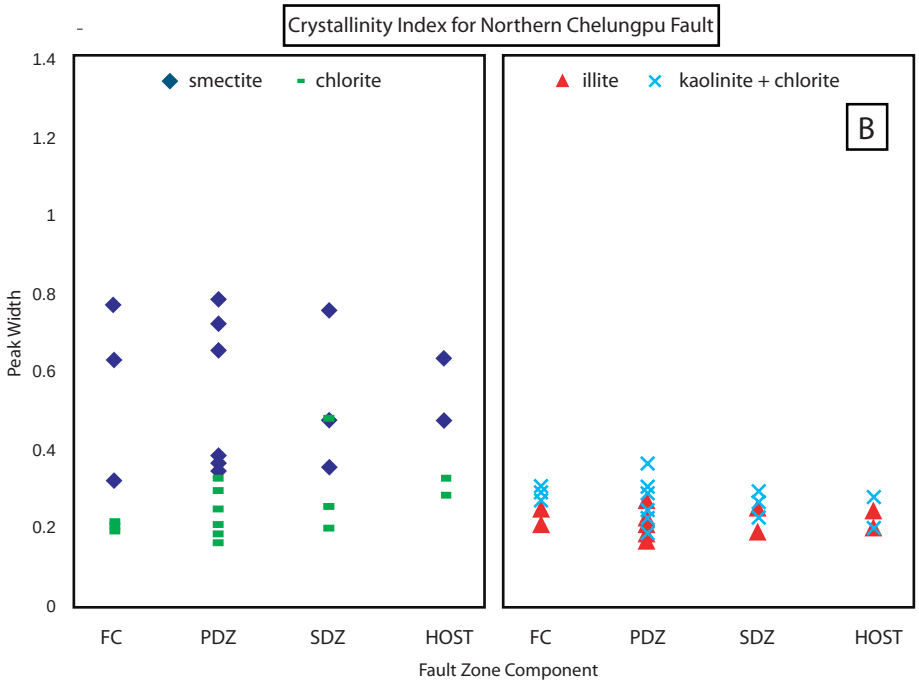
Crystallinity Index for Northern Chelungpu Fault
smectite
chlorite
illite
kaolinite + chlorite
B
Peak Width
1.4
1.2
1
0.8
0.6
0.4
0.2
0
FC
PDZ
SDZ
HOST
Fault Zone Component

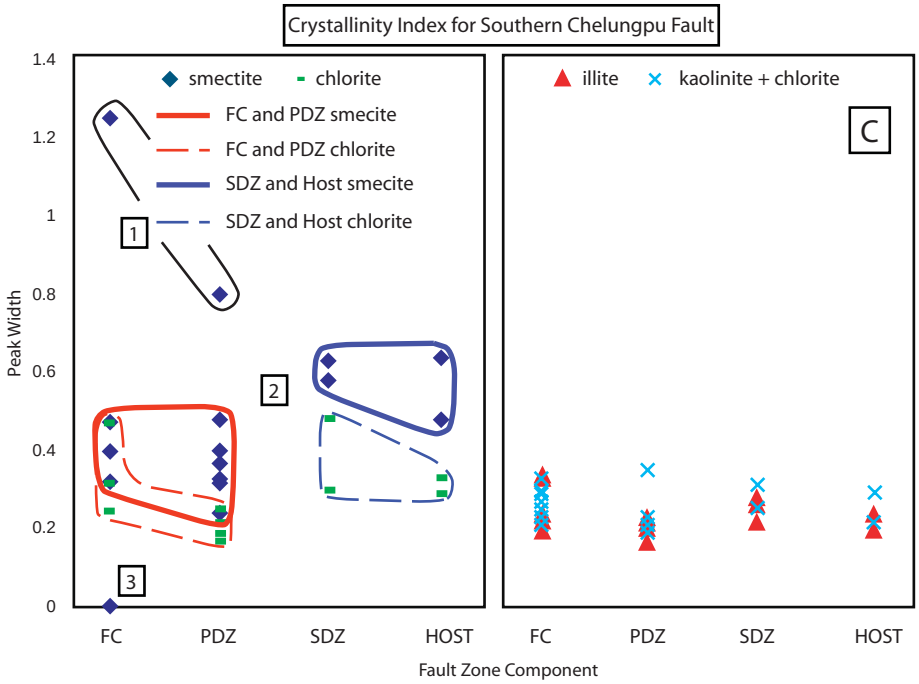
Crystallinity Index for Southern Chelungpu Fault
smectite
chlorite
illite
kaolinite + chlorite
FC and PDZ smecite
FC and PDZ chlorite
SDZ and Host smecite
SDZ and Host chlorite
C
1
2
3
Peak Width
1.4
1.2
1
0.8
0.6
0.4
0.2
0
FC
PDZ
SDZ
HOST
Fault Zone Component

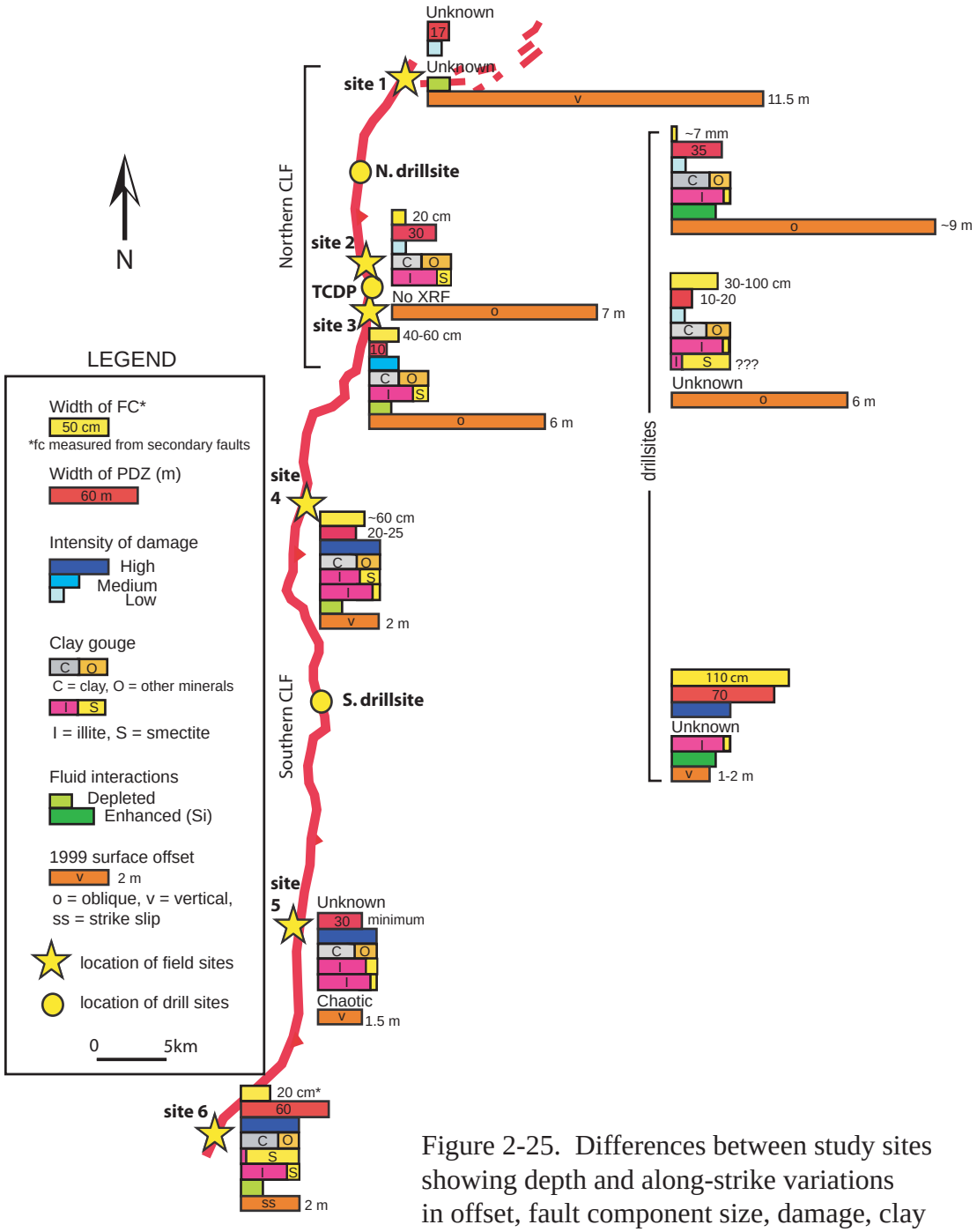

Figure 2-25. Differences between study sites showing depth and along-strike variations in offset, fault component size, damage, clay mineralogy, and geochemical signature relative to host rock. The amounts of total clays are qualitative estimates based on optical microscopy of gouge, semi-quantitative XRD, and gravity settling. Ratios of illite to smectite are based on NEWMOD™-generated patterns (Reynolds and Reynolds, 1996) and peak intensities. The intensity of damage is a relative measurement based on the type and density of damage recorded in transect of the primary damage zone and secondary damage zone.

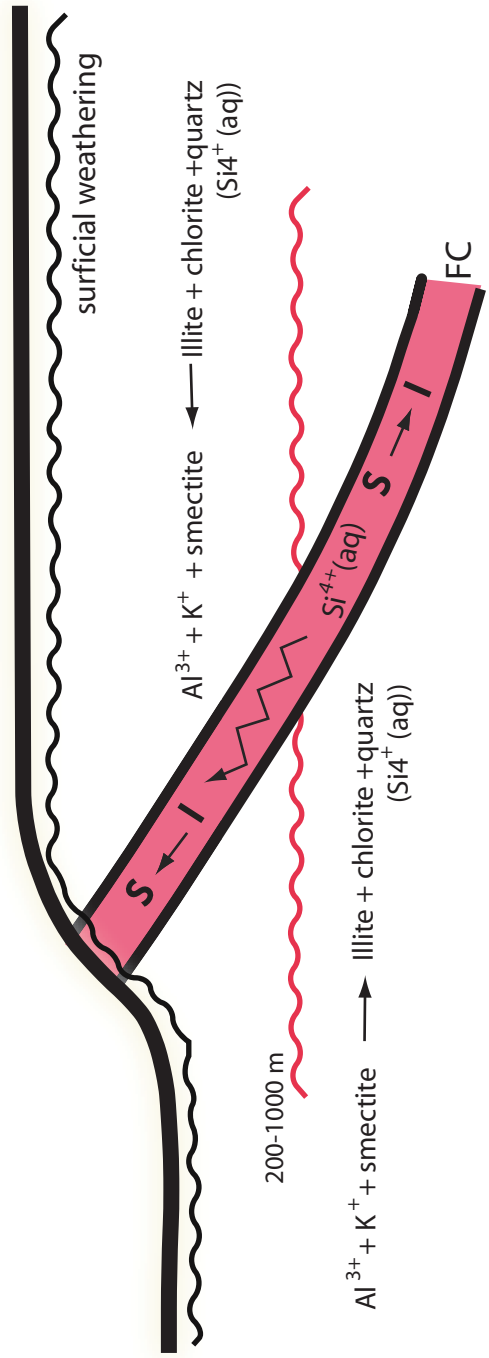

Figure 2-26. Model for illitization and retrograde illite - smectite reaction in the fault core. See text for discussion.

CHAPTER 3

PHYSICAL AND MECHANICAL PROPERTIES OF THE MOZUMI FAULT: A FINE-GRAINED, HETEROGENEOUS FAULT ZONE[2]

ABSTRACT

The Mozumi fault is an active, creeping, right-lateral strike-slip fault with 250-500 m of slip in north-central Honshu, Japan that is exposed in the Active Fault Survey Tunnel at a depth of 300-400 m. We have characterized the physical and mechanical properties of fault rock samples from the Mozumi fault using core samples and geophysical logs. Microstructures in the fault rocks indicate syn-tectonic fluid pressurization and flow, evolving fluid, and shear and plastic deformation concentrated in sericite-rich matrix. Clay mineralogy varies throughout the fault zone, with kaolinite and illite dominant in host rock and fault breccia, and smectite, illite, and kaolinite dominant in clay-rich fault breccia. Whole-rock geochemistry shows that fault rocks are mostly depleted in oxides relative to the host rock, with clay-rich fault breccia being the most depleted; up to ~90%. Resistivity values are depressed by 0-50 ohm-m across the main fault zone. The values of v_p and v_s are decreased by an average of ~0.30 km/s and ~0.40 km/s across the main fault relative to the surrounding wall rock, and an average of ~0.70 km/s and ~1.0 km/s relative to host rock, respectively. Calculated values of Young's modulus and Poisson's ratio of fault rocks range from 16.2 to 44.9 GPa and 0.263 to 0.393, respectively. The protolith has a calculated Young's modulus of 55.4 GPa and a Poisson's ration of 0.242. The lowest calculated values of Young's modulus

[2]Co-authored manuscript by A.J. Isaacs, J.P. Evans, and P.T. Kolesar

and highest calculated values of Poisson's ratio correspond to fault breccia with increased porosity, high fluid content, and low resistivity values. These variations in physical and mechanical properties throughout the fault zone demonstrate that the complex distribution of elastic properties corresponds to the permeability structure inferred to be a combined fault-parallel fluid conduit and fault-perpendicular fluid barrier. Fluid-rich pockets of fault rock also migrate through the fault zone with time, and may facilitate creep on the Mozumi fault.

3-1. INTRODUCTION

The Mozumi fault (MF) is a northeast striking right-lateral strike-slip fault system in north-central Japan with 125-500 m of slip (Figure 3-1; Ando, 1998). A tunnel excavated by the Earthquake Frontier Research for Terrestrial Subsurface in Earthquake Frontier Project at ~300-400 m below the ground surface intersects the Mozumi fault and allows for direct access and observation of this active, clay-rich fault zone. The Mozumi fault is an example of a complex, heterogeneous fault zone in sedimentary rocks (Mamada et al., 2002; Forster et al., 2003; Mizuno et al., 2004). We characterize fault rocks from the Mozumi fault zone and combine this characterization with interpretations of mechanical properties as calculated from borehole geophysical logs to illustrate the fault zone complexity. This work provides data on the *in-situ* chemical, physical, and mechanical properties of the internal portion of an active fault in clastic sedimentary rocks. These data are important as few published studies provide direct observations of fault rocks in correlation with borehole geophysics from the same area. Our results are compared to a broader scale study of the properties of the Mozumi fault by Mizuno et al.

(2004) including damage zone width, average S-wave velocity, and the Quality factor (*Q*), or wave attenuation.

Regional Setting

The Japan islands include from north to south Hokkaido, Honshu, Shikoku, and Kyushu (Figure 3-1). Japan forms an island arc located at the junction of Eurasia, and the Pacific and Philippine Sea plates. Several microplates in Japan mark the eastern edge of the Eurasia Plate (Figure 3-1; Taira, 2001). The Philippine Sea plate is obliquely subducting under southwest Honshu and Shikoku at ~4-5 cm/yr relative to stable Eurasia (Taira, 2001; Yamaji, 2003) with a N 51^{o} W vector towards the Nankai trough (Gutscher and Lallemand, 1999), and subducting under Kyushu at the Ryukyu trench (Yamaji, 2003). The Pacific plate is subducting west under northeast Honshu and Hokkaido at the Japan trench to the north at 9-11 cm/yr relative to stable Eurasia, and subducting under the Philippine Sea plate to the south at the Izu-Bonin trench (Yamaji, 1994; Taira, 2001). The current plate configuration involves 3 additional plates: the Okhotsk, Amur, and Eurasia plates, as well as a microplate or series of microplates at central Honshu (Figure 3-1; Taira, 2001). The Amur plate is converging to the east at ~1 cm/yr relative to stable Eurasia (Taira, 2001).

Horizontal velocity vectors for Japan from a continuous GPS array (Figure 3-2) show that Japan is under east-west compression with respect to stable Eurasia, with the exception of southwest Hokkaido and southern Kyushu (Sagiya et al., 2000). Western Honshu has an eastward velocity relative to stable Eurasia, whereas north and eastern Honshu and Hokkaido have strong westward velocities. A tectonic boundary across north-central Honshu is identified by a zone of high strain rates across which the GPS

velocity vectors change directions, and correlates to major historic large-magnitude earthquakes along active strike-slip faults, as well as a line of active Adakitic volcanoes (Figure 3-1; Gutscher and Lallemand, 1999; Sagiya et al., 2000; Gutscher, 2001). The zone is ~10-30 km wide and is interpreted as a zone of strain partitioning due to the oblique convergence of a low-angle subducting slab segment of the Philippine Sea plate (Gutshcer and Lallemand, 1999; Sagiya et al., 2000; Taira, 2001; Yamaji, 2003). The area between the tectonic boundary and the Median Tectonic Line to the south is characterized by a set of conjugate northwest-striking left-lateral faults and more continuous northeast-striking right-lateral faults (Figure 3-1; Matsuda and Kinusaga, 1991). The focal mechanisms and aftershock distributions of large magnitude earthquakes oriented along the tectonic boundary show nearly pure right lateral strike-slip motion (Gutscher and Lallemand, 1999).

The Chuba district in north-central Honshu, Japan, has a high density of active faults that have produced at large magnitude (M 7 and M 8) earthquakes (Figure 3-1; Matsuda and Kinusaga, 1999; Gutscher and Lallemand, 1999; Sayiya et al., 2000; Gutscher, 2001). At least 7 large magnitude earthquakes have occurred in and around the Chuba district historically (Sayiga et al., 2000). A major fault system of the Chuba district is the Atotsugawa Fault System, which includes the Atotsugawa, Mozumi, and Ushikubi faults (Figure 3-3). The Atotsugawa fault is a northeast striking, ~60 km long oblique right-lateral strike-slip fault that may have begun to move in the latest Tertiary or early Quaternary based on progressive displacements of river terraces (Figure 3-3; Matsuda, 1966). It has 3 km ($\pm$ 0.5 km) of horizontal displacement and 0.1-0.5 km of throw with the northwest side up (Matsuda, 1966).

The Mozumi fault is located ~4 km north of the Atotsugawa fault. The Mozumi fault is a 23 km long, right-lateral strike-slip fault with 125-500 m of slip. The Mozumi fault branches northwest from the southeastern end of the Atotsugawa fault (Ando, 1998, Takeuchi et al., 2003). The overall strike of the Mozumi fault is ~N 50-60^{o} E and has a near-vertical dip (Hirahara et al., 2003; Takeuchi et al., 2003). However, in the study area, the fault strikes ~N 40-45^{o} E. This is because the study area is located near the northwest termination of the Mozumi fault, where the fault appears to bend (Figure 3-3; Ito, 1999; Mizuno et al., 2004).

The Ushikubi fault is a right-lateral strike-slip fault located ~10 km north of the Atotsugawa fault. The Ushikubi fault is ~60 km long and strikes northeast. The GPS measurements surrounding the Atotsugawa Fault System are interpreted as two blocks obliquely colliding southeast-northwest at the zone bounded by the Atotsugawa-Ushikubi faults at a rate of 20 mm/yr (Figure 3-2; Hirahara et al., 2003).

Takeuchi and Onigrad (2003) determined a recurrence interval of 2,471 $\pm$ 103 years for the northeastern portion of the Atotsugawa fault, whereas the recurrence interval for the Mozumi fault is much longer: 13,500 $\pm$ 6,300 years. The most recent large magnitude event on the Atotsugawa fault was a M 6.9 earthquake in 1858. This earthquake seems to have initiated on the Atotsugawa fault system and ruptured along both the Atotsugawa and Mozumi faults (Takeuchi and Onigrad, 2003). The 1858 M 6.9 event implies that the Atotsugawa and Mozumi faults communicate at times. The two faults are probably linked at their southeastern ends (Takeuchi and Onigrad, 2003) and therefore are potentially connected at depth.

The central portion of the Atotsugawa Fault System (15-20 km), including the Mozumi fault, is believed to be creeping (Ito, 1999; Tanaka and Ito, 1999; Hirahara et al., 2003; Ito, 2003), whereas the northeastern and southwestern portions of the fault system appear to be locked, as indicated by the distribution of intense microseismicity along the Atotsugawa fault (Figure 3-4; Ito, 1999; 2003). Creep on the fault system is supported by geodetic measurements and strainmeters installed in boreholes (Ito, 1999; 2003) and low levels of seismicity along the northwestern and central sections of the Mozumi fault and the central section of the Atotsugawa fault (Mikumo et al., 1988; Wada et al., 1990). Modeling by Hirahara et al. (2003) indicates that the creep rate in the central segment is 1.5 mm/yr, and that creep extends from the surface to 7 km depth.

Geology and the Active Fault Survey Tunnel

The Active Fault Survey Tunnel (AFST) project allows for direct observation of the Mozumi fault at a depth of 300-400 m (Figure 3-5; Shingu et al., 1997). The Active Fault Survey Tunnel is located in the Gifu prefecture, Japan, and trends northwest for 480 m. Within the tunnel, the Mozumi fault cuts sandstone, shale, and siltstone of the middle Jurassic to lower Cretaceous age Tetori Group; however, at other locations the fault juxtaposes Paleozoic-Mesozoic granite with the Tetori Group (Figure 3-3; Matsuda, 1966). The Tetori Group overlies Paleozoic Hida metamorphic rocks and other circum-Hida rocks, including Paleozoic-Mesozoic granite in the area of the Atotsugawa Fault System. The group consists of alternating conglomerate, fine to very coarse-grained sandstone, shale, siltstone, and some coal seams (Fujita, 2002).

The Active Fault Survey Tunnel was mapped by geologists of the Mitsui Mining and Smelting Co. as part of the development of the tunnel for scientific research. The Mozumi fault zone within the Active Fault Survey Tunnel has been associated with two fault zones termed "crush zones" (Figure 3-5; Forster et al., 2003). Crush zone A is ~20 m wide and is interpreted as the main trace of the Mozumi fault, and crush zone B is ~65 m wide and is interpreted as a subsidiary fault to the Mozumi fault (Forster et al., 2003). Hereafter, crush zone A will be referred to as the Mozumi fault zone. The fault zones are characterized by clay gouge, fault breccia, low rock quality, and reduced seismic velocities.

Four boreholes were drilled off of the main tunnel (Figure 3-5). Borehole 1, a horizontal borehole, intersects the largest subsidiary fault (crush zone B). Boreholes A and 2 intersect the main trace of the Mozumi fault, and borehole A plunges 60^{o} north-northwest from the horizontal Active Fault Survey Tunnel. Borehole 3 samples lithology outside of the fault zones. Nine un-oriented core samples of siltstone were collected from borehole A of the Active Fault Survey Tunnel by J.P. Evans in 1998 (samples MZA-1 through MZA-10; Table 3-1). A sample of undeformed siltstone (MZ-1) was collected 50.1 m from the southwest end of borehole 1. This sample is similar to the clasts of siltstone breccia in the fault zone, has similar bulk mineralogy, and is compared to samples from the Mozumi fault zone.

3-2. CHARACTERIZATION OF MOZUMI FAULT ROCKS

Fractures and Rock Quality

Map-scale and mesoscopic structural data of borehole A were provided by Power Reactor and Nuclear Fuel Development Corporation (now Japan Atomic Energy Agency) from an internal report (Shinghu et al., 1997). Orientations of fractures are recorded for borehole A (Figure 3-6). Fractures were measured for wall rock and Mozumi fault rock; however, few fractures were measured within the Mozumi fault zone because the rocks are brecciated, resulting in a small number of discrete fractures. The fractures recorded along borehole A can be grouped into 3 main sets. A concentrated horizontal fracture set with a mean orientation of 155^{o}, 20^{o} is present perpendicular to the Mozumi fault at an angle of 82^{o} (fracture set 1). Two nearly-vertical sets are present oblique to the Mozumi fault: one with a mean orientation of 001^{o}, 71^{o} that makes a 42^{o} angle with Mozumi fault (fracture set 2), and the other with a mean orientation of 063^{o}, 74^{o} that makes a 28^{o} angle with the Mozumi fault (fracture set 3).

Rock Quality Designation (RQD) is a rock mass classification scheme that uses the frequency of jointing within rock as a measure of its quality. The Rock Quality Designation is defined as the percentage of core pieces in a given length of core that are twice the core diameter (Deere and Deere, 1987). The rock quality indices of rock masses surrounding the Mozumi fault range from 0-60%. A value of <25% indicates very poor rock quality, 25-50% indicates poor rock quality, 50-75% indicates fair rock quality, 75-90% indicates good rock quality, and 90-100% indicates excellent rock quality. Rock quality is reported as 0% across the Mozumi fault.

Core Samples and Microstructures

Sample MZ-1 is undeformed siltstone collected from borehole 1 (Figure 3-7a). A thin section of MZ-1 shows that the rock is overall very fine-grained, with some larger isolated quartz grains in the finer matrix (Figure 3-8a, Figure 3-8b). One very narrow chlorite vein is observed. The fine-grained portions of the rock are not foliated, and no deformation can be seen surrounding larger quartz grains.

Sample MZA-10 is siltstone cut by several veins and a set of narrow faults containing clay films (Figure 3-7b). The siltstone bordering the veins and narrow faults is relatively undeformed. Optical microscopy reveals some calcite-rich matrix, as well as muscovite, serecite and phyllosilicates in the matrix material. Isolated quartz grains are scattered throughout the fine-grained matrix, and, although the quartz grains show some undulatory extinction, they are relatively undeformed in the brittle sense. Veins consist of fine-grained quartz at fracture walls that progressively coarsens inward and surrounds a central and final phase of calcite vein fill (Figure 3-8c).

Sample MZA-9 marks the beginning of the Mozumi fault zone. MZA-9 is highly altered siltstone cut by a fault of unknown size (Figure 3-9). In hand sample, the fault makes a clear separation of heavily altered, indurated siltstone (MZA-9a) and highly comminuted, clay-rich, weak fault rock (MZA-9b). The fault interface is smeared with tacky, green, chlorite-rich clay. Optical microscopy also shows a clear change across the fault. Twinned calcite (Figure 3-8d) indicates plastic deformation and appears to have been injected into the rock because it is found in irregularly-shaped, discontinuous zones that have sharp boundaries with surrounding quartz grains. Towards the fault, quartz grain size decreases and additional mineral phases are present. The fault rock is

distinctly zoned. Calcite is present nearest the fault, bordered by a zone of quartz and chlorite, then less deformed quartz, calcite, and some feldspar. There are also radial growths of epidote (Figure 3-8e) and zoned quartz with styolite-like sutures indicating pressure solution (Figure 3-8f).

Sample MZA-8 was collected from siltstone fault breccia of the Mozumi fault (Figure 3-7c). This sample contains evidence for shearing and reduced grain size; however, it lacks the strong foliation of matrix present in other samples. Calcite veins are common, as are fractures partially filled with clasts ripped from the sidewalls, indicating at least some movement. The most distinct feature of MZA-8 is the anastomosing brown clay (Figure 3-8g). The clay is not foliated or continuous. It is randomly oriented in stringers, often curving, and dies out into the surrounding siltstone. It is possible that this clay has been injected into the rock from fault gouge by fault-related pressurization. In addition, the siltstone and clay bands are cut by chlorite veins that represent an additional fluid phase not recorded in quart and calcite veins.

Samples MZA-7 through MZA-2 are located within the Mozumi fault and have many similarities (Figure 3-7d-e; Figure 3-8h-k). Fine-grained, sericite-rich matrix materials are foliated (Figure 3-8h, Figure 3-8i). Quartz grains “floating” within the matrix are, on the whole, relatively undeformed, but can be brecciated, shattered, cut by veins and microfractures, or appear to have undergone pressure solution. Quartz grains are also sometimes rimmed by calcite or other minerals, and have wavy to patchy extinction. Feldspar grains commonly show evidence for dissolution including holes and ragged edges replaced by calcite. Large, twinned calcite crystals like those in sample MZA-9 and pyrite are also present.

Narrow bands of opaque brown minerals are common in samples MZA-7 through MZA-2, and are probably formed by pressure solution (Mitra, 1998) and shear (Figure 3-8i). Fluid pressurization along these shear bands is indicated by injections of clay into the surrounding wall rock that start at the shear zone and die out into the siltstone. Some of these bands have entrained portions of the matrix, indicating an origon of shear. Larger veins contain at least two mineral phases growing away from the fracture walls.

Sub-rounded and rotated porphyroclasts are present within the matrix material. Examples of porphryoclasts with release fractures (Chester and Evans, 1998) can be found in sample MZA-6 (Figure 3-8j). Fault breccia and porphyroclasts sometimes contain pieces of quartz and calcite veins, or can be identified by foliation directions that differ from surrounding foliation. Microfaults that offset clay bands, cut veins, and juxtapose foliations of different orientations are also common. Samples MZA-2, MZA-4, MZA-5, and MZA-7 all have intensely foliated matrix, whereas MZA-6 has only moderately foliated matrix, with some crenulation foliation. MZA-5 contains the largest and most abundant pyrite crystals (Figure 3-8k).

Sample MZA-1 was also collected from the Mozumi fault zone (Figure 3-7f), but has a strong crenulation foliation not seen in other samples. Crenulation foliation can be seen wrapping around relatively undeformed quartz grains (Figure 3-8l). The foliation is often truncated by microfaults. Open fractures and hematite-filled fractures are common. Fractures partially filled with randomly-oriented debris shredded from side walls are also present (Figure 3-8m). These fractures suggest that at least some movement has taken place along their interface. Fractures also commonly tip out into shear zones (Figure 3-

8n). Overall, samples from the Mozumi fault display a strong foliation parallel to the Mozumi fault, and a weaker foliation perpendicular to the Mozumi fault.

Composition

Bulk and Clay Mineralogy

Bulk XRD of powdered samples identifies quartz, feldspar, calcite, muscovite/illite, montmorillonite (smectite), kaolinite, and chlorite and/or vermicullite. X-ray diffraction results indicate that all samples contain illite/muscovite and kaolinite clays. Samples from the fault zone contain smectite mixed with combinations of illite, kaolinite, and possibly chlorite or vermicullite (Table 3-2). In the following discussion, the most abundant clay mineral in each sample is listed first. Sample MZA-1 is mostly illite and smectite as well as some kaolinite. Sample MZA-2 is abundant in smectite and illite/muscovite, and R0 I-S, kaolinite, and a small amount of chlorite. Sample MZA-6 contains illite/muscovite, smectite, and lesser kaolinite. Sample MZA-9a contains illite/muscovite, kaolinite-montmorillonite, and vermiculite or chlorite. Sample MZA-9b contains illite/muscovite, kaolinite, and chlorite. Sample MZA-10 contains illite/muscovite, kaolinite, and chlorite or vermiculite. Samples MZA-7 and MZA-8 contain only illite/muscovite and kaolinite. The protolith sample MZ-1 contains illite/muscovite and kaolinite, and possibly a small amount of R0 I-S. The relative amount of muscovite and illite in each sample is unknown, and these minerals have been considered as one mineral phase.

Chemical Composition

Figure 3-10 shows the results of ICP analysis and percent change calculation after Goddard and Evans (1995). Samples MZA-1, MZA-5, MZA-9a, and MZA-9b are depleted in oxides relative to the protolith sample MZ-1, and generally with respect to other fault zone samples. Sample MZA-1 is 60-90% depleted in all measured oxides with respect to the protolith sample MZ-1. The CaO is enriched for all other fault zone samples, with an increase of nearly 400% in sample MZA-5. The values of SiO_2, LOI, Fe_2O_3, and CaO were determined to be the most significant variables by Principal Component Analysis, and all are most significantly changed from the protolith in samples MZA-1, MZA-5, MZA-9a, and MZA-9b, with the exception of Fe_2O_3 in sample MZA-5. Samples MZA-2, MZA-6, MZA-7, and MZA-8 are all generally depleted with respect to the host rock. These data indicate fluid flow that facilitates the movement of oxides through the fault zone resulting in chemical changes in the fault rocks relative to the protolith.

3-3. PETROPHYSICS

Six borehole geophysical logs were recorded for borehole A (Shingu et al., 1997). These logs have been projected to the horizontal (Figure 3-11) and were correlated to samples collected from borehole A for petrophysical analysis. These logs measure different physical responses and are useful in determining the bulk (1-10 m) properties of Mozumi fault rocks.

Geophysical Well Logs

Spontaneous Potential (SP) Log

The Spontaneous Potential (SP) log records direct current (mV) differences between the potential of a moveable electrode in the bore hole and a fixed electrode at the surface (Doll, 1948). The SP log is primarily used for determining zones of less permeable siltstone and more permeable sandstone, but basically detects the permeability along the borehole (Asquith and Gibson, 1982).

The SP values for siltstone along the borehole typically follow a straight line called the shale baseline. Where there are deflections recorded either to the right or to the left of the shale baseline, permeable zones are present. The magnitude of the SP deflection does not record the amount of permeability, but instead the difference in resistivity of formation water (Rw) and mud filtrate (Rmf) (Dresser Atlas, 1982).

Sonic Log

The sonic log (or acoustilog) measures the time required for a compressional sound wave to traverse a 1 ft length of rock, and is dependent on lithology and porosity. The addition of porosity decreases the sonic velocity, thus increasing the travel time. The sonic log responds to density, with denser material exhibiting a faster return time (Asquith and Gibson, 1982).

Natural Gamma Ray Log

The gamma ray log measures natural radioactivity in rock. In sedimentary rocks, the gamma ray log tends to reflect shale (clay) content as the radioactive materials concentrate in shale and clays (Asquith and Gibson, 1982; Dresser Atlas, 1982).

Therefore, high gamma ray values typically indicate shale. The primary application of the gamma ray log is identification of lithology (Dresser Atlas, 1982). For the qualitative evaluation of shale content, the assumption is that no other radioactive-containing materials are present besides shale (Dresser Atlas, 1982).

Resistivity Log

Resistivity is the measure of a material's ability to resist the flow of electric current. Resistivity logs measure the voltage of a current passed through a material. Because most minerals that make up matrix and grains are non-conductive, the electric current is transmitted almost entirely by pore water (Asquith and Gibson, 1982). Low resistivity to flow of the electric current then indicates porosity and pore water. Long and short-range resistivity is recorded. A short normal resistivity curve is used for shallow depth investigation, or, in other words, to record the resistivity of the zone invaded by drilling lubricant (Dresser Atlas, 1982). The long resistivity curve theoretically records the properties of the uninvaded formation.

Seismic Velocities

Seismic body waves include p-waves and s-waves. P-waves, or primary or compressional waves, involve compression and rarefaction of materials through which they pass (Kramer, 1996). S-waves, or secondary or shear waves, cause shearing deformations in the materials that they pass through (Kramer, 1996). The speed of seismic body waves varies with the stiffness of the material that they are traveling through. Fluids have no shearing stiffness, and therefore cannot sustain s-waves. The seismic velocity logs record the speed at which s-waves and p-waves travel through rocks

cut by the borehole. The ratio of the P-wave velocity to the S-wave velocity (v_p/v_s) is an indicator of the presence of fluids, with high values of v_p/v_s indicating high fluid content.

Correlation to Borehole A Samples

Figure 3-11 shows the wireline log curves and sample positions along borehole A. Lithology was determined from core log descriptions, drilled core samples, and well logs. Wireline logs are not simply dependant on lithology; therefore the first-order approximation of lithology by each log leads to conflicting results, and does not work for formations significantly altered by faulting. It is possible that the shale and siltstone sequences along the Mozumi fault zone are more intensely fractured than sandstone sequences because they are weaker and more thinly bedded (Forster et al., 2003). This would increase the porosity and density of discontinuities, affecting the resistivity, and acoustic and seismic wave reactions to shale and siltstone. Content of radioactive elements is probably not altered by faulting, so the gamma ray log would not be significantly compromised, assuming that major chemical reactions are not taking place. With this in mind, the v_s, v_p, sonic, SP, and resistivity logs are used to evaluate fault zone properties such as increased fractures and porosity, whereas the gamma ray log supplements samples and core logs for determining lithology.

The resistivity log records nearly the same response for long and short-range curves. Low resistivity values (0-50 ohm-m) indicating increased pore fluids are recorded across the Mozumi fault. The Mozumi fault zone is dominated by fault breccia with increased porosity relative to the protolith. A deflection from the SP shale baseline across the Mozumi fault indicates a zone of permeability. The gamma-ray log indicates areas of radioactivity, or shale content, in the Mozumi fault, as do spot core logs and

physical core available for this study. The sonic log shows slower velocities for shale or siltstone within the Mozumi fault zone than shale or siltstone outside of the fault zone, indicating porosity has been created within the fault zone.

S-wave and P-wave velocities are also slower across the Mozumi fault (1.99 $\pm$ 0.05 and 4.04 $\pm$ 0.06 km/s) relative to surrounding wall rock (2.36 $\pm$ 0.05 and 4.36 $\pm$ 0.08 km/s). A Mann-Whitney U test for comparison of two sample populations of non-parametric, open data, was employed to test for statistical significance of the decrease in seismic velocity across the Mozumi fault zone. The null hypothesis of h1: velocities across the Mozumi fault zone $\geq$ velocities of wall rock was rejected at a confidence interval of 95%. In other words, the decrease in seismic wave velocity across the Mozumi fault zone is statistically significant. This indicates that fault-related activity has significantly altered the physical properties of the Mozumi fault rocks relative to wall rock.

Calculations of Elastic Moduli and Porosity

Mechanical properties of Mozumi fault zone rocks were calculated from the seismic wave velocities recorded by wireline logs and the density of the rocks. The equations used for the calculation of mechanical properties are derived from crossplots of the properties of sedimentary rocks. Density was calculated for all samples collected from borehole A by determining the mass of each sample and the volume using simple Archimedes Principle (displacement of water). The values of Lame's constant λ, and the shear modulus μ (a measure of rigidity) can be calculated given the equations for S-wave velocity and P-wave velocity

$$\nu_s = \sqrt{\mu/\rho} \quad [1]$$

and

$$\nu_p = \sqrt{(K + 4/3\mu)/\rho} = \sqrt{(\lambda + 2\mu)/\rho} \quad [2]$$

where ν_s is shear wave velocity from the wireline log, ν_p is primary (compressional) wave velocity from the wireline log, K is the bulk modulus, and ρ is calculated density (Kramer, 1996).

Using λ and μ, Young's modulus (E) and Poisson's ratio (ν) can be calculated for borehole A samples using the equations

$$E = (\mu(3\lambda + 2\mu))/(\lambda + \mu) \quad [3]$$

and

$$\nu = \lambda/2(\lambda + \mu) \quad [4]$$

where E is a material property that describes a rock's stiffness, or the ratio of extensional stress to extensional strain (E = stress/strain), and ν is the ratio of transverse contractional strain to longitudinal extensional strain in the direction of stretching force (Kramer, 1996; Mavko et al., 1998). Thus we can estimate the elastic properties of fault zone materials, and use these values in conjunction with observations of fault rock properties to infer the physical properties of the fault zone. Table 3-2 lists the results of these calculations.

Calculated values for Young's modulus and Poisson's ratio fall towards the high end or above experimentally derived values measured for intact samples of siltstone, shale, and sandstone (Figure 3-12; Haas, 1981; Szwilski, 1982; Hatheway and Kiersch,

1989; Wong et al., 1997). Laboratory values for seismic velocities and elastic moduli are often different than in-situ values due to biased sampling of un-fractured, undeformed, pure rock samples for laboratory testing (Stierman and Kovach, 1979; Sayed, 2001). This would result in faster seismic velocity, higher Young's modulus, and lower Poisson's ratio values for laboratory experiments with respect to in-situ values. Figure 3-12 shows that the Poisson's ratio is indeed lower for experimentally-derived values (average of 0.206) than values calculated from in-situ seismic velocities of the Mozumi fault zone (average of 0.320). The value of Young's modulus, however, is also lower overall for experimental values (average of 20.5 GPa) than for calculated values of Mozumi fault rocks (average of 29.9 GPa). Values of Young's modulus may be higher for Mozumi fault zone siltstone than for laboratory samples of sandstone, shale, and siltstone due to cementation and mineralization as observed in thin section (Figure 3-8). Mineralization may account for the stiffness of the fault rocks relative to pure sandstone and siltstone samples used in laboratory testing for Young's modulus. There may also be an additional scale factor at work when comparing in-situ and laboratory values.

The amount of clay in each sample was determined with a hydrometer in the Utah State University Soil Testing Laboratory (Table 3-4; Appendix B). The results for clay fraction calculated using a hydrometer are not perfect as small (<mm) pieces of breccia clasts did not completely disaggregate upon mixing. The hydrometer measures grams of soil (clay) colloids per liter. Once the clay content is estimated for each sample, it can be used to calculate porosity (ϕ) by the equation for shaley sandstones

$$\nu_p = 5.77 - 6.94\phi - 1.73\sqrt{C} + 0.446(P_e - 1.0e^{-16.7Pe}) \qquad [5]$$

where C is the clay volume fraction and P_e is the effective pressure in kilobars (Table 3-4; Eberhart-Phillips et al., 1989). The confining pressure at the tunnel depth of 350 m is 7.6 MPa, or 0.076 Kb (Forster et al., 2003). The confining pressures for core samples were calculated using the true depth below the ground surface for each sample. Calculated porosity values are listed in Table 3.3.

The ν_p/ν_s ratio (Table 3-3) is a proxy for fluid content and porosity, with high ν_p/ν_s values indicating an increased presence of fluids and porosity (Stanchits et al., 2003). S-wave and P-wave velocity both decrease with increasing fluid content, however S-wave velocity is more sensitive to the presence of fluids as shear waves can not propagate in a non-rigid medium (Stanchits et al., 2003; Hamada, 2004). According to our calculations (Table 3-3), the areas of the Mozumi fault zone where samples MZA-6 and MZA-8 were collected, as well as the area surrounding sample MZA-10 have the highest relative fluid content (ν_p/ν_s = 2.19-2.38) for samples of this study, corresponding to the lowest S-wave values (1.45-1.75 km/s). Samples MZA-1, MZA-2, MZA-5, MZA-7, MZA-9, and MZ-1 have lower values of ν_p/ν_s (1.77-1.95) and higher S-wave velocity values (2.00-2.55 km/s) than MZA-6, MZA-8, and MZA-10. Typical values of ν_p/ν_s for sandstone, shale, and siltstone range from 1.5 (dry sandstone) to ~2.5 (Castagna et al., 1985).

3-4. DISCUSSION

Complex Fault Structure of the Mozumi Fault System

Mizuno et al. (2004) analyzed fault-zone-trapped waves in order to estimate the averaged structure of the Mozumi fault. Their analysis uses trapped waves produced from 9 earthquakes and recorded by a seismic array within the Active Fault Survey Tunnel to infer fault zone structure including total damage zone width, average S-wave velocity, and wave attenuation. They estimate the width of the fault zone to be 160-400 m (which corresponds to the damage zone observed by mine geologists in the Active Fault Survey Tunnel of ~200 m), the averaged shear wave velocity to be 2.9-3.1 km/s (~1.01 km/s faster than the average value determined from the wireline log for Mozumi fault zone rocks), and wave attenuation (*Q*s) in the fault zone at a given time along a wave-length distance (Udias, 1999) to be 60-90. The parameter *Q* is a function of porosity and density, and thus ν_p, ν_s, and ν. Normal crustal values of *Q* are ~160, with stiffer rocks having larger values of *Q* (Anderson and Hart, 1978; Udias, 1999). The values of *Q*s suggest that the Mozumi fault zone rocks cause significant wave attenuation (Mizuno et al., 2004). Within the Mozumi fault rocks, shear is mostly confined to the finer-grained matrix material (Figure 3-8). The muscovite and serecite-rich matrix appears to behave plastically and shear moves around stronger quartz grains. The values of *Q* combined with these observations indicate that the Mozumi fault rocks, and particularly the matrix materials, make an effective sink for radiated energy in the fault zone, and may play a role in arresting rupture (Boatwright and Cocco, 1996; Ruina, 1983).

Mizuno et al. (2004) provide an analysis of the Mozumi fault zone over scales of 10's to 100's of meters, whereas our data provide a finer scale analysis of the elastic and compositional properties of the Mozumi fault zone. The ν_p and ν_s values from borehole A decrease from sandstone to shale to clay (Table 3-5; Figure 3-11; Shingu et al., 1997). In addition, seismic velocity values are decreased across the Mozumi fault relative to the wall rock. With the exception of one subsidiary fault, the average P-wave and S-wave velocities for wall rock in borehole A are 4.36 $\pm$ 0.08 km/s and 2.36 $\pm$ 0.05 km/s, respectively, whereas the average P-wave and S-wave velocities of the Mozumi fault rock are 4.04 $\pm$ 0.06 km/s and 1.99 $\pm$ 0.05 km/s, respectively (Table 3-5, Figure 3-11). The average P-wave and S-wave velocities for protolith are 4.75 km/s and ~3.0 km/s, respectively (Mamada et al., 2002; Mizuno et al., 2004). The fault rocks intersected by borehole A are not homogeneous or isotropic, which affects the velocity structure of the Mozumi fault zone. Four types of anisotropy are recognized, including fractures along borehole A (Figure 3-6), lithology changes, foliation and other microstructures, and heterogeneity of physical and mechanical properties (Forster et al., 2003; this study).

Fault zone samples MZA-1, MZA-9, and to some extent MZA-5 and MZA-4, have textures unique to the fault rocks sampled in this study. They are also less dense, contain less fluid based on ν_p/ν_s, ν, and resistivity values, have more clay content than other samples, and have the most depleted geochemical signatures. Samples MZA-1 and MZA-4 have high values of E (28.6 Gpa and 31.0 Gpa), low values of ν (0.264 and 0.263), and contain illite/muscovite and kaolinite clays. Samples MZA-9, MZA-2, and MZA-5 have low to intermediate fluid content (ν_p/ν_s = 1.87, 1.89, and 1.90), high values of E (40.8-44.9 GPa, 35.0 Gpa, and 30.9), intermediate values of ν (0.298-0.299,

0.306), and contain a mix of clay types including smectite. Samples MZA-7 and MZA-8 have intermediate values of elastic moduli (E = 27.1, 21.98; ν = 0.322, 0.368) and contain predominantly illite/muscovite and some kaolinite. Samples MZA-6, MZA-8, and MZA-10 have high fluid content (ν_p/ν_s = 2.38, 2.19, 2.23), depleted geochemical signatures, low values of E (16.2 Gpa, 21.8 Gpa, and 22.6 Gpa), high values of ν (0.393, 0.368, and 0.374), and contain illite/muscovite and kaolinite clays. MZA-6 also contains smectite. These samples illustrate the heterogeneous nature of the fault zone (Figure 3-13). Fault rocks of the Mozumi fault have values of Young's modulus ~11-39 GPa lower than siltstone protolith sample MZ-1, and values of Poisson's ratio 0.151-0.021 higher than siltstone protolith sample MZ-1 (Table 3-3). These values indicate that, overall, the fault zone rocks are not as stiff and have a greater porosity than their protolith.

The abundance of veins throughout the Mozumi fault zone and numerous mineral phases present around the secondary fault sampled in MZA-9 indicate that fluid flow is active during and after fault activity. Veins that fill shattered grains indicate that fluids must have transported materials into void spaces quickly before the fractures closed. Anastomosing gouge and irregular shaped blebs of coarse calcite crystals within the matrix indicate fluid pressurization and coseismic injection of fluids and saturated fault gouge. The available fluids that created these microstructures likely persisted after fault activity. Thin sections MZA-10 and MZA-9 contain veins that show evidence for evolving fluids that precipitated quartz followed by calcite or chlorite.

Permeability and porosity were measured and reported by Forster et al. (2003). They find low permeability (k) and porosity (n) values in siltstone protolith (10^{-17} m^2, 1.6%), smallest k values in clay-rich zones (10^{-18} to 10^{-19} m^2), intermediate values of k

and *n* in fault breccia with clay gouge (10^{-14} to 10^{-16} m^2, 8-9%) including samples MZA-1, MZA-2, MZA-4, and MZA-5), and the largest *k* values for fractured rock without significant clay content (10^{-13} to 10^{-14}, Table 3-3). These permeability and porosity zones are parallel to the Mozumi fault, and act as a joint fault-parallel fluid conduit and fault-perpendicular fluid barrier. The values of porosity calculated from clay content and P-wave velocity for fault rocks in this study are at least double the porosity values reported by Forster et al. (2003), and are probably closer to the true porosity values, whereas the values reported by Forster et al. (2003) measure *connected porosity* using the fluid injection method. Some error was also introduced by incomplete disaggregation of samples. There may also be error in the fit of the equation for shaley-sandstones to our samples, however, the equation is averaged over a large number of measurements. Both the values of porosity and connected porosity are lowest for the protolith sample MZ-1.

Other data presented in this study support the heterogeneous structure of the Mozumi fault as proposed by Forster et al. (2003). Permeable pockets of brecciated fault rock correspond to areas of low relative resistivity, high relative values of ν_p/ν_s, low relative values of *E*, and high relative values of ν (Figure 3-13). Fault rocks with lower values of ν_p/ν_s correspond to a greater percentage of clay, higher resistivity values, are generally more chemically altered, have higher values of *E*, and have lower values of ν than pockets of permeable fault rock (Figure 3-13). An interesting feature of Figure 3-13 is the offset of the lowest values of resistivity, ν_p/ν_s, and Young's modulus (MZA-6 and MZA-8) from the most deformed and geochemically and mineralogically altered rocks (MZA-5, MZA-1, MZA-9) that contain smectite clays. The presence of smectite (as well as the geochemical alterations) indicates fluid-rock interactions, as the protolith is illite-

siltstone. These observations suggest that pockets of fluid-rich rock may migrate through time, thus resulting in illite-smectite reactions and other alteration along the fault zone. The migration of fluid and resulting alteration may cause a gradual change in the behavior of the fault and the properties of that rock mass over time.

Bedrosian et al. (2004) note that the creeping segment of the San Andreas fault has lower P-wave velocity and higher ν_p/ν_s values than the locked portions of the fault, suggesting that it is a fluid-rich region. They believe that the central creeping segment of the San Andreas fault may be explained by fluids in the fault zone, and they propose that fluid-rich regions of faults are unlikely to maintain the shear stresses associated with brittle failure. The Atotsugawa Fault System, including the Mozumi fault, also has a central creeping segment marked by decreased seismicity (Figure 3-4; Ito, 1999; Hirahara et al., 2003; Ito, 2003). The creeping segment of the San Andreas fault has low resistivity zones distributed between the San Andreas and the Calaveras faults, which are interpreted as corresponding to "fluid pockets" in the fault zone (Bedrosian et al., 2004). Our model of a heterogeneous Mozumi fault zone with fault-parallel, fluid-rich lozenges is similar to that of the creeping portion of the San Andreas fault. Bedrosian et al. (2004) acknowledge, however, that there is still the critical question, do fluids influence seismicity on the creeping section of the San Andreas fault, or does creeping allow for open fluid-filled fractures to be maintained? Fluids in the San Andreas and Atotsugawa fault system may either simply mark creeping fault segments, or may be a necessary condition for creep.

3-5. CONCLUSIONS

We provide microstructural, mineralogical, and geochemical data, and calculated values of elastic moduli for fault rock samples from the Mozumi fault, Japan that can be combined to illustrate the in-situ macroscopic hydro-mechanical structure of the fault. The results of this and related studies include:

1) The Mozumi fault rocks are altered and mineralized fault breccias with foliated serecite/muscovite-rich matrix that show evidence for concentrating shear and plastic deformation in the matrix, evolving fluid, and syn-tectonic fluid flow and pressurization.

2) The Mozumi fault is a low velocity zone (4.04 $\pm$ 0.06 km/s and 1.99 $\pm$ 0.05 km/s) relative to wall rock in borehole A (4.36 $\pm$ 0.08 km/s and 2.36 $\pm$ 0.05 km/s) and protolith (4.75 km/s and ~3.0 km/s) as determined from wireline logs of P-wave and S-wave velocities across the fault zone and seismic wave velocities of protolith as reported in Mizuno et al. (2004; references therein).

3) Fault rocks from the Mozumi fault zone have increased porosity (10-22%) relative to the protolith (4%; Forster et al., 2003; this study).

4) Electrical and seismic properties, elastic moduli, porosity, permeability, fault-related textures, and clay content vary across the main fault zone, and these variations occur in pockets that are parallel to the Mozumi fault.

5) Pockets of fluid-rich rock and alteration migrate through the fault zone with time. This is marked by an offset of fluid-rich rocks with lower values of E (16.2-27.1 Gpa) and higher values of ν (0.322-0.393) from fault breccias that have higher values of E (28.6-44.9 Gpa), lowest to intermediate values of ν (0.262-0.308), and are more altered and contain more clay and intense microstructural deformation.

6) The parameter *Q*s, which describes wave attenuation (a function of porosity and density), for the Mozumi fault zone is 60-90, whereas average crustal values are ~160 (Mizuno et al., 2004). These values suggest that the Mozumi fault zone rocks cause significant wave attenuation.

These data indicate that the fault rocks in the Mozumi fault make an effective sink for radiated energy in the fault zone. Fluid-rich regions of faults may not be capable of maintaining the shear stresses associated with brittle failure (Bedrosian et al., 2004). Creep on the Mozumi fault may be explained by fluid-rich pockets with corresponding low relative values of Young's modulus, high relative values of Poisson's ratio, low relative resistivity, secondary porosity and permeability, and high relative values of ν_p/ν_s (Forster et al., 2003; this study). The variations of fault rock properties affect wave propagation, rupture mechanics, and fluid migration in and around the Mozumi fault zone.

References

Anderson, D.L., and R.S. Hart (1978). *Q* of the Earth, *J. Geophys. Res.* **83**, 5869-5882.

Ando, M. (1998). Overview and purpose of the active fault probe at the Mozumi-Atotsugawa fault system (Progress Report), in *The International Workshop of Frontiers in Monitoring Science and Technology for Earthquake Environments*, Toki and Kamioka, Japan, November 1998, Japan Nuclear Cycle Development Institute Report TW7400 98-001.

Asquith, G., and C. Gibson (1982). *Basic Well Log Analysis for Geologists*, Am. Assoc. Petrol. Geol. Tulsa, Oklahoma.

Bedrosian, P.A., M.J. Unsworth, G.D. Egbert, and C.H. Thurber (2004). Geophysical images of the creeping segment of the San Andreas Fault; implications for the role of crustal fluids in the earthquake process, *Tectonophysics* **385**, 137-158.

Boatwright, J., and M. Cocco (1996). Frictional constraints on crustal faulting, *J. Geophys. Res.* **B101**, 13895-13909.

Castagna, J.P. M.L. Batzle, and R.L. Eastwood (1985). Relationships between compressional-wave and shear-wave velocities in clastic silicate rocks, *Geophysics* **50**, 571-581.

Chester, F.M. and J.P. Evans (1998). Microscale vein mineralization and porphyroclast development in low-grade cataclasites, in *Fault-related Rocks, A Photographic Atlas,* A.W. Snoke, J. Tullis, and V.R. Todd (Editors), Princeton University Press, Princeton, New Jersey, 138-139.

Deere, D.U. and D.W. Deere (1987). The Rock Quality Designation (RQD) index in practice, *ASTM Spec. Tech. Publ.* **984**, 91-101.

Dresser Atlas (1982). *Well Logging and Interpretation Techniques, a Course for Home Study*, Dresser Industries, Inc., Houston, Texas.

Doll, H.G. (1948). The SP log, theoretical analysis and principles of interpretation, *Trans. AIME* **179**, 146-185.

Eberhart-Phillips, D.M. M.D. D.H. Han, and M.D. Zoback (1989). Empirical relationships among seismic velocity, effective pressure, porosity, and clay content in sandstone, Geophysics **54**, 82-89.

Forster, C.B., J.P. Evans, K. Wantanabe, H. Tanaka, R. Jeffreys, and T. Nohara (2003). Hydrological properties and structure of the Mozumi Fault, central Japan, *Geophys. Res. Lett*. **30**, doi: 10.1029/2002GL014904.

Fujita, M. (2002). A new contribution to the stratigraphy of the Tetori Group, adjacent to Lake Kuzuryu, Fukui Prefecture, central Japan, *Mem. Fukui Pref. Dinosaur Mus.* **1**, 41-53.

Goddard, J.V., and J.P. Evans (1995). Chemical changes and fluid-rock interaction in faults of crystalline thrust sheets, northwestern Wyoming, U.S.A., *J. Struc. Geol.* **17**, 533-547.

Gutscher, M. (2001). An Andean model of interplate coupling and strain partitioning applied to the flat subduction zone of SW Japan (Nankai Trough), *Tectonophysics* **33**, 95-109.

Gutscher, M., and S. Lallemand (1999). Birth of a major strike-slip fault in SW Japan, *Terra Nova* **11**, 203-209.

Haas, C.J. (1981). Static Stress-Strain Relationships, in *Physical Properties of Rocks and Minerals,* Y.S. Touloukian, W.R. Judd, and R.F. Roy (Editors), **II-2**, McGraw-Hill, Columbus, Ohio, 409-489.

Hamada, G.M. (2004). Reservoir Fluids Identification using V_p/V_s ratio, *Oil Gas Sci. Tech.* **59**, 649-654.

Hatheway, A.W., and G.A. Kiersch (1989). Engineering Properties of Rock, in *Practical Handbook of Physical Properties of Rocks and Minerals,* R.S. Charmichael (Editor), CRC Press, Boca Raton, Florida, 672-715.

Hirahara, K., Y. Ooi, M. Ando, K. Haso, Y. Wada, and T. Ohkura (2003). Dense GPS Array observations across the Atotsugawa fault, central Japan, *Geophys. Res. Lett.* **30**, doi: 10.1029/2002GL015035.

Ito, H. (1999). Studies on fault activity at the Atotsugawa fault – Is the Atotsugawa fault creeping? *Geol. Surv. Japan Info. Circ.* S-12.

Ito, H. (2003). Detailed seismicity and crustal structure in the Atotsugawa fault, a partly creeping fault, central Honshu, Japan, in *Internationall Union of Geodosy and Geophysics 2003 Scientific Program,* 30 June to 11 July 2003, Sapporo, Japan.

Kramer, S.L. (1996). Chapters 2: Seismology and Chapter 5: Earthquakes and Wave Propagation, in *Geotechnical Earthquake Engineering*, Prentice Hall, Upper Saddle River, New Jersey, 18-53 and 143-183.

Mamada, Y., Y. Kuwahara, H. Ito, and H. Takenaka (2002). 3-D finite-difference simulation of seismic fault zone waves, Application to the fault zone structure of the Mozumi-Sokenobu fault, central Japan, *Earth Plan. Space* **54**, 1055-1058.

Matsuda, T. (1966). Strike-slip faulting along the Atotsugawa fault, Japan (in Japanese with English summary), *Bull. Earth. Res. Inst.* **44**, 1179-1212.

Matsuda, T. (1978). Collision of the Izu-Bonin arc with central Honshu: Cenezoic tectonics of the Fossa Magna, Japan, *J. Phys. Earth* **26**, 409-421.

Matsuda, T., and Y. Kinugasa (1991). Active faults in Japan, *Episodes* **14**, 199-204.

Mavko, G., M. Tapan, and J. Dvorkin (1998). *The Rock Physics Handbook; Tools for Seismic Analysis in Porous Media*, Cambridge University Press, Cambridge, United Kingdom, 329 pp.

Mitra, G. (1998). Progressive development of foliation in a brittle deformation zone, in *Fault-related Rocks, A Photographic Atlas,* A.W. Snoke, J. Tullis, and V.R. Todd (Editors), Princeton University Press, Princeton, New Jersey, 52-53.

Mikumo, T., H. Wada, and M. Koizumi (1988). Seismotectonics of the Hida region, central Honshu, Japan, *Tectonophysics* **147**, 95-119.

Mizuno, T., K. Nishigama, H. Ito, and Y. Kuwahara (2004). Deep structure of the Mozumi-Sukenobu fault, central Japan, estimated from the subsurface array observation of fault zone trapped waves, *Geophys. J. Int.* **159**, 622-642.

Ruina, A.L. (1983). Slip instability and state variable friction laws, *J. Geophys. Res.* **B88**, 359-370.

Sagiya, T., S. Miyasaki, and T. Tada (2000). Continuous GPS array and present-day crustal deformation of Japan, *Pure Appl. Geophys.* **157**, 2303-2322.

Sayed, A.Y. (2001). *In Situ* compressional wave velocity across an exposed brittle fault zone, *Master's Thesis*, Polytechnic Institute and State University, Blacksburg, Virginia.

Shingu K., T. Okada, A. Saitou, K. Wada, K. Horinokuchi, and T. Nakajima (1997). Study using a drift in the active fault zone (in Japanese with English abstract), PNC TJ1174 97-001.

Stanchits, S.A., D.A. Lockner, and A.V. Ponomarev (2003). Anisotropic changes in p-wave velocity and attenuation during deformation and fluid infiltration of granite, *Bull. Seism. Soc. Am.* **93**, 1803-1822.

Stierman, D.J., and R.L. Kovach (1979). An *in situ* velocity study: The Stone Canyon Well, *J. Geophys. Res.* **B84**, 672-678.

Szwilski, A.B. (1982). Determination of elastic modulus of stress relief cores of shale, *ASTM Geotech. Testing J.* **5**, 34-41.

Taira, A. (2001). Tectonic evolution of the Japanese island arc system, *Ann. Rev. Earth Plan.* **29**, 109-134

Takeuchi, A., and H. Ongirad (2003). Recurrence interval of big earthquakes along the Atotsugawa fault system, central Japan: Results of seismo-geological survey, *Geophys. Res. Lett.* **30**, doi: 10.1029/2002GL014957.

Tanaka, H., and T. Ito (1999). Creep motion of the Mozumi-Sukenobu Fault deduced from the flow texture in the ongoing processed fault rocks, *Eos, Trans. Am. Geophys. Union*, **80**, 748.

Udias, A. (1999). Chapter 14: Anelasticity and anisotropy, in *Principles of Seismology*, Cambridge University Press, Cambridge, United Kingdom, 253-273.

Wada, H., T. Mikumo, and M. Koizumi (1990). Recent seismic activity in the northern Hida, Toyama Bay and Noto Peninsula regions, Kyoto Daigaku Bosai Kenkyujo Nenpo, *Disaster Prev. Res. Inst. Ann.* **33**, Kyoto University, Kyoto, Japan, 57-74.

Wong, T., C. David, and W. Zhu (1997). The transition from brittle faulting to cataclastic flow in porous sandstones: Mechanical deformation, *J. Geophys. Res.* **B102**, 3009-3025.

Yamaji, A. (1994). An introduction to the Cenozoic tectonics of the Japan arc, *Geofisica Internacional* **33**, 21-24.

Yamaji, A. (2003). Slab rollback suggested by latest Miocene to Pliocene forearc stress and migration of volcanic front in southern Kyushu, northern Ryukyu Arc, *Tectonophysics* **364**, 9-24.

Table 3-1
Descriptions of siltstone samples from the Mozumi fault zone used in this study including distances along the borehole and projected horizontal distances from the southeast end of borehole A.

Sample	Description	Distance along borehole (m)	Horizontal distance (m)
MZA-2	Siltstone fault breccia, abundant clay, intensely foliated matrix and shear fabric	143.2	71.6
MZA-1	Siltstone fault breccia, abundant clay, crenulation foliation in matrix, hematite and debris-filled fractures	133	66.5
MZA-4	Siltstone fault breccia, abundant clay, calcite and quartz veins, intensely foliated matrix	128.4	64.2
MZA-5	Siltstone fault breccia, abundant clay, intensely foliated matrix and shear fabric	122.4	61.2
MZA-6	Siltstone fault breccia, moderately foliated, shear fabrics	116.57	58.3
MZA-7	Siltstone fault breccia, abundant clay, intensely foliated matrix and shear fabric	111.76	55.9
MZA-8	Siltstone, angular fault breccia, calcite veins, fractures, anastomosing brown clay	104.8	52.4
MZA-9	Altered siltstone cut by subsidiary fault, indurated and mineralized siltstone against weak clay-rich fault rock	95.75	47.9
MZA-10	Siltstone, fault with clay gouge, quartz and calcite veins	38.2	19.1

Table 3-2

Bulk and clay mineralogy by sample. The first clay type listed is most abundant.

Sample	Bulk Mineralogy	Clay Mineralogy
MZA-2	quartz, feldspar, sericite	smectite, illite, kaolinite, I-S chlorite
MZA-1	quartz, calcite, sericite	illite, smectite, kaolinite
MZA-5	quartz, calcite, feldspar, sericite	illite, kaolinite, chlorite or vermiculite, smectite?
MZA-6	quartz, calcite, sericite	illite, smectite, kaolinite
MZA-7	quartz, feldspar, sericite	illite, kaolinite
MZA-8	quartz, sericite	illite, kaolinite
MZA-9a	quartz, calcite, sericite	illite, kaolinite-smectite, chlorite or vermicullite
MZA-9b	quartz, calcite, sericite	illite, kaolinite, chlorite
MZA-10	quartz, calcite, sericite	illite, kaolinite, chlorite or vermicullite
MZ-1	quartz, feldspar, sericite	illite, kaolinite, I-S?

Table 3-3

Estimated values for properties of Mozumi fault rocks including density (ρ), seismic wave velocities (v_s, v_p), calculated physical, and calculated mechanical properties for borehole A samples and a protolith sample from borehole 1, as well as permeability and porosity values from Forster et al. (2003).

Sample	ρ (g/cc)	v_s (km/s)	v_p (km/s)	μ (g/cm-sec^2)	λ (g/cm-sec^2)	Calculated E (GPa)	Calculated ν	v_p/v_s	Calculated Porosity (%)	Permeability (m^2), connected porosity (%) of Forster et al. (2003)
MZA-2	2.77	2.20	4.16	$1.34*10^{11}$	$2.11*10^{11}$	35.0	0.306	1.89	10	$3.7\ E^{-15}$, 8.0
MZA-1	2.49	2.13	3.76	$1.13*10^{11}$	$1.26*10^{11}$	28.6	0.264	1.77	17	$1.9\ E^{-15}$, 8.4
MZA-4	2.33	2.25	4.31	$1.18*10^{11}$	$1.97*10^{11}$	31.0	0.263	1.92	-	$5.3\ E^{-15}$, 9.0
MZA-5	2.80	2.05	3.90	$1.18*10^{11}$	$1.90*10^{11}$	30.9	0.308	1.90	14	$1.6\ E^{-15}$, 7.2
MZA-6	2.87	1.45	3.45	$6.03*10^{10}$	$2.21*10^{11}$	16.2	0.393	2.38	22	
MZA-7	2.56	2.00	3.90	$1.02*10^{11}$	$1.85*10^{11}$	27.1	0.322	1.95	15	
MZA-8	2.60	1.75	3.83	$7.96*10^{10}$	$2.22*10^{11}$	21.8	0.368	2.19	16	
MZA-9a	2.66	2.55	4.76	$1.73*10^{11}$	$2.57*10^{11}$	44.9	0.299	1.87	-	
MZA-9b	2.41	2.55	4.76	$1.57*10^{11}$	$2.32*10^{11}$	40.8	0.298	1.87	-	
MZA-10	2.84	1.70	3.79	$8.21*10^{10}$	$2.44*10^{11}$	22.6	0.374	2.23	18	
Borehole 1 protolith										
MZ-1	2.85	2.80	4.75	$2.23*10^{11}$	$2.10*10^{11}$	55.4	0.242	1.70	4	$4.0\ E^{-17}$, 1.6
Additional samples from Forster et al. (2003)										
MZA-143.2 (breccia)										$3.7\ E^{-15}$, 8.0
MZA-127.8 (clay gouge)										$2.2\ E^{-16}$, 11.1
“clay-rich zones”										$E^{-18} – E^{-19}$

Table 3-4
Hydrometer results for percent clay analysis.

Sample	Sample Weight	40 sec	Temp.	Corrected Hydrometer	6 hr 40 sec	Temp.	Corrected Hydrometer	% Clay
MZA-10	40	11.0	26	13.16	7.0	23	8.08	20
MZA-8	40	14.0	25	15.80	8.0	23	9.08	23
MZA-7	40	14.0	25	15.80	8.5	23	9.58	24
MZA-6	40	13.0	25	14.80	8.0	23	9.08	23
MZA-5	40	16.5	25	18.30	10.0	23	11.80	28
MZA-2	30	12.5	25	14.30	8.0	23	9.08	30
MZA-1	40	16.5	25	18.30	9.0	23	10.08	25
MZ-1	35	12.5	25	14.30	7.0	23	8.08	23
Control	0	3.0	26	5.16	3.0	23	4.08	-

Table 3-5

P-wave and S-wave velocities for borehole A by rock type, and average P-wave velocities for the Mozumi fault zone and wall rock. Typical ranges of v_p and v_s for sandstones, shaley rocks, and "mudrocks" are listed (Castagna et al., 1985)

Lithology	v_p (km/s)		v_s (km/s)	
	range	average	range	average
sandstone	3.64-5.41	4.62	1.52-2.86	2.25
mixed sandstone/shale	4.35-4.76	4.56	2.44-2.56	2.50
shale	3.70-5.26	4.24	1.85-2.50	2.19
siltstone	3.08-5.26	4.42	1.28-3.13	2.16
clay	3.33-3.85	3.59	1.67-1.69	1.68
average		4.49		2.21

average v_p of wall rock	4.36	average v_p of MF zone	4.04
average v_s of wall rock	2.36	average v_s of MF zone	1.99
typical range for v_p	3.0-5.0	typical range for v_s	1.5-2.5

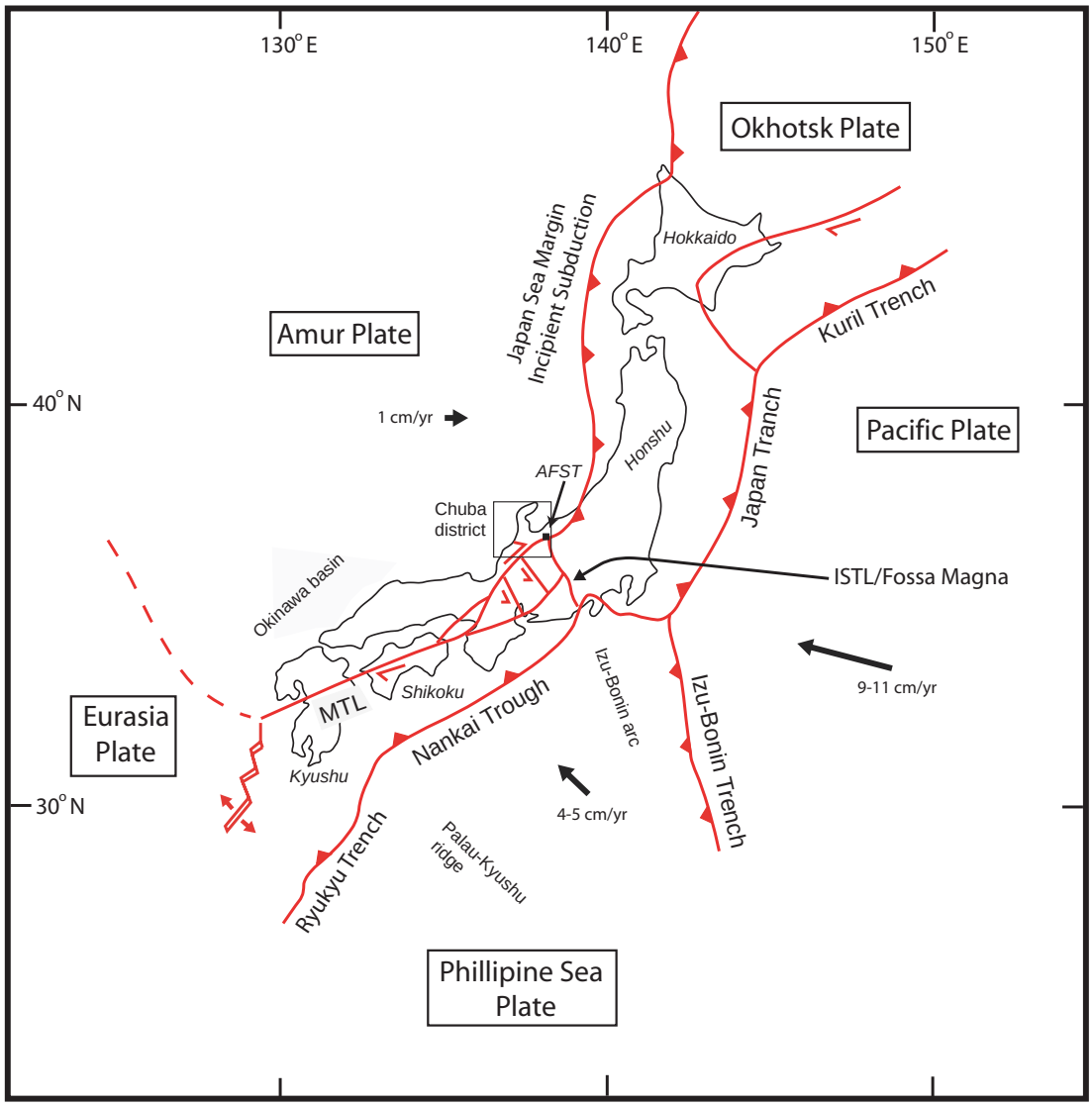

Figure 3-1. Illustration of the Japan island arc system overlain by current plate boundaries after Taira (2001). Tectonic features are labeled as well as the 4 main islands, the Chuba district of intense earthquake activity, the Active Fault Survey Tunnel (AFST), and plate motion vectors from Taira (2001) and Yamaji (1994, 2003). Notice the presence of microplates in central Honshu.

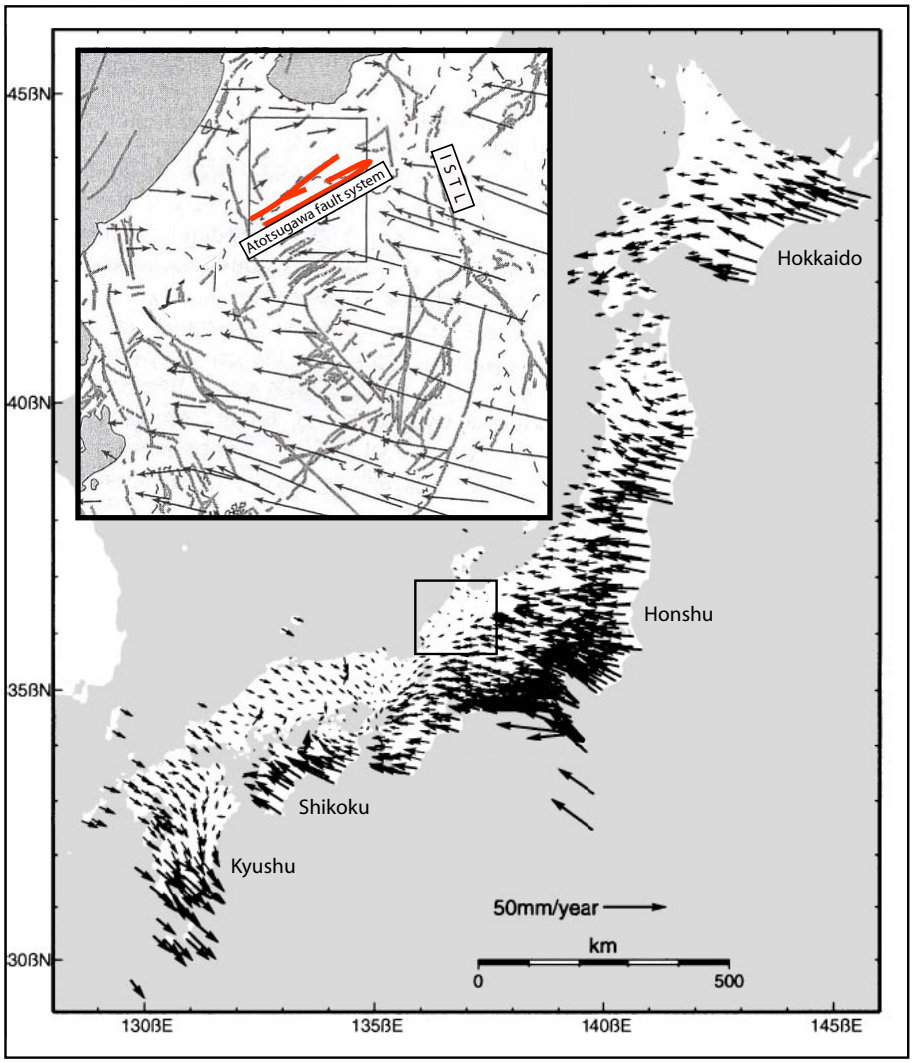

Figure 3-2. Relative plate motion vectors from GPS using stable Eurasia as a reference. The data show that most of Japan is under east-west compression, and west and northeast Honshu are converging towards one another (modified from Sagiya et al., 2000 and Hirahara et al., 2003).

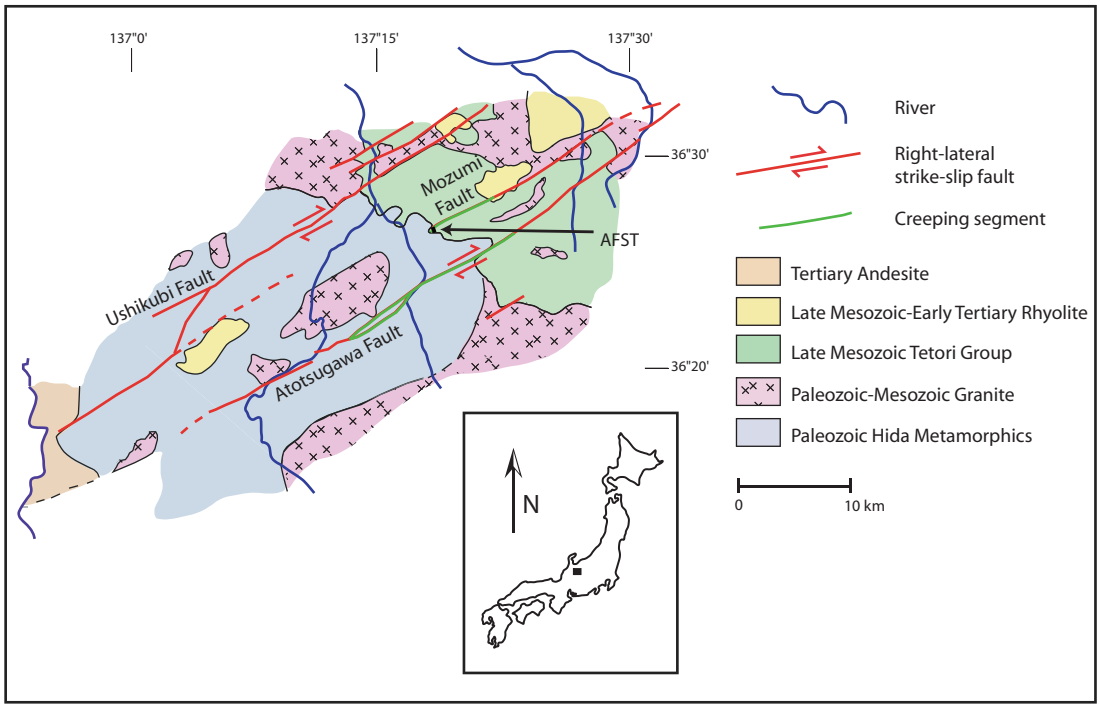

Figure 3-3. Generalized geology surrounding the Atotsugawa, Mozumi, and Ushikubi faults, Japan (Atotsugawa Fault System). The Active Fault Survey Tunnel (AFST) intersects the Mozumi fault where it cuts Jurrasic Tetori Group sandstone and shale (map modified from Matsuda, 1966).

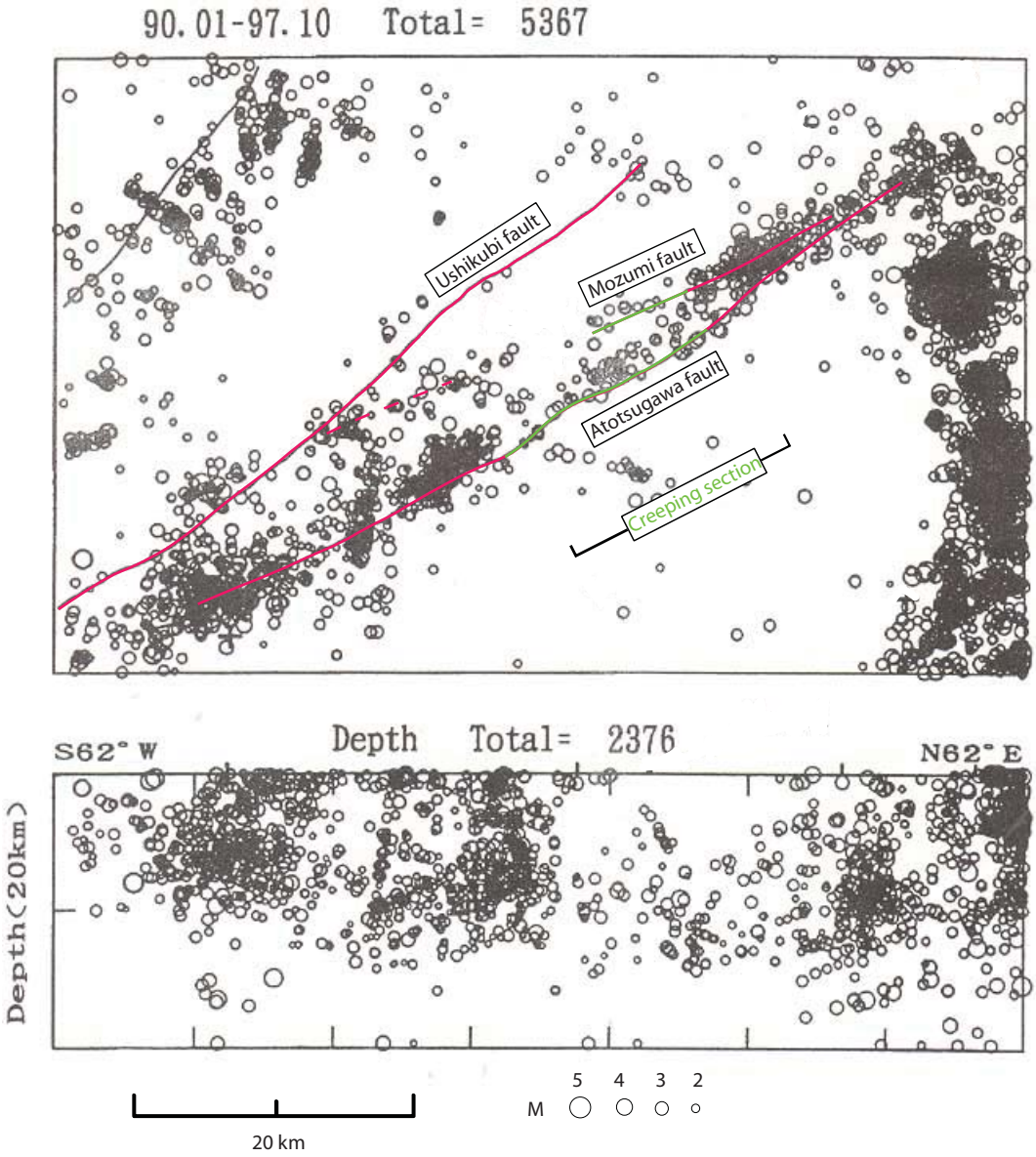

Figure 3-4. Seismicity of the Atotsugawa Fault System, Japan including the Mozumi fault. Epicenter distribution (top) and focal depths (bottom). Figure modified from Ito (1999).

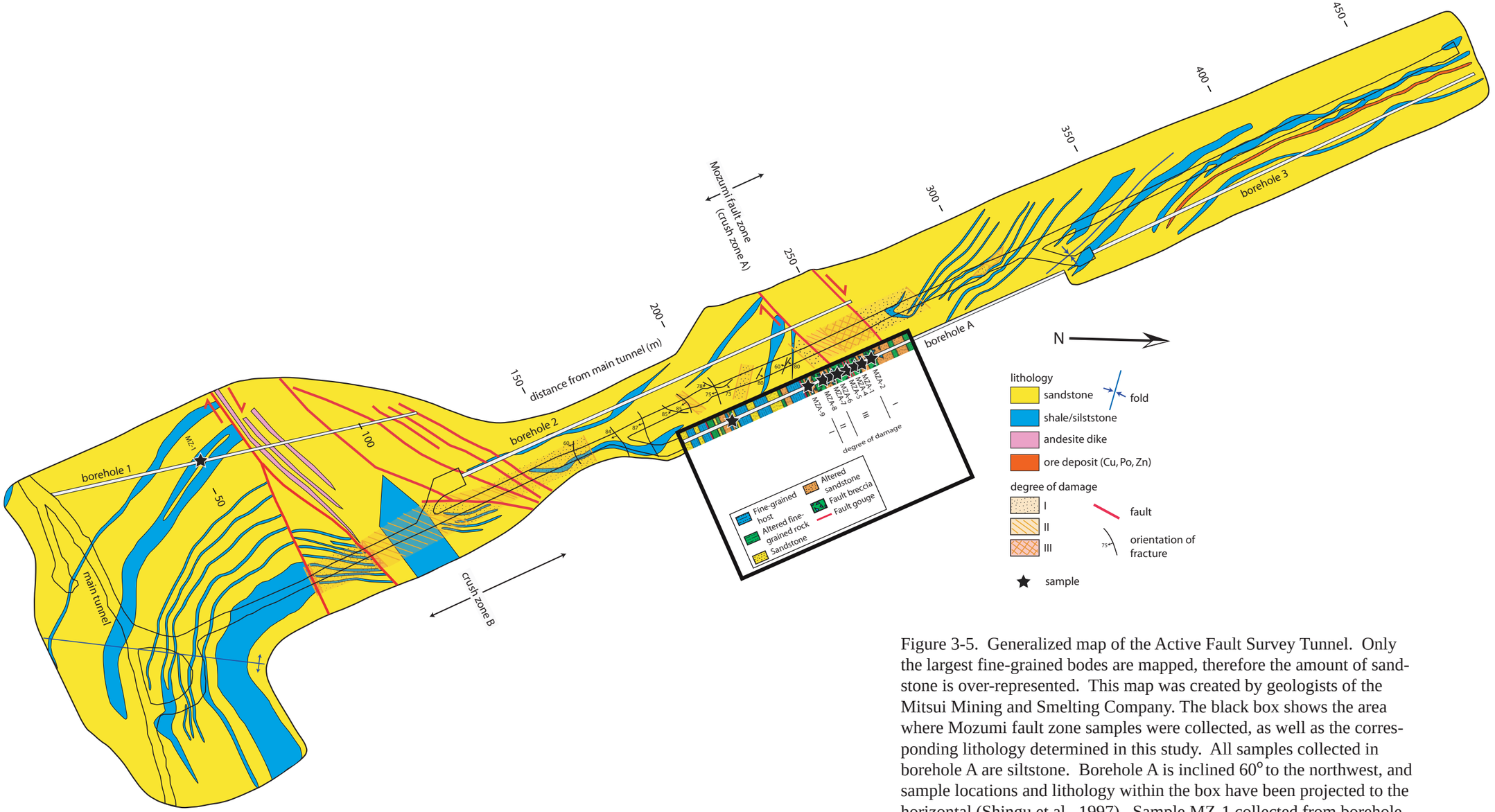

Figure 3-5. Generalized map of the Active Fault Survey Tunnel. Only the largest fine-grained bodes are mapped, therefore the amount of sandstone is over-represented. This map was created by geologists of the Mitsui Mining and Smelting Company. The black box shows the area where Mozumi fault zone samples were collected, as well as the corresponding lithology determined in this study. All samples collected in borehole A are siltstone. Borehole A is inclined 60° to the northwest, and sample locations and lithology within the box have been projected to the horizontal (Shingu et al., 1997). Sample MZ-1 collected from borehole 1 is a siltstone protolith sample.

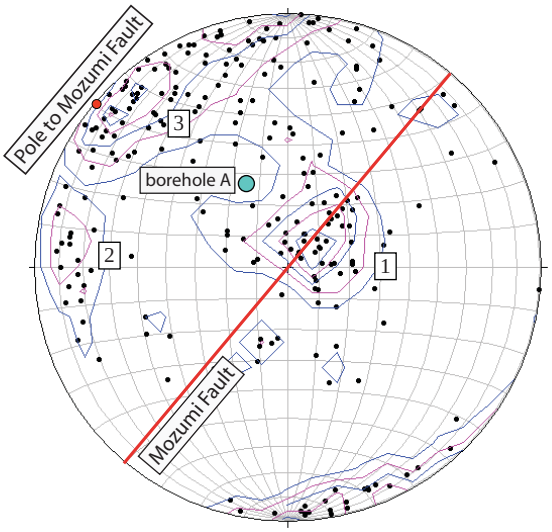

Figure 3-6. Lower hemisphere equal area stereonet of contoured poles to fracture planes recorded along borehole A of the Active Fault Survey Tunnel (Shingu et al., 1997). The orientation of borehole A and the Mozumi fault within the Active Fault Survey Tunnel are also shown for reference. Fracture set 1 has a mean orientation of 155º, 20º W. Fracture set 2 has a mean orientation of 001º, 71º E. Fracture set 3 has a mean orientation of 063º, 74º S.

Figure 3-7. Photographs of some cores samples from boreholes of the Active Fault Survey Tunnel. a) MZ-1 (protolith): sample from borehole 1 of undeformed siltstone. b) MZA-10: siltstone sample from borehole A collected from a subsidiary fault zone. c) MZA-8: siltstone sample from the Mozumi fualt zone within borehole A. The sample is wet and fault breccia and surrounding clay fabric can be seen. d) MZA-7: siltstone sample from the Mozumi fault zone in borehole A. Dry fault breccia sample with abundant clay. e) MZA-5: siltstone sample from the Mozumi fault zone within borehole A. Wet fault breccia. f) MZA-1: siltstone fault breccia from the Mozumi fault zone within borehole A.

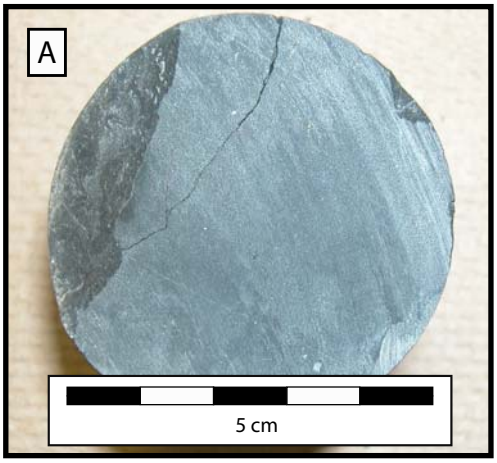

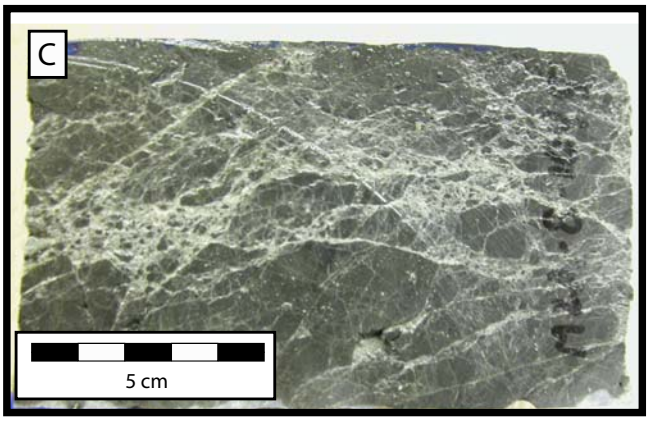

Figure 3-7 continued.

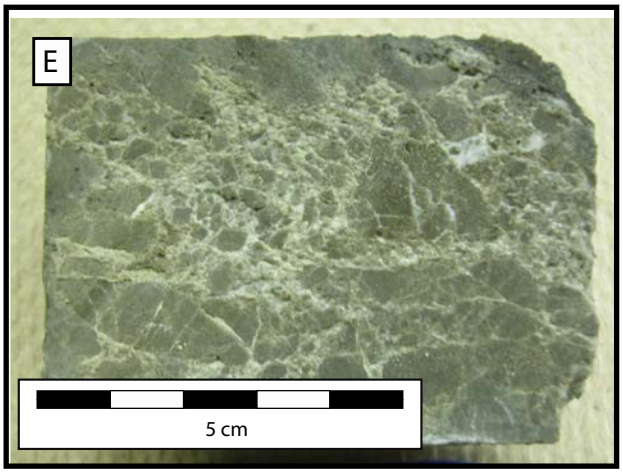

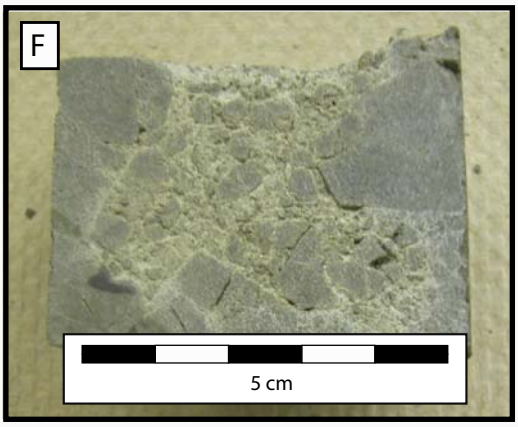

Figure 3-7 continued.

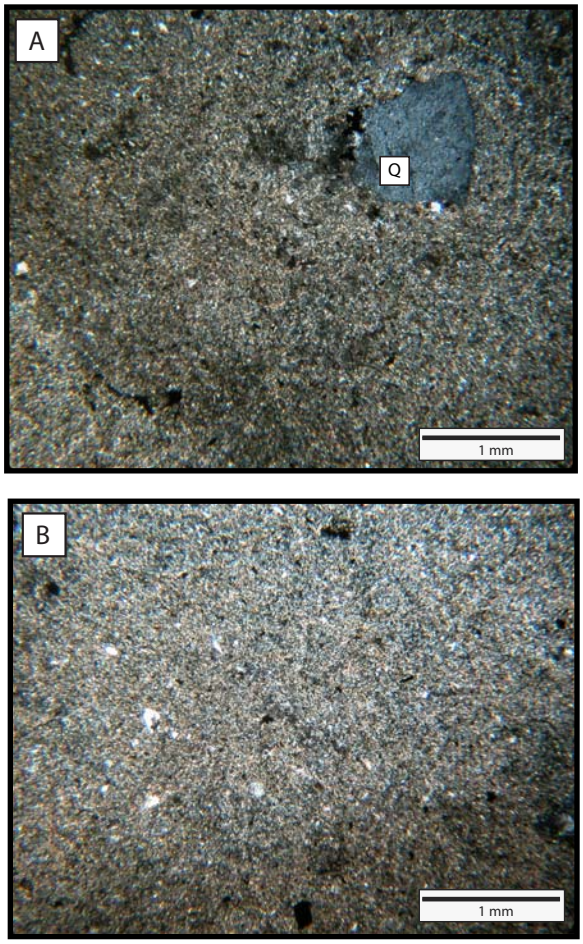

Figure 3-8. Photomicrographs of Mozumi fault zone samples and protolith. a) MZ-1: siltstone protolith. No deformation is seen in fine-grained matrix surrounding large quartz crystal. b) MZ-1: siltstone protolith. c) MZA-10: evidence for evolving fluids. d) MZA-9: plastically deformed calcite that may have been injected into surrounding rock. e) MZA-9: radial growths of epidote. f) MZA-9: zoned quartz grains with stylolites. g) MZA-8: anastomosing clay. h) MZA-2: foliated fault rocks with rotated porphyroclasts of matrix and vein material. i) MZA-7: foliated fault rocks. j) MZA-6: foliated fault rocks showing release fractures. k) MZA-5: pyrite crystals. l) MZA-1: crenulation foliation. m) MZA-1: partially open fractures with debris sheared from surrounding walls. n) MZA-1: fractures tip out into shear zones. Polarized light = a, b, c, d, e, f, g, and j. Polarized light with 530 nm plate = h and n. Plain light = i and l. Reflected light = k. Q = quartz, C = calcite.

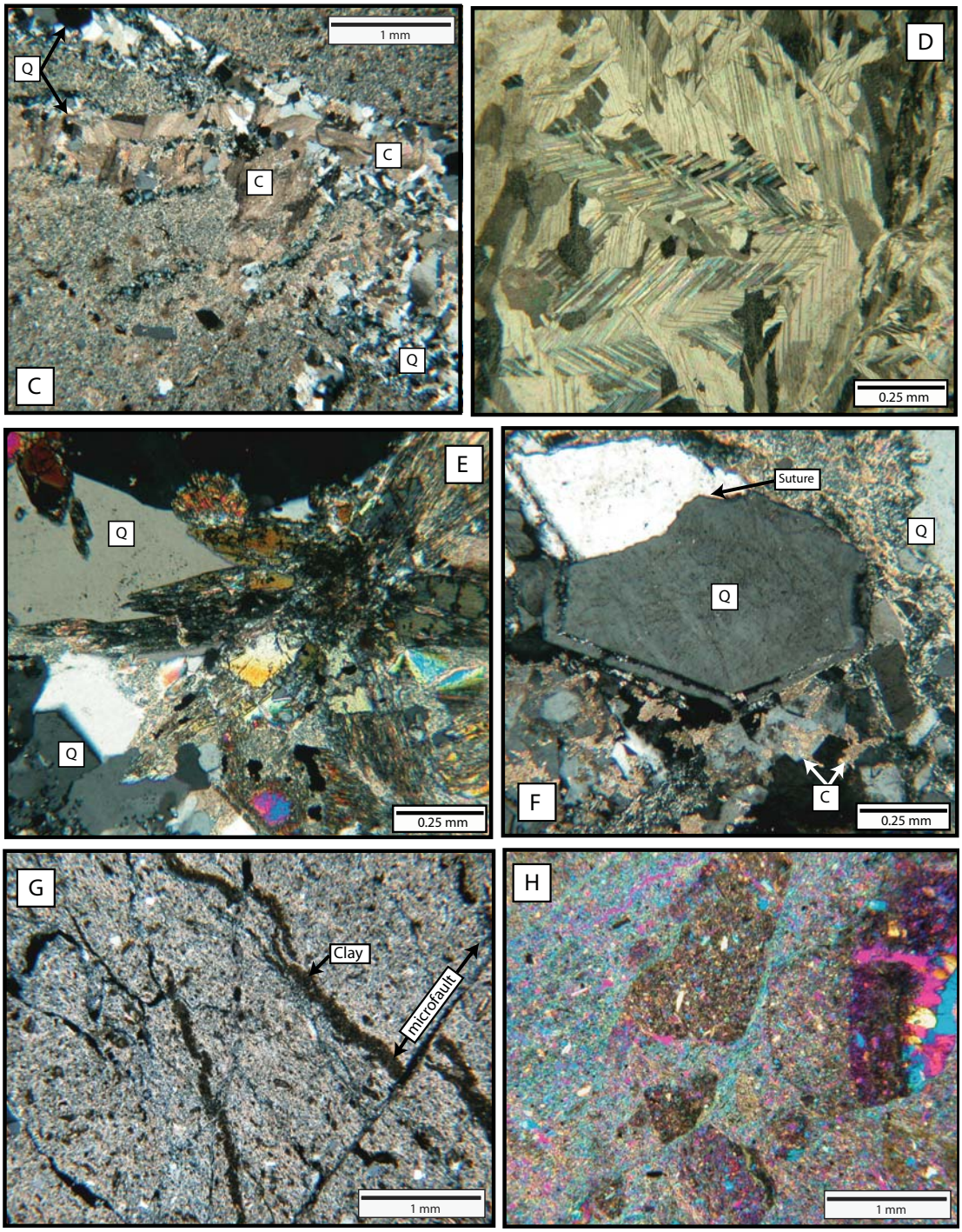

Figure 3-8 continued.

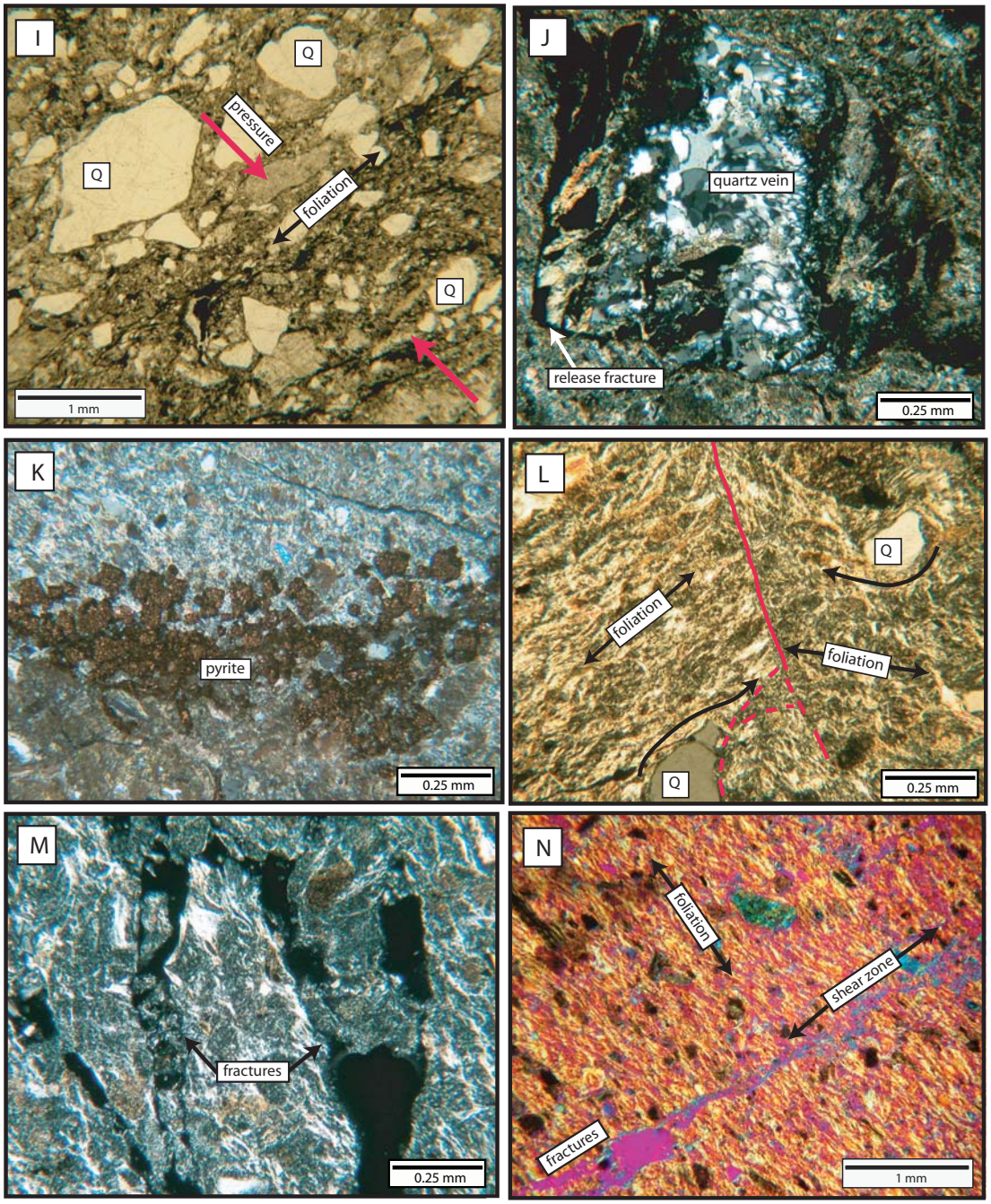

Figure 3-8 continued.

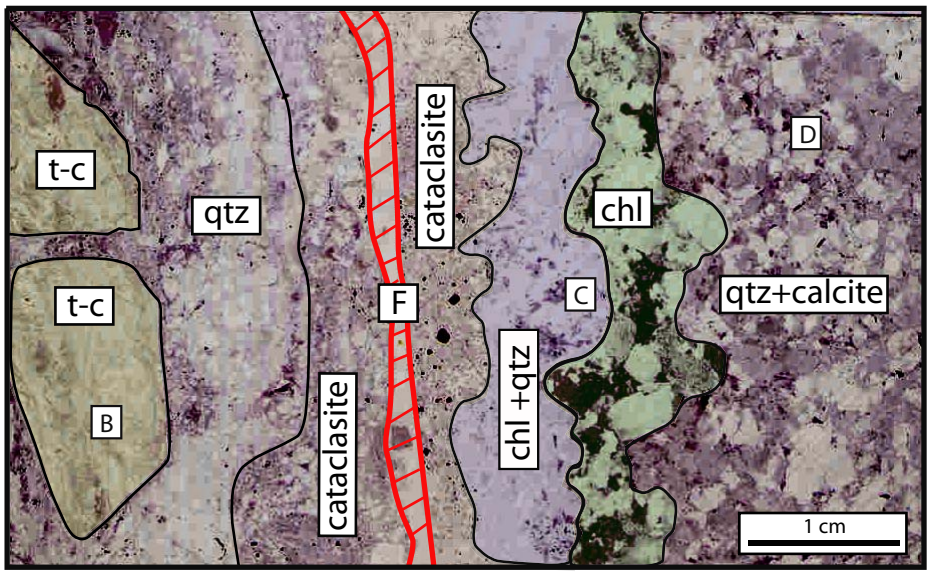

Figure 3-9. Photograph of thin section of sample MZA-9. Zones of different mineral phases have been outlined, shaded and labelled. The sections labelled t-c are purely twinned calcite. Other zones are labelled by the mineral that is dominant, however these zones are not pure. Multiple mineral phases along the fault provide evidence for fluid flow in and around the fault, and zones of twinned calcite crystals indicate fluid pressurization and injection. The locations of photomicrographs B, C, and D from Figure 3-8 are indicated. t-c = twinned calcite, qtz = quartz, chl = chlorite, F = fault.

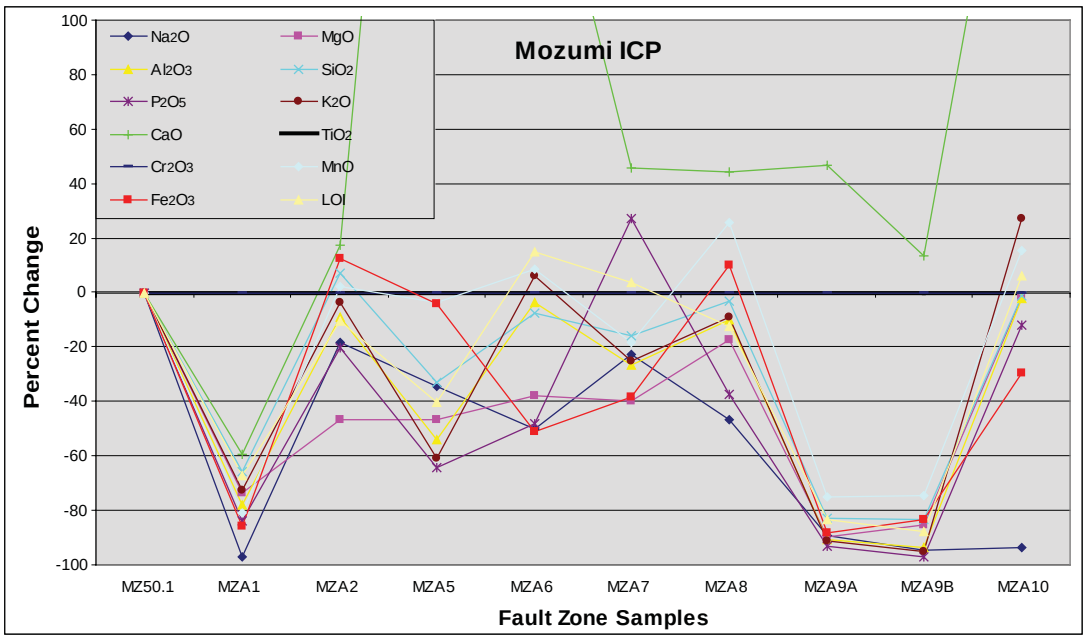

Figure 3-10. Percent changes in mobile oxides from protolith siltstone (MZ-1) in borehole 1 to fault zone rocks in borehole A of the Active Fault Survey Tunnel (Goddard and Evans, 1995). Overall, fault zone rocks are depleted in mobile oxides relative to the protolith, with the exception of CaO. Samples MZA-1 and MZA-9 are most depleted, and have under-gone very significant chemical changes relative to the protolith.

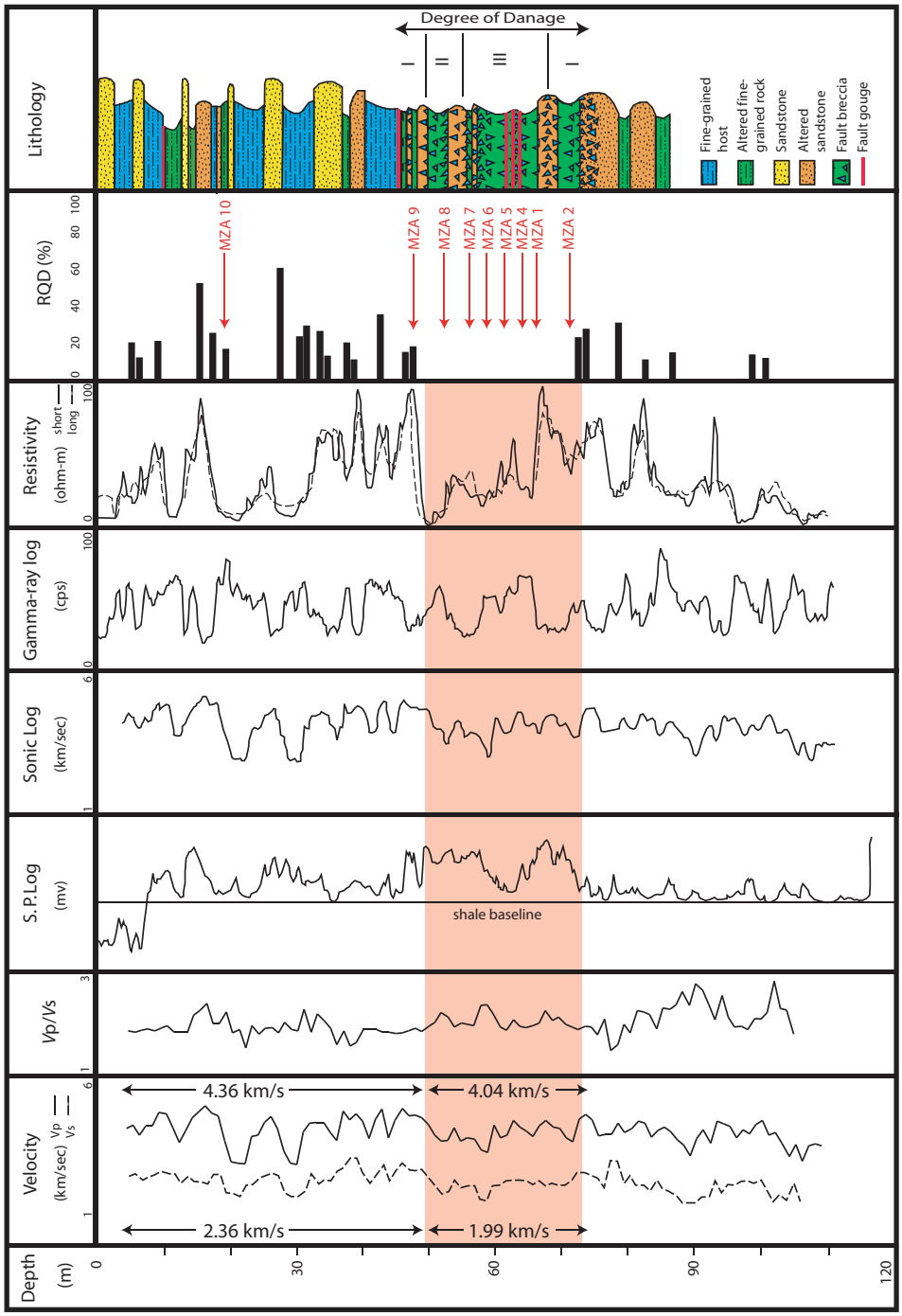

Figure 3-11. Wireline logs, sample positions, and correlated and interpreted lithology of borehole A (Shingu et al., 1997).

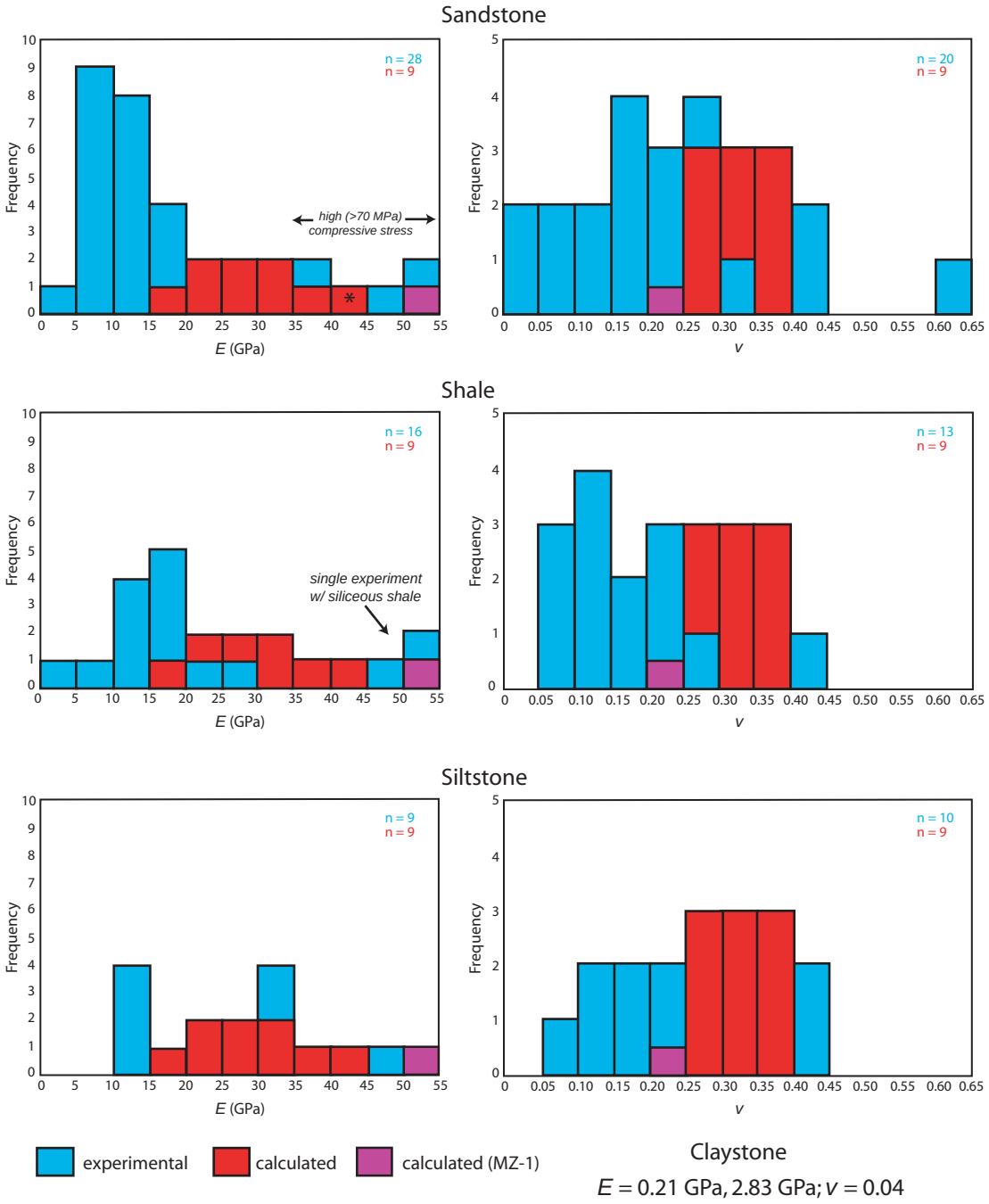

Figure 3-12. Histograms showing frequency distribution of experimentally-derived values for Young's Modulus (E) and Poisson's Ratio (v) for sandstone, shale, and siltstone, and calculated values for Mozumi fault rock samples. Data on claystone are very limited, thus values are simply listed. The calculated value for the protolith (sample MZ-1) of the Mozumi fault zone is indicated by the purple bar. The experimental data come from works referenced in Haas (1981). * = complete overlap of blue and red bars.

Figure 3-13. Representation of select properties across the Mozumi fault zone and properties of the protolith MZ-1. Stars show the location of samples used in this study. General lithology is shown at the bottom of the page with sh = shaleand ss = sandstone. Red lines indicate the locations of clay gouge. Roman numerals indicate the degree of damage as assigned by mining geologists with I having the least damage and III having the most damage. The scales for each bar graph are based on typical maximums and minimums, as well as the range of values for Mozumi fault rocks (Castagna et al., 1985), with the exception of clay amount, which is based on the values of Mozumi fault rocks and protolith so that the changes across the fault zone can be more easily observed.

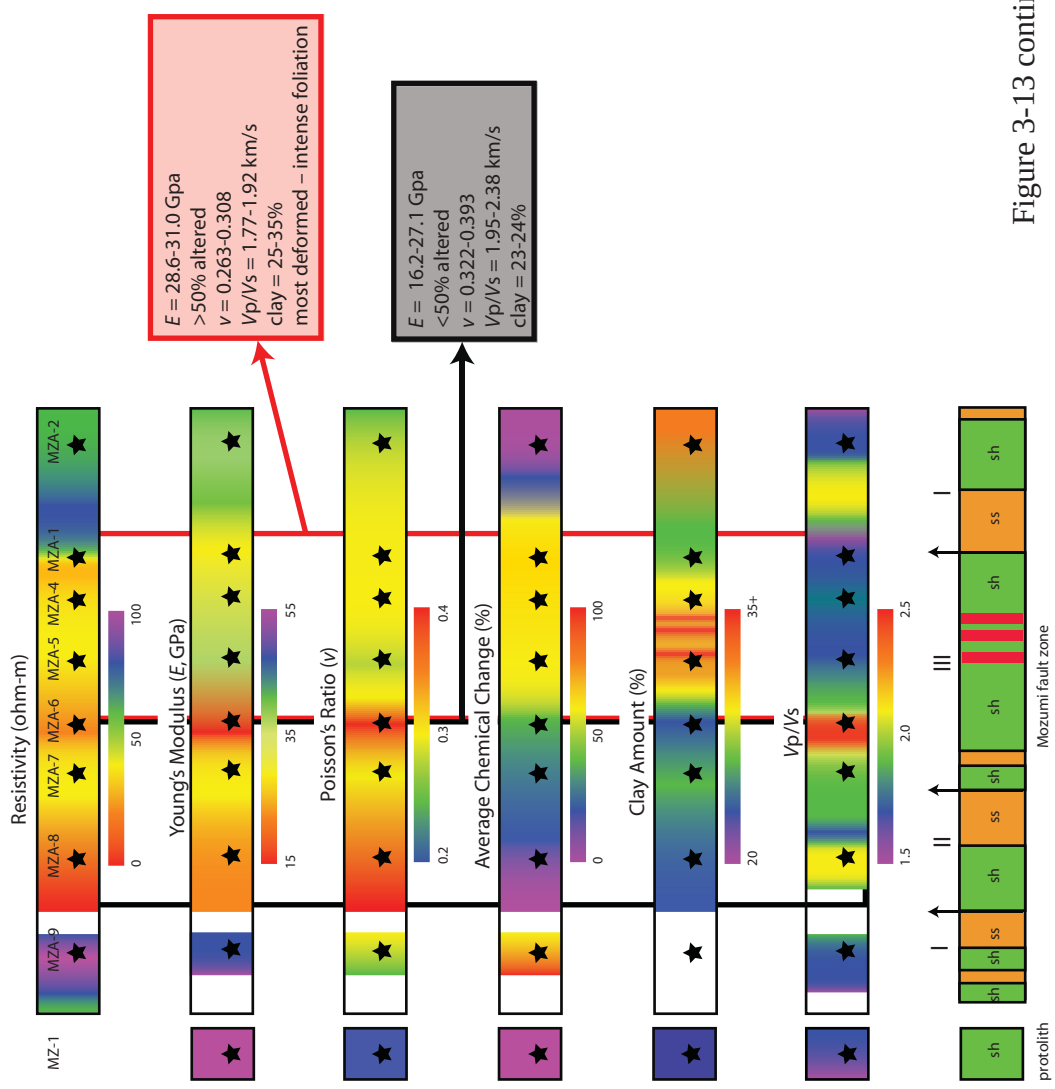

Figure 3-13 continued.

CHAPTER 4

CONCLUSIONS

The low-velocity signature and weak nature of natural faults has been attributed to fluids, clays, fractures, and other related deformation (Sibson, 1977; Li and Vidale, 1996; references therein). Fault zone properties control initiation, propagation, and termination of earthquake rupture. The data presented in this study increase our knowledge of fault zone characteristics, evolution of fault zone composition and structure, fluid flow in fault zones, and energy distribution of earthquakes in heterogeneous fault zones. For these reasons, we are motivated to explore the micro- and meso-scale physical and mechanical properties of fault zone rocks. Our characterization work can help address issues of along-strike variations in fault strength and slip properties, which may greatly affect the rupture velocity, acceleration, and displacement at a given point along the fault (Beroza, 1991; Li and Vidale, 1996; Bouchon, 1997; Spudich and Olsen, 2001). The Chelungpu fault, Taiwan, and the Mozumi fault, Japan, provide a valuable opportunity to characterize fine-grained, clay-rich fault zones.

Chapter 2 of this work presents a meso- and microstructural, mineralogical, and geochemical characterization of the exhumed and shallow portions (~1 km) of the Chelungpu Fault both along-strike and down-dip using data and samples from 6 outcrops and 3 boreholes. The variations in exhumed fault rocks in the hanging wall of the 1999 rupture were documented along an ~70 km section of the fault trace. Data from the Fengyuan and Nantou boreholes, as well as data and samples from the Taiwan Chelungpu-Fault Drilling Project (TCDP) were used in conjunction with surface data to evaluate variations in fault rock composition with depth and along-strike changes in

characteristics of fault zone components and composition of fault rocks. The major variations in the Chelungpu fault zone as discussed in Chapter 2 include:

1) The width and intensity of damage in the primary damage zone is greater, and possibly more mature for the southern section of the Chelungpu fault than the northern section. The primary damage zone of the northern Chelungpu fault is 10-30 m wide, whereas the primary damage zone of the southern Chelungpu fault is 25-70 m wide. Secondary faults are commonplace in the hanging wall of the southern Chelungpu fault (>>1 per m) and may have significant offset as indicated by fault scarps and well-developed clay gouge. Secondary faults are few in number in the northern Chelungpu fault (<<1 per 10 m), and appear to have experienced inconsequential slip.

2) The intensity and number of microstructures in fault core rocks is greater in samples from the southern Chelungpu fault field sites and drilled core than in samples from the northern field sites and drilled cores. Microscopy of southern fault core rocks shows abundant evidence for multiple deformation events including several generations of fractures, veins, microfaults, and foliations and evidence for syn-tectonic fluid flow. Microscopy of northern fault core rocks shows massive or weakly foliated fault gouge, and bordering wall rock with few deformation microstructures.

3) Smectite is present in primary fault gouge of the fault core all along the trace of the exhumed Chelungpu fault, where available. Secondary fault gouge has varied composition, including smectite-rich gouge, gouge containing moderate amounts of smectite mixed with other clays, and gouge devoid of smectite, but rich in illite. Secondary faults containing fault gouge are not found in the northern section of the

Chelungpu fault zone and multiple generations and compositions of fault gouge are confined to the southern Chelungpu fault zone.

4) Smectite is least abundant in fault gouge and most abundant in host rocks of the Fengyuan and Nantou boreholes samples from 200-1200 m depth (Liao, 2003; Lu, 2004; Hashimoto et al., *in press*; pers. comm. L.W. Kuo). A thin (~1 cm) layer of smectite gouge has been identified in the TCDP core in the immediate hanging wall of what is proposed to be the 1999 slip surface, but its nature and origin has not been determined. Other hanging wall fault gouge surrounding the smectite layer in the TCDP core is illitic (L.W. Kuo and S.R. Song, pers. comm.).

5) A systematic geochemical signature of fault zone components is better developed along the northern section of the Chelungpu fault than along the southern section, but trends are identified for each study site. The geochemical data from exhumed portions of the Chelungpu fault indicate that gouge and primary damage zone rocks are extremely depleted in CaO and enriched in SiO_2 relative to the secondary damage zone and host rocks. The CaO is also less in fault rocks from boreholes, but unlike the surface samples, SiO_2 is depleted relative to the host rock (Liao, 2003; Lu, 2004; this study).

6) The crystallinity index for clay minerals of the northern Chelungpu fault shows no significant trend. The crystallinity index for the southern Chelungpu fault shows that the exhumed fault core and primary damage zone rocks have larger crystallites than host rock with similar abundances of smectite. This indicates that the exhumed fault rocks have maintained a signature of their formation at higher P/T conditions despite weathering; presumably in relation to fault activity (Vrolijk and van der Pluijm, 1999).

Relevant differences between the northern and southern Chelungpu fault have been documented by other workers, and include:

1) Displacements from the September 21, 1999 earthquake are much larger on the northern Chelungpu fault than on the southern Chelungpu fault (Yu et al., 1999; Lin et al., 2001; Lee et al., 2002; Heermance et al., 2003).

2) High frequency ground accelerations (2-3 Hz) and fast rupture velocities (3.0 km/sec) dominated along the southern section of the Chelungpu fault during the 1999 rupture, whereas low frequency ground accelerations (<1 Hz) and slower rupture velocities (1.2 km/sec) dominated along the northern Chelungpu fault (Lin et al., 2001; Ma et al., 2001).

3) Previous work and our results show that the fault geometry and lithology juxtaposition across the fault changes along strike. In the north, the Chelungpu fault places siltstone on siltstone. In the south, the Chelungpu fault places siltstone on conglomerate in a hanging wall flat on footwall ramp geometry (Heermance, 2002; Heermance et al., 2003; this study).

4) The section of the Chelungpu fault north of Wufeng City has been active since at least ~46 ka (Heermance, 2002), whereas the section of the Chelungpu fault south of Wufeng City has been active since ~ 1 Ma and has 8-15 km of displacement (Hung and Wilschko, 1993).

We believe that the northern section of the Chelungpu fault illustrates the characteristics of a young thrust fault, and that the southern Chelungpu fault has the characteristics of a more mature fault zone. In addition, the along-strike variations in

damage intensity and composition of the Chelungpu fault may have influenced rupture style during the September 21, 1999 earthquake, and may influence future ruptures.

The depth variations in clay mineralogy that are documented in this study include more smectite at the surface and more illite at depth in the fault core, indicating that the illite-smectite reaction occurs in the Chelungpu fault zone. The reaction is likely influenced by fault activity and fluid flow, and may play an important role in the seismic to upper-aseismic transitions on the Chelungpu fault after the model proposed by Hyndman (2004) or fault gouge lithification model proposed by Marone and Saffer (*in press*) and Saffer and Marone (2003). In light of this possibility, mixed layer I-S clay needs to be documented and tested for frictional strength, as it may not have the same properties as a physical mixture of smectite and illite, and may be a major clay component of the deeper fault zone.

Chapter 3 of this work characterizes the microstructures, mineralogy and geochemistry of fault rock samples from the Mozumi fault, Japan, and combines these physical properties with data from wireline logs for a petrophysical study of the fault rocks. Elastic properties of the fault zone are also estimated. The results of this study, as well as related studies include:

1) The Mozumi fault rocks are altered and mineralized foliated fault breccias that show evidence for multiple deformation events and mechanisms, evolving fluid, and syn-tectonic fluid flow.

2) The Mozumi fault is a low velocity zone (4.04 $\pm$ 0.06 km/s and 1.99 $\pm$ 0.05 km/s) relative to wall rock in borehole A (4.36 $\pm$ 0.08 km/s and 2.36 $\pm$ 0.05 km/s) and protolith (4.75 km/s and ~3.0 km/s) as determined from wireline logs of P-wave and S-wave

velocities across the fault zone and seismic wave velocities of protolith as reported in Mizuno et al. (2004; references therein).

3) Fault rocks from the Mozumi fault zone have increased porosity (10-22%) relative to its protolith (4%; Forster et al., 2003; this study).

4) Electrical and seismic properties, elastic moduli, porosity, permeability, fault-related textures, and clay content vary across the main fault zone, and these variations have a trend that is parallel to the Mozumi fault.

5) The parameter *Q*s, a function of porosity and density, for the Mozumi fault zone is 60-90, whereas average crustal values are ~160 (Mizuno et al., 2004). These values suggest that the Mozumi fault zone rocks cause significant wave attenuation.

These data indicate that the fault rocks in the Mozumi fault make an effective sink for radiated energy in the fault zone. Fluid-rich regions of faults may not be capable of maintaining the shear stresses associated with brittle failure (Bedrosian et al., 2004). Creep on the Mozumi fault may be explained by fluid-rich pockets with corresponding low relative values of Young's modulus, high values of Poisson's ratio, low resistivity, secondary porosity and permeability, and high values of ν_p/ν_s (Forster et al., 2003; this study).

In addition to providing data concerning the characteristics of fault zones, this study documents the complex, heterogeneous nature of active fault zones. Clay mineralogy and deformation of the Chelungpu fault are extremely variable along-strike and with depth. These observations resemble those of the Mozumi fault zone, where, within the Mozumi fault zone, clay content and type vary between fault breccia samples, and lozenges of fluid-rich fault rocks are present throughout the crush zone. Some

smectite-rich fault breccias in the Mozumi fault were sampled, and indicate fluid-rock interactions, as the protolith is illite-shale. Some of the rocks (MZA-1, MZA-2, MZA-9) containing smectite clay were sampled from regions that presently have low to intermediate fluid content, suggesting that fluid pockets may move along the fault. Smectite in the Chelungpu fault may also be a result of dynamic syn-tectonic fluid flow. Pockets of fluid-rich rock may change both spatially and temporally, and thus illite-smectite and similar reactions may occur in zones throughout the fault at different times, resulting in a gradual change in the behavior of the fault. Elastic properties and responses to electrical resistivity and seismic waves also occur in pockets and distributed across the Mozumi fault zone. This is marked by an offset of fluid-rich rocks with lower values of E (16.2-27.1 Gpa) and higher values of ν (0.322-0.393) from fault breccias that have higher values of E (28.6-44.9 Gpa), lowest to intermediate values of ν (0.263-0.308), and are more altered and contain more clay and intense microstructural deformation; further indication of migrating fluid pockets and resulting alteration.

Seismological studies of trapped and fault-zone-guided waves in fault zones are used to image fault zones with a resolution of several tens of meters (Mamada et al., 2002; references therein), and this study addresses fault zone variations at that scale, and at finer scales that can not be resolved using trapped waves. Integrating seismic models with the physical characteristics of fault zones is very valuable. This study shows that several samples or one study site can not possibly describe an entire fault zone as they are highly heterogeneous. Also, surface samples can not completely describe the fault zone at depth because the composition of fault rocks can change significantly, so care must be

used when studying exhumed fault zones. And finally, active fault zones are temporally dynamic and spatially heterogeneous.

References

Bedrosian, P.A., M.J. Unsworth, G.D. Egbert, and C.H. Thurber (2004). Geophysical images of the creeping segment of the San Andreas Fault; implications for the role of crustal fluids in the earthquake process, *Tectonophysics* **385**, 137-158.

Beroza, G.C. (1991). Near-source modeling of the Loma Prieta earthquake: evidence for heterogeneous slip and implications for earthquake hazard, *Bull. Seism. Soc. Am.* **81**, 1603-1621.

Bouchon, M. (1997) The state of stress on some faults of the San Andreas system as inferred from near-field strong motion data. *J. Geophys. Res.* **B102**, 11731-11744.

Forster, C.B., J.P. Evans, K. Wantanabe, H. Tanaka, R. Jeffreys, and T. Nohara (2003). Hydrological properties and structure of the Mozumi Fault, central Japan, *Geophys. Res. Lett*. **30**, doi: 10.1029/2002GL014904.

Hashimoto, Y., K. Ujiie, A. Sakaguchi, and H. Tanaka (*in press*). Characteristics and implication of clay minerals in the northern and southern Chelung-pu fault, Taiwan, *Tectonophysics*.

Heermance, R.V. (2002). Geometry and physical properties of the Chelungpu Fault, Taiwan, and their effect on fault rupture, *Master's Thesis*, Utah State University, Logan, Utah.

Heermance, R.V., Z.K. Shipton, and J.P. Evans (2003). Fault structure control on fault slip and ground motion during the 1999 rupture of the Chelungpu fault, Taiwan, *Bull. Seism. Soc. Am*. **93**, 1034-1050.

Hung, J.H., and D.V. Wiltschko (1993). Structure and kinematics of arcuate thrust faults in the Mioli-Cholan area of western Taiwan, *Petrol. Geol. Taiwan* **28**, 59-96.

Hyndman, R.D. (2004). Controls on subduction thrust earthquakes: downdip changes in composition and state, in *Rheology and Deformation of the Lithosphere at Continental Margins,* G.D. Karner, B. Taylor, N.W. Driscoll, and D.L. Kohlstedt (Editors), Columbia University Press, New York, New York, 166-178.

Lee, J.C., H.T., Chu, J. Angelier, Y.C. Chan, J C. Hu, C.Y. Lu, and R.J. Rau (2002). Geometry and structure of northern surface ruptures of the 1999 Mw=7.6 Chi-Chi, Taiwan, earthquake: influence from inherited fold belt structures, *J. Struc. Geol*. **24**, 173-192.

Liao, C.F. (2003). Analysis of fault rock deformation and clay minerals from fault cores of Chelungpu fault zone, *Master's Thesis* (in Chinese with English Summary), National Taiwan University, Taipei, Taiwan.

Li, Y.G., and J.E Vidale (1996). Low-velocity fault-zone guided waves: Numerical investigations of trapping efficiency, *Bull. Seism. Soc. Am.* **86**, 371-378.

Lin, A., T. Ouchi, A. Chen, and T. Maruyama (2001). Co-seismic displacements, folding and shortening structures along the Chelungpu surface rupture zone occurred during the 1999 Chi-Chi (Taiwan) earthquake, *Tectonophysics* **330**, 225-244.

Lu, C.B. (2004). Fluid infiltration after seismic faulting: examining chemical and mineralogical composition of the fault rocks in the drilling cores from Nantou well of the Chelungpu fault, *Master's Thesis* (in Chinese with English summary), National Central University, Jhongli, Taiwan.

Ma, K.F., J. Mori, S.J. Lee, and S.B. Yu (2001). Spatial and temporal distribution of slip for the 1999 Chi-Chi, Taiwan, Earthquake, *Bull. Seism. Soc. Am.* **91**, 1069-1087.

Mamada, Y., Y. Kuwahara, H. Ito, and H. Takenaka (2002). Discontinuity of the Mozumi-Sukenobu fault low-velocity zone, central Japan, inferred from 3-D finite-difference simulation of fault zone waves excited by explosive sources, *Tectonophysics* **378**, 209-222.

Marone, C., and D.M. Saffer (*in press*). Fault friction and the upper transition from seismic to aseismic faulting, in *The Seismogenic Zone of Subduction Thrust Faults*, T.H. Dixon, J.C. Moore, and R.D. Hyndman (Editors), Columbia University Press, New York, New York.

Mizuno, T., K. Nishigama, H. Ito, and Y. Kuwahara (2004). Deep structure of the Mozumi-Sukenobu fault, central Japan, estimated from the subsurface array observation of fault zone trapped waves, *Geophys. J. Int.* **159**, 622-642.

Saffer, D.M., and C. Marone (2003). Comparison of smectite- and illite-rich gouge frictional properties; application to the updip limit of the seismogenic zone along subduction megathrusts, *Earth Plan. Sci. Lett.* **215**, 219-235.

Sibson, R.H. (1977). Fault rocks and fault mechanisms, *J. Geol. Soc. Lond.* **133**, 191-213.

Spudich, P., and K.B. Olsen (2001). Fault zone amplified waves as a possible seismic hazard along the Calaveras fault in central California, *Geophys. Res. Lett.* **28**, 2533-2536.

Vrolijk, P. J., and B. A. van der Pluijm (1999). Clay Gouge, *J. Struc. Geol*. **21**, 1039-1048.

Yu, S.B., L.C. Kuo, Y.J. Hsu, C.S. Huo, C.C. Liu, H.H. Su, J.F. Lee, and T.C. Lai (1999). Coseismic and postseismic deformations associated with the 1999 Chi-Chi earthquake, *Nat. Sci. Newslett.* **11**, 156-161.

APPENDICES

APPENDIX A

ABBREVIATED FIELD SITE DESCRIPTIONS AND TRANSECT DETAILS

Following are abbreviated field notes listed by site including outcrop descriptions and details of transects. The locality and Taiwan grid UTM coordinates for each field site are listed. The bearing of the transect line is listed, as well as orientations of bedding, faults, fractures, and fault gouge listed in azimuth, dip, and dip direction. The locations along the transect line of orientation measurements are also listed. Structural samples that were collected for optical microscopy are listed.

Site 1, Tachia River, 224823 E 2686232 N

Hanging wall transect at site 1, northern Chelungpu fault

Transect bearing: 140^{o}

Samples were collected for laboratory analysis at 5 meter intervals from 0 to 30 meters along the line of transect. Additional structural samples were collected.

0 m
Fault scarp that creates a waterfall in the river (Figure A-1, Figure A-2)

```
050 40 SE     0.0 m
```

0-17 m
The first ~17 meters of Chinshui Shale in the hanging wall has an increased fracture density and a brecciated zone 20+ cm wide. Structural sample PDZ 0+1 was collected along a secondary fault.
Bedding orientations:

```
035 54 SE     1.0 m     042 45 SE    3.0 m
040 40 SE     6.0 m     060 45 SE    8.0 m
050 47 SE    10.0 m     042 46 SE   12.0 m
035 47 SE    13.0 m
```

Secondary faults:

```
050 40 SE     0.0 m
017 57 SE     1.0 m  PDZ 0+1
```

17-50 m
Chinshui Shale containing two dominant fracture sets and several bedding-parallel secondary faults. Structural samples were collected from secondary faults; SDZ 0+25.
Bedding orientations:

051 55 SE 18.3 m	042 48 SE 26.0 m	046 45 SE 32.0 m
040 40 SE 34.6 m	047 56 SE 39.5 m	051 50 SE 44.1 m
042 46 SE	044 74 SE	050 51 SE
050 52 SE	035 34 SE	050 47 SE
060 45 SE	060 45 SE	040 40 SE
050 40 SE		

Secondary faults:	*Fractures:*	
025 59 SE 25.0 m	024 51 SE	022 46 SE
042 49 SE	020 40 SE	070 45 S
	084 45 S	024 36 SE
	068 45 SE	

Site 3, Pu Tze River, 223036 E 2672882 N

Hanging wall transect at site 3, northern/transition Chelungpu fault (Figure A-3, Figure A-4)

Transect bearing: 260^{o}

Samples were collected for laboratory analysis along the transect at 5 m intervals, with increased density near the fault and within the fault gouge.

0m
Fault contact of altered and highly fractured siltstone on Quaternary gravel. Black cataclasite is present within 40-60 cm thick orange fault gouge. Samples FC 0+0 were collected (37-1 through 37-6).
Orientation of main fault*:*
040 35 SE 0.0 m

0-10m
Zone of dense fractures and little to no relict bedding near the fault. This zone has been altered and leached, and is a yellow color.

~10-20m
Folded bedding becomes obvious, but the folds are not oriented as expected. First set of folds (A; Figure A-5).
Bedding orientations:

267 56 N 3.5 m	266 69 N 4.0 m	264 81 N 6.0 m
262 68 N 8.0 m	264 55 N 9.0 m	067 85 S 9.2 m
294 49 N 9.3 m	265 90 N 10.0 m	264 87 N 12.0 m
070 87 S	080 66 S 14.0 m	078 69 S 17.0 m
078 69 S		

~27-43m
Second fold (B; Figure A-5). Bedding is indistinct in the core of the fold.
Bedding orientations:

078 69 S	17.0 m	066 69 S	23.0 m	074 83 S	26.0 m
078 90 S	26.5 m	283 64 N	31.0 m	310 77 N	33.0 m
296 73 N	36.5 m	295 70 N	37.0 m	300 74 N	38.0 m
297 71 N	40.0 m	290 86 N	42.3 m		

~30-51m
Possible weak gouge developed at 41 m. Third fold (C; Figure A-5).
Bedding orientations:

283 64 N	31.0 m	310 77 NE	33.0 m	293 64 N	34.0 m
296 73 N	36.5 m	295 70 N	37.0 m	300 74 NE	38.0 m
297 71 N	40.0 m	290 86 N	42.3 m	100 76 S	47.5 m
095 78 s	49.0 m	090 81 S	51.0 m		

51-55.5m
Cover.

55.5-76m
Complex, tight folds cut by a subsidiary fault. Bedding at 62.5 m is overturned.
Orientation of subsidiary fault:

040 68 SE	68.0 m

Orientation of bedding:
fourth fold (D; Figure A-5):

300 73 NE	58.0 m	302 70 NE	59.5 m	315 69 NE	59.5 m
341 51 NE	59.5 m	330 66 NE	61.0 m	340 70 NE	62.0 m
024 64 SE	62.5 m				

fifth fold (E; Figure A-5):

340 70 NE	62.0 m	024 64 SE	62.5 m	055 53 SE	62.5 m

sixth fold (F; Figure A-5):

037 56 SE	70.0 m	041 63 SE	70.0 m	009 47 E	70.0 m
335 65 NE	69.5 m	054 64 SE	71.5 m	053 63 SE	73.0 m
350 35 W					

~76-91m
Between ~75-80m there are possible three small subsidiary thrust faults with tight folds in the immediate hanging wall. Seventh major fold (G; Figure A-5).
Orientation of bedding:

066 76 SE	82.0 m	059 59 SE	85.0 m	085 85 S	87.0 m
319 56 NE	88.0 m	315 57 NE	90.0 m	335 06 NE	91.0 m

~88-97.5m
Eighth fold (H; Figure A-5).
Orientation of bedding:

319 56 NE	88.0 m	315 57 NE	90.0 m	335 56 NE	91.0 m
308 57 NE	92.0 m	030 75 SE	95.0 m	027 70 SE	97.5 m

~95-114m
Zone of complex structures including the ninth major fold (I; Figure A-5). At ~98 m there is a small normal fault. From 102-107 m – there are ~4 very tight synthetic, faulted folds within the core and west limb of the ninth major fold. A secondary thrust fault is present at ~102m, an oblique fault is perpendicular to and cut by the secondary fault, and 1 or 2 small normal faults are present just west of the secondary thrust. Bedding is overturned from ~96-103 m.
Orientation of secondary thrust fault:
`065 subvertical  102.0 m`

Orientation of bedding:

030 75 SE 95.0 m	030 75 SE	027 70 SE 97.5 m
285 57 N 106.5 m	316 47 NE 113.0 m	327 47 NE 113.0 m

Site 4, N Branch of Wu River, 218125 E 2656546 N

Hanging wall transect at site 4, southern Chelungpu fault (Figure A-6)

Transect bearing: 290-310^{o}

Samples were collected for laboratory analysis along the transect at 5 m intervals, with increased density in areas of interest.

0 m
Orange/yellow siltstone on gravel contact – exact position of the fault is in question – could be either here or in a slumped gully filled with trash and waste (I didn't dig around in it to find out). This particular exposure MAY be a slumped block, but parts of the outcrop are continuous down-dip with in-place siltstone. The gully is within a few meters of this contact, so the fault is well constrained. The very weathered siltstone is clay rich and saturated – no textures were observed, but the siltstone here definitely has different properties than the neighboring siltstone. Possibly the main fault gouge.
Orientation of main fault*:*
`040 25 SE  0.0 m`

0-5 m
Yellow leaching pattern following dense fracture and vein network.

5-22 m
Highly fractured shale partially covered in mud drape – bedding can not be identified. Fractures have divided the siltstone into small (cm's) broken blocks, and shear bands are present throughout. No obvious clay gouge.

22 m
Bedding becomes discernible – rock is still highly fractured, but wavy lamination and bedding are obvious.

22-33 m
Bedding orientation:
029 37 SE 28.9 m

Fault gouge orientations:
020 40 E 30.0 m 019 33 E 30.0 m FG 0+30

33-47 m
Shale with thin sandstone beds ~1-5 inches thick with ½ m to 1 m spacing. The sandstone is very fine-grained, silty sandstone. Subsidiary faults show small offset but the fault planes could not be measured, only bearings (Figure A-7).
Bedding orientations:
045 42 SE 33.0 m 045 49 SE 38.3 m 075 49 SE 41.3 m
060 50 SE 44.8 m 060 54 SE 45.0 m

Fault gouge orientation:
095 31 S 46.0 m FG 0+46

Subsidiary fault bearings:
260 39-46 m 035-040 46.0 m

47 m
First thick (½ m) sandstone bed. The bedding here abruptly changes from E-dipping to W-dipping, and then back to E -dipping. Subsidiary faults can be seen on either side.
Bedding orientation:
040 69 NW 47.0 m

47-57 m
Bedding continues to dip E; gouge and bedding-parallel secondary faults are present throughout.
Bedding orientations:
060 56 SE 49.0 m 070 55 SE 49.1 m 070 55 SE 52.2 m

Fault gouge orientation:
060 50 SE 53.5 m FG 0+53.5

57-70 m
Bedding continues to dip E, Shale/siltstone now has fine-grained sandstone-filled vertical burrows (Figure A-8).
Bedding orientation:
059 45 SE 58.5 m 071 44 SE 67.0 m

70-77 m
Cover.

77 m
Two subsidiary faults: one is parallel to bedding, one trends ~ 300^{o} (at a high angle to the main fault).

77-83 m
Sandstone-filled burrows continue, and gradually disappear (Figure A-8).
Bedding orientation:
035 44 SE 78.0 m

83-110 m
Highly fractured siltstone with numerous secondary faults or large fractures with bearings parallel or sub-parallel to the transect line. Bedding becomes hard to distinguish.

110-120 m
Sandstone-filled burrows present; bedding is obvious again.

120-130 m
Bedded shale; burrows disappear.
Orientation of bedding:
063 62 SE 128.0 m

130-171m
Folded shale and sandstone (Figure A-9). The large fold contains synthetic faults and folds (Figure A-10), as well as clay gouge along the fold limbs. The sandstone bodies have small shale beds within, and gouge is commonly present along contacts between sandstone and thin shale beds. 130-134.5 m is predominantly sandstone. 134.5-136 m is shale (the thickness of the shale increases up the outcrop). 136-150 m is predominantly sandstone. 150-165m is shale. 165-171 is sandstone.
Orientations of folded bedding:

242 60 NW	134.8 m	050 67 SE	135.0 m	060 90	135.0 m
045 60 S	135.0 m	243 70 NW	135.5 m	030 46 SE	136.0 m
045 25 SE	138.0 m	250 70 NW	143.0 m	260 58 N	146.0 m
235 76 NW		040 60 SE	164.0 m	044 80 SE	164.0 m
040 60 SE	164.0 m	054 80 SE			

Orientations of gouge in fold limbs:

067 34 SE	134.8 m	030 46 SE		045 60 SE	
050 67 SE	135.0 m	045 60 SE	135.0 m	098 63 S	135.2 m
243 70 NW	135.5 m	235 76 NW		250 70 NW	143.0 m
260 58 N	146.0 m				

FG 0+135, FG 0+143, FG 0+146

171-240m
East-dipping shale until ~215m. Alternating sandstone and shale.
Wavelength of folds increases away from the fault. Clay gouge found at ~240 m.

Field Site 5, Dong Pu Ruey River, 219604 E 2631775 N

Hanging wall transect at site 5 through a portion of the primary damage zone, southern Chelungpu fault.

The 1999 rupture at site 5 cuts across the Dong Pu Ruey River here, and then follows the river to the north and south (Figure A-11). Recent construction at this site has excavated part of the primary damage zone in the hanging wall.

Shear fabric, clay gouge, and slip surfaces are present throughout the outcrop. Bedrock is typically leached in zones that follow fractures, secondary faults, and clay gouge, and at the contact with overlying gravel (Figure A-12). Bedding could not be identified.

Field Site 6, Chin-sui River, 214402 E 2616438 N

Hanging wall transect at site 6, southern Chelungpu fault (Figure A-13)

Transect bearing: 140^{o}

Orientation of main fault:
030 80 SE 0.0 m

1.5 m
Black, extremely sticky gouge found in numerous, sub-vertical strands.
Orientation of discontinuous bedding:
045 71 SE 1.5 m

4-7 m
Brecciated zone – no clear textures; dark gray/black angular shale or siltstone clasts in sandstone matrix.

9 m
Gouge following disrupted bedding
Gouge orientations:
026 64 SE 9.0 m 032 45 SE 9.0 m 025 39 SE 9.0 m

10 m
Zone of black, very sticky clay gouge; found in anastomosing strands, but has a general orientation.
Gouge zone orientation:
050 56 SE 10.0 m FG 0+10

Fault orientations:
023 75 NW 10.0 m 045 76 SE 10.0 m

12-21 m
Cover.

23 m
Bedding is difficult to identify – some possible sedimentary structures.
Secondary fault orientation:
058 82 SE 23.0 m

28 m
Strands of gouge following folded 2 cm thick sandstone bed.
General orientation of anastomosing gouge:
043 56 SE 28.0 m

31 m
Brecciated sandstone bed is surrounded by shale or siltstone with lots of anastomosing gouge; some gouge has brecciated sandstone clasts within. White or gray sandstone is poorly cemented; fine-grained, compositionally immature: quartz and black lithics (wacke); quartz grains are well-rounded.
Gouge orientations:
060 90 31.0 m 061 90 31.0 m

35-36 m
Numerous secondary faults – these are some of the more easily identified fault planes.
Fault orientations:
045 74 NW (rake: 84)
057 82 SE (rake: 22)
000 61 W (rake: 19)
056 87 SE (rake: 24)
347 62 SW (rake: 01)

37-46 m
Anastomosing gouge throughout; 2 or 3 sets of slicken lines - very numerous. Fault gouge at 37 m is a 9 cm-thick black gouge zone, very soft and foliated – orientation is curviplanar and approaches vertical upwards.
Fault gouge orientations:
212 60 SE 37.0 m FG 0+37 (112-3)
045 75 NW 41.0 m with curving slicken lines

47 m
Siltstone/mudstone is better consolidated, but still highly fractured; gouge seems less developed, and is thinner, lighter gray, and harder to distinguish from the surrounding wall rock.
Approximate gouge orientation:
049 50 NW 47.0 m

47-59 m
Faults with slicken lines throughout; less clay gouge, increased slicken lines; rock is more fractured – possibly a lithology change.
Fault orientations:
036 83 NW
011 89 W (rake: 50)
061 54 SE
010 75 W (rake: 04)

58 m
No gouge.
Fault orientations:
039 90 (rake: 74 and 03 @ 20 cm below on the same plane)

047 68 NW (rake: 77)
044 83 NW

59-64 m
Some gouge and shear fabric, but mostly highly fractured siltstone or mudstone.

64 m
Intense gouge zone; 19 cm thick gouge and 12 cm wide secondary gouge zone ~6 cm from main gouge zone. Gouge has a green-gold sheen and is very dark and sticky.
Gouge orientation:
035 80 SE 64.0 m FG 0+64 (112-1, 112-2 and 112-6)

69 m
Bedding becomes easy to define; planar laminated sandstone interbedded with mudstone or siltstone.

Bedding orientations:
053 70 SE 059 81 SE
060 76 SE 055 81 SE

69-78 m
Cover.

78-83 m
Distorted bedding – interbedded sandstone and siltstone; numerous fractures but no obvious faults.

83 m
Sticky black gouge in white, altered, poorly consolidated sandstone – sandstone is the same as seen previously, but is more disrupted – looks like hydrothermal alteration.
SDZ 0+70 (112-8), SDZ 0+83 (112-9)

83-90 m
Intensely foliated shale, brecciated in places. Discontinuous sandstone bed ~1/2 m thick in contact with secondary fault.
Fault orientation:
064 66 NW 80.0 m (rake: 00)

Bedding orientations:
064 66 NW 80.0 m

90-95 m
Cover.

95-125 m
Siltstone with this, mostly discontinuous sandstone beds. By ~100 m, the bedding is getting more continuous and less deformed. At least 4 secondary faults are identified; 2 appear to have sandstone slivers caught up in them.

Fault orientations:
030 85 SE 105.0 m
052 67 SE 110.0 m

Bedding orientations:
060 87 SE 113.0 m 042 75 SE 115.0 m 005 25 E 116.0 m
005 70 E 118.0 m 240 35 NW 120.0 m 355 45 E 120.0 m

125-140 m
Cover (grass) at the base of the outcrop, but bedding is exposed above. Sandstone and shale are bioturbated in places.
Bedding orientations:
050 61 SE 125.0 m 075 74 SE 127.0 m 070 44 SE 129.0 m
066 50 SE 131.0 m

140-160 m
Interbedded shale and sandstone. Beds are folded into a tight fold pair. Beds at ~140 m are overturned at the base of the outcrop. 135-145 m contains a lot of sandstone beds. 145-160 m has 5-10 cm-thick bed of alternating shale and sandstone.
Bedding orientations:
070 44 SE 129.0 m 066 50 SE 131.0 m 320 04 SW 135.0 m
090 70 N 139.0 m 250 67 NW 140.0 m 070 84 SE 145.0 m
070 87 SE 149.0 m 060 89 SE 151.0 m

160-180 m
Cover.

180 m
Secondary fault with 4 cm-thick sheared clay gouge, bedding parallel and steeply dipping.

180-190 m
Cover.

190-250 m
Sandstone is more abundant. The outcrop is divided into fault blocks. Bedding at ~196 m is overturned. There is a lot of cover on the upper part of the outcrop from ~240-250 m. A major fault and associated fault gouge are present at ~240 m. The anastomosing gouge zone is 20-30 cm-thick with white, brecciated sandstone clasts and striations. Within the gouge is a a 3-5 cm-thick section of black clay gouge. The fault is identified in the upper sections of the outcrop, and offsets terrace gravels. A fault scarp of ~3 m is present, and large boulders are present in the footwall of the scarp. The immediate bedrock of the footwall is relatively undeformed. Drag folds are present in the hanging wall.
Fault orientation:
053 85 NW 240.0 m

Bedding orientations:
055 90 190.0 m 055 90 191.0 m 070 88 SE 196.0 m

```
047 85 SE  200.0 m      057 68 SE  201.0 m      055 63 SE  201.5 m
030 48 SE  225.0 m      042 58 SE  225.0 m      025 55 SE  235.0 m
040 46 SE  239.0 m      020 39 SE  250.0 m
```

250-300 m

Bedding dips change significantly across fault 50, with dips consistently more shallow.

Bedding orientations:

```
080 30 S   251.0 m      010 30 E   253.0 m      040 34 SE  265.0 m
340 30 NE  275.0 m      314 30 NE  300.0 m      300 50 NE  300+  m
```

References

September 21 Earthquake Geology Research, Econ. Dept., Geol. Res. Dept., Taiwan, 2001.

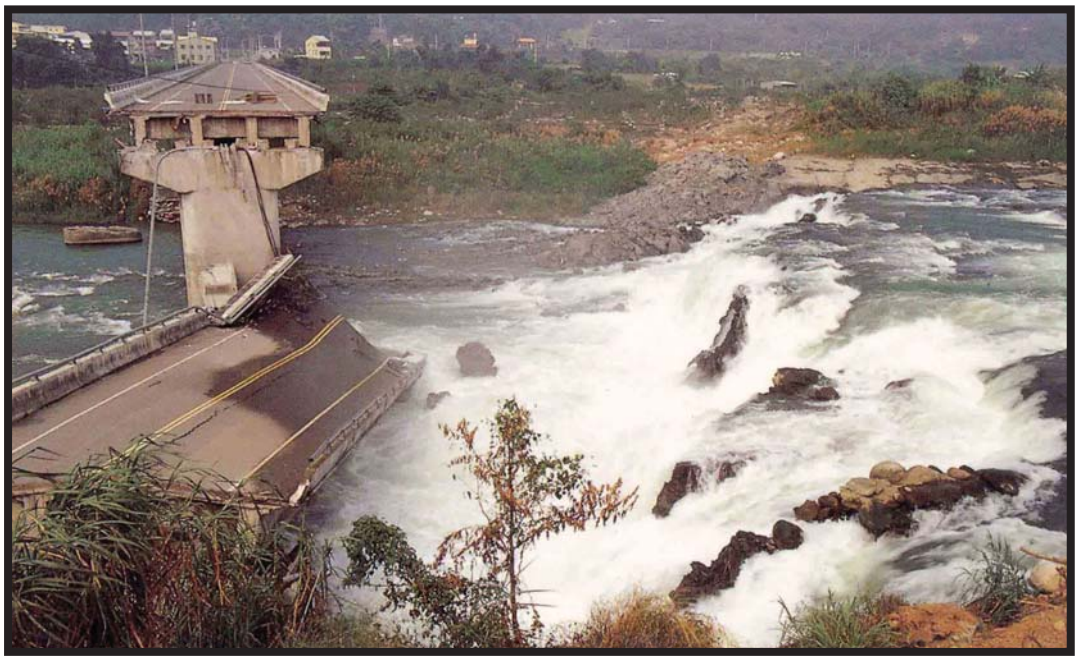

Figure A-1. Looking north at the 11.5-m high scarp (11.5 m) at the Tachia River, 1999 (September 21 Earthquake Geology Research).

Figure A-2. Looking north at the fault scarp at the Tachia River, 2002.

Figure A-3. Damage near the Pu Tze River, 1999 (September 21 Earthquake Geology Research).

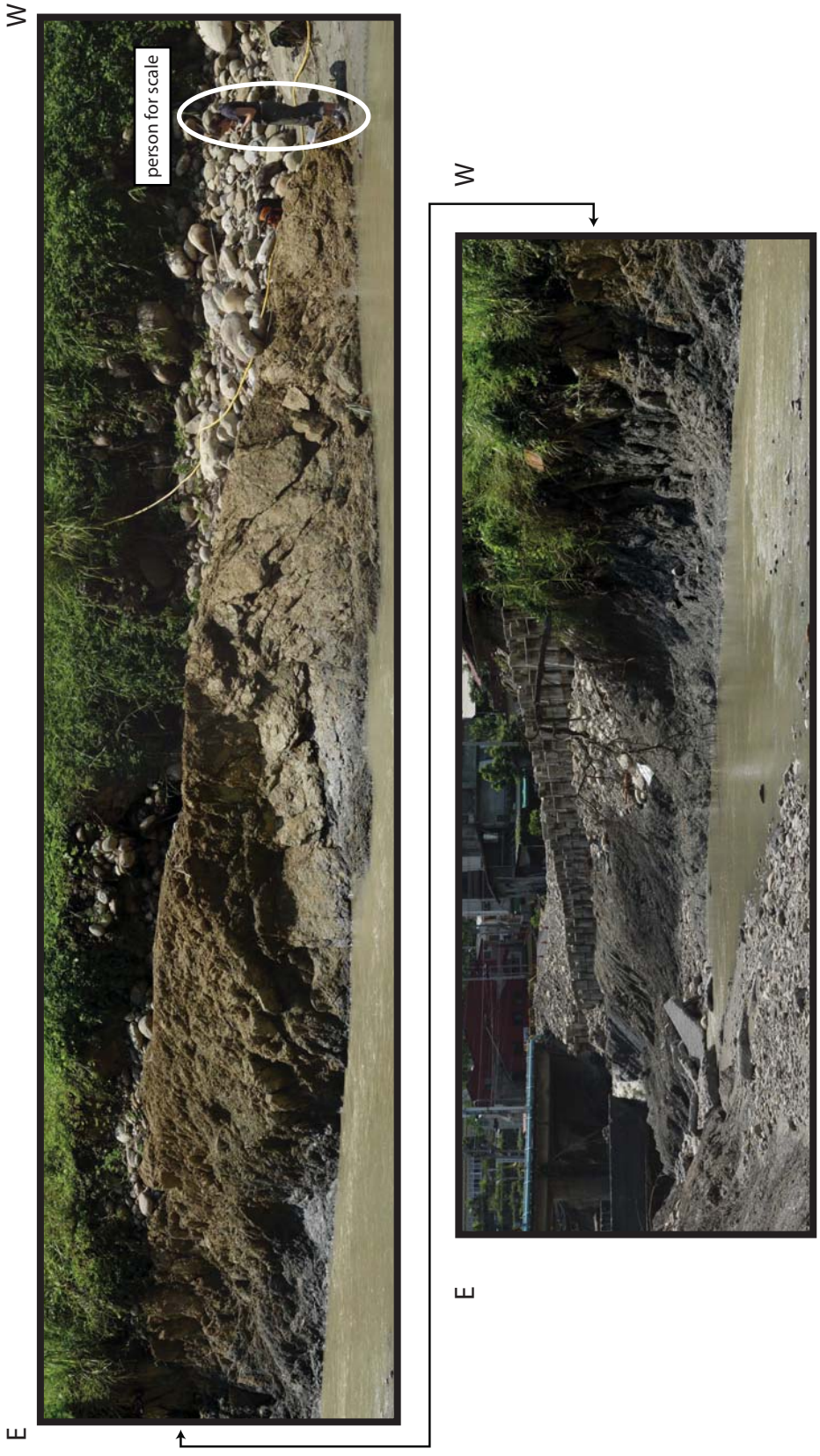

Figure A-4. Photograph mosaic of the outcrop at field site 3 from the fault contact along the line of transect.

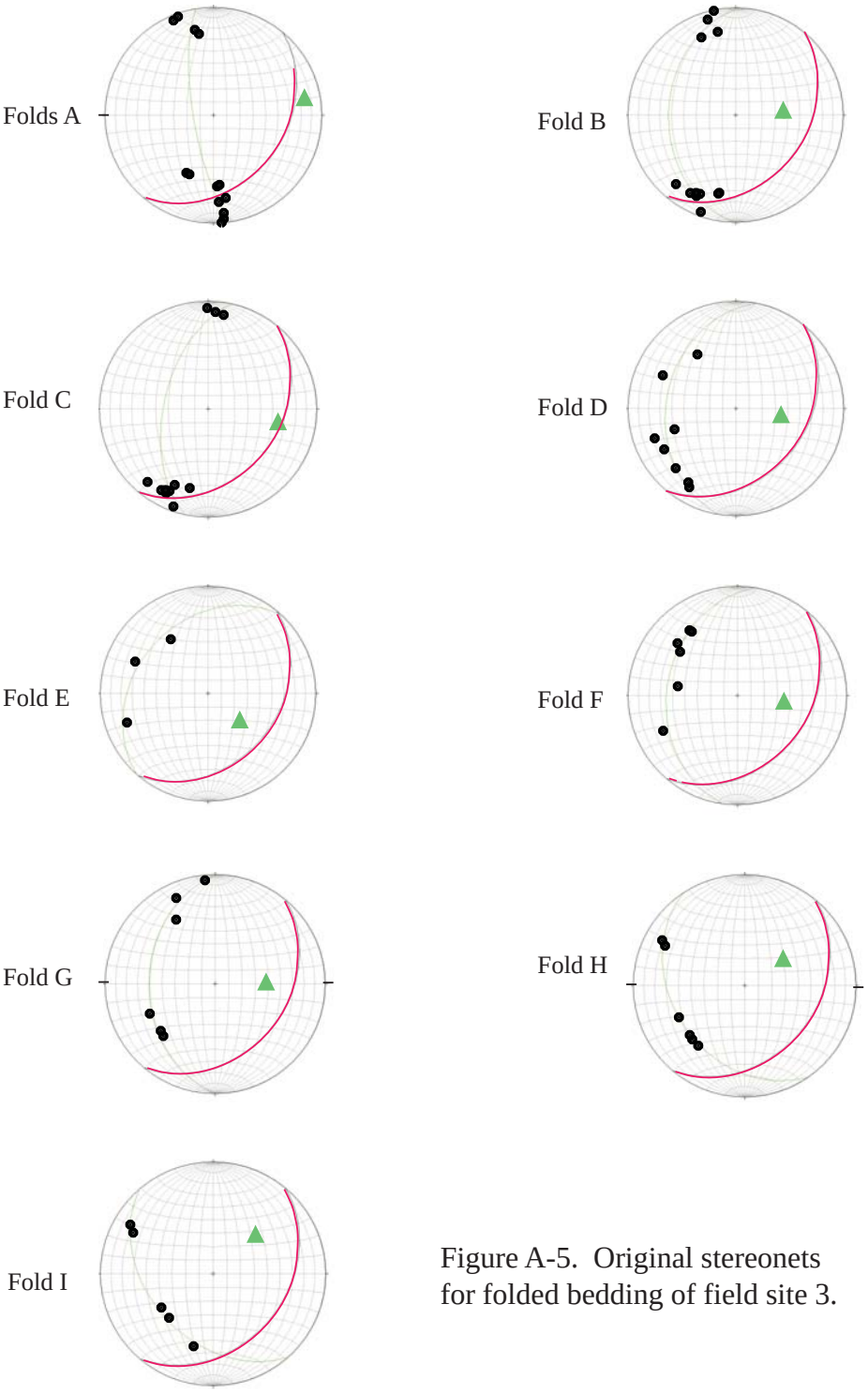

Figure A-5. Original stereonets for folded bedding of field site 3.

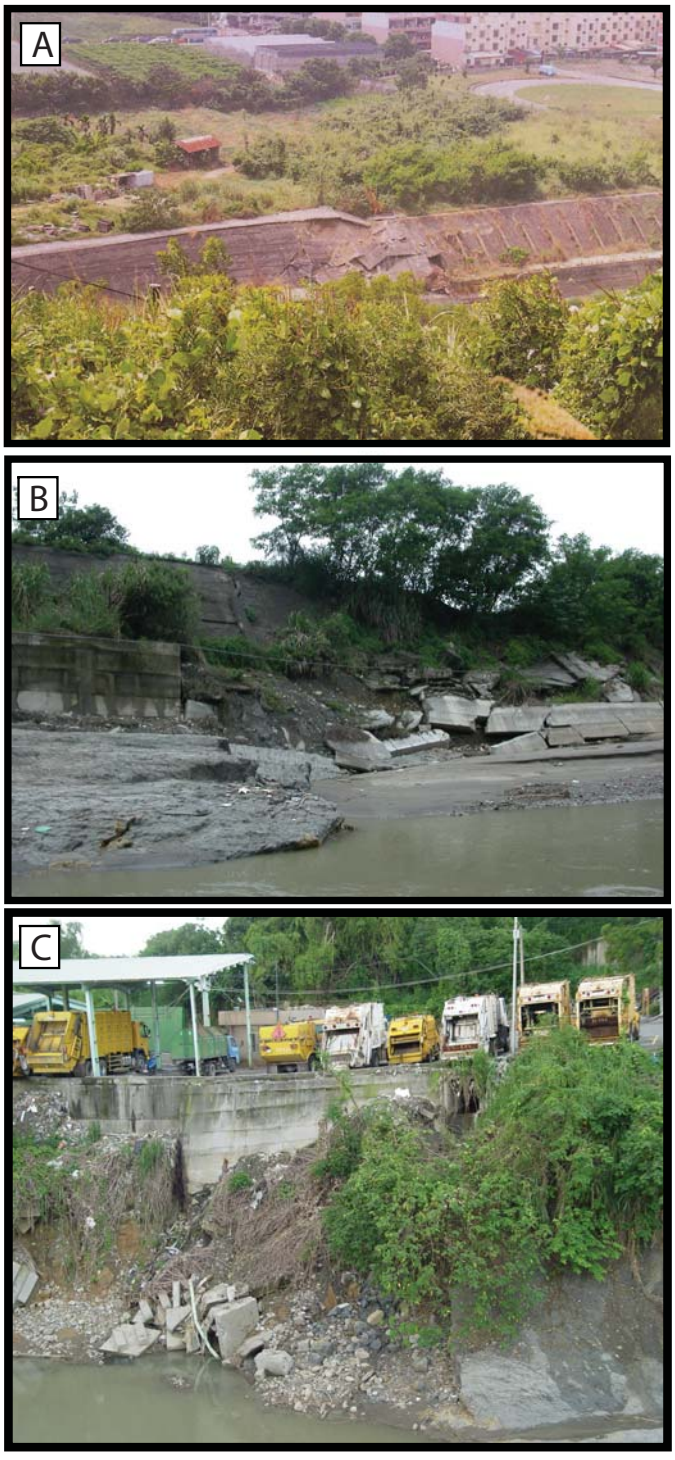

Figure A-6. Photographs of the 1999 rupture at site 4: a) View to the southwest of cement lining the walls of a branch of the Wu River, 1999 (September 21 Earthquake Geology Research). b) View to the southwest, 2004. c) View to the north of the 1999 rupture, 2004.

Figure A-7. Small subsidiary faults at 33-47 m. Field site 4, 2004.

Figure A-8. Sandstone filled burrows in shale at 57-70 m and 77-83 m Field site 4, 2004.

Figure A-9. Looking south at folded bedding at ~130-175 m along the transect line. Field site 4, 2004.

Figure A-10. Looking north at a chevron fold within a larger fauld and faulted sandstone bed at ~165 m. Field site 4, 2004.

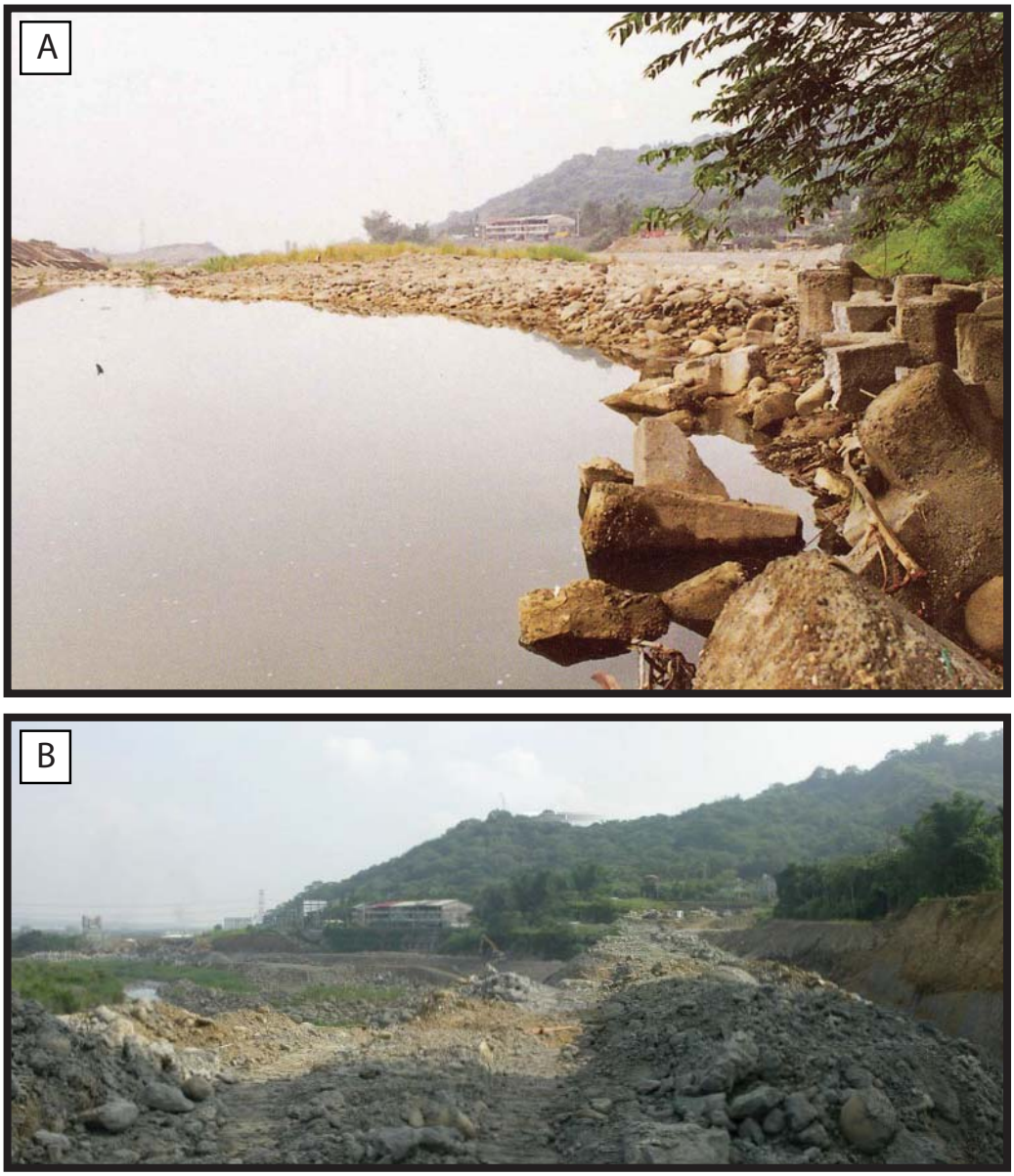

Figure A-11. Looking northwest at the 1999 rupture: a) The Dong Pu Ruey River temporarily dammed by the rupture, 1999 (September 21 Earthquake Geology Research). b) Looking across construction at site 5. The outcrop where samples were collected is in the left of the photograph, 2004.

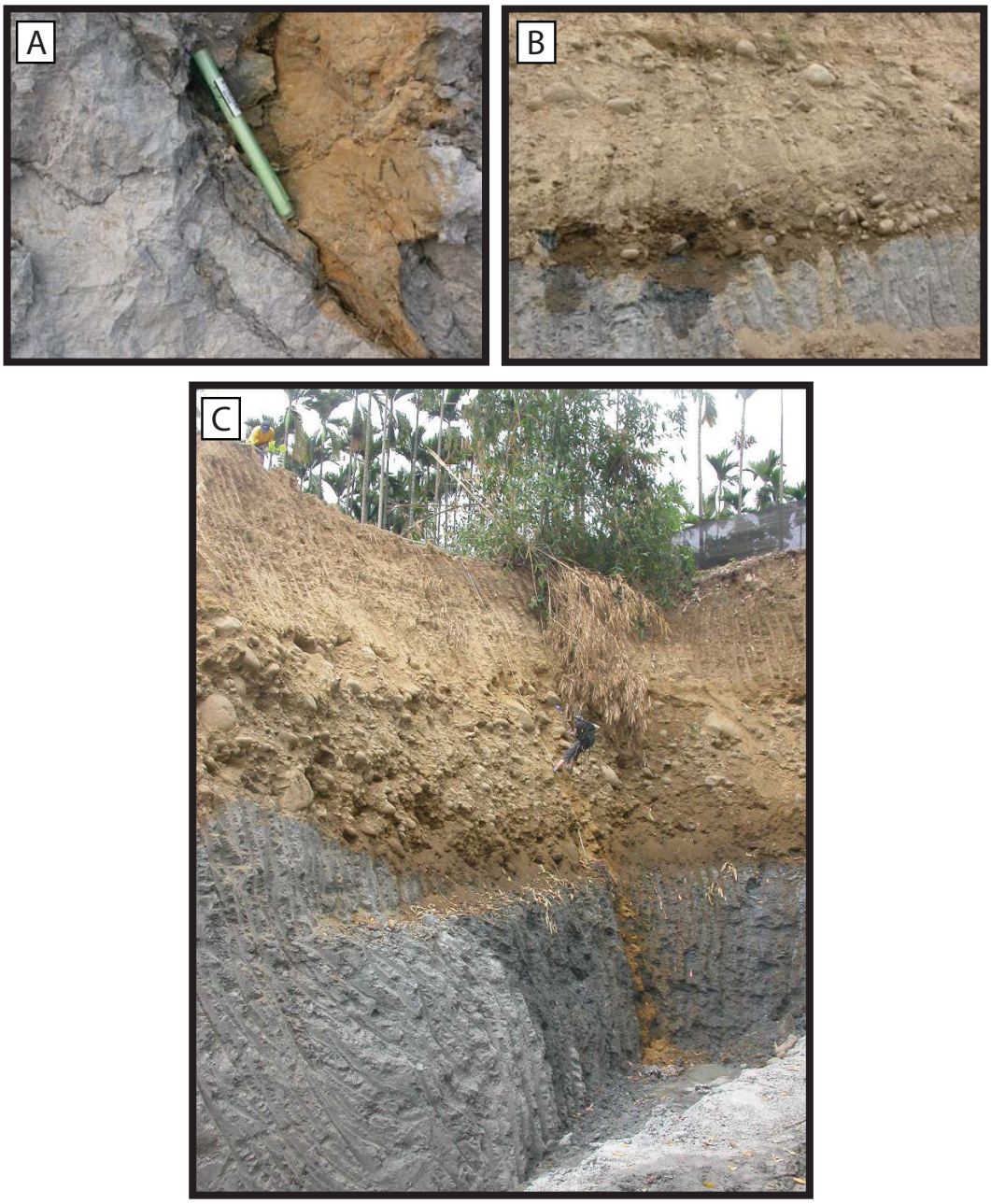

Figure A-12. Photographs of the hanging wall of the Chelungpu fault at site 5: a) Alteration along a secondary fault and associated shear fabric. b) Groundwater flows along the gravel-bedrock contact. c) The excavated outcrop at site 5.

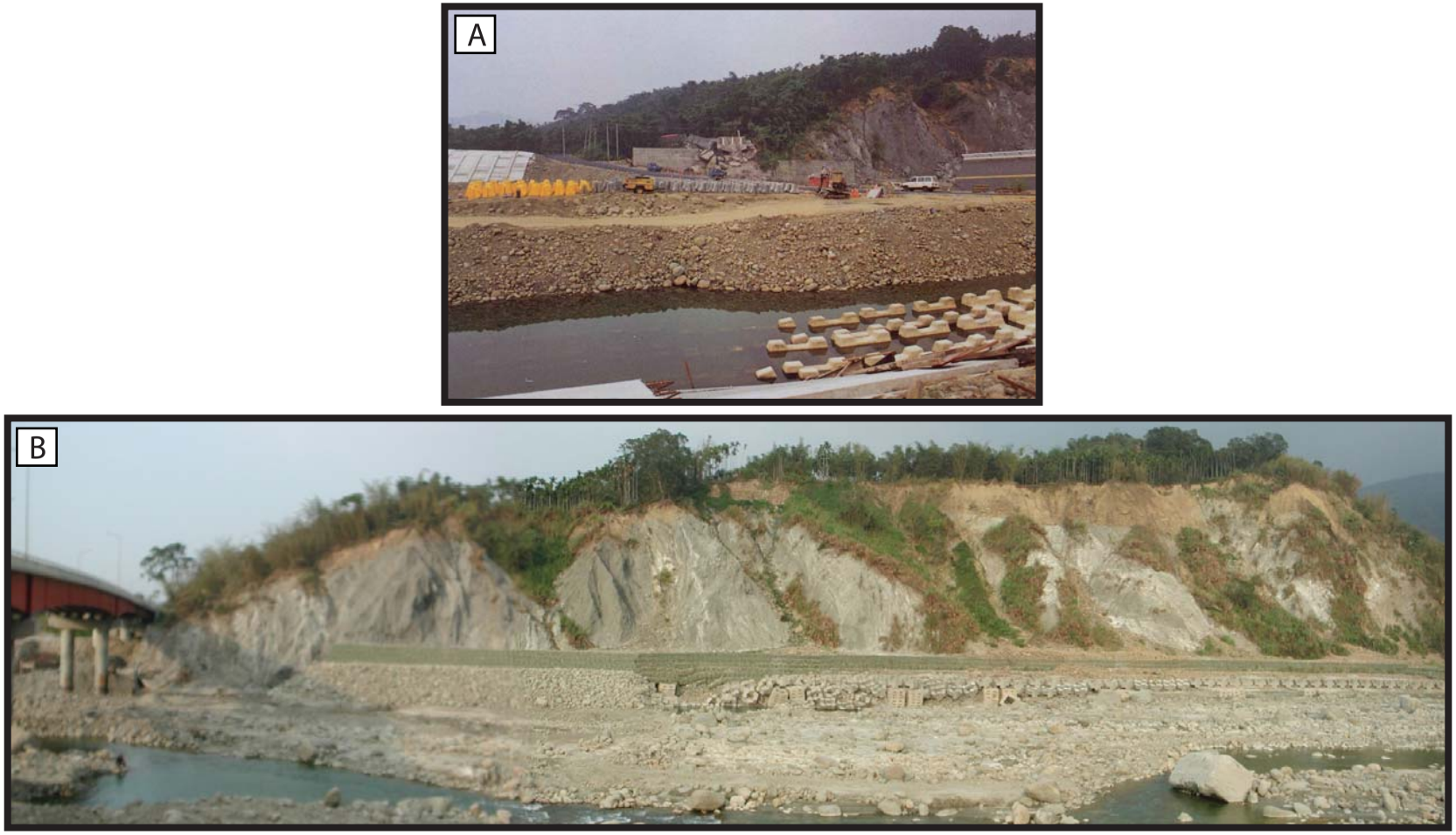

Figure A-13. Photographs of the outcrop at site 6: a) View to the northeast of rebuilding efforts at site 6 after the 1999 rupture (September 21 Earthquake Geology Research). b) View to the north of the outcrop at site 6, 2002.

APPENDIX B

DETAILS OF LABORATORY METHODS

There are several things to keep in mind when you are preparing samples for x-ray diffraction (XRD).

- Avoid heating samples at temperatures >50^{o} C. The smectite – illite reaction typically initiates at 100-150^{o} C; however, has been reported to occur at lower temperatures.
- The presence of quartz in bulk powder samples assists random orientation of clay, however use caution when packing powder into sample holders. Mechanical powder packers may induce orientation of clays, using a side-packing or hand-packing method.
- Disaggregate samples when possible, however some samples will not completely disaggregate. Do not use a grinding machine. If the sample is a fine-grained sedimentary rock, grind a portion of the sample by hand with mortar and pestle until the texture of the sample is smooth.

Methods for Preparation of Oriented Clay XRD Samples

There are many methods for preparing samples for XRD analyses. You should choose a method that is appropriate to your goals and is cost-efficient. For example, the method that delivers the best quantitative XRD results (the Millpore-transfer method; Moore and Reynolds, 1997) is extremely time-consuming, and much more expensive than other methods. Quantitative XRD is also very time-consuming and difficult. If you only need to know which types of clay are present in a sample, but do not plan to do any

semi-quantitative or quantitative analyses, simple preparations can be made. It may even be possible to interpret possible clay types from random powder patterns. However, additional tests with oriented clay samples are required to verify the presence of most clay types. The following text describes some alternate methods to the Millpore-transfer method that were explored through the course of this thesis work that may be applicable to many standard XRD analyses.

Simple Oriented Clay Samples

Add disaggregated sediment to de-ionized or distilled water and allow settling for ~1 min. Extract a small portion from the top of the water with an eye-dropper or syringe and deposit this on a glass slide. Allow this to air-dry. If you wish to compare XRD pattern to each other, you must try to make the mixtures as consistent as possible. Extract 1 ml from the top of a mixture of 1 g of sample in 10 ml of water, and deposit this on a glass slide.

Clay Smear for Oriented Clay XRD

The clay smear (Moore and Reynolds, 1997) is similar to the simple oriented clay sample described above; however, the smear allows for a random grain-size distribution, which may be a problem for the simple oriented clay sample. To make a clay smear, simply add a few drops of water to a powdered sample, creating a mud or slurry, and smooth evenly on a glass slide. This can be used with bulk powder samples to intensify the clay 001 peaks, or can be incorporated into methods which involve separating the clay fraction from the coarser fraction of a sample. The clay smear can easily be incorporated into the *collection of clay by settling* method described later.

Size Analysis and Oriented Samples

This method is courtesy of Peter Kolesar from his "Introduction to Clay XRD" class taught at Utah State University. This method should be used to determine the grain-size distribution of an unknown sample, and to prepare oriented samples of the different grain sizes for XRD analyses.

1. Weigh out approximately 150-200 grams of sample. The actual amount is not critical, but be sure you record the weight; estimate the amount needed to give you approximately 20-30 grams of <250 mesh sample.
2. Be sure all sieves in the stack are clean. Pour your sample into the top sieve. Place the lid on the stack and put the stack into the sieve shaker.
3. Seive for 15 minutes.
4. When the sieve shaker stops, remove the stack of sieves and carefully separate each sieve. Weigh the material caught on each sieve and record the weights and corresponding sieve sizes (Table B-1). Discard the weighed material <u>EXCEPT</u> for the material caught on the 170 mesh sieve. Save that material to prepare a random powder mount for x-ray diffraction.
5. Put the material that passed the 250 mesh sieve into a pre-weighed 250 - 300 ml beaker and reweigh to the nearest 0.01 gm. Add 50 ml of de-ionized water to the beaker and then add 5 ml of 6% H_2O_2 for each gram of sample. Stir thoroughly and cover. If oxidation is slow or after it has slowed, heat the sample to 93^o C, add a little more 6% H_2O_2 and stir. After reaction has completely stopped, wash the sediment 2-3 times using de-ionized water and centrifuge. (This step is not required if there are NO organics in your sample).

6. Place the <250 mesh material into a tall-form 250 ml beaker and add 10 ml of sodium hexametaphosphate (or similar clay dispersant). Add de-ionized water to make up about 200 ml of "dirt" and water.

7. Thoroughly mix the water and sediment; for example, use an ultrasonic dismembrator.

8. Transfer ALL of the sediment-water mixture into a 1-liter graduated cylinder, and bring the volume up to 1 liter with de-ionized water.

9. Mark 6 clean 50 to 100 ml beakers so you can identify them later. Weigh the beakers and record the weights. Mark 5 clean x-ray glass slides for identification. Mark the following on a 20 ml pipette: 3 cm from the pipette tip, 5 cm from the pipette tip, 10 cm from the pipette tip, and 15 cm from the pipette tip.

10. Mix the water/sediment in the graduated cylinder well for approximately 1 min.

11. **Begin timing as soon as you finish mixing**. The time of withdrawal depends on the viscosity of the water, which is a function of temperature, so record the temperature. Withdraw a 20 ml aliquot of the sediment/water mixture at the appropriate time from a depth of 15 cm. Drain the pipette into one of the dry, weighed beakers. Do not blow out any remaining liquid drops; the pipette is calibrated to deliver the correct volume. The first aliquot requires you to work relatively quickly. Withdraw the filled pipette from the graduated cylinder, quickly lower the meniscus to the etched line, then drain the sample into a clean, labeled beaker. Rinse the pipette with de-ionized water. After the first withdrawal, mix the sample again for 1 minute.

12. Begin timing as soon as you finish mixing. Follow the withdrawal time and depth schedule (Table B-2) to obtain 20 ml aliquots of sample that contain the appropriate grain sizes. After the first aliquot (Table B-2), drain the excess sample (the water/sediment above the etched line on the pipette) onto a clean, labeled glass slide, and then drain the pipette into a clean, labeled beaker. Rinse the pipette with de-ionized water after each sample. (**You do not need to remix after each withdrawal now – only the first time!**)
13. Let the mixture in the beakers air-dry. Then place the beakers in the oven at 105^{o} C overnight. Cool the beakers in a desiccator and weigh them (Table B-3).

Collection of Clay Fraction by Settling

This method is used in the geochemistry laboratories at Nation Taiwan University, and is designed to collect the clay fraction of a sample by settling, as well as calculate the percent amount of clay. This method is appropriate for creating a clay smear for oriented clay XRD. Use an appropriate method to disaggregate the sample, and then proceed with this method.

1. Weigh (and record) and label 600 ml beakers to be used for clay extraction.
2. Weigh and label ceramic crucibles for extracted clay to be dried in.
3. Add 20 g of a random sample of disaggregated material to 600 ml beakers.
4. Mix in ~10 g of dry tri-sodium phosphate crystals, 30 ml of sodium-hexametaphosphate solution, or similar clay dispersant.
5. Add de-ionized water to the 600 ml line.
6. Stir well with an ultrasonic dismembrator, plunger, or other similar method.
7. Allow to settle for 6 hrs.

8. Extract the top 6 in/400 ml of water-sediment mixture using a bulb and pipette and deposit into separate, clean containers. This will theoretically extract the <2 μm size grains.
9. Allow the remainder of the coarse sediment and water to dry (evaporate in oven at 50-110^{o} C).
10. Centrifuge the clay-water mixture and CAREFULLY pour off excess water.
11. Remove ALL clay and deposit in ceramic crucibles. Dry at 50^{o} C.
12. Once dry, weigh and record the clay + ceramic crucibles and the beakers + coarse sediment fraction. Calculate the clay fraction of each sample.
13. The clay fraction can now be analyzed by XRD.

Utah State University Soils
Laboratory Hydrometer

1. Break samples in a jaw crusher.
2. Disaggregate the samples; either:

   a. By hand using mortar and pestle.

   b. Ultrasonic disaggregator. Centrifuge and carefully pour off extra water. Dry.
3. Add 100 ml of a 10% Calgon – distilled water mixture to 40 g of loose, dry sample in Erlenmeyer flasks.
4. Mix the solutions in an Eberbach box shaker for ~4 hours – overnight.
5. Transfer the solutions to 1000 ml graduated cylinders.
6. Add distilled water to a volume of 1000 ml.
7. Mix the first sample with a plunger for 1 minute.
8. Take a reading on the hydrometer at 40 sec after the cessation of mixing.

9. Repeat steps 7-8 for each remaining sample.

10. Allow settling and take a second reading for each sample at 6 hrs 40 sec.

References

Moore, D.M., and R.C. Reynolds Jr. (1997). *Individual Clay Minerals, X-ray Diffraction and the Identification and Analysis of Clay Minerals*, Oxford University Press, New York, New York.

Table B-1
Data table for sieve analysis of a sample.

Sieve mesh size	Sieve size (mm)	Sieve size (N)	Weight (gms)	Weight percent of total sample
#5	2.794	-1.5		
#10	1.981	-1.0		
	1.397	-0.5		
#16	0.991	0		
	0.701	0.5		
#32	0.495	1.0		
	0.351	1.5		
#60	0.246	2.0		
	0.175	2.5		
#115	0.124	3.0		
	0.088	3.5		
#250	0.061	4.0		
	<0.061	>4.0		
			Sum of weights on sieves = gms	Initial sample weight = gms
			Weight percent lost = %	

Table B-2

Time of pipette withdrawal for given temperature, depth of withdrawal and diameter of particles.

Diameter of particle (mm) [Φm]	#0.062 [#62]	#0.031 [#31]	#0.016 [#16]	#0.008 [#8]	#0.004 [#4]	#0.002 [#2]
Depth of withdrawal (cm)	15	15	10	10	5	3
Temperature EC	sec	min - sec	min-sec	min-sec	min-sec	hr - min
20	44	2 - 52	7 - 40	30 - 40	61 - 19	2 - 27
21	42	2 - 48	7 - 29	29 - 58	59 - 50	2 - 24
22	41	2 - 45	7 - 18	29 - 13	58 - 22	2 - 20
23	40	2 - 41	7 - 08	28 - 34	57 - 05	2 - 17
24	39	2 - 38	6 - 58	27 - 52	55 - 41	2 - 14
25	38	2 - 34	6 - 48	27 - 14	54 - 25	2 - 11
26	37	2 - 30	6 - 39	26 - 38	53 - 20	2 - 08
27	36	2 - 27	6 - 31	26 - 02	52 - 02	2 - 05
28	36	2 - 23	6 - 22	25 - 28	50 - 52	2 - 02
29	35	2 - 19	6 - 13	24 - 53	49 - 42	1 - 59
30	34	2 - 16	6 - 06	24 - 22	48 - 42	1 - 57

Table B-3

Data table for pipette analysis of grain size in your sample. Column 6 lists the weights of each size fraction. To obtain those weights, for example, the weight of the 62 -31: size fraction, subtract the weight of the sample (x 50) in beaker #2 from the weight of the sample (x 50) in beaker #1.

#	Beaker + sample (g)	Empty beaker (g)	Sample weight (g)	Sample weight x 50 (g)	Weight of each size fraction (g)	Size fraction wgt % of total sample
1				*	#1 - #2 = g	62 - 31 : wgt %
2					#2 - #3 = g	31 - 16 : wgt %
3					#3 - #4 = g	16 - 8 : wgt %
4					#4 - #5 = g	8 - 4 : wgt %
5					#5 - #6 = g	4 - 2 : wgt %
6						# 2 : wgt %

* Weight of sample (x 50) in beaker #1 should be the same as the weight of sample on the pan at the base of the sieve set.

APPENDIX C

RAW ICP AND XRF DATA BY STUDY SITE

Scheme Code	Na2O ICP95A	MgO ICP95A	Al2O3 ICP95A	SiO2 ICP95A	P2O5 ICP95A	K2O ICP95A	CaO ICP95A	TiO2 ICP95A	Cr2O3 ICP95A	MnO ICP95A	Fe2O3 ICP95A	Sr ICP95A	Y ICP95A	Zr ICP95A	Nb ICP95A	Ba ICP95A	Sc ICP95A	LOI ICP95A	Sum ICP95A
Analysis Unit	%	%	%	%	%	%	%	%	%	%	%	ppm	ppm	ppm	ppm	ppm	ppm	%	%
Detection Limit	0.01	0.01	0.01	0.01	0.01	0.01	0.01	0.01	0.01	0.01	0.01	10	10	10	10	10	10	0.01	0.01
FIELD SITE 1																			
T1-PDZ 0+0	1.44	1.83	12.99	64.35	0.12	2.36	1.4	0.76	0.01	0.06	5.39	112	26	215	16	381	11	4.6	95.39
T1-PDZ 0+5	1.56	1.8	12.22	67.17	0.12	2.39	1.92	0.74	0.01	0.06	5.24	128	25	232	19	390	11	4.8	98.14
T1-PDZ 0+15	1.57	2.19	14.19	61.82	0.12	2.66	1.87	0.85	0.01	0.07	6.07	125	28	179	19	398	14	5.5	97.01
T1-SDZ 0+30	1.34	2.55	15.75	58.1	0.12	3.01	2.21	0.89	0.01	0.08	6.79	137	29	172	19	432	16	6.2	97.15
FIELD SITE 2																			
T2-FC 0+0 (37-2)	0.99	1.23	10.94	71.68	0.09	2.22	0.44	0.66	0.01	0.04	4.48	83	22	246	21	442	<10	4.5	96.68
T2-FC 0+0	1.25	1.06	10.88	73.07	0.1	2.29	0.4	0.64	<0.01	0.05	4.39	95	22	202	16	421	<10	3.1	97.33
T2-PDZ 0+3	1.21	1.43	9.85	71.25	0.1	2.15	2.49	0.6	<0.01	0.09	3.93	108	22	253	14	381	<10	4.6	97.81
T2-PDZ 0+10	1.26	1.56	10.52	70.07	0.1	2.22	2.52	0.62	0.01	0.09	4.34	117	23	231	15	388	<10	4.6	98
T2-PDZ 0+15	1.44	1.9	11.7	66.03	0.12	2.31	2.62	0.7	0.01	0.07	4.97	118	25	210	17	373	11	5.3	97.26
T2-SDZ 0+20	1.45	2.02	12.75	65.59	0.12	2.48	2.11	0.76	0.01	0.06	5.46	119	26	204	18	395	12	5.3	98.21
T2-SDZ 0+30	1.33	2.21	13.8	62.54	0.12	2.72	1.94	0.79	0.01	0.06	6.03	129	26	181	18	414	13	5.3	96.94
T2-SDZ 0+40	1.11	2.24	16.17	61.9	0.11	3.08	1	0.86	0.01	0.05	6.47	116	26	179	18	432	16	5.2	98.29
T2-SDZ 0+100	1.51	1.78	11.54	68.43	0.12	2.33	1.76	0.7	0.01	0.06	4.84	124	26	217	18	401	11	4.3	97.48
T2-SDZ 0+110	1.35	2.28	14.27	61.68	0.12	2.81	1.91	0.84	0.01	0.07	6.14	128	29	237	22	427	14	5.7	97.27
FIELD SITE 4																			
T4-PDZ 0+0	1.24	0.86	9.43	76.72	0.08	1.95	0.24	0.58	<0.01	0.02	2.81	82	21	347	14	357	<10	2.3	96.35
T4-FC 0+0F	1.15	1.07	10.65	73.81	0.11	2.24	0.33	0.65	0.01	0.11	5.38	100	24	372	15	436	<10	3.3	98.91
T4-PDZ 0+5	1.45	1.68	12	70.36	0.12	2.36	1.34	0.73	0.01	0.06	5.05	109	24	216	15	388	11	4.2	99.46
T4-PDZ 0+10	1.52	1.52	11.19	73.6	0.11	2.25	1.16	0.69	<0.01	0.04	4.56	114	24	217	15	397	<10	3.5	100.3
T4-PDZ 0+20	1.45	1.35	9.6	75.71	0.09	2.08	1.26	0.58	<0.01	0.04	4.06	106	22	249	11	382	<10	3.2	99.52
T4-FG 0+39.8	1.5	1.6	12.29	71.37	0.1	2.48	0.64	0.77	0.01	0.06	5.22	108	25	271	15	425	11	3.7	99.85
T4-FG 0+40	1.31	1.62	13.07	70.36	0.1	2.69	0.48	0.78	0.01	0.05	4.98	103	25	255	16	444	12	3.6	99.14
T4-FG 0+53.2	1.19	2.44	14.89	62.17	0.21	2.92	1.47	0.91	0.01	0.1	6.58	131	33	238	18	455	16	5.8	98.8
T4-FG 0+135	1.1	1.29	9.32	77.6	0.08	2.1	0.61	0.63	<0.01	0.04	3.97	91	24	347	13	378	<10	2.4	99.24
T4-SDZ 0+139	1.19	1.75	11.92	72.02	0.11	2.57	0.56	0.73	0.01	0.05	5.52	92	24	280	16	401	11	3.6	100.1
T4-SDZ 0+128	1.39	2.42	13.5	60.54	0.23	2.65	4.81	0.79	0.01	0.17	5.77	147	28	168	16	410	13	7.3	99.67
T4-FG 0+143	1.07	1.56	10.53	74.4	0.08	2.21	0.61	0.61	<0.01	0.05	4.97	84	21	159	16	376	10	3.2	99.36
T4-FG 0+145	0.94	0.73	5.48	86.47	0.05	1.65	0.37	0.31	<0.01	0.04	2.58	67	12	148	<10	345	<10	1.6	100.3
T4-FG 0+146	1.36	2.35	15.8	63.02	0.14	3.02	0.63	0.98	0.01	0.06	7.4	102	30	234	23	439	16	5.1	99.98
T4-SDZ 0+155	1.14	0.57	4.76	88.7	0.05	1.48	0.38	0.29	<0.01	0.03	2.08	62	11	189	<10	323	<10	1.5	101.1
T4-SDZ 0+170	1.31	2.34	15.28	63.4	0.12	3	1.59	0.87	0.01	0.06	6.65	121	28	195	18	437	15	5.4	100.1
T4-SDZ 0+185	1.31	1.9	11.71	67.2	0.13	2.38	3.76	0.71	0.01	0.08	4.98	122	25	215	16	377	11	6	100.2
FIELD SITE 7																			
T7-2	1.35	1.84	12.79	66.69	0.11	2.63	1.28	0.8	0.01	0.05	5.21	110	28	256	19	403	12	4.3	97.15
T7-F	1.33	1.08	9.63	76.15	0.09	2.11	0.47	0.6	<0.01	0.02	3.58	83	20	274	15	370	<10	2.7	97.87
T7-W1 0-10	1.36	1.88	12.08	66.8	0.13	2.5	1.87	0.74	0.01	0.06	5.03	130	26	284	17	407	11	4.7	97.27
T7-W1 0-12	1.58	1.49	10.73	70.53	0.1	2.2	1.13	0.7	<0.01	0.05	4.42	129	25	285	16	384	<10	3.8	96.84
T7-W2 0-8g	1.29	1.57	11.55	70.14	0.09	2.39	0.85	0.73	0.01	0.04	4.6	93	25	284	18	386	10	3.9	97.27
T7-W2 0-8h	1.33	1.04	7.41	79.75	0.08	1.94	0.53	0.43	<0.01	0.03	2.93	86	18	226	<10	381	<10	2.5	98.07

	Na2O	MgO	Al2O3	SiO2	P2O5	K2O	CaO	TiO2	Cr2O3	MnO	Fe2O3	Sr	Y	Zr	Nb	Ba	Sc		LOI	Sum
Scheme Code	XRF	XRF	XRF	XRF	XRF	XRF	XRF	XRF	XRF	XRF	XRF		-	-	-	-	-	- XRF		XRF
Analysis Unit	%	%	%	%	%	%	%	%	%	%	%		-	-	-	-	-	- %		%
FIELD SITE 8																				
T8-FG 0+10	1.41	1.55	12.5	68.48	0.1	2.48	0.88	0.69	0.01	0.05	5.03	107	23	208	18	379	11	4	97.27
T8-PDZ 0+11	1.48	1.39	11.21	72.11	0.09	2.3	0.74	0.64	0.01	0.05	4.64	100	23	281	14	365	10	3.2	97.97
T8-FG 0+12	1.45	1.97	15.61	62.97	0.1	2.94	0.97	0.85	0.01	0.07	6.41	118	29	202	19	410	15	4.4	97.85
T8-PDZ 0+21	1.3	2.41	17.6	58.2	0.11	3.43	0.53	0.89	0.01	0.06	7.41	114	29	173	21	472	17	5	97.05
T8-PDZ 0+25	1.34	1.09	8.32	78.04	0.08	1.87	0.85	0.55	<0.01	0.05	3.73	89	22	500	13	323	<10	2.6	98.65
T8-PDZ 0+27	1.66	1.66	11.94	69.62	0.11	2.35	0.98	0.71	0.01	0.05	5.09	108	24	222	14	411	11	3.7	97.98
T8-PDZ 0+31	1.58	1.94	12.97	67.14	0.13	2.74	1.41	0.72	0.01	0.06	5.51	119	24	179	15	548	12	4.5	98.82
T8-FG 0+33	1.64	1.22	9.29	76.52	0.08	2.17	0.58	0.55	<0.01	0.03	3.67	89	19	303	12	396	<10	2.5	98.35
T8-FG 0+40	1.53	2.22	14.54	62.4	0.13	2.84	2.23	0.84	0.01	0.06	6.09	133	29	181	19	398	14	5.5	98.49
T8-PDZ 0+55	1.57	1.97	13.15	65.48	0.14	2.54	2.43	0.8	0.01	0.07	5.61	130	26	204	19	400	13	4.9	98.76
T8-FG 0+64 (112-1)	2.04	2.6	12.67	62.75	0.1	0.85	0.57	0.74	0.01	0.03	6.74	132	24	293	21	276	11	9.1	97.68
T8-FG 0+64 (112-6)	2.02	2.61	11.58	63.17	0.1	0.53	0.99	0.69	0.01	0.07	6.37	151	24	313	23	150	<10	10	97.6
T8-SDZ 0+ 69 (112-8)	1.41	1.06	7.24	73.96	0.08	1.67	4.87	0.42	<0.01	0.12	2.96	164	15	207	14	365	<10	6	99.16
T8-FG 0+240 (F50)	1.34	1.44	10.74	71.94	0.09	2.24	1.06	0.63	<0.01	0.05	4.05	96	22	246	20	424	<10	4.2	97.19
TCDP BOREHOLE																				
TCDP511.6-511.7	1.38	2.15	15.12	61.24	0.12	2.89	0.87	0.83	0.01	0.06	6.04	108	26	184	26	456	13	8.2	98.4
TCDP796.0-796.1	1.6	2.28	12.54	63.18	0.14	2.51	2.97	0.78	0.01	0.08	4.96	128	28	249	25	418	11	6.1	96.63
TCDP1016.5-1016.6	1.23	0.79	6.24	74.47	0.06	1.7	4.23	0.36	<0.01	0.1	2.19	168	19	196	<10	375	<10	4.6	95.33
TCDP1031.0-1030.97	1.64	2.14	12.24	62.24	0.12	2.45	4.32	0.75	0.01	0.15	5.02	134	24	198	23	395	11	7.1	97.66
FZ1111.605-1111.63	1.37	2.65	16	56.07	0.13	3.14	2.05	0.89	0.01	0.08	6.69	125	28	178	28	444	15	7.9	96.52
FZ1152.81-1152.84	1.22	1.62	9.89	67.77	0.11	2.14	2.87	0.61	0.05	0.14	5.2	130	23	315	15	379	<10	6	97.05
TCDP1300.25	1.38	2.45	14.37	58.81	0.11	2.7	2.63	0.79	0.01	0.09	6.96	154	25	198	24	421	13	7.9	97.72
TCDP1304.7	0.77	0.56	4.53	84.17	0.03	1.56	0.17	0.2	0.06	0.02	2	60	<10	62	<10	365	<10	1.9	95.2
FENGYUAN BOREHOLE																				
BH-2 50.5 gouge	1.27	1.08	8.08	78.52	0.13	1.5	1.44	0.88	-	0.04	2.56	-	-	-	-	-	-	-	95.5
BH-2 53.8 host	0.98	1.5	10.37	73.96	0.09	2.19	1.36	0.65	-	0.05	3.99	-	-	-	-	-	-	-	95.14
BH 1 221.9 gouge	0.97	2.24	18.35	59.62	0.13	2.9	0.87	1.05	-	0.04	6.16	-	-	-	-	-	-	-	92.33
BH 1 221.85 host	0.36	10.33	8.34	32.6	0.56	1.68	17.31	0.48	-	0.53	4.93	-	-	-	-	-	-	-	77.12
BH-1A 223.45 gouge	0.98	1.69	14.16	64.98	0.14	2.32	0.94	1.07	-	0.04	5.12	-	-	-	-	-	-	-	91.42
BH-1A 223.5 host	0.68	4.72	12.25	51.9	0.31	2.43	6.79	0.74	-	0.28	5.69	-	-	-	-	-	-	-	85.78
BH-1A 283.25 gouge	0.93	2.22	18.19	59.31	0.15	2.8	0.51	1.52	-	0.05	6.93	-	-	-	-	-	-	-	92.58
BH-1A 283.3 host	0.95	1.47	10.17	73.62	0.1	2.07	1.67	0.74	-	0.06	3.94	-	-	-	-	-	-	-	94.79
BH-1A 329.65 gouge	0.76	1.85	12.16	69.04	0.1	2.48	1.14	0.84	-	0.05	5.07	-	-	-	-	-	-	-	93.49
BH-1A 329.7 host	0.69	0.97	7.75	80.44	0.07	1.88	0.78	0.55	-	0.03	2.8	-	-	-	-	-	-	-	95.96
NANTOU BOREHOLE																				
CLF57 gouge	1.01	2.23	12.6	63.6	0.123	2.56	3.39	0.82	-	0.113	5.38	-	-	-	-	-	-	7.06	-
CLF58 gouge	0.612	2.81	15.8	60.3	0.123	2.94	1.94	0.935	-	0.087	6.78	-	-	-	-	-	-	6.8	-
CLF55 DZ	0.891	2.19	11.7	64.2	0.129	2.27	4.32	0.795	-	0.083	4.77	-	-	-	-	-	-	7.6	-
CLF52 DZ	0.93	2.17	12.7	67.1	0.119	2.24	1.88	0.817	-	0.047	5.15	-	-	-	-	-	-	5.76	-
CLF48 host	0.93	1.23	8.19	71.4	0.111	1.17	5.58	0.591	-	0.8	3	-	-	-	-	-	-	6.51	-
CLF47-1 host	1.04	1.53	9.11	69.2	0.133	1.88	5.33	0.693	-	0.093	3.29	-	-	-	-	-	-	6.58	-
CLF35 host	0.917	0.86	7.44	7.61	0.079	1.73	3.91	5.05	-	0.067	3.06	-	-	-	-	-	-	4.91	-
CLF39 host	0.974	1.49	8.19	7.56	0.089	1.83	2.84	5.69	-	0.075	3.14	-	-	-	-	-	-	3.37	-
CLF33 DZ	0.923	0.892	8.05	8.6	0.073	1.96	0.687	5.13	-	0.027	3.1	-	-	-	-	-	-	2.51	-
CLF43 DZ	0.925	2.17	13.6	6.61	0.117	2.6	1.9	8.74	-	0.055	5.59	-	-	-	-	-	-	5.68	-
CLF36 gouge	0.906	2.55	15.5	6.21	0.111	3	1.18	9.27	-	0.053	6.93	-	-	-	-	-	-	6.29	-
CLF41 gouge	0.759	2.86	17.1	5.85	0.122	3.26	1.26	10.5	-	0.069	7.46	-	-	-	-	-	-	6.97	-

APPENDIX D

PERMISSION LETTER

December 10, 2005

Angela J. Isaacs
Utah State University
Department of Geology
4505 Old Main Hill
Logan, Utah 84322
1-435-7971273
angela.isaacs@usu.edu

Dear Dr. S.R. Song:

I am currently preparing my thesis in the Department of Geology at Utah State University. I hope to complete in the Fall of 2005.

I am requesting your permission to include you as a co-author on the second chapter of my thesis manuscript, and also requesting permission to use outcrop and borehole data collected from the Chelungpu fault, Taiwan, as well as X-ray diffraction and X-ray fluorescence data collected at National Taiwan University under your direction as my host during my stay. Proper citation and acknowledgement will be given in my thesis.

Please indicate your approval of this request by signing in the space provided. If you have any questions, please contact me.

Thank you,

Angela Isaacs

I hereby give permission to Angela Isaacs to use the material described above in her thesis.

Signed 

Sheng-Rong Song

Associate Professor ; Department of Geosciences, National Taiwan University